Photomagnetic compounds based on [MIV(CN)8]4- (M = Mo and W)

Xinghui Qi

université de BORDEAUX

THÈSE PRÉSENTÉE POUR OBTENIR LE GRADE DE

DOCTEUR DE L'UNIVERSITÉ DE BORDEAUX

ÉCOLE DOCTORALE DES SCIENCES CHIMIQUES (SC)

SPÉCIALITÉ : Physico-chimie de la matière condensée

Par Xinghui QI

Photomagnetic compounds based on $[M(CN)_8]^{4-}$ building blocks ($M = Mo^{IV}$ and W^{IV})

Sous la direction de Corine MATHONIERE

Soutenue le : 08 Décembre 2021

Membres du jury :

Mme. Limin ZHENG	Professeur, Université de Nanjing, Chine	Rapportrice
M. Talal MALLAH	Professeur, Université Paris-Saclay	Rapporteur
Mme. Xin BAO	Professeur, Université des Sciences et de la Technologie de Nangjing, Chine	Examinatrice
M. Mario MAGLIONE	Directeur de recherche CNRS	Examinateur
M. Guillaume CHASTANET	Directeur de Recherche CNRS	Examinateur
Mme. Corine MATHONIERE	Professeur, Université de Bordeaux	Directrice de thèse

Acknowledgements

I am very grateful to spent four years PhD study in the lab of the Institut de Chimie de la Matière Condensée de Bordeaux (ICMCB). All the ups and downs are turned out to be precious memories. This offers me great opportunities to let me improve both internally and externally. I would like to thank all the people I meet in this short journey for helping me become better version of me and giving me the courage to go through all the difficult days.

First of all, I am honored to have this important opportunity to pursue my PhD study in France with the financial support by China Scholarship Council. Then I need to thank Mario MAGLIONE for welcome me in ICMCB as director who has helped create a wonderful condition for doing research.

I would like to thank Prof. Talal MALLAH and Prof. Limin ZHENG for their time and consideration to review this thesis in great detail. I also needs to thank Prof. Mario MAGLIONE, Prof. Xin BAO and Prof. Guillaume CHASTANET for their participation in the thesis defense jury.

Most importantly, I want to express my heartfelt thanks to my supervisor, Prof. Corine MATHONIERE, for everything she has done for me. Following her lead and supervision in every aspects, I have transformed a lot to carry out the systematic research both experimentally and theoretically. She has taught and trained me in a pedagogical way for this intriguing research project. I am very impressed with her passion and good instinct for research. She is always rigorous, dynamic and very lovely to give me tremendous advices and discussions whenever I need. The writing of this thesis cannot be completed without her valuable efforts, suggestions and criticisms which deserves my sincere appreciation. She has a charming personal character and always encourages me to go through the hardships.

I could not have carried out my research work without the patient help of Dr. Nathalie DARO. I want to thank her for all the advices for the experiments, purchase of necessary chemicals and helping me handle procedures for the scientific trips. I want to express my heartfelt thanks for the time and patience of Prof. Philippe GUIONNEAU with professional skills in respect of the crystallography. Prof. Guillaume CHASTANET deserves my endless gratitude for leading so great research group oriented around magnetism and his valuable advices for my phD project. Special thanks should be given to Dr. Patrick ROSA for all he has done for the SQUID and VSM experiments, which is time-consuming and exhausting. I want to show my respect to other high-level researchers in our group: Prof. Mathieu

MARCHIVIE, Prof. Cédric DESPLANCHES and Dr. Mathieu GONIDEC for all the daily interactions, which demonstrates me the beauty of the academia.

Special thanks should be given to Prof. Sébastien PILLET and Prof. El-Eulmi BENDEIF of CRM2 group in Lorraine University for providing me remarkable chances to stay one month in their lab. They did their best to create the best experimental conditions for my stay there.

I would like to thank Prof. Coen DE GRAAF in Universitat Rovira i Virgili for the important theoretical calculations to shed light for my PhD project.

I also owe special thanks to Prof. Dawid PINKOWICZ and Michał MAGOTT in Jagiellonian University for their contribution in this research project.

I would like to express thanks to all the experienced researchers in our lab for their important technical assistances: Stanislav PECHEV and Eric LEBRAUD for X-ray diffraction studies, Mathieu DUTTINE for EPR experiments, Sonia BUFFIERE for SEM analysis and training, Dominique DENUX for TGA measurements, and Alexandre FARGUES for IR and UV-Vis measurements.

I also appreciate all the nice scientifical discussions with the M3 group in the Centre de Recherche Paul Pascal (CRPP). I was inspired a lot from Prof. Rodolphe CLÉRAC for his enthusiasm for magnetism. I also need to thank Dr. Mathieu ROUZIÈRES for his help for the reflectivity measurement, and Dr. Xiaozhou MA, Dandan LOU, Dr. Panagiota PERLEPE, Dr. Itziar OYARZABAL for their help for IR measurements.

I would like to thank the research work of Dr. Olaf STEFAŃCZYK who have laid important foundation for my PhD project.

I will forever be grateful to my former supervisor for master thesis, Prof. Xiaoying HUANG who influenced me a lot by his own serious attitude toward pursuing the truth in research. He guided me with his endless interest for crystal structure determination. He also encouraged me to study abroad and he is always willing to offer me discussions of some of crystals in this thesis.

I do appreciate all the enjoyable moment with Dr. Juan HÉCTOR GONZALEZ ESTEFAN, Dr. Wenbin GUO, Dr. Liza EL KHOURY and Margaux PENICAUD in the same office D23. The culture differences and similarities open my perspectives to the world. I also

need to thank Dr. Marlène PALLUEL, Dr. Elodie TAILLEUR, Thiết VŨ THỊ and Dr. Ram KUMAR for their friendship and meaningful help.

I want to express thanks to Zhengyan SHEN, Fenghuan ZHAO, Qingguo BAI, Zaicheng ZHANG, Lina WANG and Yuechao DONG for their accompany for all the good time spent together in Bordeaux.

The redaction of this thesis witnessed the pandemic of Covid-19 hitting the whole world, which is a big tragedy. Due to the inconvenience for travel in this special period, it is a pity for me that I cannot pass the last several months of my phD study in Bordeaux because I am trapped in China due to the pregnancy.

I want to dedicate my heart to my parents, my brothers Xingguo and Xingjun who always support me to achieve my self-actualization. I would like to thank my baby Rangyan DU, just a couple of months old, who keep accompanying me for the last year of my PhD. I want to thank him for the joyful pregnant period and all the precious moments at the very beginning of his life. Last but not least, no words can describe my gratitude towards my husband Kezhao DU for his accompany, continuous support, a good demonstration of being a professional researcher by himself. Especially, he undertakes all the chores and ensures Rangyan be well fed and cared during my thesis correction.

Merci à tous!

Xinghui QI

Fuzhou, September 2021

Acknowledgements

Abbreviations

SCO	Spin CrossOver
HS	High Spin
LS	Low Spin
SCXRD	Single-Crystal X-Ray Diffraction
PXRD	Powder X-Ray Diffraction
MMCT	Metal-to-Metal Charge Transfer
MLCT	Metal-to-Ligand Charge Transfer
LIESST	Light-Induced Excited Spin State Trapping
T_c	Curie temperature
T_{relax}	Relaxation temperature: temperature for which the system is back to its initial state
LD-CISSS	Light-Driven Coordination-Induced Spin-State Switching
PBA	Prussian Blue Analogue
XAS	X-ray Absorption Spectroscopy
XMCD	X-ray Magnetic Circular Dichroism
IR	Infrared spectroscopy
CShM	Analysis of Continuous Shape measures
1D	One-dimensional
2D	Two-dimensional
3D	Three-dimensional
en	ethylenediamine
tren	tris(2-aminoethyl)amine
phen	1,10-phenanthroline
ptz	1-propyltetrazole
THz-TDS	Terahertz time-domain spectroscopy
tpa	tris(2-pyridylmethyl)amine
bapa	bis(3-aminopropyl)amine
pn	1,3-diaminopropane
bpmen	N, N′-dimethyl-N, N′-bis(2-pyridylmethyl)1,2-diaminoethane
cyclam	1,4,8,11-tetraazacyclodecane
bpy	2,2’-bipyridyl
meen	N-methylethylenediamine
eten	N-ethyl-ethylenediamine
dppip	1,4-di(4-pyridinyl)piperazine
dpop	2,13-dimethyl-3,6,9,12,18-pentaazabicyclo-[12.3.1]octadeca-1(18),2,12,14,16-pentaene
enpnen	N,N′-bis(2-aminoethyl)-1,3-propanediamine

Abbreviations

List of compounds studied in this thesis

	Compounds
1	$K_4[Mo(CN)_8]\cdot 2H_2O$
2	$[K(crypt\text{-}222)]_3[Mo^{IV}(CN)_7]\cdot 3CH_3CN$
3	$Rb_4[Mo(CN)_8]\cdot 2H_2O$
4	$Cs_{20}[Mo(CN)_8]_5\cdot 7H_2O$
5	$Na_4[Mo(CN)_8]\cdot 4H_2O$
6	$Li_2K_2[Mo(CN)_8]\cdot 5H_2O$
7	$K_4[W(CN)_8]\cdot 2H_2O$
8	$Rb_4[W(CN)_8]\cdot H_2O$
9	$K_6Cs_{16}[W(CN)_8]_5Cl_2\cdot 4H_2O$
10	$[Zn(en)_3]_2[Mo(CN)_8]\cdot 5H_2O$
11	$[\{Zn(tren)\}_3(\mu\text{-}tren)]_2[Mo(CN)_8]_3\cdot 18H_2O$
12	$[\{Cd(tren)\}_3(\mu\text{-}tren)]_2[Mo(CN)_8]_3\cdot xH_2O$
13	$[\{Cu(tren)\}_3(\mu\text{-}tren)]_4[Mo(CN)_8]_6\cdot 45H_2O\cdot 2CH_3OH$
14	$[Zn(en)_3]_2[W(CN)_8]\cdot 5H_2O$
15	$[\{Zn(tren)\}_3(\mu\text{-}tren)]_2[W(CN)_8]_3\cdot 17H_2O$
16	$Cd_2[Mo(CN)_8]\cdot 8H_2O$
17	$KCu^{I}Cu^{II}Mo(CN)_8\cdot 3H_2O$
18	$K_2Cu^{I}_3(\mu\text{-}CN)Mo(CN)_8\cdot 4H_2O$
19	$K_2Cu^{I}_3(\mu\text{-}CN)W(CN)_8\cdot 4H_2O$
20	$[Cu(en)_2]_2[Mo(CN)_8]$
21	$[Cu(en)]_3[Cu(en)_2]_2[Mo(CN)_8]_{2.5}\cdot 2MeOH\cdot 5H_2O$

List of compounds studied in this thesis

Table of contents

Table of contents

Table of contents

General Introduction

In recent years, molecular functional materials have attracted tremendous attention for their potential technological applications in electronics, magnetism, sensors, actuators and/or data treatment unit. As an attractive class of materials, the molecular based materials show important features including low density, easy synthesis with low energy cost and simple tuning of properties at the molecular level. It is well demonstrated that molecular based materials can be synthesized at room temperature with high yield and good reproducibility. A broad range of molecular materials has been prepared by the easy self-assembly of well-designed precursors considering the target applications, with properties relatively well-predictable from chemical components.

Switchable molecular materials can be converted between different states by external stimuli, such as light, temperature, pressure, magnetic or electric field.[1] For example, molecular based photomagnetic materials allow the manipulation of their magnetic states by light with the modification of the spin centers of molecular units. Photomagnetic molecules can be used as molecular bits and can be addressed by light of different wavelengths. Thus, molecular based photomagnetic materials can drastically improve the storage capacity by manipulating magnetic states at the molecular level rather than at the level of a magnetic domain as realized in existing recording materials. They are thus promising for high-density information storage, molecular electronic devices and rewriting displays.[2-3]

A wide range of transition metal ions complexes have attracted great research interest with different photomagnetic mechanisms such as spin crossover (SCO), metal-to-metal charge transfer (MMCT), and photoinduced isomerizations. However, the photoinduced excited states are usually only stable at cryogenic temperatures, below 100 K. To be used in applications, the photomagnetic material operating at ambient temperature is still a great demand.

The photomagnetic compounds reported so far are mainly made of 3d metal ions, while the incorporation of 4d/5d metal ions has been less investigated. 4d/5d octacyanidometalate (named after OCM) building blocks, $[M^{IV}(CN)_8]^{4-}$ (M = Mo, W) are studied for constructing photomagnetic magnets since the first discovery of the intriguing light induced spontaneous magnetization for $Cu_2[Mo^{IV}(CN)_8]\cdot xH_2O$.[4-8] Versatile $[M(CN)_8]^{n-}$ building blocks can exhibit variable oxidation numbers (M^{IV} and M^{V}) and structural flexibility (e.g., M^{n+} site can adopt several coordination geometries, such as square antiprism, dodecahedron and bicapped trigonal prism). About the photomagnetic properties of such systems, a surprisingly high relaxation temperature (~ 300 K), temperature for which the system is totally back to its initial state, has been observed for a heptanuclear complex $[Mo^{IV}(CN)_2(CN\text{-}CuL)_6](ClO_4)_8$ (**Cu_6Mo**, L = tris(2-amino)ethylamine).[9]

During the last two decades, the photomagnetic mechanisms involving $[M^{IV}(CN)_8]^{4-}$ building blocks have been subjected to a continuous debate. The net increase of the magnetic response upon light irradiation has first been explained by the photo-induced electron transfer phenomenon in cyanido bridged Cu^{II}-$[Mo^{IV}(CN)_8]^{4-}$ systems.[4-5, 8, 10-12] Subjected to light irradiation, the Mo^{IV} ion ($4d^2$, $S = 0$) can donate one electron to Cu^{II} ($3d^9$, $S = 1/2$), producing paramagnetic Mo^{V} ($4d^1$, $S = 1/2$) and diamagnetic Cu^{I} ($3d^{10}$, $S = 0$). The photogenerated Mo^{V} centers can be ferromagnetically coupled with the remaining paramagnetic Cu^{II} centers.[7-8] However, an alternative photomagnetic mechanism has been identified as a singlet to triplet mechanism (named after S-T, S for singlet state with $S = 0$ and T for triplet state with $S = 1$) based on Mo^{IV} by X-ray absorption spectroscopy (named after XAS) and X-ray magnetic circular dichroism (named after XMCD) spectra studies in 2010.[13-14] More recently, coexistence of MMCT and S-T photomagnetic mechanisms has been confirmed for the photoresponsive Cu(II)–Mo(IV) bridged assembly $[Cu^{II}(enpnen)]_2[Mo^{IV}(CN)_8]\cdot 6.75H_2O$ (enpnen = N,N′-bis(2-aminoethyl)-1,3-propanediamine).[10] Despite the numerous studies of the intriguing Cu/Mo system, the clear evidences of only electron transfer process involving Cu^{II}–NC−Mo^{IV} linkages or only S-T process based on Mo^{IV} or both processes are still limited. Therefore, more research works are still required for the in depth elucidation of photomagnetic mechanisms in OCM systems.

In this thesis, we have focused our attention on the study $[M(CN)_8]^{4-}$ anions to evaluate their photoinduced magnetic properties. Different structural assemblies have been studied by incorporating various types of metal cations with or without blocking ligands with $[M(CN)_8]^{4-}$ anions. The influence of the structural features (geometries of $[M(CN)_8]^{4-}$, the nature of the cyanide ligands, terminal or bridge and crystal packing) on the photomagnetic properties will be extensively studied. Especially, instead of the most investigated polymeric systems, we mainly focus on discrete $[M(CN)_8]^{4-}$ compounds to gain more insights of the intrinsic photomagnetic properties of OCMs.

In chapter I, we give a general introduction for the representative classes of photomagnetic coordination compounds, with diverse mechanisms involving spin crossover, valence tautomerism, metal-to-metal electron-transfer and ligand-driven spin-state switching. Then we fully describe the recent progresses on photomagnetic materials based on octacyanidometallates.

In chapter II, we focus on the study of the ionic salts in which the negative charge of the $[M^{IV}(CN)_8]^{4-}$ complex is compensated by different alkali cations. $A_4[M(CN)_8]\cdot xH_2O$ (A = Alkali cations: Li^I, Na^I, K^I, Rb^I, Cs^I) are systematically studied by photocrystallography, UV-Vis spectroscopy, infrared (IR) spectroscopy, and photomagnetic properties to evaluate the role of different alkali cations.

In chapter III, we extend our research work to other ionic compounds by incorporating different metal cations with blocking ligands (i.e., $[Zn(en)_3]^{2+}$ (en = ethylenediamine) and $[\{M'(tren)\}_3(\mu\text{-tren})]^{6+}$ (M' = Cu^{2+}, Zn^{2+} and Cd^{2+}; tren = tris(2-amino)ethylamine). The introduction of coordination cations allows diverse possibilities of in the crystal construction and in the study of the relationship between the photomagnetic properties and the structural features (coordination geometries, intermolecular interactions and crystal packing).

In chapter IV, to better understand the electron transfer process involving Cu^{II}–NC–Mo^{IV} units, we study the inorganic Cu^{II}-$[Mo^{IV}(CN)_8]^{4-}$ system to gain insights into the MMCT process when Cu^{II} is not blocked by organic ligands. In addition, we also study an inorganic-organic hybrid Cu^{II}-$[Mo^{IV}(CN)_8]^{4-}$ system when Cu^{II} is blocked by the simple bidentate ligand, ethylenediamine.

At the end of the thesis, general conclusions are provided for this work, and perspectives are also proposed to further contribute to the field of octacyanidemetalate based photomagnetic compounds.

References:

1. Shinkai, S.; Feringa, B., Molecular Switches. Wiley-VCH Verlag GmbH: Weinheim, Germany: 2001.
2. Halcrow, M. A., *Spin-crossover Materials: Properties and Applications*. John Wiley & Sons: 2013.
3. Létard, J.-F.; Guionneau, P.; Goux-Capes, L., Towards Spin Crossover Applications. *Top. Curr. Chem.* **2004,** *235*, 221-249.
4. Ohkoshi, S. I.; Machida, N.; Abe, Y.; Zhong, Z. J.; Hashimoto, K., Visible Light-Induced Reversible Photomagnetism in Copper(II) Octacyanomolybdate(IV). *Chem. Lett.* **2001,** (4), 312-313.
5. Ohkoshi, S.-i.; Machida, N.; Zhong, Z. J.; Hashimoto, K., Photo-induced magnetization in copper(II) octacyanomolybdate(IV). *Synth.Met.* **2001,** *122* (3), 523-527.
6. Rombaut, G.; Mathonière, C.; Guionneau, P.; Golhen, S.; Ouahab, L.; Verelst, M.; Lecante, P., Structural and photo-induced magnetic properties of M_2^{II} $[W^{IV}(CN)_8]\cdot xH_2O$ (M = Fe and x=8, Cu and x=5). Comparison with $Cu_2^{II}[Mo^{IV}(CN)_8]\cdot 7.5H_2O$. *Inorg. Chim. Acta* **2001,** *326* (1), 27-36.
7. Rombaut, G.; Verelst, M.; Golhen, S.; Ouahab, L.; Mathonière, C.; Kahn, O., Structural and Photomagnetic Studies of Two Compounds in the System $Cu^{2+}/Mo(CN)_8^{4-}$: From Trinuclear Molecule to Infinite Network. *Inorg. Chem.* **2001,** *40* (6), 1151-1159.
8. Ohkoshi, S. I.; Tokoro, H.; Hozumi, T.; Zhang, Y.; Hashimoto, K.; Mathonière, C.; Bord, I.; Rombaut, G.; Verelst, M.; Cartier Dit Moulin, C.; Villain, F., Photoinduced Magnetization in Copper Octacyanomolybdate. *J. Am. Chem. Soc.* **2006,** *128* (1), 270-277.
9. Herrera, J. M.; Marvaud, V.; Verdaguer, M.; Marrot, J.; Kalisz, M.; Mathonière, C., Reversible Photoinduced Magnetic Properties in the Heptanuclear Complex $[Mo^{IV}(CN)_2(CN\text{-}CuL)_6]^{8+}$: A Photomagnetic High-Spin Molecule. *Angew. Chem. Int. Ed.* **2004,** *43* (41), 5468-5471.
10. Stefanczyk, O.; Pelka, R.; Majcher, A. M.; Mathoniere, C.; Sieklucka, B., Irradiation Temperature Dependence of the Photomagnetic Mechanisms in a Cyanido-Bridged $Cu_2^{II}Mo^{IV}$ Trinuclear Molecule. *Inorg. Chem.* **2018,** *57* (14), 8137-8145.
11. Bridonneau, N.; Quatremare, P.; von Bardeleben, H. J.; Cantin, J.-L.; Pillet, S.; Bendeif, E.-E.; Marvaud, V., Direct Evidence of a Photoinduced Electron Transfer in Diluted "Molybdenum-Copper" Molecular Compounds. *Eur. J. Inorg. Chem.* **2017**, 370–377.
12. Hozumi, T.; Hashimoto, K.; Ohkoshi, S. I., Electrochemical synthesis, crystal structure, and photomagnetic properties of a three-dimensional cyano-bridged copper-molybdenum complex. *J. Am. Chem. Soc.* **2005,** *127* (11), 3864-3869.
13. Arrio, M.-A.; Long, J. r. m.; Cartier dit Moulin, C.; Bachschmidt, A.; Marvaud, V. r.; Rogalev, A.; Mathonière, C.; Wilhelm, F.; Sainctavit, P., Photoinduced Magnetization on Mo Ion in Copper Octacyanomolybdate: An X-ray Magnetic Circular Dichroism Investigation. *J. Phys. Chem. C.* **2010,** *114* (1), 593-600.
14. Brossard, S.; Volatron, F.; Lisnard, L.; Arrio, M. A.; Catala, L.; Mathoniere, C.; Mallah, T.; dit Moulin, C. C.; Rogalev, A.; Wilhelm, F.; Smekhova, A.; Sainctavit, P., Investigation of the Photoinduced Magnetization of Copper Octacyanomolybdates Nanoparticles by X-ray Magnetic Circular Dichroism. *J. Am. Chem. Soc.* **2012,** *134* (1), 222-228.

Chapter I. Photomagnetism in Coordination Chemistry

Switchable molecular materials can be converted between two states, for which magnetic, electronic, optical, or mechanical properties are controlled by external stimuli, such as light, temperature, pressure, magnetic or electric field.[1] Switchable materials are intriguing because they can be potentially applied as sensors, optical switches or memory devices. Light with different wavelengths in the visible range serves as a convenient tool to access significant modification of electronic states. In this thesis, we are interested in photomagnetic materials because the spin states of metal centers can be switched by light irradiation. Due to their intriguing light tunability of magnetic states, switchable molecular materials have the promising applications in the high-density information storage, molecular electronics devices and rewriting displays .[2-3]

In the first part of this chapter, we concisely review the representative classes of photomagnetic compounds, exhibiting diverse mechanisms involving spin crossover, valence tautomerism, metal-to-metal electron-transfer and light-driven spin-state switching. In addition, other related categories of photomagnetic materials are introduced to illustrate the diversity of photomagnetic materials. Then the second part focuses on the detail description of recent progresses for photomagnetic materials based on octacyanidometallates. Finally, the conclusions and motivations of this thesis are presented at the end of this chapter.

I.1 The classification of photomagnetic coordination compounds

I.1.1 Spin crossover (SCO) systems

For certain molecular systems constituted by transition metal ions with d^4-d^7 configurations in medium donor ligand-field strength, the ligand field splitting energy and electron pairing energy are close. An entropy-driven spin crossover (SCO) from low spin (LS) state to high spin (HS) state upon external stimuli can be activated. This effect has been extensively studied for Fe^{II},[2] Fe^{III}[4] and Co^{II}.[5]

The most well-known example is iron (II) ($3d^6$ electronic configuration) based compound which can undergo spin-crossover. The SCO behavior for Fe^{II} was first discovered in solution by McGarvey et al.,[6] then in solid state for the complex $[Fe(phen)_2(SCN)_2]$ (phen = 1,10-phenanthroline) by Baker et al.[7] The spin crossover between a diamagnetic state Fe^{II}_{LS} and a paramagnetic state Fe^{II}_{HS} can be accessed by the variation of temperature (Figure I. 1). Most commonly, LS and HS states are observed to be interconverted with each other in cooling and heating modes. Crossover temperature $T_{1/2}$ at which the LS and HS fractions are equal to 50 % is a useful parameter to characterize this thermal induced spin crossover. When intermolecular interactions ranging from weak to strong, the types of thermal spin crossover can be modified from gradual to abrupt or even abrupt with hysteresis, for which the $T_{1/2}$ are different in cooling or heating modes (Figure I. 1).[8] In the temperature range within the hysteresis loop, it is possible to access two different states (HS and LS); this property is known as bistability.

The access of bistability with irradiation of light was first reported for $[Fe(ptz)_6](BF_4)_2$ (ptz = 1-propyltetrazole) by Decurtins et al.[9] At temperature much lower than that of the thermal crossover, through irradiating the sample in the spin-allowed d-d or metal-ligand charge transfer (MLCT) absorption bands of the stable LS species, the metastable HS state can be trapped because of structural deformation (e.g. different bond distances, bond angles, octahedron volume, distortion of coordination polyhedron). This effect, which is termed as "light-induced excited spin-state trapping", abbreviated as LIESST, is thermally and/or light reversible.[10-11]

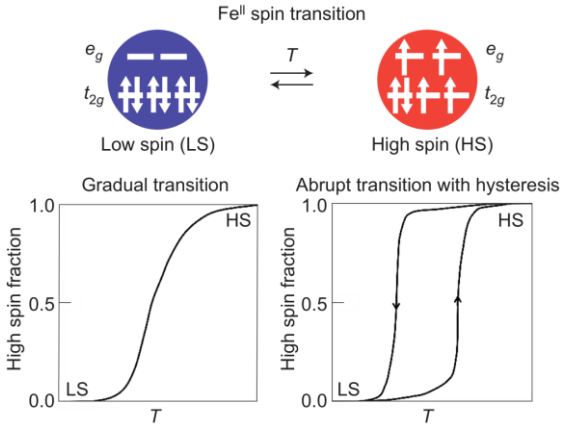

Figure I. 1 (Top) Spin crossover behavior regarding 3d orbitals in Fe^{II} based compounds. Different types of spin crossover depending on the force of intermolecular interactions: gradual (Below left) and abrupt crossover with hysteresis (Below right). Reproduced from Ref. [12] with permission from the Nature 2016.

Owing to the low energy barrier, the relaxation temperature (= temperature for which the system is back to its initial state) is usually below 50 K for most of spin crossover systems, as illustrated for $[Fe(ptz)_6](BF_4)_2$ (ptz = 1-propyltetrazole) (Figure I. 2).

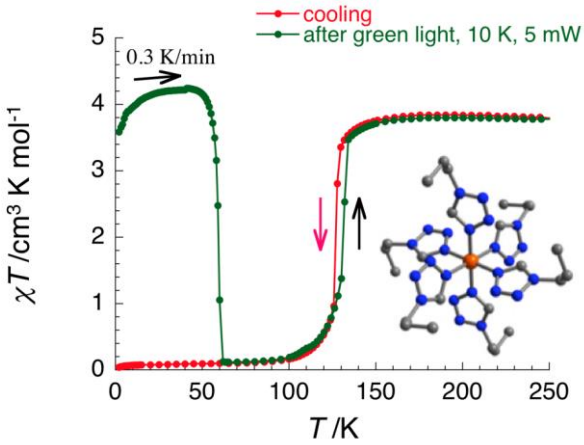

Figure I. 2 Temperature dependence of the χT product for $[Fe(ptz)_6](BF_4)_2$ (ptz = 1-propyltetrazole) before (red) and after (green) 505 nm irradiation at 10 K.

Direct transformation from LS ground state to HS state is forbidden by the spin selection rules. However, the accessing of the HS state ($^5T_2$) is possible by excitation of LS state ($^1A_1$) into metal-to-ligand-charge-transfer (MLCT) band or lower-lying spin-allowed $^1T_1$ or $^1T_2$ states. These excited states decay fast through intersystem crossing processes to the HS state. The population of antibonding e_g orbital for the HS state results in the elongation of Fe-L bond lengths around 0.2 Å for high spin state than the low spin state with the concomitant expansion of the coordination sphere. The light reversibility, the conversion from the HS state ($^5T_2$) to LS state ($^1A_1$), is possible by excitation to lower-lying spin-allowed ^5E state (Figure I. 3).

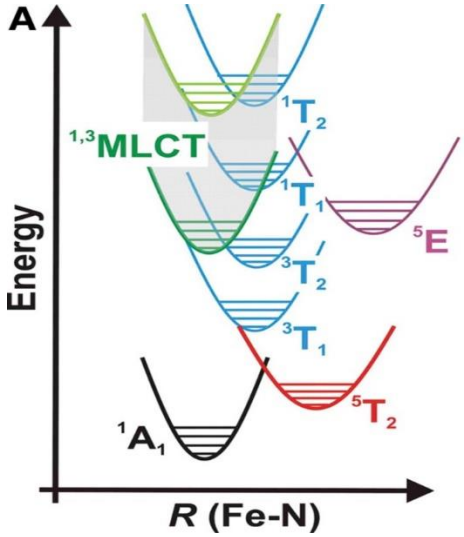

Figure I. 3 Representative potential energy curves of Fe(II)-based SCO complexes as a function of the Fe-N bond distance. The manifold of MLCT states is shown as a shaded area. Reproduced from Ref. [13] with permission from the Science 2009.

In addition to the spin states change during the SCO process, the markedly different absorption behaviors of LS state and HS state also create a distinct color change. To follow the SCO process, magnetic susceptibility, Mössbauer spectroscopic, optical and Raman/FT-IR spectroscopic measurements are the most used methods. Except the vast amount studies for mononuclear SCO complexes, the research of SCO properties have been widely achieved in polynuclear clusters, networks, gels, liquid crystals and thin films.[2] A variety of physical and chemical properties/functions such as ferroelectric, conducting and mechanical properties are able to be tuned by the spin state change.[12] Multifunctional/hybrid materials can be achieved by a synergy between a desired chosen second property and the SCO process.[14]

I.1.2 Electron transfer (ET) systems

Cyanido-bridged complexes exhibiting metal-to-metal electron transfer (MMCT) are another important class of photomagnetic materials. The cyanide bridge can provide a pathway for the electron transfer and further mediate magnetic interaction between the paramagnetic metal ions. The most representative photoactive pair is $Fe^{II}_{LS}Co^{III}_{LS}/Fe^{III}_{LS}Co^{II}_{HS}$. The first photomagnetic activity was observed in a three dimensional Prussian blue network $A_xCo_y[Fe(CN)_6]\cdot nH_2O$ (A: Na^+ , K^+ , Cs^+ , Rb^+) (Figure I. 4).

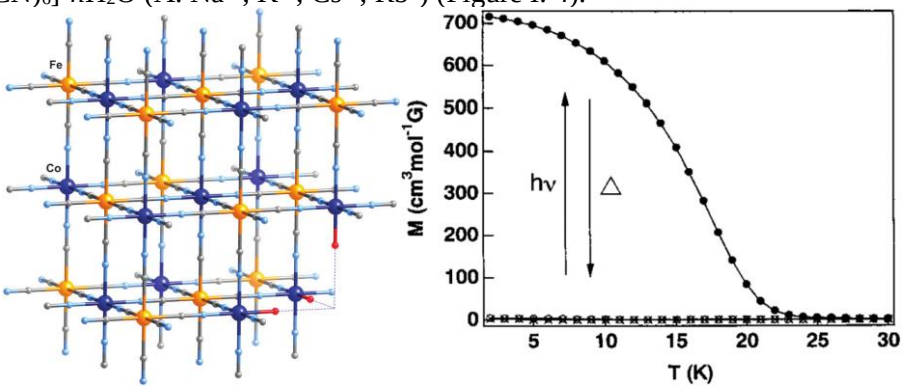

Figure I. 4 (Left) Schematic representation of a Fe/Co Prussian blue network with formula $A_xCo_y[Fe(CN)_6]\cdot nH_2O$ (A: alkaline ions, which have been omitted for clarity). (Right) Dependence of field-cooled magnetization of $Rb_{0.66}Co_{0.25}Co[Fe(CN)_6][\,\square\,]_{0.25}\cdot 4.3H_2O$ ($\square$ is $[Fe^{III}(CN)_6]^{3-}$ vacancy) with temperature under an applied field H = 0.5 mT before (empty dots) and after (black dots) light irradiation, and after the thermal treatment at 150 K (crosses). Reproduced from Ref. [15] with permission from the Royal Society of Chemistry 2016.

Upon thermal heating or light irradiation, the diamagnetic pair $Fe^{II}_{LS}(3d^6, S = 0)$-$Co^{III}_{LS}(3d^6, S = 0)$ can be transformed into paramagnetic pair $Fe^{III}_{LS}(3d^5, S = 1/2)$-$Co^{II}_{HS}(3d^7, S = 3/2)$ by electron transfer from Fe^{II}_{LS} to Co^{III}_{LS} with subsequent change of crystal field strength on Co site (Co^{III}_{LS} with strong field and Co^{II}_{HS} with weak crystal field) (Figure I. 5). In the literature, the full process has been described as charge-transfer-induced spin transition (CTIST) or electron-transfer-induced spin transition (ETIST).[16]

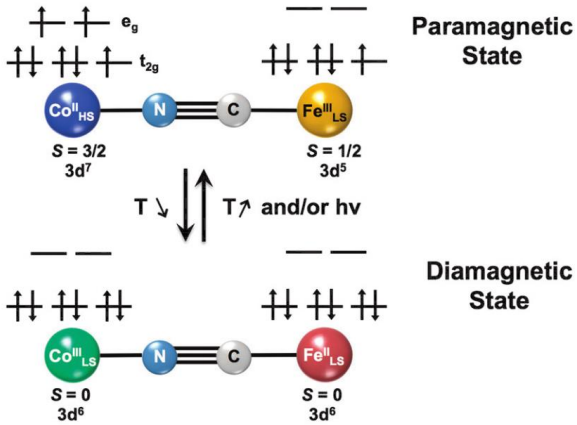

Figure I. 5 Interconversion between the paramagnetic (Fe^{III}_{LS}–CN–Co^{II}_{HS}) and diamagnetic (Fe^{II}_{LS} –CN–Co^{III}_{LS}) electronic configurations due to thermally and photo-induced metal-to-metal electron transfer processes. Reproduced from Ref. [15] with permission from the Royal Society of Chemistry 2016.

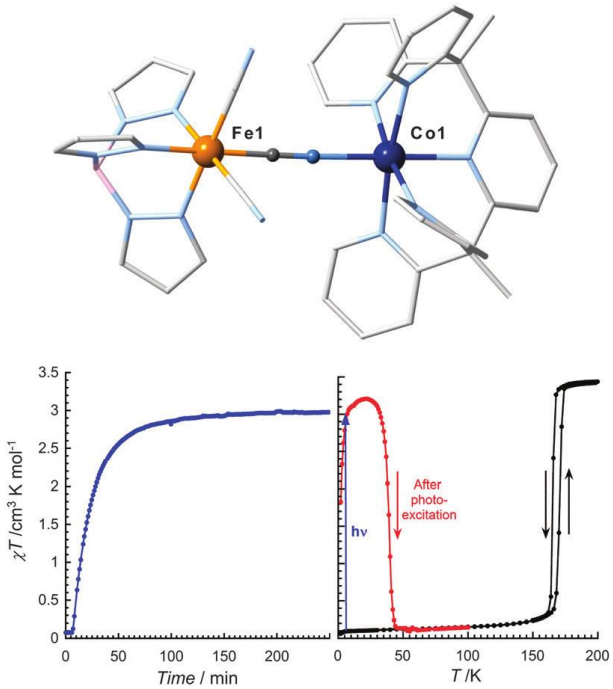

Figure I. 6 (Top) Representation of the molecular structure of $[(Tp)Fe(CN)_3Co(PY5Me_2)](OTf)\cdot 2DMF$. Hydrogen atoms, triflate and lattice-solvent molecules are omitted for clarity. Fe, Co, N and C atoms are indicated in orange, dark blue, light blue and light grey, respectively. (Bottom left) χT versus time (blue circles) of the desolvated compound at 1 T and 10 K under white light irradiation, and (Bottom right) χT versus temperature before (black dots) and after (red dots) white light irradiation. Reproduced from Ref. [15] with permission from the Royal Society of Chemistry 2016.

The low solubility and the lacunary studies of three dimensional Prussian blue analogues have complicated their technological application into devices. To overcome these drawbacks, the switchable properties have been extensively studied for molecule-based Fe/Co cyanide complexes with low dimensionalities, which allows a better control of coordination environment around the metal ion coupled with higher solubility.[17-19] The photomagnetism has

been demonstrated in an octanuclear cube (relaxation temperature ~ 170 K), tetranuclear square (relaxation temperature ~ 100 K) and dinuclear complex (relaxation temperature ~ 50 K).[20] In Figure I. 6, the first dinuclear Fe/Co complex $[(Tp)Fe(CN)_3Co(PY5Me_2)](OTf)\cdot 2DMF$ demonstrates a thermally and light-induced electron transfer in the solid state. The low relaxation temperature observed ~50 K in this compound suggests that the relaxation temperature tends to decrease with the miniaturization of the complex.

In a similar vein as the prototypical $Co^{III}Fe^{II}$ Prussian blue analogs, a large variety of cyanide bridged bimetal assemblies such as $Fe^{III}Mn^{II}$,[21] $Fe^{II}Fe^{III}$,[22] $Fe^{II}Ni^{III}$,[23] $Os^{II}Fe^{III}$,[24] $Os^{II}Co^{III}$,[25] $W^{IV}Mn^{II}$,[26] $W^{IV}Fe^{III}$,[27] $W^{IV}Co^{III}$,[28-30] and $Mo^{IV}Co^{III}$,[31] have been investigated for their charge transfer behaviors as summarized in Figure I. 7. Electron transfer behavior in $Cu^{II}Mo^{IV}$ pair will be discussed in detail in the following part. These chemical systems can be divided into two categories: charge transfer and charge transfer coupled with spin crossover (CTIST). It is worth noting that all the systems involving cobalt possibly exhibit not only a MMCT but also a CTIST.

The ligand field and the redox potential for the metal sites can be rationally manipulated to promote the electron transfer processes by the modification of the respective coordination environment during synthesis. Because of different absorption bands in the visible range for low temperature and high temperature phases, the reversible electron transfer processes can be controlled by light of different wavelengths.[15]

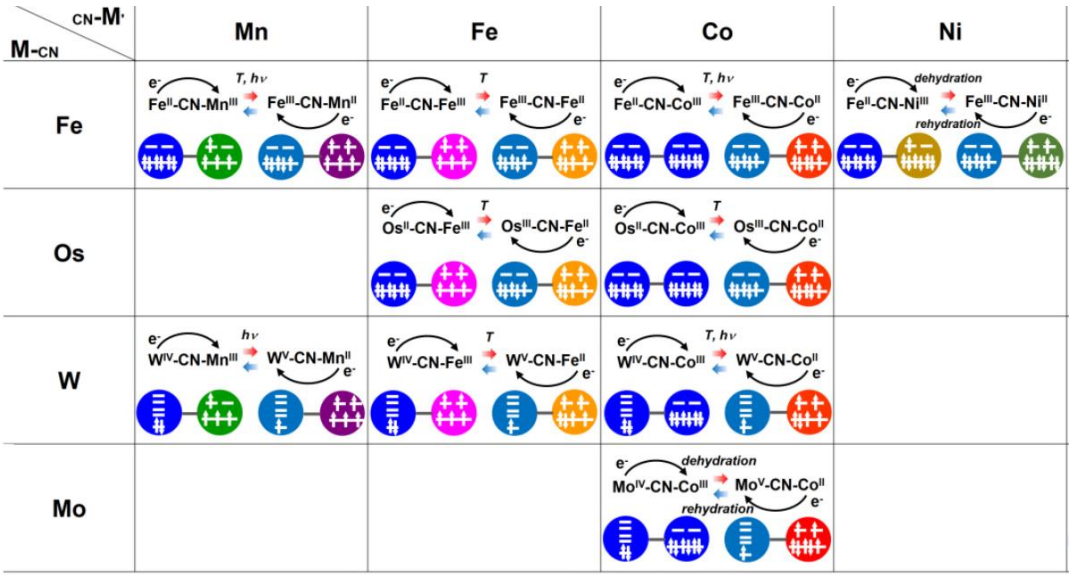

Figure I. 7 Schematic illustration of various external stimuli tuned MMCT (i.e., Fe-CN-Mn) and CTIST (i.e., Fe-CN-Co) in M-C≡N-M' linkages. The notations "*T*" and "*hν*" represent thermal treatment and light irradiation, respectively. Reproduced from Ref. [32] with permission from the Wiley 2018.

The variation of magnetic properties can also be achieved by the charge transfer between a metal center and a redox-active ligand, which may also accompanied by the spin crossover for the metal center. This valence tautomerism has been extensively investigated for cobalt-quinone systems.[33-34] The quinone molecule can be one-electron reduced to "semiquinone" or two-electron reduced to "catecholate". As illustrated in the compound [Co-(3,5-dbsq)$_2$(bpy)],[34] upon light irradiation in the ligand–metal charge-transfer (LMCT) band, an electron transfer occurs resulting in the transformation of $Co^{III}{}_{LS}$ species with the catecholate ligand to the $Co^{II}{}_{HS}$ species with the semiquinone ligand (Figure I. 8). For this kinds of compounds, the photoinduced effect is usually observed below 50 K.

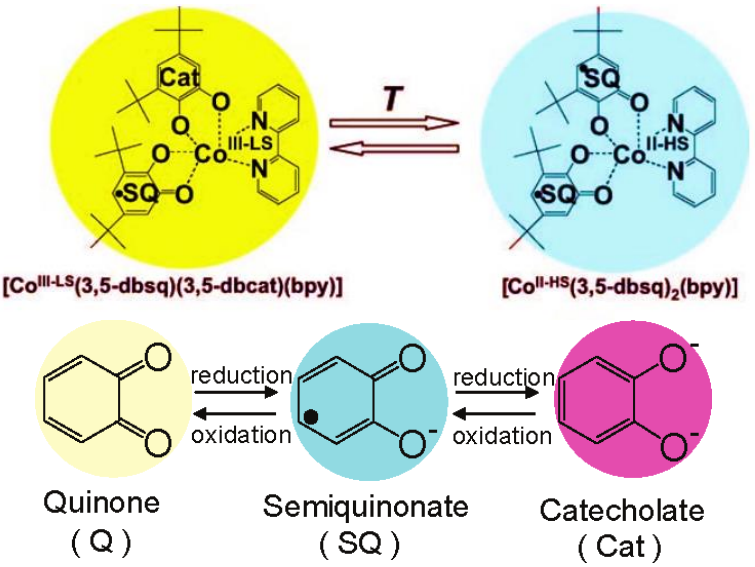

Figure I. 8 (Top) Valence tautomerism of $[Co^{II}_{HS}(3,5\text{-dbsq})_2(bpy)]$. Reproduced from Ref. [35] with permission from the Wiley 2007. (Below) Quinone molecules used as redox-active ligands undergo two-step redox reactions. Reproduced from Ref. [33] with permission from the American Chemical Society 2007.

I.1.3 Ligand-driven spin-state switching systems

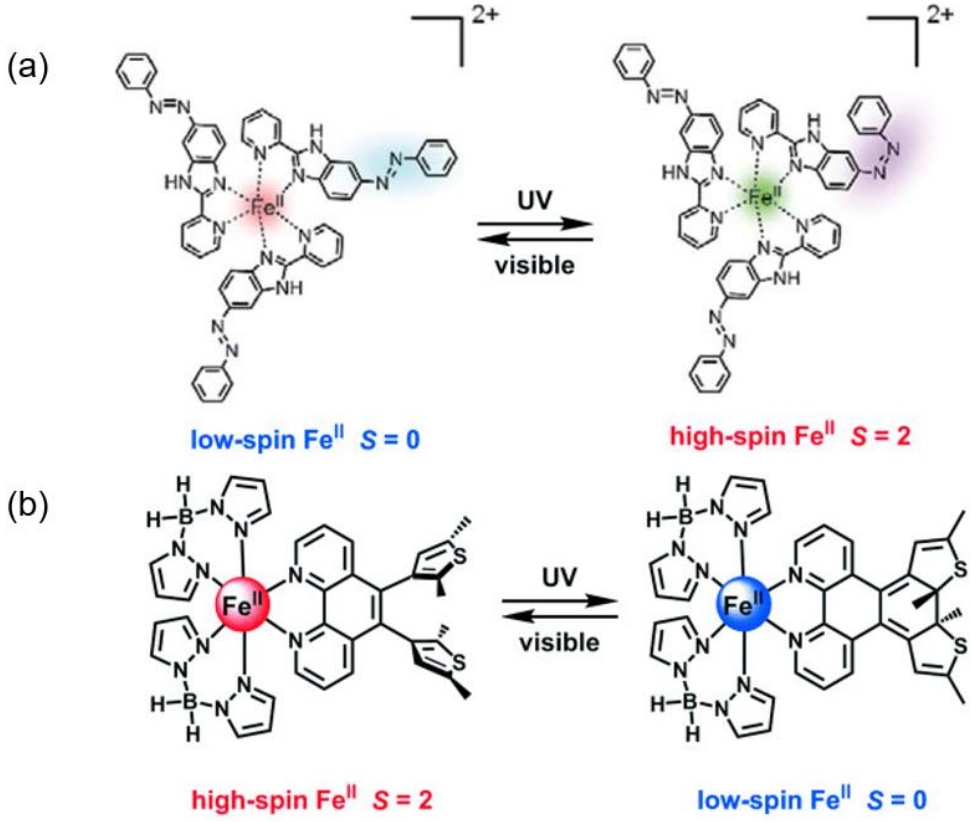

Figure I. 9 (a) An iron(II) complex with azobenzene-attached ligands showing reversible magnetization change. (b) An iron(II) complex with diarylethene ligands switching between open ring (left) and close ring (right) isomerizable moiety. (a) Reproduced from Ref. [42] with permission from the Royal Society of Chemistry 2009. (b) Reproduced from Ref. [37] with permission from the Wiley 2015.

Ligand driven photo-isomerization involving cis-trans or ring opening/closing isomerizations has been intensively investigated.[36] Cis–trans photo-isomerization induced spin-state switching effect is reported for azobenzene ligands coordinated to Fe(II) ion.[10] Open/close switching has been observed for diarylethene ligands coordinated to Fe(II) ion.[37-

[38] It has been established that those photo-isomerization can be achieved by the application of UV light at relatively high temperature, even at room temperature.[39] Even though these types of ligands are diamagnetic, the photo-isomerization of ligands could induce the variation of the ligand-field strength and indirectly mediate the exchange interaction when they are linked to the metal ion (Figure I. 9). This in turn may allow the elevation of the photoresponsive temperature of this type of photomagnetic materials.[39-41] The first example of ligand driven light-induced spin change was evidenced for the compound $Fe^{II}(4\text{-styrylpyridine})_4(NCBPh_3)_2$, with cis–trans isomerization of styrylpyridine at 140 K. Besides for Fe^{II}, the ligand-driven spin-state switching has also been investigated for Fe^{III} and Co^{II} coordination compounds.[36]

Another class of switching effect relevant to the isomerization of the ligand is the photoinduced coordination mode change, as discovered in sodium nitroprusside (SNP) $Na_2[Fe(CN)_5(NO)]\cdot 2H_2O$.[43] The nitrosyl ligand (NO) can exhibit different coordination modes in the metastable states (Figure I. 10). The stable nitrogen-coordinated ground state (**GS**) can be photoconverted into the oxygen-coordinated state (**SI**) by blue-light irradiation. Further near-infrared light irradiation can convert oxygen-coordinated state to side-coordinated one (**SII**). The photochromic nitroprusside incorporated with magnetic complex in polymeric systems has been tested as a viable approach in some compounds to develop photomagnetic materials.[44-45] The photo-induced nitrosyl linkage isomerization usually can be achieved at relatively high temperature, for example at 77 K or 100 K.[46] Similar photo-induced isomerization has also been reported for other small ligands, such as sulfur dioxide, nitrite and thiocyanate groups.[47-50]

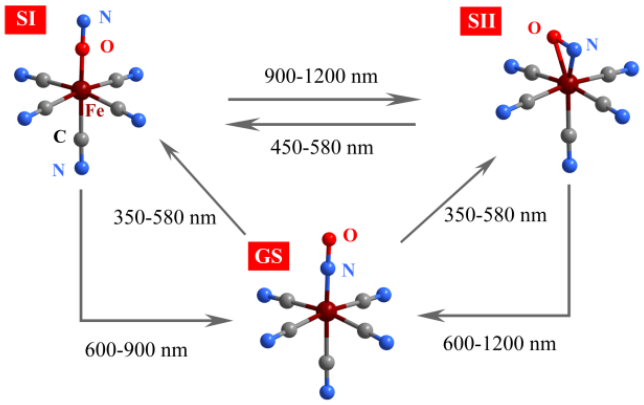

Figure I. 10 Schematic view of photo-induced linkage isomers **GS**, **SI**, and **SII** in coordination unit $[Fe(CN)_5(NO)]^{2-}$. Reproduced from Ref. [46] with permission from the American Chemical Society 2020.

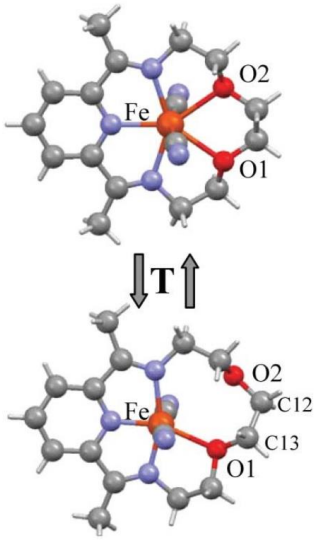

Figure I. 11 View of the two X-ray diffraction molecular structures of $[Fe^{II}(LN_3O_2)(CN)_2]\cdot H_2O$ complex in HS state (Top) and LS state (Bottom). Reproduced from Ref. [51] with permission from the Royal Society of Chemistry 2007.

A reversible Fe-O formation is observed in Fe^{II} complex, $[Fe^{II}(LN_3O_2)(CN)_2]\cdot H_2O$ (LN_3O_2 = 2,13-dimethyl-6,9-dioxa-3,12,18-triazabicyclo[12.3.1]octadeca-1(18),2,12,14,16-pentaene), with the coordination number changing from six at low spin state to seven at high spin state.[51-52] Thus, the coordination sphere for Fe^{II} is $FeC_2N_3O_2$ in the HS state and FeC_2N_3O in the LS state (Figure I. 11).[51]

Intriguingly, light-driven coordination-induced spin-state switching (LD-CISSS) effect has been reported for nickel-porphyrins based compound. Ni(II)-Tetrakis(pentafluorophenyl)porphyrin with 4,4'-disubstituted 3-azopyridines as axial ligands in homogeneous solution. It is able to switch between a diamagnetic state ($3d^8$, $S = 0$ in square planar geometry) and a paramagnetic state ($3d^8$, $S = 1$ in square pyramidal geometry) of the nickel center at room temperature. In this compound, azopyridine also exhibits cis-trans photoisomerization. The spin state change is accomplished by the transformation of azopyridine as an axial ligand in its cis conformation from its trans conformation upon 365 nm wavelength light irradiation (Figure I. 12).[53] This process is photoreversible with a 455 nm wavelength light irradiation. Similar behavior has also been demonstrated for Fe^{III}.[54]

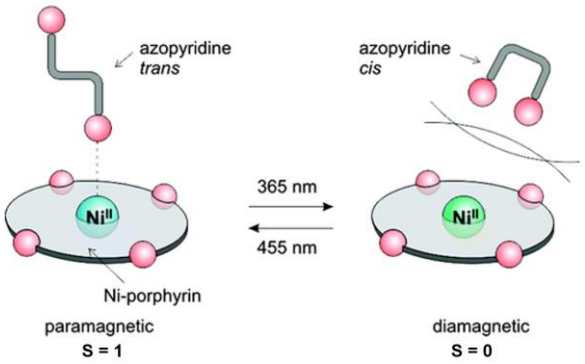

Figure I. 12 Schematic representation of the spin-state switching of square planar Ni(II) complexes by light-induced association and dissociation of a photochromic axial ligand. Reproduced from Ref. [55] with permission from the American Chemical Society 2011.

I.1.4 Other related categories of photomagnetic systems

Numerous photoswitchable systems have been reported so far and it is impossible to list them all. A common problem for the state-of-the-art photomagnetic materials is the low-temperature photoresponsive behavior usually below cryogenic temperature (the boiling point of liquid nitrogen ~77 K). The low working temperature hinders the development of photomagnetic materials towards the practical applications.[2] In this part, we limit ourselves the description of other related photomagnetic systems able to work above cryogenic temperature.

One approach has been developed for existing systems with wide thermal hysteresis loops at high temperature, showing a long lifetime for the high temperature phase. Some Fe^{II} based spin crossover complexes and Prussian Blue analogues with strong cooperativity in their structures demonstrate the realization of the photoswitchable magnetism around room temperature with One-Shot-Laser-Pulse within the thermal hysteresis loop.[56-57]

Additionally, inorganic-organic hybrid photochromic materials have been reported to open the perspective for the design of photomagnetic materials operating above cryogenic temperature. Notably, a room temperature photoinduced magnetization is achieved for $[Eu^{III}(18C_6)(H_2O)_3]Fe^{III}(CN)_6\cdot 2H_2O$ ($18C_6$ = 18-crown-6), ascribed to a photoinduced electron transfer from crown to Fe^{III} metal center (Figure I. 13).[58]

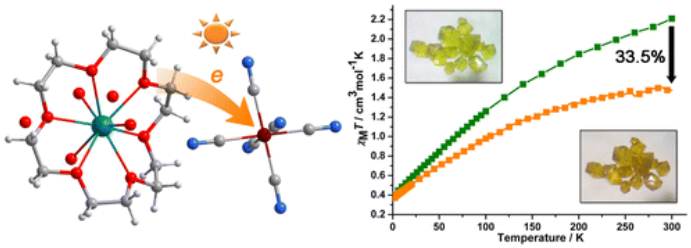

Figure I. 13 The molecular structure of $[Eu^{III}(18C_6)(H_2O)_3]Fe^{III}(CN)_6{\cdot}2H_2O$ and the corresponding photomagnetic properties and photochromism at room temperature. Reproduced from Ref. [58] with permission from the American Chemical Society 2015.

An unusual photoinduced on/off single-molecule magnet behavior in a Dy(III)-based photochromic complex has been reported at room temperature recently.[59] In $[Dy_3(H–HEDP)_3(H_2–HEDP)_3]\cdot 2H_3–TPT\cdot H_4–HEDP\cdot 10H_2O$ (**QDU-1**; HEDP = hydroxyethylidene diphosphonate; TPT = 2,4,6-tri(4-pyridyl)-1,3,5-triazine), a photoinduced electron transfer is realized from HEDP units to TPT ligands. A remarkable single-molecule magnet behavior is observed owing to the strong ferromagnetic coupling between Dy^{III} ions and photogenerated $O^{\bullet}$ radical (Figure I. 14).[59]

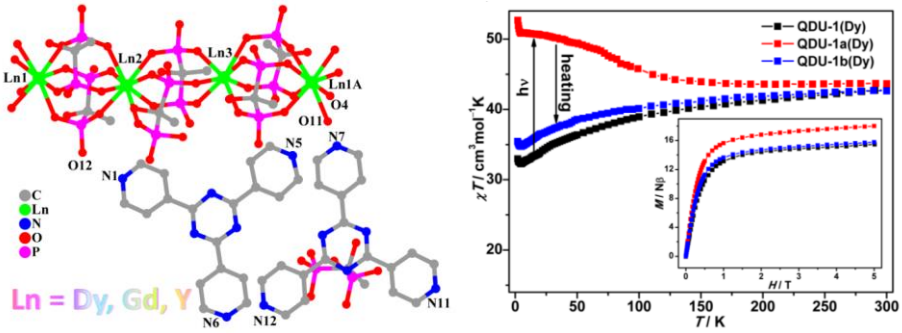

Figure I. 14 (Left) The crystal structure of **QDU-1**. Water molecules and H atoms are omitted for clarity. Atomic codes: Ln Green; P Pink; C Gray; O Red; N blue. (Right) Temperature-dependent susceptibilities for **QDU-1** before and after light irradiation. Reproduced from Ref. [59] with permission from the American Chemical Society 2020.

I.2 Photoinduced magnetism of octacyanidometallate compounds

Cyanidometallate-based compounds can demonstrate a metal-to-metal charge transfer (MMCT) induced magnetism with light irradiation. It is well known that cyanide ligand can serve as an efficient bridge for electron transfer and can mediate exchange coupling between spin carriers.[60] 3d metal hexacyanidometallates are well reported in this field since the discovery of photomagnetism born by coordinated metal centers in $K_{0.2}Co_{1.4}[Fe(CN)_6]\cdot 6.9H_2O$.[15, 19] Later, 4d and 5d metal octacyanidometallates (OCMs) made of $[M(CN)_8]^{n-}$ (M = Mo and W) building blocks have emerged as promising photomagnetic systems owing to a high number of potential magnetic interaction pathways and structural flexibility.[61] Sensitive to the chemical environment, flexible OCM building blocks can adopt various coordination geometries including square antiprism (D_{4h}), dodecahedron (D_{2d}), and bicapped trigonal prism (C_{2v}).

I.2.1 Evidences of the photo-induced magnetization in CoW networks

Pentavalent octacyanidometallates have been under intense investigation due to their diffusing orbitals with high magnetic ordering temperatures and abilities to incorporate various additional functionalities such as thermally or photoinduced charge transfer, chirality, photoluminicence, et etc.[62-66]

Attractively, pentavalent octacyanidometallates have the potential to be photomagnetic as illustrated in $Co^{II}W^{V}$ compounds.[28-30, 67-68] For example, 3D-$[\{Co^{II}(pyrimidine)(H_2O)\}_2\{Co^{II}(H_2O)_2\}\{W^{V}(CN)_8\}_2](pyrimidine)_2\cdot 2H_2O$ (**CoWprm**) undergoes a photo-induced phase crossover from the Co^{III}_{LS}(S = 0)-NC-W^{IV} (S = 0) to the Co^{II}_{HS} (S = 3/2)-NC-W^{V} (S = 1/2) (Figure I. 15).[28, 67-68] It demonstrates a Curie temperature (T_c) of 40 K and a gigantic magnetic coercive field (H_c) of 12000 Oe in the photoexcited state.

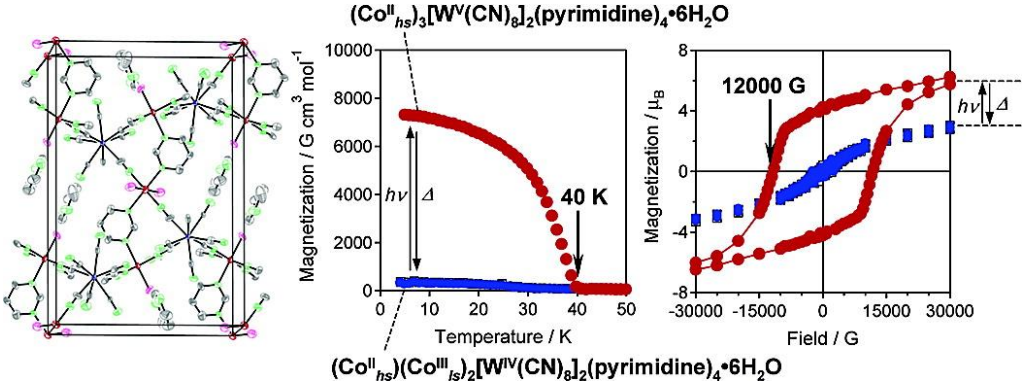

Figure I. 15 (a) Crystal structure of the **CoWprm** octacyano-complex (b) Magnetization vs temperature curves before and after light irradiation. (c) Magnetic hysteresis loops before and after light irradiation (at 2 K). Before irradiation (black lines), after irradiation with 840 nm light (red lines), and after thermal treatment of 150 K or irradiation with 532 nm light (blue lines). Reproduced from Ref. [28] with permission from the American Chemical Society 2006.

I.2.2 Evidences of the photo-induced magnetization in CuMo networks

In the 20th century, photochemistry studies of $[M^{IV/V}(CN)_8]^{3-/4-}$ ions in solution have caused great interest leading to fruitful results.[64] The photoreaction of $[M^{V}(CN)_8]^{3-}$ by irradiation in ligand metal charge transfer (LMCT) band can lead to $[M^{IV}(CN)_8]^{4-}$ as a final photoproduct (Scheme 1). The light irradiation in charge-transfer-to-solvent (CTTS) band of $[M^{IV}(CN)_8]^{4-}$ can produce $[M^{V}(CN)_8]^{3-}$ (Scheme 2). Particularly, the photolysis of $[M^{IV}(CN)_8]^{4-}$ by light irradiation in ligand field (LF) band in alkaline medium can form photoproducts with a variable number of CN ligands (Scheme 3).

Moreover, the excitation within the ion-pair charge transfer (IPCT) band for $Cu^{II}/[Mo^{IV}(CN)_8]^{4-}$ pairs leads to the formation of $[Mo^{V}(CN)_8]^{3-}$ by a metal-to-metal electron transfer process. The $[Mo^{V}(CN)_8]^{3-}$ can be further photoreduced in $[Mo^{IV}(CN)_8]^{4-}$ by irradiation within its LMCT band (Figure I. 17).

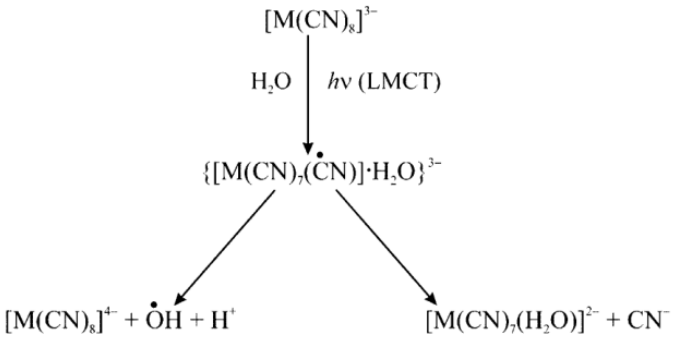

$$[M(CN)_8]^{3-} + [M(CN)_7(H_2O)]^{2-} + 3H_2O \rightarrow [M(CN)_8]^{4-} + MO_4^{2-} + 7CN^- + 8H^+$$

$$8[M(CN)_8]^{3-} + 8CN^- \rightarrow 8[M(CN)_8]^{4-} + 8\dot{C}N$$

Scheme 1.

Scheme 2.

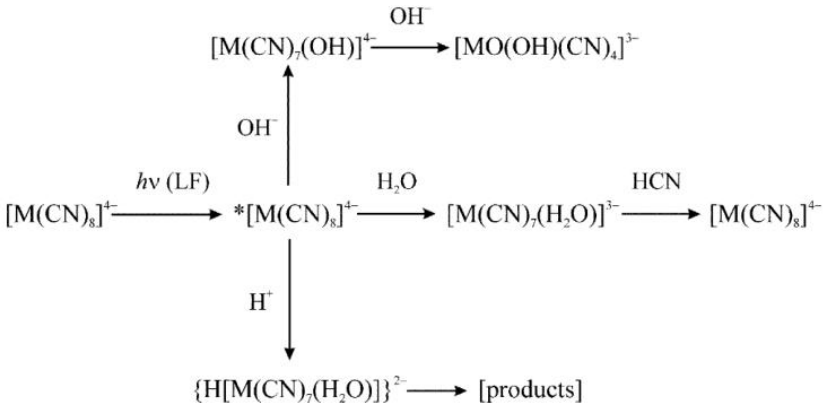

Scheme 3.

Figure I. 16 Schematic illustration of studies of the photosubstitution and photoredox processes of $[M^{IV/V}(CN)_8]^{3-/4-}$ ions in solution. Reproduced from Ref. [64] with permission from the Elsevier 2006.

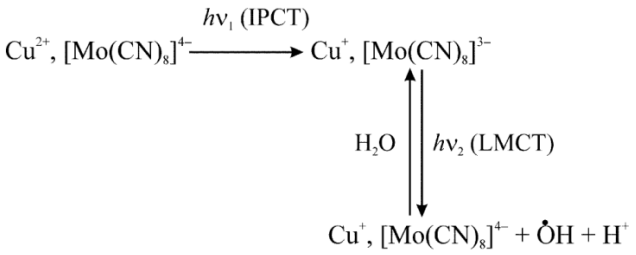

Figure I. 17 Schematic illustration of photochemistry of mixed-valence ion-pairs $Cu^{II}/[M^{IV}(CN)_8]^{4-}$. Reproduced from Ref. [64] with permission from the Elsevier 2006.

Because of the diamagnetic nature of tetravalent octacyanidometallates, the exploration of heterometallic coordination frameworks based on tetravalent octacyanidometallates remains fairly limited until the discovery of interesting photomagnetic properties at the beginning of the 21st-century.[69]

The complexity of their photomagnetic mechanisms has been revealed by the researchers: photooxidation from M^{IV} to M^{V},[70] metal-to-metal charge transfer between M^{II}-M^{IV}[70-71] and singlet to triplet crossover for M^{IV}.[72] In this respect, special attention will be paid for several milestones to discuss their photomagnetic properties.

A series of inorganic three-dimensional compounds $M^{II}_2[Mo^{IV}(CN)_8]\cdot nH_2O$ (M = Mn, Fe, Co, Ni) have been reported,[73-74] in which the square-antiprismatic $[Mo^{IV}(CN)_8]^{4-}$ is connected to M^{II} sites by eight cyanide bridges, and the octahedral M^{II} sites are surrounded by four N-C-Mo linkages in equatorial positions and two water ligands in axial positions. A poor crystalline compound can be prepared for $Cu_2[Mo(CN)_8]\cdot nH_2O$ (named **Cu_2Mo**). But its structure has been determined as similar to that of $Fe^{II}_2(H_2O)_4[Mo^{IV}(CN)_8]\cdot 4H_2O$ by wide-angle X-ray scattering (WAXS). Only the Cu-Mo compound presents in its optical spectrum a metal-to-metal charge transfer band around 510 nm by the conversion of Cu^{II}-Mo^{IV} pair to Cu^{I}-Mo^{V} pair.[75-76] A simple superposition of the absorption bands of their components is present for Mn, Fe, Co, Ni compounds based on UV-Vis spectra, ruling out of the presence of MMCT in these materials.

Upon light irradiation in the intervalence band of Cu-Mo system, an important photomagnetic effect was reported by our group and the group of Ohkoshi in 2001,[77] and has been further investigated by a large variety of techniques in 2006.[71] A spontaneous magnetization (Curie temperature = 25 K) appears after light irradiation as well as a field hysteresis below 5 K (Figure I. 18). The proposed mechanism is a MMCT to stabilize the mixed-valence isomer of $Cu^{I}Cu^{II}[Mo^{V}(CN)_8]\cdot 8H_2O$. The significant photomagnetic property is deriving from the modification of electronic states from Cu^{II}(S = 1/2)–Mo^{IV} (S = 0) to Cu^{I} (S = 0)–Mo^{V} (S = 1/2). Importantly, the Mo^{V} ion can participate in ferromagnetic interactions with the residual Cu^{II} centers in the structure. Additionally, the magnetization induced by 520 nm light irradiation can be erased by the light irradiations in reverse-IT band ranging from 600 to 900 nm (the maximum is 710 nm).[78] An improvement of the crystallinity of this compound was achieved in 2016. The well crystalized $\{[Cu^{II}(H_2O)]_2[Mo^{IV}(CN)_8]\cdot 2H_2O$ is revealed to be constructed by square-pyramidal $[Cu^{II}(H_2O)(NC)_4]^{2-}$ complexes and square-antiprismatic $[Mo^{IV}(CN)_8]^{4-}$ ions.[79] The photomagnetic mechanism of this compound has been elucidated as a MMCT mechanism by first principle calculations of the visible-light absorption band.

In parallel, 3D-$Cs^{I}_2Cu^{II}_7[Mo^{IV}(CN)_8]_4\cdot 6H_2O$ (**CsCuMo**)[80-81] has been electrochemically prepared with good crystallinity. It exhibits a spontaneous magnetization with T_c = 23 K upon exposure to 450-500 nm light at 5 K. The coercive field H_c value 350 G is higher than 34 G for $Cu_2[Mo(CN)_8]\cdot 8H_2O$ at 3 K. The MMCT mechanism for $Cs^{I}_2Cu^{II}_7[Mo^{IV}(CN)_8]_4\cdot 6H_2O$ is believed to be similar with that of $Cu_2[Mo(CN)_8]\cdot 7H_2O$ which is confirmed spectroscopically by IR, EPR and PXRD.[81]

In contrast with the lack of photoreversiblity for **CsCuMo**, an isostructural 3D-$Rb^{I}_{3/2}Cu^{II}_7[Mo^{IV}(CN)_8]_{31/8}\cdot 12H_2O$ (**RbCuMo**) shows that the spontaneous magnetization can be cycled with the alternative application of 473 nm/785 nm lights.[82] This is owing to the more flexibility in the structure of **RbCuMo** according to terahertz time-domain spectroscopy (THz-TDS) studies. The vibrational mode of the intercalated Rb ion (1.11 THz) is lower than that for the Cs ion (1.35 THz), suggesting that the Rb trapping force in **RbCuMo** is weaker than the Cs trapping force because of the structural flexibility.

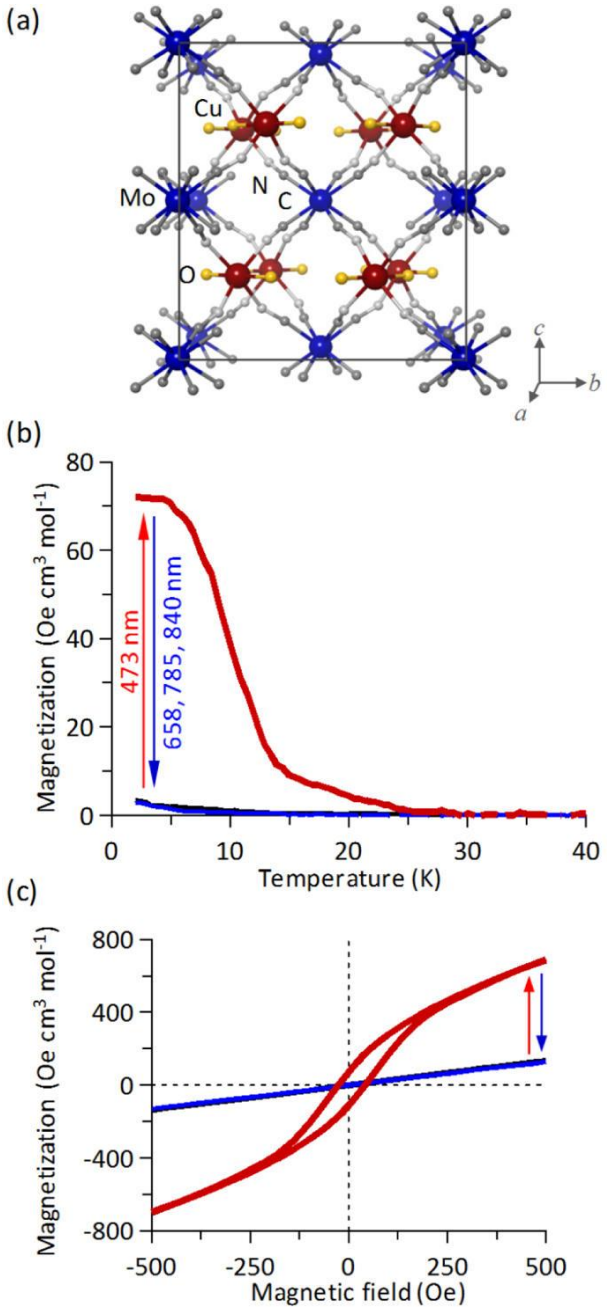

Figure I. 18 (a) Schematic crystal structure for $Cu_2[Mo(CN)_8]\cdot 8H_2O$. (b) Magnetization vs temperature curves before (black line) and after irradiating with 473 nm light (red line) and after irradiating with 658, 785, or 840 nm light (blue line). (c) Magnetic hysteresis loop at 3 K before (black line) and after irradiating with 473 nm light (red line), after thermal treatment of 250 K (blue line). Reproduced from Ref. [60] with permission from the American Chemical Society 2012.

I.2.3 Design of molecular analogues of photomagnetic CuMo compounds

After the first report of the light induced spontaneous magnetization for 3D-$Cu_2[Mo^{IV}(CN)_8]\cdot xH_2O$,[71, 74, 76-78] a series of blocking ligands have been employed for copper center to assemble Cu^{II}-$[Mo^{IV}(CN)_8]^{4-}$ molecular complexes. The eight cyanide ligands of OCMs can possibly behave as bridges or terminal ligands which offers several opportunities for the structures. In case of Cu^{II}-Mo^{IV} cyanide bridged compounds, the observation of MMCT band is quite important and can be a sign of potential light-induced MMCT behavior as demonstrated by the pioneering study of Hennig et. al in solution.[83-85]

The exploitation of aliphatic polyamines as the blocking ligands has been proved to be an effective approach for tuning the structures in Cu(II)–Mo(IV) systems.[86] A large amount of photoresponsive compounds with different dimensionalities ranging from 0D (zero-dimensional) to 3D (three-dimensional) have been reported. Polynuclear Cu–Mo molecules with different number of cyanide ligands engaged as bridges towards copper centers are the most common systems.

As the first attempt in this direction, trinuclear $\{Cu^{II}(bipy)_2\}_2\{Mo^{IV}(CN)_8\}]\cdot xH_2O\cdot CH_3OH$ has been studied by UV-light and 488 nm light irradiation.[74, 87] The irreversible photomagnetic effect has been observed with UV light irradiation explained by the formation of Mo^{V}. However, a thermally reversible photomagnetic effect has been observed with 488 nm light irradiation attributed as a MMCT mechanism.

Heptanuclear $[Mo^{IV}(CN)_2(CN\text{-}CuL)_6](ClO_4)_8$ (**Cu_6Mo**, L = tris(2-amino)ethylamine) is presented as a benchmark illustration.[88] Upon irradiation by a blue light 406–415 nm, the value of χT increases from 2.5 to 5 $cm^3\,mol^{-1}$ K. The relaxation temperature (= temperature for which the system is back to its initial state) is 300 K (Figure I. 19). The mechanism is believed to be a MMCT accompanied by the change of geometry for Cu, considering that the usual coordination geometries of the Cu^{I} and Cu^{II} ion are tetrahedral and trigonal-bipyramid, respectively. A kinetic model is introduced to describe quantitatively the transformation from $Mo^{IV}Cu^{II}_6$ (six independent S = 1/2) to $Mo^{V}Cu^{I}Cu^{II}_5$ (one S = 3).[89] Six partly filled 3d orbitals for the six Cu^{II} sites and two lowest energy 4d orbitals for the Mo^{IV} site are involved during the computation which confers a great challenge for calculation.[90] However, a similar heptanuclear $[\{Cu(TPA)CN\}_6Mo(CN)_2][ClO_4]_8$ (TPA = tris(2-pyridylmethyl)amine) is reported as being not photomagnetic. The reason explained by the authors is that the molybdenum does not adopt an intermediate geometry between SAPR and TDD to stabilize the high-spin Mo(IV) state.[91]

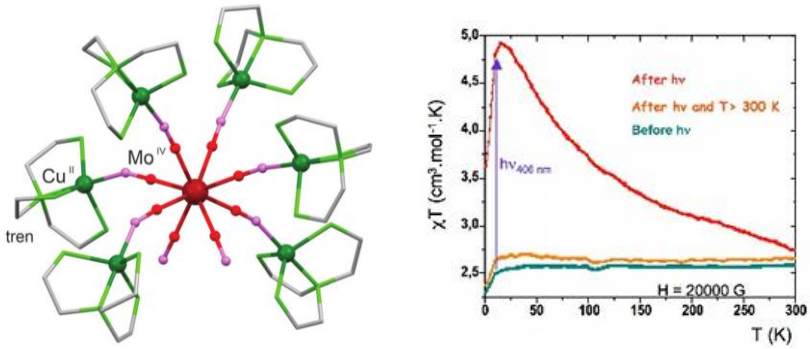

Figure I. 19 (Left) Structural view of the heptanuclear $[Mo^{IV}(CN)_2(CN\text{-}CuL)_6]^{8+}$. (Right) The temperature dependence of χT under a 2 kOe DC field before and after blue light (406–415 nm) irradiation and after thermal relaxation up to 300 K. The left part is adapted from Ref. [61] with permission from the Royal Society of Chemistry 2020 and the right part is adapted from Ref. [88] with permission from the Wiley 2004.

Six photomagnetic compounds with diverse dimensionalities have been reported with the use of UV-light irradiation by Zhang et al. choosing different peripheral polyamines for Cu(II) ions: 0D-$[Cu(tpa)]_2[Mo(CN)_8]\cdot 15H_2O$ (**1**, tpa = tris(2-pyridylmethyl)amine), 0D-$[Cu(tren)]_2[Mo(CN)_8]\cdot 5.25H_2O$ (**2**, tren = tris(2-aminoethyl)amine), 1D-$[Cu(en)_2][Cu_{0.5}(en)]$-$[Cu_{0.5}(en)(H_2O)][Mo(CN)_8]\cdot 4H_2O$ (**3**, en = ethylenediamine), 2D-$[Cu(bapa)]_3[Mo(CN)_8]_{1.5}\cdot 12.5H_2O$ (**4**, bapa = bis(3-aminopropyl)amine), 2D-$[Cu(bapen)]_2[Mo(CN)_8]\cdot 4H_2O$ (**5**, bapen = N,N-bis(3-aminopropyl)-ethylenediamine), and 3D-$[Cu(pn)_2][Cu(pn)][Mo(CN)_8]\cdot 3.5H_2O$ (**6**, pn = 1,3-diaminopropane).[92] Although the photoresponsive properties are common in these Mo(IV)–Cu(II) complexes, their correlations with structures are not clear. **4** and **6** are more photoresponsive among these six complexes, maybe owing to high dimensional structures and relatively short Cu–NC distances (2.0–2.5 Å). On irradiating **4** or **6** at 77 K, the intensity of the Cu(II) signal decreases in EPR spectra but without detectable signal relating to Mo^{V} ions.

A number of photomagnetic high-nuclearity clusters have been synthesized by

employing blocking ligands that leave different available CN bridging positions with the Cu^{II} ions. For instance, if only one coordinating position on copper center is available, the previously mentioned **$MoCu_6$** is successfully obtained, in which Cu^{II} site is in a trigonal-bipyramidal environment coordinated by one cyanide nitrogen atom and four nitrogen atoms from tren (tris(2-amino)ethylamine) ligand.[88] By employing blocking ligand with two free coordination positions, tacn (1,4,7-triazacyclononane), **Mo_6Cu_{14}** is obtained, in which one square pyramidal Cu^{II} site is coordinated with one tacn ligand and two cyanide bridges. It exhibits a significant increase for χT from 5.22 to 8.97 $cm^3\ mol^{-1}$ K at 5 K and a remarkably high relaxation temperature (T_{relax} ~ 230 K). The corresponding EPR signal is in agreement with the electron transfer mechanism.[93] In contrary, the **Mo_6Zn_{14}** analogue does not exhibit any photomagnetic effect, further supporting the MMCT mechanism for **Mo_6Cu_{14}**.[93]

Another trinuclear complex $[Cu^{II}_2(bpmen)_2][Mo^{IV}(CN)_8]\cdot 8H_2O$ (bpmen = N, N′-dimethyl-N, N′-bis(2-pyridylmethyl)1,2-diaminoethane) experiences an increase of χT value under UV- light irradiation resulting from a Mo^{IV} to Cu^{II} charge transfer. The photoexcited state is quite stable which demonstrates a high thermally reversible temperature ~ 300 K.[94]

The use of Schiff base ligands featured by negative charge of the ligand can lead to polynuclear compounds. For example, $[Cu(L_1)(py)]_4[Mo^{IV}(CN)_8]\cdot 14H_2O$ (L_1 = N-(quinolin-8-yl)pyridine-2-Carboximidate) (**Cu_4Mo**) and $[Cu(L_2)]_2[Mo^{IV}(CN)_8]\cdot 9H_2O$ (**Cu_2Mo**) (L_2 = N,N′-propane-1,3-diylbis[1-(pyridin-2-yl)methanimine]) have been studied structurally and photomagnetically. The photomagnetic mechanisms are proposed as MMCT (**Cu_4Mo**) and S-T crossover (**Cu_2Mo**), respectively.[95] Compared with **Cu_2Mo**, **Cu_4Mo** displays an additional metal-to-metal charge-transfer (MMCT) band between 400 and 610 nm in the solid state electronic spectrum. The wavelengths of irradiation light employed are 470 nm for **Cu_4Mo** and 436 nm for **Cu_2Mo**, respectively. The photoconversion rates for systems containing Schiff base ligands are not high, presumably due to the electron density withdrawal effect by the Schiff base ligands.

Other photoresponsive Cu^{II}-Mo^{IV} examples with tridentate Schiff ligands are pentanuclear $[Mo(CN)_8\{CuL_1\}_2\{CuL_1(H_2O)\}_2]\cdot 6H_2O$ and decanuclear $[Mo(CN)_8\{CuL_2\}_3\{CuL_2(H_2O)\}]_2\cdot 10H_2O$ (HL_1 and HL_2 are obtained by reacting salicylaldehyde with 2-aminomethylpyridine and 2-aminoethyl-pyridine, respectively).[96] In this study, the authors mention that the lack of flexibility in the structures can be responsible for low efficiency of the MMCT process.

Interestingly, a room temperature photo-switching effect has been observed for 2D-$[Cu(cyclam)]_2[Mo(CN)_8]\cdot 10.5H_2O$ (Cyclam =1,4,8,11-Tetraazacyclodecane) (**$MoCu_2$**).[97] The variation of magnetic data and IR spectra before and after irradiation have been investigated for this compound. The room temperature effect is evidenced as the formation of new CN stretching frequencies in the range of 2090-2130 cm^{-1} in IR data (Figure I. 20). This is due to the new vibrations of Cu^{I}–NC–Mo^{IV}, Cu^{I}–NC–Mo^{V}, and Cu^{II}–NC–Mo^{V} when subjected to 410 nm light and a partial reversion can be achieved with 658 nm light.[98] By analysis of IR spectra before and after irradiation, the activation energy and additional activation energy due to the cooperativity are estimated to be 4002 and 546 cm^{-1}.[97] A larger value of E_a than that for typical spin crossover systems (~150 cm^{-1})[8] is desirable for the observation of room temperature effect (Figure I. 21).

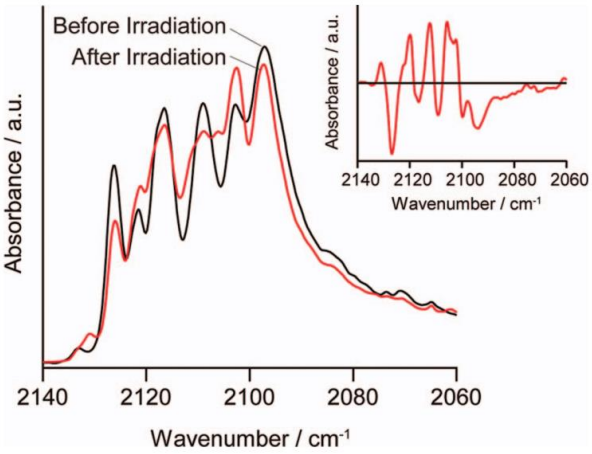

Figure I. 20 IR spectra before and after light irradiation at 410 nm at 273 K. Insert: differential IR spectra before and after irradiation at 273 K. Reproduced from Ref. [97] with permission from the American Institute of Physics 2013.

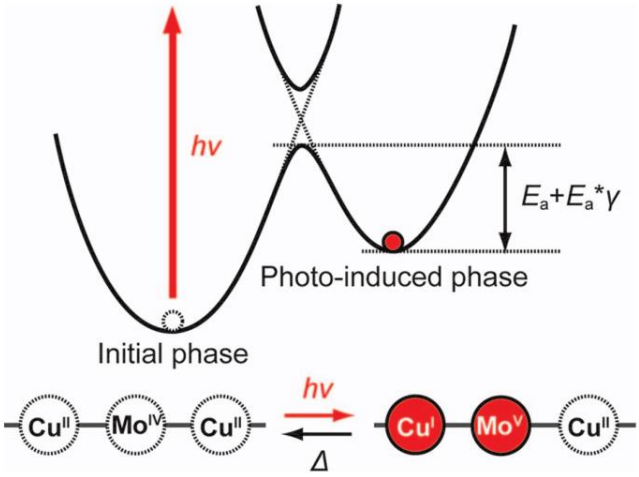

Figure I. 21 Schematic energy diagram of the bistable states Cu^{II}-Mo^{IV}-Cu^{II} and Cu^{I}-Mo^{IV}-Cu^{II}. *Ea* is activation energy and *Ea** is additional activation energy due to the cooperativity. γ is the fraction of photoinduced phase. Reproduced from Ref. [97] with permission from the American Institute of Physics 2013.

I.3 Photomagnetic systems for other couples $M'/Mo^{IV}(CN)_8$ (M' = Mn^{II}, Ni^{II} and Co^{III})

A clear identification of MMCT band around 510 nm is achieved for the cyanide bridged $Cu^{II}Mo^{IV}$ OCM materials by the comparison of the absorption spectra of $[Mo(CN)_8]^{4+}$ and $[Cu(L)]^{2+}$ components, which confers a violet color for the corresponding systems.[87] The MMCT mechanism has been proposed initially by analogy with the Fe/Co Prussian Blue analogs which also exhibit a MMCT band in their optical spectra.[15] In this part, we will describe early works on the photomagnetic OCMs systems by incorporating 3d metal ions other than Cu^{II}, with different photomagnetic mechanisms proposed.

The solution photolysis of $K_4Mo(CN)_8{\cdot}2H_2O$ is confirmed to be photooxidation from Mo^{IV} (S = 0) to Mo^{V} (S = 1/2) accompanied with the ejection of a solvated electron.[99-104] The photomagnetic study of the precursor $K_4Mo(CN)_8{\cdot}2H_2O$ reveals an irreversible photomagnetic effect in the solid state upon the light irradiation with wavelength below 400 nm (337-356 nm), selected to be close with the d-d bands of $[Mo^{IV}(CN)_8]^{4-}$.[70] A photooxidation of Mo^{4+} to Mo^{5+} in solid state is proposed for $K_4Mo(CN)_8{\cdot}2H_2O$ and a chain compound $[Mn^{II}_2(L)_2(H_2O)][Mo^{IV}(CN)_8]{\cdot}5H_2O$ (L = 2,13-dimethyl-3,6,9,12,18-

pentaazabicyclo-[12.3.1]octadeca-1(18),2,12,14,16-pentaene, macrocyclic ligand), by the analysis of EPR spectra of samples after photomagnetic measurements in superconducting quantum interference device (SQUID).[70]

In 2005, the studies of an hexanuclear complex $[Mn(bpy)_2]_4[Mo(CN)_8]_2 \cdot 14H_2O$ (bpy = 2,2'-bipyridyl)[26] also support the photooxidation of Mo^{4+} to Mo^{5+}, revealing that the interaction in the Mo^{V}-CN-Mn^{II} linkage is antiferromagnetic. The X-ray photoelectron spectroscopy (XPS) analysis of the sample after photomagnetic measurement in SQUID (337-356 nm) at 10 K without O_2 was performed. By comparison with reference compound $K_4[Mo^{IV}(CN)_8]$, the intensity of binding energies of $Mo3d_{3/2}$ of the photoproduct increases significantly, suggesting the additional presence of Mo^{V}. The binding energies of Mn2p doublet are lowered by 1 eV, confirming the presence of diverse oxidation states for Mn: Mn^{II}, Mn^{I}. This is consistent with an incomplete photoconversion involving a photoinduced electron transfer from Mo^{IV} to Mn^{II}. While for the sample irradiated at room temperature in the presence of O_2, the presence of M^{IV}, M^{VI}, and Mn^{II} centers in the photoproduct suggests the formation of $[M^{VI}(CN)_4(O_2)]$.

A photoswitchable heterotrimetallic chain $[(Ni^{II}(cyclam))(Mo^{IV}(CN)_8)_2(Cu^{II}(Me_2en)_2)_7](ClO_4)_8$ has been delicately designed by the combination of photoresponsive $[Mo^{IV}\text{-}(CN)_4(CNCu^{II}(Me_2en)_2)_4]^{4+}$ and $[Ni^{II}(cyclam)]^{2+}$.[105] Upon irradiation with 460 nm light, the value of χT increases from 3.7 to 4.4 $cm^3\ mol^{-1}$ K due to the electron transfer from Mo^{IV} to Cu^{II}. Although the compound does not behave as a photoinduced single-chain magnet,[106] confirmed by the absence of slow relaxation of the magnetization of the metastable state, the present strategy might be useful to design compounds with high-spin values and anisotropy in their photo-induced state. Then a deliberate replacement of Ni^{2+} by Mn^{3+} has been achieved to successfully increase the overall uniaxial anisotropy, but unfortunately the photomagnetic behavior is absent.[107] The reason is attributed to the not distorted geometry of $[Mo(CN)_8]^{4-}$ by the authors. $[Ni(cyclam)]_2[Mo(CN)_8] \cdot 3H_2O$ which is isostructural with $[Cu(cyclam)]_2[Mo(CN)_8] \cdot 10.5H_2O$ (Cyclam =1,4,8,11-Tetraazacyclodecane),[97, 108] has been prepared by Nowicka et. al, but the photomagnetic properties are not investigated.[109]

Ionic pair, $[Ni(bipy)_3]_2[Mo(CN)_8] \cdot 12H_2O$,[110] has been prepared and it displays an ion-pair charge-transfer (IPCT) band at 390 nm. The photomagnetic investigation with 406–415 nm light irradiation is assumed to be the formation of paramagnetic $[Mo^{V}(CN)_8]^{3-}$ and $[Ni^{II}(bipy)_2(bipy^{-\cdot})]^{+}$ radical by the outer-sphere electron transfer (Figure I. 22).

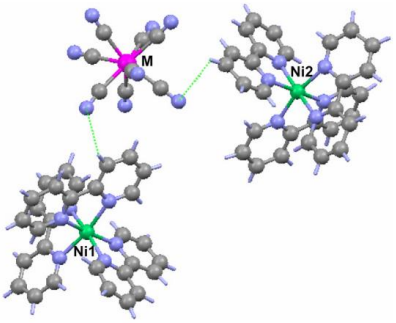

$$[Ni^{II}(bipy)_3]_2[Mo^{IV}(CN)_8] \underset{kT}{\overset{h\nu\ IPCT}{\rightleftharpoons}} [Ni^{II}(bipy)_3][Mo^{V}(CN)_8]\ [Ni^{II}(bipy)_2(bipy^{-\cdot})]$$

$d^8\ d^2 \qquad d^8\ d^1\ d^8$

2x S=1 S=0 S=1 S=1/2 S=1 S=1/2

Figure I. 22 (Top) Asymmetric unit of $[Ni(bipy)_3]_2[Mo(CN)_8] \cdot 12H_2O$ and presentation of shortest intermolecular contacts. (Below) Schematic illustration of outer-sphere electron transfer process.

An Outer-Sphere (Ion-Pair) Charge Transfer (OSCT, IPCT) band around 650 nm from Mo^{IV} to Co^{III} is also observed for ionic compounds: $M^{I}[Co^{III}(bpy)_3][Mo(CN)_8]_3\ nH_2O$ (M^{I} = Li, K, Rb, Cs; n = 7-8).[31] The electron delocalization parameter (R) and coupling parameter (H_{if}) calculated from the Hush theory ($\alpha_2 = 8.6\times10^{-4}$, H_{if} = 463 cm^{-1}) indicate weak-to-moderate coupling between Co(III) and Mo(IV), which is in agreement with the redox potentials of the

$[Mo(CN)_8]^{3-/4-}$ and $[Co(bpy)_3]^{3+/2+}$ complexes ($E_{MoV/IV}^{o}$= 0.78 V vs NHE, $E_{CoIII/II}^{o}$=0.61 V vs NHE). Based on EPR studies, the Mo^{V} is generated after the dehydration. In parallel, when heating the original compound to 340-350 K, a significant increase of magnetization is observed, which confirms the existence of an equilibrium between the bimetallic pairs $Co^{III}Mo^{IV}/Co^{II}Mo^{V}$. A photoinduced increase of χT from 0.26 to 0.32 cm^3 mol^{-1} K at 10 K by the light irradiation of 647 nm is observed for dehydrated phase, while no effect is observed for pristine sample. One possible explanation is that the loss of water molecules can modify the redox potentials of the metal centers and render the whole system flexible to facilitate the $Co^{III}_{LS}Mo^{IV}$- $Co^{II}_{HS}Mo^{V}$ equilibrium shift.

I.4 ET or SCO ?

Based on the results described in I.2, we have seen that the researchers have tried different techniques to prove the MMCT mechanism. X-ray absorption spectroscopy (XAS) and X-ray magnetic circular dichroism (XMCD) are powerful techniques to investigate the oxidation state of the metal centers. In this section, we are discussing the results obtained by XAS and XMCD for several Cu/Mo OCM systems.

I.4.1 Evidences of the formation of Mo^{IV}_{HS} by XAS and XMCD studies

The light-induced formation of Mo^{IV}_{HS} (S = 1) has been firstly revealed by the XAS and XMCD studies of $Cs_2Cu_7[Mo(CN)_8]_4$ nanoparticles, a 3D network[111] and $MoCu_2$-Meen, a molecular complex.[112] By investigation of $Cs_2Cu_7[Mo(CN)_8]_4$, a significant modification for XAS signals is observed at the Mo L_3 edge after light irradiation, and this modification is generally reversible. However, nearly no effect is observed for Cu K edge (Figure I. 23).

The analysis of local magnetization of $[Mo^{IV}(CN)_8]^{4-}$ for $Cs_2Cu_7[Mo(CN)_8]_4$ confirms the formation of high spin Mo^{IV} after light irradiation by the comparison of calculated experimental values considering Mo^{IV} and Mo^{V} species with the corresponding theoretical spin magnetization curves (Figure I. 24). Thus, the photomagnetic mechanism is revealed to be a photoconversion of Mo(IV) ions from low spin (LS) configuration ($4d^2$, S = 0) to high spin configuration ($4d^2$, S = 1). This process can be called as S-T crossover or light-induced excited spin state trapping (LIESST) effect. Thus the MMCT mechanism is completely ruled out by the authors. Theoretical calculations suggest that the low spin−high spin transition on the molybdenum atom is accompanied by the loss of one CN ligand.[113-115]

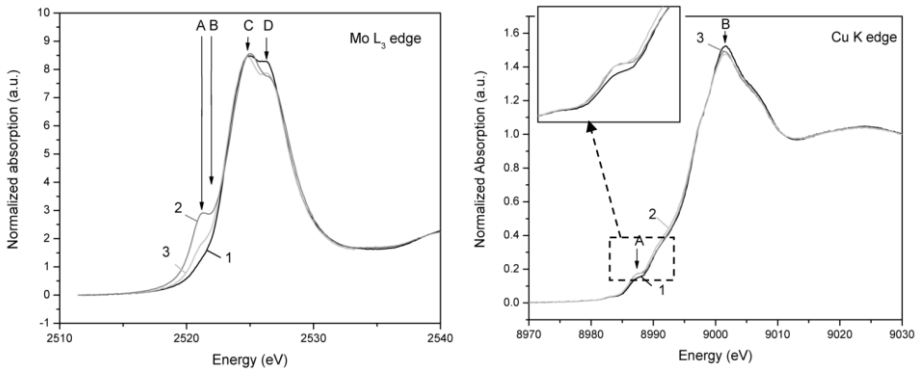

Figure I. 23 Absorption spectra for $Cs_2Cu_7[Mo(CN)_8]_4$ at the Mo L_3 edge (Left) and Cu K edge (Right): (1) before illumination (T = 9 K); (2) after illumination (T = 9 K) and (3) after relaxation at room temperature (T = 300 K).

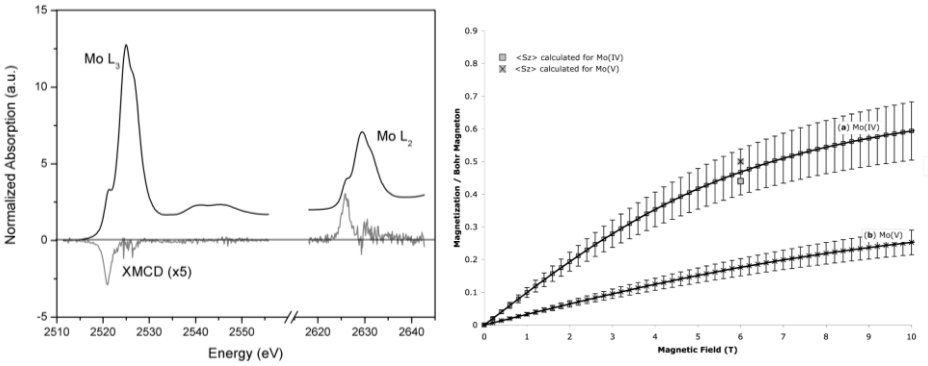

Figure I. 24 (Left) Isotropic XAS spectra and XMCD signals for $Cs_2Cu_7[Mo(CN)_8]_4$ at the Mo $L_{2,3}$ edges recorded at T = 9 K and H = ± 6 T. (Right) Theoretical spin magnetization per Mo ion along with the experimental values measured for 2521 eV at H = 6 T. Curve a and the shadowed square are for Mo(IV) and curve b and the shadowed cross are for Mo(V). Reproduced from Ref. [111] with permission from the American Chemical Society 2012.

I.4.2 Other experimental observations of the photoinduced formation of Mo^{IV}_{HS}

I.4.2.1 Formation of Mo^{IV}_{HS} incorporated with non-redox active metal ions

As the MMCT involves oxidation of Mo^{4+} and reduction of Cu^{2+}, the interpretation of Cu/Mo OCM may be complicated due to the possible coexistence of the MMCT and S-T mechanisms. To confirm the formation of only photoinduced Mo^{IV}_{HS}, the studies of a series of compounds made with the non-redox active metal ions such as $Zn^{II}(3d^{10})$, $Cd^{II}(4d^{10})$ and the $[Mo^{IV}(CN)_8]^{4-}$ building block reveal that the S-T crossover pathway are important.

The first evidence of photomagnetic properties in a Zn-$[Mo(CN)_8]$ system has been obtained with $[Zn(tren)]_2[Mo(CN)_8]$ (**$MoZn_2$-tren**) (Figure I. 25).[72] This system show two crystallographically independent Mo sites: the geometry for Mo1 is revealed to be pure SAPR, while Mo2 has a distorted coordination environment between TDD and SAPR. Mo-C bond lengths are slightly longer for Mo2, but cyanide ligand distances are similar for the two Mo sites. A color change of the crystal from yellow to bright red is observed after irradiation under 4 K, and the pristine yellow color is restored after increasing temperature. The value of χT increases from 0 to 0.47 $cm^3\ mol^{-1}\ K$ for the photoinduced state at 8.5 K, which suggests that only 50% of Mo sites are irradiated, considering that 100% of conversion of $S = 1$ with $g = 2$ leads to a χT value of 1 $cm^3\ mol^{-1}\ K$.

For the S-T mechanism, the flexible geometry of $[Mo^{IV}(CN)_8]^{4-}$ is the key factor, because different coordination geometries can lead to different d-orbital splitting patterns (Figure I. 26). The geometry of OCMs is known to be very sensitive to the chemical environment.[61] The degree of distortion can be quantitatively estimated by the analysis of continuous shape measures (CShM).[116-117]

Supported by the photocrystallography data of **$MoZn_2$-tren** at 10 K, the authors suggest that only the spin state of Mo2 is modified with light irradiation. The strong modification of the structure is only observed for Mo2, and the corresponding Mo–C bond distances are elongated. The elongation of Mo-C bond is almost aligned with the *y* axis, causing an energy decrease of the empty d_{x2-y2} molecular orbital for the SAPR Mo^{IV}_{LS} cation (Figure I. 26).

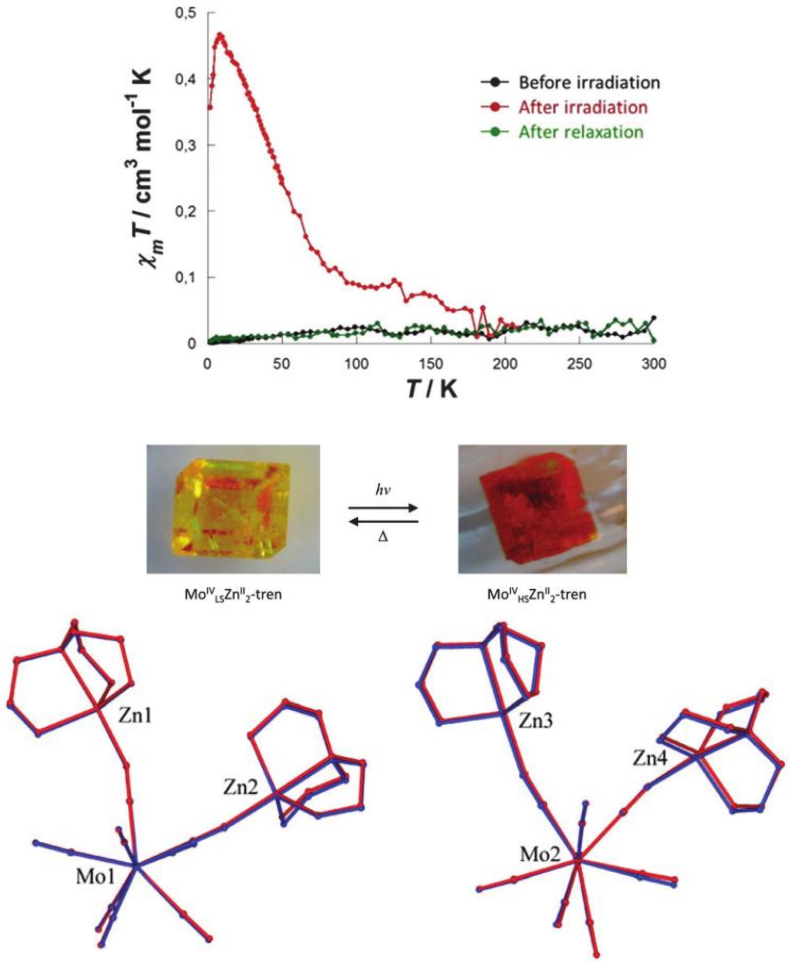

Figure I. 25 (Top) Temperature dependence of χT for **MoZn$_2$-tren** before and after light irradiation. (Middle) Colour change of crystal upon light irradiation. (Below) Superposition of the structural models of the ground state (in blue) and an average photo-irradiated state (in red). Reproduced from Ref. [72] with permission from the Royal Society of Chemistry 2015.

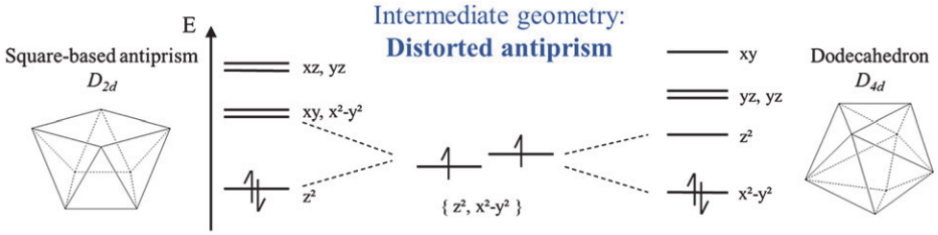

Figure I. 26 The intermediate geometry of molybdenum Mo2 center could stabilize the triplet state of the Mo^{IV} system. Reproduced from Ref. [72] with permission from the Royal Society of Chemistry 2015.

One example of a compound made with $[Mo^{IV}(CN)_8]^{4-}$ and Cd^{2+} ion is the hexanuclear compound $\{[Cd^{II}(bpy)_2]_4[Mo^{IV}(CN)_8]_2\}\cdot 10H_2O$ (Figure I. 27).[118] This compound shows a single-crystal-to-single-crystal (SCSC) transformation upon dehydration with significant color change. This SCSC transformation is accompanied by the coordination geometry change of the $[Mo^{IV}(CN)_8]^{4-}$ from the square antiprism toward the dodecahedra upon dehydration, showing that the coordination geometry is very sensitive to the environment. An undenied photomagnetic effect is observed for solvated form of Mo analogue with the mechanism believed to be S-T crossover, because the innocent Cd^{2+} cannot be involved in a charge transfer process, with Cd^{+} being unstable.

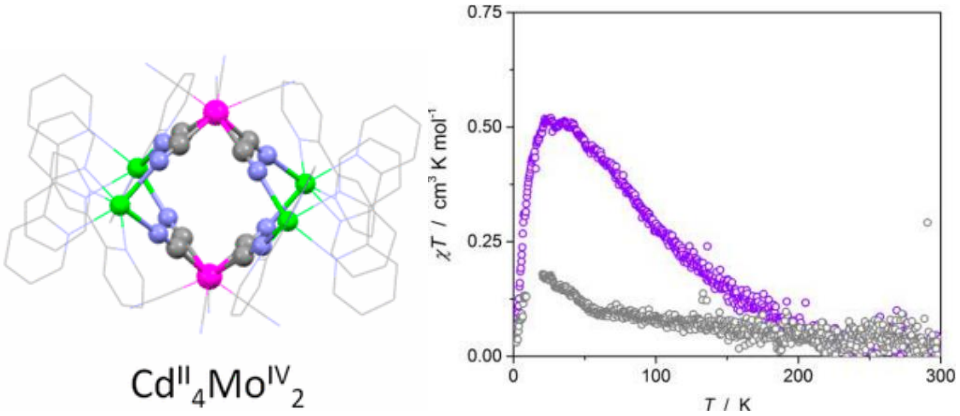

Figure I. 27 (Left) Hexanuclear octahedral core of **Cd_4Mo_2** complex. H atoms are omitted for the sake of clarity. (Right) χT in function of temperature at 0.1 T after irradiation using 436 nm light (violet points) and after heating to 300 K (gray points). Reproduced from Ref. [118] with permission from the American Chemical Society 2017.

In 2017, the coordination chain compound $\{[Mn^{II}(bpy)_2][Mn^{II}(bpy)(H_2O)_2][Mo^{IV}(CN)_8]\cdot 5H_2O\}_n$ was studied, comprising Mn_2Mo_2 corner sharing squares. The photomagnetic effect for this compound is also explained by light-induced excited spin state trapping (LIESST) effect for Mo.[119] To support this, the authors also study the photomagnetic properties of the monomer salt $(H_4cyclam)[Mo^{IV}(CN)_8]\cdot 1.5H_2O$ (Figure I. 28),[119] proving the intrinsic photomagnetic properties of the $Mo^{IV}(CN)_8$ building blocks. The magnetic interactions between Mn^{II} and high-spin Mo^{IV} is determined to be antiferromagnetic.

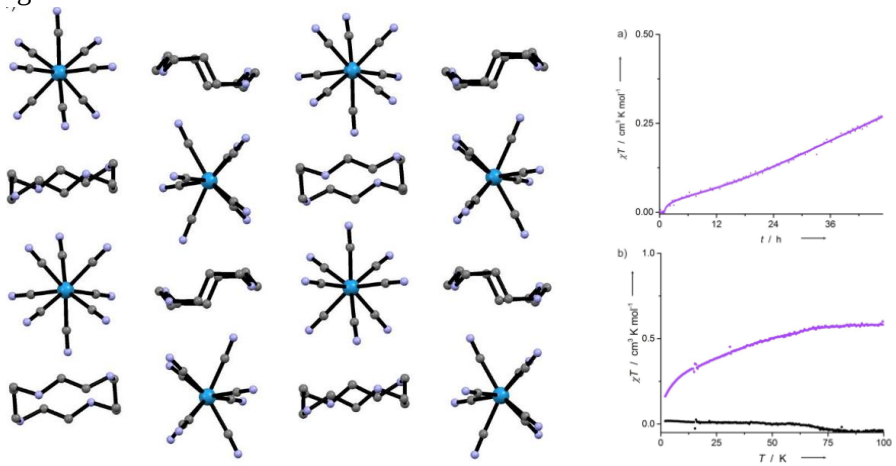

Figure I. 28 (Left) Crystal packing of $(H_4cyclam)[Mo^{IV}(CN)_8]\cdot 1.5H_2O$ (H atoms and H_2O molecules omitted for the sake of clarity). (Right a) χT(time) at H = 0.1 T and T = 10 K during 436 nm irradiation and (Right b) $\chi T(T)$ at H = 0.1 T for $(H_4cyclam)[Mo^{IV}(CN)_8]\cdot 1.5H_2O$ after irradiation (violet points) and after thermal relaxation (black points). Reproduced from Ref. [119] with permission from the Wiley 2017.

Most recently, the hexanuclear complex $\{[Fe^{II}(tmphen)]_4[Mo^{IV}(CN)_8]_2\}\cdot$solv (solv = crystallization solvent MeOH/H_2O) is reported to display site-selective photoswitching effect, with the possible formation of $Fe^{II}{}_{HS}$ and $Mo^{IV}{}_{HS}$ with violet light irradiation or the formation of $Fe^{II}{}_{HS}$ and $Mo^{IV}{}_{LS}$ with red light irradiation in the photo-induced state.[120]

I.4.2.1 Formation of $Mo^{IV}{}_{HS}$ incorporated with Cu^{II} cation

Apart from the incorporation of innocent M^{II} ions mentioned above which experimentally confirms that $[Mo^{IV}(CN)_8]^{4-}$ can behave as photomagnetic unit, the recent investigations of other Cu^{II}-Mo^{IV} compounds also tend to ascribe the photomagnetic effects observed to be a S-T crossover mechanism.

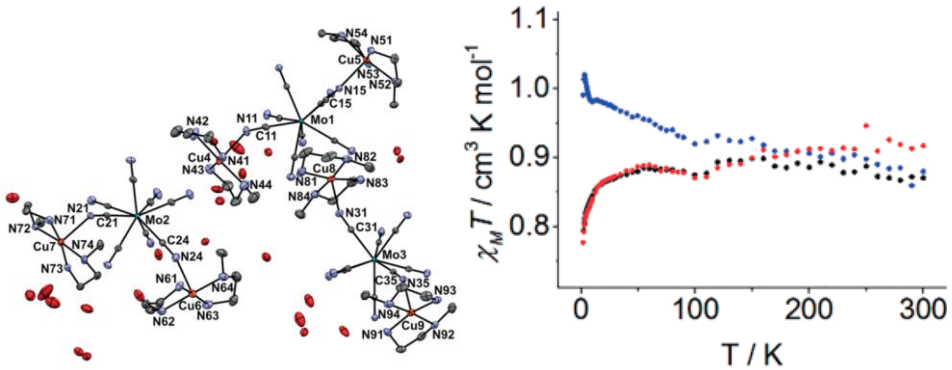

Figure I. 29 (Left) The asymmetric unit of $[Cu(meen)_2]_2[Mo^{IV}(CN)_8]\cdot 5H_2O$. (Right) The corresponding χT (T) plots: before irradiation (black); after irradiation of 436 nm light (blue) and after thermal relaxation (red).

In 2018, the group of Sieklucka prepared two trinuclear compounds $[Cu(meen)_2]_2[Mo^{IV}(CN)_8]\cdot 5H_2O$ and $[Cu(eten)_2]_2[Mo(CN)_8]\cdot 7H_2O$ (meen = N-methylethylenediamine; eten = N-ethyl-ethylenediamine) which witness photomagnetic effects under irradiation of 436 nm light (Figure I. 29). The mechanism is believed to be singlet–triplet crossover of Mo^{IV}. The S-T mechanism is justified by the authors considering the significant bent cyanido bridge (average Cu–N–C angle of 139.2(3)°) and the associated long Cu–N distance (within the 2.245(4)–2.331(3) Å range). The low yield of photoconversion is ascribed to the distorted dodecahedral geometry of molybdenum site and ineffective electron delocalization through long cyanide bridges.[121]

The chiral (1-D) compounds $[Cu((R,R)\text{-chxn})_2]_2[Mo(CN)_8]\cdot H_2O$ and $[Cu((S,S)\text{-chxn})_2]_2[Mo(CN)_8]\cdot H_2O$ have also been reported as photomagnetic. The authors explain the photomagnetic properties by the formation of $Mo^{IV}{}_{HS}$.[122] The photomagnetic properties are also slightly different with the Rac form, which indicates that the photomagnetic properties are vulnerable even with slight structural differences.

To achieve the rational design of heterotrimetallic coordination framework, a photomagnetic trinuclear salt $(dppipH_2)_2[(NC)_7Mo^{IV}\text{-}CN\text{-}Pt^{IV}(NH_3)_4\text{-}NC\text{-}Mo^{IV}(CN)_7]\cdot 15H_2O$ (**MoPtMo**) (dppip = 1,4-di(4-pyridinyl)piperazine) has been prepared. This trinuclear salt has been used to synthesize a two-dimensional honeycomb network $[Cu^{II}(cyclam)]_2[(NC)_7Mo^{IV}\text{-}CN\text{-}Pt^{IV}(NH_3)_4\text{-}NC\text{-}Mo^{IV}(CN)_7]\cdot 40.89H_2O$ (**CuMoPtMo**). (cyclam = 1,4,8,11-tetraazacyclotetradecane) and a one-dimensional chain $[Mn^{II}(dpop)][Mn^{II}(dpop)(H_2O)][(NC)_7Mo^{IV}\text{-}CN\text{-}Pt^{IV}(NH_3)_4\text{-}NC\text{-}Mo^{IV}(CN)_7]\cdot 36H_2O$ (**MnMoPtMo**) (dpop = 2,13-dimethyl-3,6,9,12,18-pentaazabicyclo-[12.3.1]octadeca-1(18),2,12,14,16-pentaene). The **CuMoPtMo** inherits the photomagnetic properties of **MoPtMo**. The change of spin states is interpreted to be based on solely $[Mo(CN)_8]^{4-}$, instead of the possible formation of $[Pt^{II}(NH_3)_4]^{2+}$-$[Mo^{V}(CN)_8]^{3-}$ or Cu^{+}-$[Mo^{V}(CN)_8]^{3-}$ units due to the charge transfer.[123] This is because no MMCT band could be detected. On contrary with the interpretation of EPR data in other references,[92-93] the decrease of Cu^{II} signal during light irradiation is just due to the thermal effect of light and not because of the generation of Cu^{+}-$[Mo^{V}(CN)_8]^{3-}$. The EPR signal cannot be ascribed as the generation of $Mo^{IV}{}_{HS}$ which is supposed to be "EPR silent" due to zero-field splitting, in disagreement with the previous report.[124] However, **MnMoPtMo**, the combination of **MoPtMo** unit with Mn^{II}, exhibits no photomagnetic effect. This is explained by the authors that the d−d transitions centered at Mo^{IV} are masked by the strong absorption of the $[Mn^{II}(dpop)(NC)_2]$ unit.

I.4.3 Presence of the two mechanisms

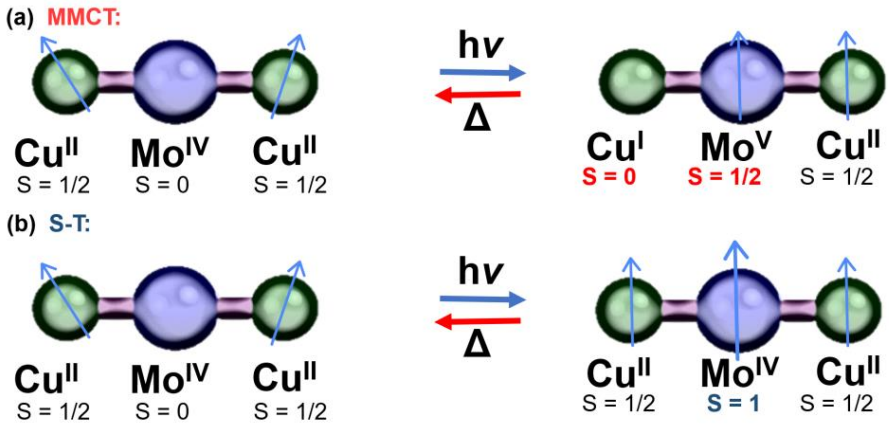

Scheme I. 1 Schematic illustration of (a) light-induced metal-to-metal charge transfer (MMCT) and (b) singlet-triplet (S-T) crossover in Cu^{II}-$[Mo^{IV}(CN)_8]$ system.

If S-T or MMCT have been proposed in different cases,[72, 93, 124-125] the combination of the two mechanisms in the same compound is an interesting question. Different pathways can result in different photomagnetic behaviors (Scheme I. 1). One feature of the MMCT mechanism is that no new spin is formed during the transformation from Cu^{II} (S = 1/2)–Mo^{IV} (S = 0) to Cu^{I} (S = 0)–Mo^{V} (S = 1/2). When the atomic ratio of Cu:Mo is above 2, the ferromagnetic interactions between the residual proximal Cu^{II} and Mo^{V} can explain the enhancement of magnetic properties. For the S-T mechanism, the total spin number increases, which leads to the noticeable increase of saturation magnetization, M_{sat}. Additional magnetic coupling between Mo^{IV}_{HS} and Cu^{II} also influences the magnetic properties.

1D ribbon $[Cu^{II}(bapa)]_2[Mo^{IV}(CN)_8]\cdot 7H_2O$ (bapa = bis(3-aminopropyl)amine) is described as photoresponsive with blue, green and white light.[86] The efficiency of light is proved with the following sequence 532 nm > 405 nm > white light, whereas 647, 830 and 980 nm laser lines have no effect. The photomagnetic effect is thermally reversible when heated to 253 K or partially photoreversible with a subsequence of irradiations by 532, 647, 843 and 980 nm laser lines. The photomagnetic effect is attributed to both a spin crossover on Mo(IV) centers and a metal-to-metal charge transfer mechanism in the Cu(II)–Mo(IV) units.

A series of solid solutions, $[Mo(Zn_{(1-x)}Cu_x)_2$-tren] (x = 0, ε, 1, 5 and 10 %, with ε corresponding to ppm ratio), have been developed as new model compounds to provide direct evidences for the coexistence of two mechanisms.[124] Highly diluted copper compounds in such matrix can facilitate the analysis of EPR spectra for the eventual observation of the signal for Mo^{IV}_{HS}. Highly concentrated copper compounds are good candidates for X-ray diffraction and SQUID magnetometry studies. Comparison of the photomagnetic properties of $[Mo(Zn_{(1-x)}Cu_x)_2$-tren] (x = 5 %) and the pure zinc compound suggests that the maximum χT values are reached at different temperatures (20 K for 5% doped one, 8.5 K for pure $MoZn_2$). This indicates for the authors that an additional photoinduced MMCT mechanism occurs when incorporating with copper. Systematic investigation of Zn^{II}/ Cu^{II} (tren)-Mo^{IV} solid solution systems suggests that the strongly bent cyanide bridge can efficiently lower the orbital overlap and trap the Mo^{V}–Cu^{I} excited state, which is against the interpretation of bent cyanide bridge favoring the SCO process.[121] Moreover, the low extent of orbital overlap can favor the ferromagnetic interactions between Mo^{V} and Cu^{II}.

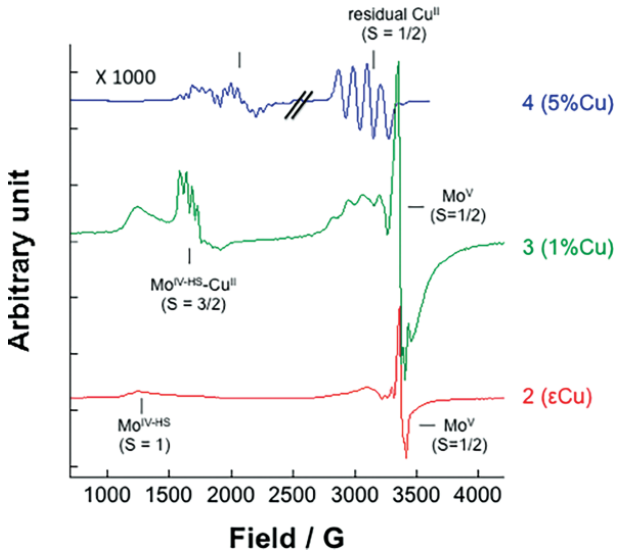

Figure I. 30 EPR spectra for $[Mo(Zn_{(1-x)}Cu_x)_2$-tren] (x = ε, 1 and 5 %) compounds after light irradiation. Reproduced from Ref. [124] with permission from the Wiley 2017.

The EPR spectra under irradiation for the doped compound <10% show the presence of the Mo^V (S = 1/2), Mo^{IV}_{HS} (S = 1) and ferromagnetic pairs Mo^{IV}_{HS}-Cu^{II} (S = 3/2), which are related to the two mechanisms (Figure I. 30). But the coexistence of the mechanisms is still unclear for the doped compounds with high concentration of Cu^{2+} because the eventual signal of Mo^V can be masked by the strong presence of Cu^{II}.

In 2018, an important example to support the coexistence of two mechanisms is shown in a trinuclear $Cu^{II}_2Mo^{IV}$ molecule, $[Cu^{II}(enpnen)]_2[Mo^{IV}(CN)_8]\cdot 6.75H_2O$ (enpnen = N,N′-bis(2-aminoethyl)-1,3-propanediamine) (Figure I. 31).[125] The selection of the temperatures to perform irradiations may have an impact on the dominant mechanisms. As evidenced by χT-T relaxation curves, the shape can be strongly modified with different irradiation temperatures, even if the final relaxation temperatures are always around 255 K (Figure I. 32). The low-temperature magnetization values in high fields increase from 1.94 $N_A\mu_B$ to 2.24 $N_A\mu_B$ for the sample irradiated at 10 K (expected values: 2 $N_A\mu_B$ for MMCT and 4 $N_A\mu_B$ for LIESST). This increase is a proof of LIESST mechanism rather than only a photo-induced electron transfer mechanism.

A model considering the exchange coupling J, the fraction of different states (SCO or MMCT states), the lifetime τ_0 of the two mechanisms is employed to analyze the magnetic data. The obtained energy barrier for the relaxation of the LIESST excited state ($\Delta_2 \approx 4400$ K) is higher than the one for MMCT excited state ($\Delta_1 \approx 100$K). Thus, the S-T mechanism is responsible for the relaxation behaviour at high temperature. The estimations of the exchange couplings in both the MMCT excited state (J_{1MMCT} = 11 cm^{-1}) and the LIESST excited state ($J_{2LIESST}$ = 109 cm^{-1}) derived from the fitting confirm the ferromagnetic character of the interaction in the excited state.

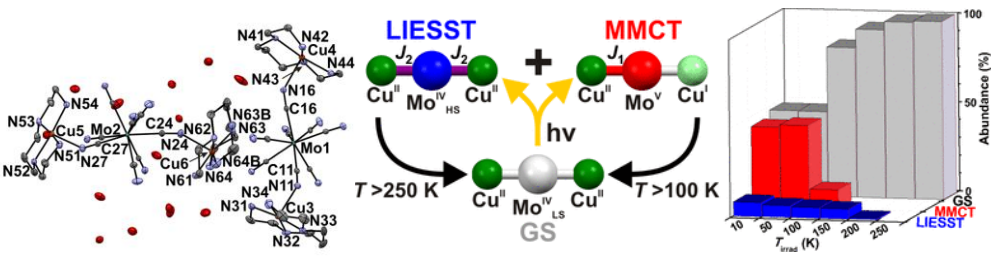

Figure I. 31 (Left) The asymmetric unit of $[Cu^{II}(enpnen)]_2[Mo^{IV}(CN)_8]\cdot 6.75H_2O$. (Middle) Schematic of the ground-state model, the MMCT excited-state model, and the LIESST excited-state model. (Right) Abundances of the ground state (GS), light-induced MMCT and LIESST states for the irradiation at 10, 50, 100, 150, and 200 K. Reproduced from Ref. [125] with permission from the American Chemical Society 2018.

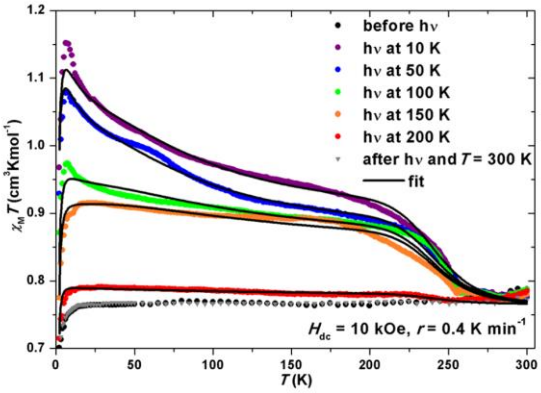

Figure I. 32 χT (T) plots for $[Cu^{II}(enpnen)]_2[Mo^{IV}(CN)_8]\cdot 6.75H_2O$ before and after excitation with 405 nm laser line performed at diverse temperatures and after heating to 300 K. Reproduced from Ref. [125] with permission from the American Chemical Society 2018.

Recently, the photomagnetic properties for 2-D coordination polymer $K_4\{[Cu(ida)]_2[Mo(CN)_8]\}\cdot 4H_2O$ (ida^{2-} = iminodiacetate) are revealed as analogous with $[Cu^{II}(enpnen)]_2[Mo^{IV}(CN)_8]\cdot 6.75H_2O$. The coexistence of MMCT and S-T mechanisms is reasonable to correlate χT and $M(H)$ curves observed.[126]

Photomagnetic compounds based on $[Mo^{IV}(CN)_8]^{4-}$ in literature are listed in Table I. 1. A wide range of light (UV-light, 400-530 nm and 647 nm) has been employed to access different photoexcited states, which shows that formation of the photoproducts is quite wavelength dependent. To de-excite the photogenerated state, red and near infrared light are employed for 3-D $Cu^{II}_2[Mo^{IV}(CN)_8]\cdot 8H_2O$, 2-D $[Cu^{II}(cyclam)]_2[Mo^{IV}(CN)_8]\cdot 10.5H_2O$, and only a partial photoreversibility is achieved for $[Cu^{II}(bapa)]_2[Mo^{IV}(CN)_8]\cdot 7H_2O$.[86] There are numerous valuable attempts to elucidate the corresponding photomagnetic mechanism by following the variation of IR, UV-Vis, EPR, XPS, XAS spectra upon light irradiation. EPR may not suitable for the clarification of photomagnetic mechanism in this system, because the exact signal for Mo^{IV}_{HS} is still unknown. More convincing evidences for the clear identification of the mechanisms are still needed by the complete study of one compound using different techniques such as XAS, XPS, IR, UV-Vis spectra and photocrystallography with light irradiation at 10 K. Different than Co/Fe and Co/W systems which clearly demonstrate the MMCT mechanism, it is not easy to confirm the MMCT process for Cu/Mo system based on these routine analysis, which needs further proofs.

Table I. 1 List of photomagnetic compounds based on $[Mo^{IV}(CN)_8]^{4-}$ in literature.

Compound	$[Mo(CN)_8]^{4-}$	MMCT band	Light source; Proposed mechanism	Experimental evidences	Ref.
0D-$K_4[Mo(CN)_8]\cdot 2H_2O$	TDD	-	UV-light; formation of Mo^V	Photomagnetic measurements (irreversible); EPR (sample measured after SQUID measurement)	70
1D-$[Mn^{II}_2(L1)_2(H_2O)][Mo(CN)_8]\cdot 5H_2O$	SAPR	-	UV-light; formation of Mo^V	Photomagnetic measurements (irreversible)	70
3D-$\{[Cu^{II}(H_2O)]_2[Mo(CN)_8]\}\cdot x H_2O$	SAPR	483 nm	480 nm, 400–430 nm,413 nm, 530 nm or 473 nm; MMCT	Photomagnetic measurements (CuW is not photomagnetic); IR (decrease of the peak for Mo^{IV}-CN-Cu^{II}); UV-Vis spectra (reverse-IT band after irradiation); Theoretical calculation; XAS on Mo and Cu	71, 74, 76-79
0D-$\{Cu^{II}(bipy)_2\}_2\{Mo(CN)_8\}]\cdot x H_2O\cdot CH_3OH$	SAPR	530 nm	488 nm; MMCT or UV-light; formation of Mo^V	Photomagnetic measurements (irreversible with UV-light)	74, 87
0D-$[Mo(CN)_2(CN\text{-}CuL)_6](ClO_4)_8$ (**Cu_6Mo**)	TDD	440 nm	406–415 nm; MMCT or S-T	Photomagnetic measurements; XAS (formation of Mo^{IV}_{HS}); Theoretical calculation (formation of Mo^{IV}_{HS})	MMCT [88] or S-T[112-113, 115]
3D-$Cs^I_2Cu^{II}_7[Mo(CN)_8]_4\cdot 6H_2O$ (**CsCuMo**)	BTP	520 nm	450-500 nm; MMCT or S-T	Photomagnetic measurements; XAS (MMCT or formation of Mo^{IV}_{HS}); IR and EPR (decrease of Cu^{II} signal)	MMCT [80-81] or S-T[111]
0D-$[Mn(bpy)_2]_4[Mo(CN)_8]_2\cdot x H_2O$	SAPR	n/a	337-356 nm; MMCT	Photomagnetic measurements; XPS(the formation of Mn^I-M^V without O_2 and the formation of $[M^{VI}(CN)_4(O_2)]$ with O_2)	26
0D-$[Ni(bipy)_3]_2[Mo(CN)_8]\cdot 12H_2O$	TDD	390 nm for Mo and at 410 nm for W	406–415 nm; The formation of $[Mo^V(CN)_8]^{3-}$ and $Ni^{II}(bipy)_2(bipy)]^+$	Photomagnetic measurements	110
1D-$[(Ni^{II}(cyclam))(Mo(CN)_8)_2(Cu^{II}(Me_2en)_2)_7](ClO_4)_8$	n/a	-	460 nm; MMCT	Photomagnetic measurements	105
0D-$[Mo(CN)_8\{CuL_1\}_2\{CuL_1(H_2O)\}_2]\cdot 6H_2O$	n/a	470 nm	488 nm; MMCT	Photomagnetic measurements	96
0D-$[Mo(CN)_8\{CuL_2\}_3\{CuL_2(H_2O)\}]_2\cdot 10H_2O$	n/a	504 nm	488 nm; MMCT	Photomagnetic measurements	96
2D-$[Cu(cyclam)]_2[Mo(CN)_8]\cdot 10.5H_2O$ (**$MoCu_2$**)	TDD	-	410 nm; MMCT	Photomagnetic measurements; IR(variation of IR spectra at 273 K and 3 K)	97-98, 108
0D-$[Cu(meen)_2]_2[Mo(CN)_8]\cdot 5H_2O$	SAPR	-	436 nm; S-T	XAS, Theoretical calculation	112, 114, 121
0D-$M^I[Co(bpy)_3][Mo(CN)_8]_3$ Mixture of Co^{III}/Mo^{IV} and Co^{II}/Mo^V	SAPR	650 nm	647 nm; MMCT	Photomagnetic measurements; EPR (decrease of the signal for both molybdenum and cobalt region)	31

(continue of Table I. 1)

1D-[Cu(tren)][Cu(bapa)][Mo(CN)$_8$]·4H$_2$O	BTP	460 nm	UV light;MMCT	Photomagnetic measurements; EPR(77K, decrease of Cu^{II})	127
0D-[Cu(tpa)]$_2$[Mo(CN)$_8$]·15H$_2$O (**1**)	BTP	400–500 nm	UV-light; MMCT	Photomagnetic measurements; EPR(77K, decrease of Cu^{II})	92
0D-[Cu(tren)]$_2$[Mo(CN)$_8$]·5.25H$_2$O (**2**)	BTP	400–500 nm	UV-light; MMCT	Photomagnetic measurements; EPR(77K, decrease of Cu^{II})	92
1D-[Cu(en)$_2$][Cu$_{0.5}$(en)][Cu$_{0.5}$(en)(H$_2$O)][Mo(CN)$_8$]·4H$_2$O (**3**)	BTP	400–500 nm	UV-light; MMCT	Photomagnetic measurements; EPR(77K, decrease of Cu^{II})	92
2D-[Cu(bapa)]$_3$[Mo(CN)$_8$]$_{1.5}$·12.5H$_2$O (**4**)	SAPR	400–500 nm	UV-light; MMCT	Photomagnetic measurements; EPR(77K, decrease of Cu^{II})	92
2D-[Cu(bapen)]$_2$[Mo(CN)$_8$]·4H$_2$O (**5**)	SAPR	400–500 nm	UV-light; MMCT	Photomagnetic measurements; EPR(77K, decrease of Cu^{II})	92
3D-[Cu(pn)$_2$][Cu(pn)][Mo(CN)$_8$]·3.5H$_2$O (**6**)	SAPR	400–500 nm	UV-light; MMCT	Photomagnetic measurements; EPR(77K, decrease of Cu^{II})	92
0D-[Cu$^{II}_2$(bpmen)$_2$][Mo(CN)$_8$]·8H$_2$O	TDD	n/a	UV-light; MMCT	Photomagnetic measurements(thermally reversible)	94
0D-[Zn(tren)]$_2$[Mo(CN)$_8$] (**MoZn$_2$-tren**)	SAPR	-	405 nm; S-T	Photomagnetic measurements; Photocrystallography; IR(2178 cm^{-1} as Mo^{HS}-CN-Zn)	72
1D-[Cu^{II}(bapa)]$_2$[Mo(CN)$_8$]·7H$_2$O	BTP and SAPR	466 nm	405nm, 532 nm or with white light; S-T and MMCT	Photomagnetic measurements (photoreversibility studies with red and IR light)	86
0D-[Mo$_6$Cu$_{14}$-tacn]	Distorted SAPR	n/a	405 nm; MMCT	Photomagnetic measurements ([Mo$_6$Zn$_{14}$] is not photomagnetic); EPR	93
0D-[Mo$_3$Cu$_4$-Me$_3$tacn]	Distorted SAPR	n/a	405 nm; MMCT	Photomagnetic measurements; EPR	93
0D-[Cu(L$_1^O$)(py)]$_4$[Mo(CN)$_8$]·14H$_2$O (**Cu$_4$Mo**)	TDD	400-610 nm	436 nm; MMCT	Photomagnetic measurements; difference in electronic spectra	95
0D-[Cu(L$_2$)]$_2$[Mo(CN)$_8$]·9H$_2$O (**Cu$_2$Mo**)	SAPR	-	470 nm; S-T	Photomagnetic measurements; difference in electronic spectra	95
0D-[Mo(Zn$_{(1-x)}$Cu$_x$)$_2$-tren]	SAPR	n/a	405 nm; S-T and MMCT	Photomagnetic measurements; Photocrystallography; EPR(signal for Mo$^{IV}_{HS}$)	124
0D-{[Cd^{II}(bpy)$_2$]$_4$[Mo(CN)$_8$]$_2$}·10H$_2$O (**Cd$_4$Mo$_2$**)	SAPR	-	436 nm; S-T	Photomagnetic measurements (W analogue is not photomagnetic)	118
1D-{[Mn^{II}(bpy)$_2$][Mn^{II}(bpy)(H$_2$O)$_2$][Mo(CN)$_8$]·5H$_2$O}$_n$	SAPR	-	436 nm; S-T	Photomagnetic measurements	119
0D-(H$_4$cyclam)[Mo(CN)$_8$]·1.5H$_2$O	SAPR	-	436 nm; S-T	Photomagnetic measurements	119
0D-[Cu(eten)$_2$]$_2$[Mo(CN)$_8$]·7H$_2$O	SAPR	-	436 nm; S-T	Photomagnetic measurements	121

(continue of Table I. 1)

2D-$[Cu(aepa)]_{10}[Mo(CN)_8]_5\cdot 30H_2O$	SAPR and TDD	-	450 nm; MMCT and S-T	Photomagnetic measurements (bent cyanido linkages for the observation of MMCT)	128
0D-$[Cu^{II}(enpnen)]_2[Mo(CN)_8]\cdot 6.75H_2O$	SAPR	432 and 568 nm	405 nm; MMCT and S-T	Photomagnetic measurements (data fitting)	125
0D-$\{[Fe^{II}(tmphen)]_4[Mo(CN)_8]_2\}\cdot$solv	n/a	-	405 nm; S-T	Photomagnetic measurements	120
0D-$\{[Mn^{II}(tmphen)]_4[Mo(CN)_8]_2\}\cdot$solv	n/a	-	405 nm; S-T	Photomagnetic measurements	120
1D-$[Cu((R,R)\text{-chxn})_2]_2[Mo(CN)_8]\cdot H_2O$	SAPR	-	436 nm; S-T	Photomagnetic measurements	122
1D-$[Cu((S,S)\text{-chxn})_2]_2[Mo(CN)_8]\cdot H_2O$	SAPR	-	436 nm; S-T	Photomagnetic measurements	122
0D-$(dppipH_2)_2[(NC)_7Mo\text{-}CN\text{-}Pt^{IV}(NH_3)_4\text{-}NC\text{-}Mo(CN)_7]\cdot 15H_2O$ (**MoPtMo**)	SAPR and TDD	-	450 nm; S-T	Photomagnetic measurements	123
2D-$[Cu^{II}(cyclam)]_2[(NC)_7Mo\text{-}CN\text{-}Pt^{IV}(NH_3)_4\text{-}NC\text{-}Mo(CN)_7]\cdot 40.89H_2O$ (**CuMoPtMo**)	SAPR	-	450 nm; S-T	Photomagnetic measurements; EPR to exclude the MMCT	123
1D-$[Mn^{II}(dpop)][Mn^{II}(dpop)(H_2O)][(NC)_7Mo\text{-}CN\text{-}Pt^{IV}(NH_3)_4\text{-}NC\text{-}Mo(CN)_7]\cdot 36H_2O$ (**MnMoPtMo**)	SAPR and TDD	-	Not photomagnetic	--	123
2D-$K_4\{[Cu(ida)]_2[Mo(CN)_8]\}\cdot 4H_2O$	TDD	500 nm	407 nm; S-T and MMCT	Photomagnetic measurements (data fitting)	126
3D-$Rb^{I}_{3/2}Cu^{II}_7[Mo(CN)_8]_{31/8}\cdot 12H_2O$ (**RbCuMo**)	BTP	520 nm	473 nm; MMCT	Photomagnetic measurements; IR(decrease of Cu^{II}), XRD (cell expansion) and THz-TDS	82

I.4.4 The photomagnetic properties of the $[W^{IV}(CN)_8]^{4-}$ anion

Being isoelectronic with octacyanidomolybdate(IV) ($4d^2$), octacyanidotungstate(IV) ($5d^2$) also has a diamagnetic ground state and can construct isostructural crystal structures as molybdenum analogues. Only a few number of photomagnetic compounds based on $[W^{IV}(CN)_8]^{4-}$ are reported in literature (Table I. 2). The detailed studies of the photomagnetic properties for compounds containing $[W^{IV}(CN)_8]^{4-}$ remain quite limited until now.

Table I. 2 The summarization of photomagnetic compounds based on $[W^{IV}(CN)_8]^{4-}$ in literature.

Compound	$[W(CN)_8]^{4-}$	Light source; mechanism	Photomagnetic properties	Ref.
3D-$\{[Cu^{II}(H_2O)]_2[W^{IV}(CN)_8]\}\cdot xH_2O$	SAPR	480 nm, 400–430 nm,413 nm, 530	Not photomagnetic	76-78
0D-$[Mn(bpy)_2]_4[W(CN)_8]_2\cdot xH_2O$	SAPR	337-356 nm; MMCT	Less photomagnetic	26
0D-$[W_6Cu_{14}$-tacn]	SAPR	405 nm; MMCT	Less photomagnetic	93
0D-$[W_3Cu_4$-Me_3tacn]	SAPR	405 nm; MMCT	Less photomagnetic	93
0D-$\{[Cd^{II}(bpy)_2]_4[W^{IV}(CN)_8]_2\}\cdot 10H_2O$ (**Cd_4W_2**)	SAPR	436 nm; S-T	Not photomagnetic	118
1D-$\{[Mn^{II}(bpy)_2][Mn^{II}(bpy)(H_2O)_2][W^{IV}(CN)_8]\cdot 5H_2O\}_n$	SAPR	436 nm; S-T	Similar as Mo analogue	119
0D-(H_4cyclam)$[W(CN)_8]\cdot 1.5H_2O$	SAPR	436 nm; S-T	Similar as Mo analogue	119
3D-$\{[Mn^{II}$(imidazole)$_2]_2[W^{IV}(CN)_8]\}_n$	n/a	450 nm; S-T	Photomagnetic	129
0D-$\{[Fe^{II}$(tmphen)$]_4[W^{IV}(CN)_8]_2\}\cdot$solv	n/a	405 nm; S-T	Similar as Mo analogue	120
0D-$\{[Mn^{II}$(tmphen)$]_4[W^{IV}(CN)_8]_2\}\cdot$solv	n/a	405 nm; S-T	Similar as Mo analogue	120
2D-$K_4\{[Cu(ida)]_2[W(CN)_8]\}\cdot 4H_2O$	TDD	407 nm; S-T and MMCT	Less photomagnetic	126

In 2005, the first confirmation of photomagnetic properties for $[W^{IV}(CN)_8]^{4-}$-based compound, the hexanuclear cluster $[Mn(bpy)_2]_4[W(CN)_8]_2\cdot 9H_2O$ (bpy = 2,2′-bipyridyl), has been achieved by our group. The photomagnetic properties have been interpreted as the formation of Mn^{I} and W^{V}.[26] But in 2017, the photomagnetic effect for $\{[Mn^{II}(bpy)_2][Mn^{II}(bpy)(H_2O)_2][W^{IV}(CN)_8]\cdot 5H_2O\}_n$ has been explained by light-induced excited spin state trapping (LIESST) effect for W^{IV},[119] in parallel with the study of the monomer salt (H_4cyclam)$[W^{IV}(CN)_8]\cdot 1.5H_2O$.[119] These results provide direct proofs of the intrinsic photomagnetic properties of the $W^{IV}(CN)_8$ building block.

Later on, upon dehydration of $\{[Mn^{II}(imidazole)(H_2O)_2]_2[W^{IV}(CN)_8]\cdot 4H_2O\}_n$ ladder motifs, corrugated square grids $\{[Mn^{II}(imidazole)_2]_2[W^{IV}(CN)_8]\}_n$ is generated by the formation of the new cyanide bridges.[129] The photoexcitation is achieved for dehydration form of $\{[Mn^{II}(imidazole)_2]_2[W^{IV}(CN)_8]\}_n$ with blue light (450 nm) corresponding to the d−d transitions of the octacyanotungstate(IV) anion. It exhibits high light-induced magnetic ordering temperature ~ 93 K and magnetic hysteresis loop at 90 K, whereas the fully hydrated phase is not photomagnetic. Owing to the absence of charge transfer band, the proposed mechanism is the formation of photoexcited octacyanotungstate(IV) (W^{IV}_{HS}, S = 1) moiety engaged in antiferromagnetic coupling with manganese(II).

However, a lot of octacyanotungstate compounds are reported as not photoresponsive,[77, 93, 118, 126] such as for 0D-$\{[Cd^{II}(bpy)_2]_4[W^{IV}(CN)_8]_2\}\cdot 10H_2O$ (**Cd_4W_2**) [118] and 3D-$\{[Cu^{II}(H_2O)]_2[W^{IV}(CN)_8]\}\cdot xH_2O$.[77] The octacyanotungstate compounds are less photosensitive compared to their Mo analogues. For example, in the 2-D coordination polymers $K_4\{[Cu(ida)]_2[M(CN)_8]\}\cdot 4H_2O$ (ida^{2-} = iminodiacetate, M = Mo or W), the light irradiation at 10 K with a 407 nm light for 24 h results in 30% and 3% increases of

magnetization for molybdenum and tungsten analogue, respectively.[126]

I.5 Tuning the structure and morphology based on photomagnetic octacyanidometallates at the nanometer scale

With the aim to improve the photomagnetic properties and to have a better understanding of size effect on photo-magnetic properties, the control of the structures and morphologies of the photoresponsive octacyanidomolybdate(IV) compounds at the nanoscale has been achieved.[130] The first Langmuir–Blodgett films involving surfactant-functionalized ligands and photomagnetic molybdenum–copper cyanidometallates **$MoCu_6$** or **$MoCu_2$** allow the precise control of the thickness and the orientation of the nano-objects.[131] The EPR spectra demonstrate the retention of the photomagnetic characteristics even at the monolayer scale. The decrease of the EPR signal intensity for Cu^{II} ions confirms the MMCT mechanism. In addition, $Cs^{I}_2Cu^{II}_7[Mo^{IV}(CN)_8]_4$ nanoparticles have been organized as anisotropic Langmuir–Blodgett films with a preferential orientation of the nano-objects. It exhibits an enhanced photo-transformation compared to the bulk material.[132] 3 nm $CuNiMo(CN)_8$ nanoparticles have been also prepared, in which half of the Cu^{II} ions are replaced with Ni^{II}.[133] This gives a single ion magnetic anisotropy. These nanoparticles exhibit a long relaxation time of magnetization, generating a light induced superparamagnetic behavior.

I.6 Conclusions and perspectives

Photomagnetic materials have raised numerous interests due to their switching properties (color, magnetism, dielectric constant, structure), and they can be applied as active element in optical recording materials. In the first part of this section, we summarized appealing photomagnetic materials involving different photomagnetic mechanisms (spin crossover, charge transfer, isomerization of ligands).

Even though a variety of photomagnetic systems have been studied, the rational design of materials applicable above cryogenic temperature is still challenging. It is still puzzling to relate the photomagnetic behavior and the structural features (i.e. the coordination geometry, crystal packing, hydrogen-bonding, π–π interactions, redox potential and linearity of the cyanide bridge). These correlations will help guide the exploration of more fascinating switchable materials with the expectation of switching around room-temperature.

The photomagnetic compounds reported are mainly involving 3d metal ions, while the incorporation of 4d/5d metal ions is less investigated. Compared with the 3d metal hexacyanidemetallates, 4d/5d octacyanidemetallates (OCM) can offer higher coordination numbers and stronger magnetic interactions caused by their diffuse orbitals. Thus, in the second part of this chapter, we have mainly focused on the reported photomagnetic compounds based on octacyanometallate building blocks.

The complexity of the photomagnetic mechanisms have been studied for the photoresponsive OCMs systems, especially for the Cu(II)–Mo(IV) bridged assemblies. The photomagnetic mechanisms have been subjected to continuous debate: metal-to-metal charge-transfer (MMCT) and/or a SCO at the Mo^{IV} center. To clarify the photomagnetic properties, a series of compounds with different dimensionalities have been studied in literature both structurally and photomagnetically. Different hypotheses have been posed based on the experimental proofs (photomagnetic data and the spectroscopic data after light irradiation).

However, more experimental evidences are still shorted for the clear ascription of photomagnetic mechanisms. The structural factors influencing photomagnetic mechanisms and properties are still unclear, and more investigations for this peculiar OCMs systems are needed. Motivated by this, judicious structural assembling is demanded by incorporating various simple types of cations with/without blocking ligands and the $[M(CN)_8]^{4-}$ units. The optimization of electronic characteristics by appropriate control of the geometries of $[M(CN)_8]^{4-}$ is essential. Especially, instead of the most investigated polymeric systems, the investigation of monomeric compounds is desirable to gain more insights of the intrinsic photomagnetic properties of OCMs units.

I.7 References

1. Shinkai, S.; Feringa, B., Molecular Switches. Wiley-VCH Verlag GmbH: Weinheim, Germany: 2001.
2. Halcrow, M. A., *Spin-crossover Materials: Properties and Applications*. John Wiley & Sons: 2013.
3. Létard, J.-F.; Guionneau, P.; Goux-Capes, L., Towards Spin Crossover Applications. *Top. Curr. Chem.* **2004,** *235*, 221-249.
4. Nihei, M.; Shiga, T.; Maeda, Y.; Oshio, H., Spin crossover iron(III) complexes. *Coord. Chem. Rev.* **2007,** *251* (21), 2606-2621.
5. Hayami, S.; Komatsu, Y.; Shimizu, T.; Kamihata, H.; Lee, Y. H., Spin-crossover in cobalt(II) compounds containing terpyridine and its derivatives. *Coord. Chem. Rev.* **2011,** *255* (17-18), 1981-1990.
6. McGarvey, J. J.; Lawthers, I., Photochemically-induced perturbation of the 1A-reversible-5T equilibrium in Fe^{II} complexes by pulsed laser irradiation in the metal-to-ligand charge-transfer absorption-band. *J. Chem. Soc.,-Chem. Commun.* **1982,** (16), 906-907.
7. Baker, W. A.; Bobonich, H. M., Magnetic Properties of Some High-Spin Complexes of Iron(II). *Inorg. Chem.* **1964,** *3* (8), 1184-1188.
8. Hauser, A.; Jeftić, J.; Romstedt, H.; Hinek, R.; Spiering, H., Cooperative phenomena and light-induced bistability in iron(II) spin-crossover compounds. *Coord. Chem. Rev.* **1999,** *190-192*, 471-491.
9. Decurtins, S.; Gütlich, P.; Köhler, C.; Spiering, H.; Hauser, A., Light-Induced Excited Spin State Trapping in a Transition-Metal Complex: The Hexa-1-propyltetrazole-iron(II) Tetrafluoroborate Spin-Crossover System. *Chem. Phys. Lett.* **1984,** *105* (1), 1-4.
10. Roux, C.; Zarembowitch, J.; Gallois, B.; Granier, T.; Claude, R., Toward Ligand-Driven Light-Induced Spin Changing. Influence of the Configuration of 4 Styrylpyridine (stpy) on the Magnetic Properties of $Fe^{II}(stpy)_4(NCS)_2$ Complexes. Crystal Structures of the Spin-Crossover Species $Fe(trans\text{-}stpy)_4(NCS)_2$ and of the High-Spin Species $Fe(cis\text{-}stpy)_4(NCS)_2$. *Inorg. Chem.* **1994,** *33* (10), 2273-2279.
11. Gütlich, P.; Gaspar, A. B.; Garcia, Y., Spin state switching in iron coordination compounds. *Beilstein J. Org. Chem.* **2013,** *9*, 342-391.
12. Sato, O., Dynamic molecular crystals with switchable physical properties. *Nat. Chem.* **2016,** *8*, 644.
13. Bressler, C.; Milne, C.; Pham, V.-T.; ElNahhas, A.; van der Veen, R. M.; Gawelda, W.; Johnson, S.; Beaud, P.; Grolimund, D.; Kaiser, M.; Borca, C. N.; Ingold, G.; Abela, R.; Chergui, M., Femtosecond XANES Study of the Light-Induced Spin Crossover Dynamics in an Iron(II) Complex. *Science* **2009,** *323* (5913), 489-492.
14. Gaspar, A. B.; Ksenofontov, V.; Seredyuk, M.; Gütlich, P., Multifunctionality in spin crossover materials. *Coord. Chem. Rev.* **2005,** *249* (23), 2661-2676.
15. Aguilà, D.; Prado, Y.; Koumousi, E. S.; Mathonière, C.; Clérac, R., Switchable Fe/Co Prussian Blue Networks and Molecular Analogues. *Chem. Soc. Rev.* **2016,** *45* (1), 203-224.
16. Shimamoto, N.; Ohkoshi, S. I.; Sato, O.; Hashimoto, K., Control of charge-transfer-induced spin transition temperature on cobalt-iron Prussian blue analogues. *Inorg. Chem.* **2002,** *41* (4), 678-684.
17. Berlinguette, C. P.; Dragulescu-Andrasi, A.; Sieber, A.; Galán-Mascarós, J. R.; Güdel, H.-U.; Achim, C.; Dunbar, K. R., A Charge-Transfer-Induced Spin Transition in the Discrete Cyanide-Bridged Complex $\{[Co(tmphen)_2]_3[Fe(CN)_6]_2\}$. *J. Am. Chem. Soc.* **2004,** *126* (20), 6222-6223.
18. Li, D.; Clérac, R.; Roubeau, O.; Harté, E.; Mathonière, C.; Le Bris, R.; Holmes, S. M., Magnetic and Optical Bistability Driven by Thermally and Photoinduced Intramolecular Electron Transfer in a Molecular Cobalt-Iron Prussian Blue Analogue. *J. Am. Chem. Soc.* **2008,** *130* (1), 252-258.
19. Mathonière, C., Metal-to-Metal Electron Transfer: A Powerful Tool for the Design of Switchable Coordination Compounds. *Eur. J. Inorg. Chem.* **2018,** (3), 248-258.

20. Koumousi, E. S.; Jeon, I. R.; Gao, Q.; Dechambenoit, P.; Woodruff, D. N.; Merzeau, P.; Buisson, L.; Jia, X.; Li, D.; Volatron, F.; Mathonière, C.; Clérac, R., Metal-to-metal electron transfer in Co/Fe prussian blue molecular analogues: The ultimate miniaturization. *J. Am. Chem. Soc.* **2014,** *136* (44), 15461-15464.
21. Ohkoshi, S.; Tokoro, H.; Hashimoto, K., Temperature- and photo-induced phase transition in rubidium manganese hexacyanoferrate. *Coord. Chem. Rev.* **2005,** *249* (17-18), 1830-1840.
22. Zhang, K.; Kang, S.; Yao, Z. S.; Nakamura, K.; Yamamoto, T.; Einaga, Y.; Azuma, N.; Miyazaki, Y.; Nakano, M.; Kanegawa, S.; Sato, O., Charge-Transfer Phase Transition of a Cyanide-Bridged Fe^{II}/Fe^{III} Coordination Polymer. *Angew. Chem. Int. Ed.* **2016,** *55* (20), 6047-50.
23. Nowicka, B.; Reczyński, M.; Rams, M.; Nitek, W.; Żukrowski, J.; Kapusta, C.; Sieklucka, B., Hydration-switchable charge transfer in the first bimetallic assembly based on the $[Ni(cyclam)]^{3+}$ - Magnetic CN-bridged chain $\{(H_3O)[Ni^{III}cyclam)][Fe^{II}(CN)_6]\cdot 5H_2O\}_n$. *Chem. Commun.* **2015,** *51* (57), 11485-11488.
24. Hilfiger, M. G.; Chen, M.; Brinzari, T. V.; Nocera, T. M.; Shatruk, M.; Petasis, D. T.; Musfeldt, J. L.; Achim, C.; Dunbar, K. R., An unprecedented charge transfer induced spin transition in an Fe-Os cluster. *Angew. Chem. Int. Ed.* **2010,** *49* (8), 1410-3.
25. Avendano, C.; Hilfiger, M. G.; Prosvirin, A.; Sanders, C.; Stepien, D.; Dunbar, K. R., Temperature and Light Induced Bistability in a $Co_3[Os(CN)_6]_2\,6H_2O$ Prussian Blue Analog. *J. Am. Chem. Soc.* **2010,** *132* (38), 13123-13125.
26. Mathonière, C.; Podgajny, R.; Guionneau, P.; Labrugere, C.; Sieklucka, B., Photomagnetism in Cyano-Bridged Hexanuclear Clusters $[Mn^{II}(bpy)_2]_4[M^{IV}(CN)_8]_2\cdot xH_2O$ (M = Mo, x= 14, and M = W, x= 9). *Chem. Mater.* **2005,** *17* (2), 442-449.
27. Chorazy, S.; Podgajny, R.; Nogaś, W.; Nitek, W.; Kozieł, M.; Rams, M.; Juszyńska-Gałązka, E.; Zukrowski, J.; Kapusta, C.; Nakabayashi, K.; Fujimoto, T.; Ohkoshi, S. I.; Sieklucka, B., Charge transfer phase transition with reversed thermal hysteresis loop in the mixed-valence $Fe_9[W(CN)_8]_6\cdot$xMeOH cluster. *Chem. Commun.* **2014,** *50* (26), 3484-3487.
28. Ohkoshi, S. I.; Ikeda, S.; Hozumi, T.; Kashiwagi, T.; Hashimoto, K., Photoinduced magnetization with a high Curie temperature and a large coercive field in a cyano-bridged cobalt-tungstate bimetallic assembly. *J. Am. Chem. Soc.* **2006,** *128* (16), 5320-5321.
29. Ozaki, N.; Tokoro, H.; Hamada, Y.; Namai, A.; Matsuda, T.; Kaneko, S.; Ohkoshi, S. I., Photoinduced Magnetization with a High Curie Temperature and a Large Coercive Field in a Co-W Bimetallic Assembly. *Adv. Funct. Mater* **2012,** *22* (10), 2089-2093.
30. Arimoto, Y.; Ohkoshi, S. I.; Zhong, Z. J.; Seino, H.; Mizobe, Y.; Hashimoto, K., Photoinduced Magnetization in a Two-Dimensional Cobalt Octacyanotungstate. *J. Am. Chem. Soc.* **2003,** *125* (31), 9240-9241.
31. Koziel, M.; Podgajny, R.; Kania, R.; Lebris, R.; Mathoniere, C.; Lewinski, K.; Kruczala, K.; Rams, M.; Labrugere, C.; Bousseksou, A.; Sieklucka, B., Series of $M^I[Co(bpy)_3][Mo(CN)_8].nH_2O$ (M^I = Li (1), K (2), Rb (3), Cs (4); *n* = 7-8) exhibiting reversible diamagnetic to paramagnetic transition coupled with dehydration-rehydration process. *Inorg. Chem.* **2010,** *49* (6), 2765-72.
32. Meng, Y. S.; Sato, O.; Liu, T., Manipulating Metal-to-Metal Charge Transfer for Materials with Switchable Functionality. *Angew. Chem. Int. Ed.* **2018,** *57* (38), 12216-12226.
33. Sato, O.; Cui, A.; Matsuda, R.; Tao, J.; Hayami, S., Photo-induced Valence Tautomerism in Co Complexes. *Acc. Chem. Res.* **2007,** *40* (5), 361-369.
34. Buchanan, R. M.; Pierpont, C. G., Tautomeric catecholate-semiquinone interconversion via metal-ligand electron transfer. Structural, spectral, and magnetic properties of (3,5-di-tert-butylcatecholato)(3,5-di-tert-butylsemiquinone)(bipyridyl)$cobalt^{III}$, a complex containing mixed-valence organic ligands. *J. Am. Chem. Soc.* **1980,** *102* (15), 4951-4957.
35. Sato, O.; Tao, J.; Zhang, Y. Z., Control of magnetic properties through external stimuli. *Angew. Chem. Int. Ed.* **2007,** *46* (13), 2152-2187.
36. Brachňaková, B.; Šalitroš, I., Ligand-driven Light-induced Spin Transition in Spin Crossover Compounds. *Chem. Pap.* **2018,** *72* (4), 773-798.

37. Rösner, B.; Milek, M.; Witt, A.; Gobaut, B.; Torelli, P.; Fink, R. H.; Khusniyarov, M. M., Reversible Photoswitching of a Spin-Crossover Molecular Complex in the Solid State at Room Temperature. *Angew. Chem. Int. Ed.* **2015,** *54* (44), 12976-12980.
38. Hojorat, M.; Al Sabea, H.; Norel, L.; Bernot, K.; Roisnel, T.; Gendron, F.; Guennic, B. L.; Trzop, E.; Collet, E.; Long, J. R.; Rigaut, S., Hysteresis Photomodulation via Single-Crystal-to-Single-Crystal Isomerization of a Photochromic Chain of Dysprosium Single-Molecule Magnets. *J. Am. Chem. Soc.* **2020,** *142* (2), 931-936.
39. Boillot, M.-L.; Chantraine, S.; Zarembowitch, J.; Lallemand, J.-Y.; Prunet, J., First ligand-driven light-induced spin change at room temperature in a transition-metal molecular compound. *New J. Chem.* **1999,** *23* (2), 179-184.
40. Paquette, M. M.; Plaul, D.; Kurimoto, A.; Patrick, B. O.; Frank, N. L., Opto-Spintronics: Photoisomerization-Induced Spin State Switching at 300 K in Photochrome Cobalt-Dioxolene Thin Films. *J. Am. Chem. Soc.* **2018,** *140* (44), 14990-15000.
41. Boillot, M.-L.; Zarembowitch, J.; Sour, A., Ligand-Driven Light-Induced Spin Change (LD-LISC): A Promising Photomagnetic Effect. *Top. Curr. Chem.* **2004,** *234*, 261-276.
42. Hasegawa, Y.; Kume, S.; Nishihara, H., Reversible light-induced magnetization change in an azobenzene-attached pyridylbenzimidazole complex of iron(II) at room temperature. *Dalton Trans.* **2009,** (2), 280-4.
43. Gütlich, P.; Garcia, Y.; Woike, T., Photoswitchable coordination compounds. *Coord. Chem. Rev.* **2001,** *219*, 839-879.
44. Faulmann, C.; Chahine, J.; Valade, L.; Chastanet, G.; Létard, J.-F.; de Caro, D., Photomagnetic Studies of Spin-Crossover- and Photochromic-Based Complexes. *Eur. J. Inorg. Chem.* **2013,** *2013* (5-6), 1058-1067.
45. Gu, Z.-Z.; Sato, O.; Iyoda, T.; Hashimoto, K.; Fujishima, A., Spin switching effect in nickel nitroprusside: Design of a molecular spin device based on spin exchange interaction. *Chem. Mater.* **1997,** *9* (5), 1092-1097.
46. Xu, W. J.; Romanyuk, K.; Martinho, J. M. G.; Zeng, Y.; Zhang, X. W.; Ushakov, A.; Shur, V.; Zhang, W. X.; Chen, X. M.; Kholkin, A.; Rocha, J., A Photo-Responsive Organic-Inorganic Hybrid Ferroelectric Designed at Molecular Level. *J. Am. Chem. Soc.* **2020,** *40* (142), 16990–16998.
47. Sylvester, S. O.; Cole, J. M.; Waddell, P. G., Photoconversion bonding mechanism in ruthenium sulfur dioxide linkage photoisomers revealed by in situ diffraction. *J. Am. Chem. Soc.* **2012,** *134* (29), 11860-3.
48. Sheu, C. F.; Shih, C. H.; Sugimoto, K.; Cheng, B. M.; Takata, M.; Wang, Y., A long-lived photo-induced metastable state of linkage isomerization accompanied with a spin transition. *Chem. Commun.* **2012,** *48* (46), 5715-5717.
49. Warren, M. R.; Brayshaw, S. K.; Johnson, A. L.; Schiffers, S.; Raithby, P. R.; Easun, T. L.; George, M. W.; Warren, J. E.; Teat, S. J., Reversible 100% linkage isomerization in a single-crystal to single-crystal transformation: photocrystallographic identification of the metastable [Ni(dppe)(η^1-ONO)Cl] isomer. *Angew. Chem. Int. Ed.* **2009,** *48* (31), 5711-4.
50. Buckingham, D. A., The linkage isomerism of thiocyanate bonded to cobalt (III). *Coord. Chem. Rev.* **1994,** *135-136*, 587-621.
51. Guionneau, P.; Le Gac, F.; Kaiba, A.; Costa, J. S.; Chasseau, D.; Létard, J. F., A Reversible Metal-Ligand Bond Break Associated to a Spin-Crossover. *Chem. Commun.* **2007,** (36), 3723-3725.
52. Aguila, D.; Dechambenoit, P.; Rouzieres, M.; Mathoniere, C.; Clerac, R., Direct Crystallographic Evidence of the Reversible Photo-formation and Thermo-rupture of a Coordination Bond Inducing Spin-crossover Phenomenon. *Chem. Commun.* **2017,** *53* (84), 11588-11591.
53. Farcaș, A.-A.; Beu, T. A.; Bende, A., Light-induced spin transitions in Ni(II)-based macrocyclic-ligand complexes: A DFT study. *J. Photoch. and Photobio. A: Chemistry* **2019,** *376*, 316-323.
54. Peters, M. K.; Hamer, S.; Jakel, T.; Rohricht, F.; Sonnichsen, F. D.; von Essen, C.; Lahtinen, M.; Naether, C.; Rissanen, K.; Herges, R., Spin Switching with Triazolate-Strapped Ferrous Porphyrins. *Inorg. Chem.* **2019,** *58* (8), 5265-5272.

55. Thies, S.; Sell, H.; Schütt, C.; Bornholdt, C.; Näther, C.; Tuczek, F.; Herges, R., Light-Induced spin change by photodissociable external ligands: A new principle for Magnetic Switching of Molecules. *J. Am. Chem. Soc.* **2011,** *133* (40), 16243-16250.
56. Freysz, E.; Montant, S.; Létard, S.; Létard, J. F., Single laser pulse induces spin state transition within the hysteresis loop of an Iron compound. *Chem. Phys. Lett.* **2004,** *394* (4-6), 318-323.
57. Naonobu, S.; Shin-ichi, O.; Osamu, S.; Kazuhito, H., One-Shot-Laser-Pulse-Induced Cooperative Charge Transfer Accompanied by Spin Transition in a Co-Fe Prussian Blue Analog at Room Temperature. *Chem. Lett.* **2002,** *31* (4), 486-487.
58. Cai, L. Z.; Chen, Q. S.; Zhang, C. J.; Li, P. X.; Wang, M. S.; Guo, G. C., Photochromism and Photomagnetism of a 3d-4f Hexacyanoferrate at Room Temperature. *J. Am. Chem. Soc.* **2015,** *137* (34), 10882-5.
59. Ma, Y.-J.; Hu, J.-X.; Han, S.-D.; Pan, J.; Li, J.-H.; Wang, G.-M., Manipulating On/Off Single-Molecule Magnet Behavior in a Dy(III)-Based Photochromic Complex. *J. Am. Chem. Soc.* **2020,** *142* (5), 2682-2689.
60. Ohkoshi, S. I.; Tokoro, H., Photomagnetism in Cyano-Bridged Bimetal Assemblies. *Acc. Chem. Res.* **2012,** *45* (10), 1749-1758.
61. Chorazy, S.; Zakrzewski, J. J.; Magott, M.; Korzeniak, T.; Nowicka, B.; Pinkowicz, D.; Podgajny, R.; Sieklucka, B., Octacyanidometallates for multifunctional molecule-based materials. *Chem. Soc. Rev.* **2020**.
62. Pinkowicz, D.; Podgajny, R.; Nowicka, B.; Chorazy, S.; Reczyński, M.; Sieklucka, B., Magnetic clusters based on octacyanidometallates. *Inorg. Chem. Front.* **2015,** *2* (1), 10-27.
63. Sieklucka, B.; Podgajny, R.; Przychodzeń, P.; Korzeniak, T., Engineering of octacyanometalate-based coordination networks towards functionality. *Coord. Chem. Rev.* **2005,** *249* (21-22), 2203-2221.
64. Przychodzeń, P.; Korzeniak, T.; Podgajny, R.; Sieklucka, B., Supramolecular coordination networks based on octacyanometalates: From structure to function. *Coord. Chem. Rev.* **2006,** *250* (17-18), 2234-2260.
65. Bleuzen, A.; Marvaud, V.; Mathoniere, C.; Sieklucka, B.; Verdaguer, M., Photomagnetism in clusters and extended molecule-based magnets. *Inorg. Chem.* **2009,** *48* (8), 3453-3466.
66. Reczyński, M.; Nakabayashi, K.; Ohkoshi, S.-i., Tuning the Optical Properties of Magnetic Materials. *Eur. J. Inorg. Chem.* **2020,** *2020* (28), 2669-2678.
67. Ohkoshi, S. I.; Hamada, Y.; Matsuda, T.; Tsunobuchi, Y.; Tokoro, H., Crystal structure, charge-transfer-induced spin transition, and photoreversible magnetism in a cyano-bridged cobalt - Tungstate bimetallic assembly. *Chem. Mater.* **2008,** *20* (9), 3048-3054.
68. Le Bris, R.; Tsunobuchi, Y.; Mathonière, C.; Tokoro, H.; Ohkoshi, S. I.; Ould-Moussa, N.; Molnar, G.; Bousseksou, A.; Létard, J. F., Spectroscopic and magnetic properties of the metastable states in the coordination network $[\{Co(prm)_2\}_2\{Co(H_2O)_2\}\{W(CN)_8\}_2]\cdot 4H_2O$ (prm = pyrimidine). *Inorg. Chem.* **2012,** *51* (5), 2852-2859.
69. Ohkoshi, S.-i.; Hashimoto, K., Photo-magnetic and magneto-optical effects of functionalized metal polycyanides. *J. Photoch. and Photobio. C: Photochemistry Reviews* **2001,** *2* (1), 71-88.
70. Rombaut, G.; Golhen, S.; Ouahab, L.; Mathonière, C.; Kahn, O., Structural and Photomagnetic Studies of a 1-D Bimetallic Chain $[Mn_2^{II}(L)_2(H_2O)][Mo^{IV}(CN)_8]\cdot 5H_2O$ (L = macrocycle): Analogy with the Photo-Oxidation of $K_4[Mo^{IV}(CN)_8]\cdot 2H_2O$. *J. Chem. Soc., Dalton Trans.* **2000,** (20), 3609-3614.
71. Ohkoshi, S. I.; Tokoro, H.; Hozumi, T.; Zhang, Y.; Hashimoto, K.; Mathonière, C.; Bord, I.; Rombaut, G.; Verelst, M.; Cartier Dit Moulin, C.; Villain, F., Photoinduced Magnetization in Copper Octacyanomolybdate. *J. Am. Chem. Soc.* **2006,** *128* (1), 270-277.
72. Bridonneau, N.; Long, J.; Cantin, J. L.; Von Bardeleben, J.; Pillet, S.; Bendeif, E. E.; Aravena, D.; Ruiz, E.; Marvaud, V., First Evidence of Light-induced Spin Transition in Molybdenum(IV). *Chem. Commun.* **2015,** *51* (39), 8229-8232.
73. Willemin, S.; Larionova, J.; Clérac, R.; Donnadieu, B.; Henner, B.; Le Goff, X. F.; Guérin, C., Crystal structures and intercalation reactions of three-dimensional coordination

polymers $[M(H_2O)_2]_2[Mo(CN)_8]\cdot 4H_2O$ (M = Co, Mn). *Eur. J. Inorg. Chem.* **2003,** (10), 1866-1872.
74. Rombaut, G.; Verelst, M.; Golhen, S.; Ouahab, L.; Mathonière, C.; Kahn, O., Structural and Photomagnetic Studies of Two Compounds in the System $Cu^{2+}/Mo(CN)_8^{4-}$: From Trinuclear Molecule to Infinite Network. *Inorg. Chem.* **2001,** *40* (6), 1151-1159.
75. Mitroova, Z.; Mihalik, M.; Zentko, A.; Bokor, M. Z.; Kamarás, K., Synthesis, structural and magnetic properties of $TM_2^{2+}[Mo^{IV}(CN)_8]\cdot nH_2O$. *Ceramics-Silikaty* **2005,** *49* (3), 181-187.
76. Ohkoshi, S.-i.; Machida, N.; Zhong, Z. J.; Hashimoto, K., Photo-induced magnetization in copper(II) octacyanomolybdate(IV). *Synth.Met.* **2001,** *122* (3), 523-527.
77. Rombaut, G.; Mathonière, C.; Guionneau, P.; Golhen, S.; Ouahab, L.; Verelst, M.; Lecante, P., Structural and photo-induced magnetic properties of M_2^{II} $[W^{IV}(CN)_8]\cdot xH_2O$ (M = Fe and x=8, Cu and x=5). Comparison with $Cu_2^{II}[Mo^{IV}(CN)_8]\cdot 7.5H_2O$. *Inorg. Chim. Acta* **2001,** *326* (1), 27-36.
78. Ohkoshi, S. I.; Machida, N.; Abe, Y.; Zhong, Z. J.; Hashimoto, K., Visible Light-Induced Reversible Photomagnetism in Copper(II) Octacyanomolybdate(IV). *Chem. Lett.* **2001,** (4), 312-313.
79. Umeta, Y.; Chorazy, S.; Nakabayashi, K.; Ohkoshi, S. I., Synthesis of the Single-Crystalline Form and First-Principles Calculations of Photomagnetic Copper(II) Octacyanidomolybdate(IV). *Eur. J. Inorg. Chem.* **2016,** *2016* (13-14), 1980-1988.
80. Hozumi, T.; Hashimoto, K.; Ohkoshi, S. I., Electrochemical synthesis, crystal structure, and photomagnetic properties of a three-dimensional cyano-bridged copper-molybdenum complex. *J. Am. Chem. Soc.* **2005,** *127* (11), 3864-3869.
81. Ma, X. D.; Yokoyama, T.; Hozumi, T.; Hashimoto, K.; Ohkoshi, S. I., Electronic states and local structures of the photomagnetic Cu-Mo cyanides $Cu_2Mo(CN)_8\cdot 8H_2O$ and $Cs_{0.5}Cu_{1.75}Mo(CN)_8\cdot 1.5H_2O$ studied by X-ray absorption fine structure spectroscopy. *Phys. Rev. B* **2005,** *72* (9), 094107-1-094107-6.
82. Ohkoshi, S.-i.; Shiraishi, K.; Nakagawa, K.; Ikeda, Y.; Stefanczyk, O.; Tokoro, H.; Namai, A., Reversible photoswitchable ferromagnetic thin film based on a cyanido-bridged RbCuMo complex. *J. Mater. Chem. C* **2021,** *9* (9), 3081-3087.
83. Hennig, H.; Rehorek, A.; Rehorek, D.; Thomas, P., Photocatalytic systems. LXIII. Intervalence transfer (IT) behaviour and IT photochemistry of mixed-valence compounds with cyanometallates. *Inorg. Chim. Acta* **1984,** *86* (1), 41-49.
84. Hennig, H.; Rehorek, A.; Ackermann, M.; Rehorek, D.; Thomas, P., Photocatalrtie Systems. XLIV. On the Intervalence Charge Transfer Behavionr of Ion Pairs of Oetacyanoniolybdate. *Z. anorg. allg Chem.* **1983,** *496* (1), 186-196.
85. McKnight, G. F.; Haight, G. P., Reactions of Octacyanomolybdate(IV). III. Infrared and Magnetic Studies of Compounds with Divalent First-Row Transition Metals. *Inorg. Chem.* **1973,** *12* (12), 3007-3008.
86. Stefańczyk, O.; Majcher, A. M.; Rams, M.; Nitek, W.; Mathonière, C.; Sieklucka, B., Photo-induced magnetic properties of the $[Cu^{II}(bapa)]_2[Mo^{IV}(CN)_8]\cdot 7H_2O$ molecular ribbon. *J. Mater. Chem. C* **2015,** *3* (33), 8712-8719.
87. Mathonière, C.; Kobayashi, H.; Le Bris, R.; Kaïba, A.; Bord, I., Reversible photomagnetic properties of the molecular compound $[\{Cu^{II}(bipy)_2\}_2\{Mo^{IV}(CN)_8\}]\cdot 9H_2O\cdot CH_3OH$. *C. R. Chimie* **2008,** *11* (6-7), 665-672.
88. Herrera, J. M.; Marvaud, V.; Verdaguer, M.; Marrot, J.; Kalisz, M.; Mathonière, C., Reversible Photoinduced Magnetic Properties in the Heptanuclear Complex $[Mo^{IV}(CN)_2(CN\text{-}CuL)_6]^{8+}$: A Photomagnetic High-Spin Molecule. *Angew. Chem. Int. Ed.* **2004,** *43* (41), 5468-5471.
89. Raghunathan, R.; Ramasesha, S.; Mathonière, C.; Marvaud, V., A kinetic model for photoswitching of magnetism in the high spin molecule $[Mo(IV)(CN)_2(CN\text{-}Cu(II)(tren))_6(ClO4)_8$. *Phys. Chem. Chem. Phys.* **2008,** *10* (35), 5469-5474.
90. Raghunathan, R.; Ramasesha, S.; Mathonière, C.; Marvaud, V., Microscopic model for photoinduced magnetism in the molecular complex $[Mo(IV)(CN)_2(CN\text{-}CuL)_6]^{8+}$ perchlorate. *Phys. Rev. B* **2006,** *73* (4).

91. Yu, F.; Li, A. H.; Hu, S. Q.; Li, B., Structure and magnetism of heptanuclear complex encapsulated the octacyanomolybdate(IV) core. *Inorg. Chem. Commun.* **2013,** *35*, 58-60.
92. Zhang, W.; Sun, H. L.; Sato, O., Synthesis, characterization, and photoresponsive properties of a series of Mo(IV)-Cu(II) complexes. *Dalton Trans.* **2011,** *40* (12), 2735-2743.
93. Bridonneau, N.; Chamoreau, L. M.; Gontard, G.; Cantin, J. L.; von Bardeleben, J.; Marvaud, V., A High-Nuclearity Metal-Cyanide Cluster [Mo_6Cu_{14}] with Photomagnetic Properties. *Dalton Trans.* **2016,** *45* (23), 9412-9418.
94. Xu, H.; Sato, O.; Li, Z.; Ma, J., A thermally reversible photoinduced magnetic trinuclear complex [$Cu_2(bpmen)_2$][$Mo^{IV}(CN)_8$]·$8H_2O$. *Inorg. Chem. Commun.* **2012,** *15*, 311-313.
95. Korzeniak, T.; Pinkowicz, D.; Nitek, W.; Dańko, T.; Pełka, R.; Sieklucka, B., Photoswitchable $Cu_4^{II}Mo^{IV}$ and $Cu_2^{II}Mo^{IV}$ cyanido-bridged molecules. *Dalton Trans.* **2016,** *45* (42), 16585-16595.
96. Maxim, C.; Mathonière, C.; Andruh, M., New photomagnetic cyanido-bridged Cu^{II}-Mo^{IV} oligonuclear complexes: Slight modification of the blocking ligands induces different structures. *Dalton Trans.* **2009,** (37), 7805-7810.
97. Umeta, Y.; Tokoro, H.; Ozaki, N.; Ohkoshi, S. I., Room-temperature thermally induced relaxation effect in a two-dimensional cyano-bridged Cu-Mo bimetal assembly and thermodynamic analysis of the relaxation process. *AIP Adv.* **2013,** *3* (4), 042133-1-042133-6.
98. Tokoro, H.; Nakagawa, K.; Nakabayashi, K.; Kashiwagi, T.; Hashimoto, K.; Ohkoshi, S. I., Photoreversible switching of magnetic coupling in a two-dimensional copper octacyanomolybdate. *Chem. Lett.* **2009,** *38* (4), 338-339.
99. Sieklucka, B.; Samotus, A., Photoreactivity of $Mo(CN)_8^{3-}$ ion: photoredox and photosubstitution processes. *J. Photoch. and Photobio. A: Chemistry* **1993,** *74* (2-3), 115-120.
100. Samotus, A.; Szklarzewicz, J., Photochemistry of transition metal octacyanides and related compounds. Past, present and future. *Coord. Chem. Rev.* **1993,** *125* (1), 63-74.
101. Sieklucka, B.; Samotus, A.; Sostero, S.; Traverso, O., A photochemical route to tungsten(IV) dioxygen-cyanocomplexes. *Inorg. Chim. Acta* **1984,** *86* (2), L51-L54.
102. Samotus, A.; Sieklucka, B., Proton transfer equilibria of aquoheptacyanotungstate(IV). *J. Inorg. Nucl. Chem.* **1978,** *40* (2), 315-318.
103. Waltz, W. L.; Adamson, A. W.; Fleischauer, P. D., Photolytic production of hydrated electrons from aqueous potassium octacyanomolybdate(IV) and potassium octacyanotungstate(IV). *J. Am. Chem. Soc.* **1967,** *89* (15), 3923-3924.
104. Shirom, M.; Siderer, Y., Wavelength dependence of electron formation from photoexcited $Mo(CN)_8^{4-}$ in 10N NaOH glasses at 77°K. *J. Chem. Phys.* **1973,** *58* (3), 1250-1251.
105. Long, J.; Chamoreau, L. M.; Mathonière, C.; Marvaud, V., Photoswitchable heterotrimetallic chain based on octacyanomolybdate, copper, and nickel: Synthesis, characterization, and photomagnetic properties. *Inorg. Chem.* **2009,** *48* (1), 22-24.
106. Clérac, R.; Miyasaka, H.; Yamashita, M.; Coulon, C., Evidence for Single-Chain Magnet Behavior in a MnIII−NiII Chain Designed with High Spin Magnetic Units: A Route to High Temperature Metastable Magnets. *J. Am. Chem. Soc.* **2002,** *124* (43), 12837-12844.
107. Long, J.; Chamoreau, L. M.; Marvaud, V., Supramolecular heterotrimetallic assembly based on octacyanomolybdate, manganese, and copper. *Eur. J. Inorg. Chem.* **2011,** (29), 4545-4549.
108. Larionova, J.; Clérac, R.; Donnadieu, B.; Willemin, S.; Guérin, C., Synthesis and Structure of a Two-Dimensional Cyano-Bridged Coordination Polymer [Cu(cyclam)]$_2$[$Mo(CN)_8$]·$10.5H_2O$ (Cyclam = 1,4,8,11-Tetraazacyclodecane). *Cryst. Growth Des.* **2003,** *3* (2), 267-272.
109. Nowicka, B.; Hagiwara, M.; Wakatsuki, Y.; Kisch, H., Syntheses and Magnetic Properties of 1,4,8,11-Tetraazacyclotetradecanenickel(II) Tetra-, Hexa-, and Octa-cyanometalates. *Bull. Chem. Soc. Jpn.* **1999,** *72* (3), 441-445.
110. Korzeniak, T.; Mathonière, C.; Kaiba, A.; Guionneau, P.; Koziel, M.; Sieklucka, B., First example of photomagnetic effects in ionic pairs [Ni(bipy)$_3$]$_2$[$Mo(CN)_8$]·12H2O. *Inorg. Chim. Acta* **2008,** *361* (12-13), 3500-3504.

111. Brossard, S.; Volatron, F.; Lisnard, L.; Arrio, M. A.; Catala, L.; Mathoniere, C.; Mallah, T.; dit Moulin, C. C.; Rogalev, A.; Wilhelm, F.; Smekhova, A.; Sainctavit, P., Investigation of the Photoinduced Magnetization of Copper Octacyanomolybdates Nanoparticles by X-ray Magnetic Circular Dichroism. *J. Am. Chem. Soc.* **2012,** *134* (1), 222-228.
112. Arrio, M.-A.; Long, J. r. m.; Cartier dit Moulin, C.; Bachschmidt, A.; Marvaud, V. r.; Rogalev, A.; Mathonière, C.; Wilhelm, F.; Sainctavit, P., Photoinduced Magnetization on Mo Ion in Copper Octacyanomolybdate: An X-ray Magnetic Circular Dichroism Investigation. *J. Phys. Chem. C.* **2010,** *114* (1), 593-600.
113. Carvajal, M. A.; Caballol, R.; de Graaf, C., Insights on the Photomagnetism in Copper Octacyanomolybdates. *Dalton Trans.* **2011,** *40* (28), 7295-303.
114. Bunau, O.; Arrio, M. A.; Sainctavit, P.; Paulatto, L.; Calandra, M.; Juhin, A.; Marvaud, V.; Cartier dit Moulin, C., Understanding the photomagnetic behavior in copper octacyanomolybdates. *J. Phys. Chem. A.* **2012,** *116* (34), 8678-83.
115. Carvajal, M. A.; Reguero, M.; de Graaf, C., On the Mechanism of the Photoinduced Magnetism in Copper Octacyanomolybdates. *Chem. Commun.* **2010,** *46* (31), 5737-5739.
116. Casanova, D.; Cirera, J.; Llunell, M.; Alemany, P.; Avnir, D.; Alvarez, S., Minimal Distortion Pathways in Polyhedral Rearrangements. *J. Am. Chem. Soc.* **2004,** *126* (6), 1755-1763.
117. Llunell, M.; Casanova, D.; Cirera, J.; Alemany, M.; Alvarez, S., SHAPE, v. 2.0; University of Barcelona: Barcelona, Spain **2010**.
118. Korzeniak, T.; Jankowski, R.; Kozieł, M.; Pinkowicz, D.; Sieklucka, B., Reversible Single-Crystal-to-Single-Crystal Transformation in Photomagnetic Cyanido-Bridged Cd_4M_2 Octahedral Molecules. *Inorg. Chem.* **2017,** *56* (21), 12914-12919.
119. Magott, M.; Stefanczyk, O.; Sieklucka, B.; Pinkowicz, D., Octacyanidotungstate(IV) Coordination Chains Demonstrate a Light-Induced Excited Spin State Trapping Behavior and Magnetic Exchange Photoswitching. *Angew. Chem. Int. Ed.* **2017,** *56* (43), 13283-13287.
120. Arczyński, M.; Stanek, J.; Sieklucka, B.; Dunbar, K. R.; Pinkowicz, D., Site-Selective Photoswitching of Two Distinct Magnetic Chromophores in a Propeller-Like Molecule To Achieve Four Different Magnetic States. *J. Am. Chem. Soc.* **2019,** *141* (48), 19067-19077.
121. Korzeniak, T.; Sasmal, S.; Pinkowicz, D.; Stefańczyk, O.; Sieklucka, B., Light-Induced Spin-State Switching of the Mo^{IV} Centre in Trinuclear $[Cu^{II}(diamine)_2]_2[Mo^{IV}(CN)_8]$ Molecules. *Eur. J. Inorg. Chem.* **2018,** *2018* (19), 2019-2025.
122. Korzeniak, T.; Sasmal, S.; Pinkowicz, D.; Nitek, W.; Pełka, R.; Czernia, D.; Stefańczyk, O.; Sieklucka, B., Chiral Photomagnets Based on Copper(II) complexes of 1,2-Diaminocyclohexane and Octacyanidomolybdate(IV) Ions. *Inorg. Chem.* **2020,** *59*, 5872-5882.
123. Magott, M.; Sarewicz, M.; Buda, S.; Pinkowicz, D., Heterotrimetallic Cyanide-Bridged 3d-4d-5d Frameworks Based on a Photomagnetic Secondary Building Unit. *Inorg. Chem.* **2020,** *59* (13), 8925-8934.
124. Bridonneau, N.; Quatremare, P.; von Bardeleben, H. J.; Cantin, J.-L.; Pillet, S.; Bendeif, E.-E.; Marvaud, V., Direct Evidence of a Photoinduced Electron Transfer in Diluted "Molybdenum-Copper" Molecular Compounds. *Eur. J. Inorg. Chem.* **2017**, 370–377.
125. Stefanczyk, O.; Pelka, R.; Majcher, A. M.; Mathoniere, C.; Sieklucka, B., Irradiation Temperature Dependence of the Photomagnetic Mechanisms in a Cyanido-Bridged $Cu_2^{II}Mo^{IV}$ Trinuclear Molecule. *Inorg. Chem.* **2018,** *57* (14), 8137-8145.
126. Stefańczyk, O.; Ohkoshi, S.-i., Synthesis of Two-Dimensional Photomagnetic $K_4\{[Cu^{II}(ida)]_2[M^{IV}(CN)_8]\}\cdot 4H_2O$ (M^{IV} = Mo, W) Materials. *Inorg. Chem.* **2020,** *59* (7), 4292-4299.
127. Zhang, W.; Sun, H. L.; Sato, O., A one-dimensional homochiral Mo(iv)-Cu(ii) coordination polymer: Spontaneous resolution and photoresponsive properties. *CrystEngComm.* **2010,** *12* (12), 4045-4047.
128. Korzeniak, T.; Sasmal, S.; Pinkowicz, D.; Sieklucka, B., The photomagnetic effect in 2-D cyanido-bridged coordination polymer $[Cu(aepa)]_{10}[Mo(CN)_8]_5\cdot 30H_2O$. *New J. Chem.* **2018**.
129. Magott, M.; Reczyński, M.; Gaweł, B.; Sieklucka, B.; Pinkowicz, D., A

photomagnetic sponge: high-temperature light-induced ferrimagnet controlled by water sorption. *J. Am. Chem. Soc.* **2018,** *140* (46), 15876-15882.
130. Catala, L.; Mathoniere, C.; Gloter, A.; Stephan, O.; Gacoin, T.; Boilot, J. P.; Mallah, T., Photomagnetic nanorods of the $Mo(CN)_8Cu_2$ coordination network. *Chem. Commun.* **2005,** (6), 746-8.
131. Bridonneau, N.; Long, J.; Cantin, J. L.; Von Bardeleben, J.; Talham, D. R.; Marvaud, V., Photomagnetic molecular and extended network Langmuir-Blodgett films based on cyanide bridged molybdenum-copper complexes. *RSC Adv.* **2015,** *5* (22), 16696-16701.
132. Volatron, F.; Heurtaux, D.; Catala, L.; Mathoniere, C.; Gloter, A.; Stephan, O.; Repetto, D.; Clemente-Leon, M.; Coronado, E.; Mallah, T., Photo-induced magnetic bistability in a controlled assembly of anisotropic coordination nanoparticles. *Chem. Commun.* **2011,** *47* (7), 1985-7.
133. Brinzei, D.; Catala, L.; Mathonière, C.; Wernsdorfer, W.; Gloter, A.; Stephan, O.; Mallah, T., Photoinduced Superparamagnetism in Trimetallic Coordination Nanoparticles. *J. Am. Chem. Soc.* **2007,** *129* (13), 3778-3779.

Chapter II. The influence of alkali cations on photomagnetic properties of octacyanometallate-based ionic salts

II.1 Introduction

Octacyanometallate based complexes draw particular attention for their intriguing photomagnetic properties. As illustrated in a variety of compounds (see in chapter I),[1-20] they demonstrate high relaxation temperatures or high Curie temperatures in their photo-induced states.[21,8, 20, 22-25,15,26] Although octacyanometallate complexes have been investigated for more than two decades, the photomagnetic mechanisms for these systems have been continuously under discussion. At the beginning, the photomagnetic mechanisms have been attributed as the formation of Mo^{V} by charge transfer with neighboring metal ions (Cu^{2+}, Mn^{2+}),[15, 27] crystallized water,[23] or ligands[28] in the structure. Particularly, the observation of MMCT optical band for the well-studied $Cu^{II}/Mo^{IV}(CN)_8$ family leads to an interpretation of MMCT process between Cu^{II} and Mo^{IV} centers.[15] A new explanation based on spin singlet-triplet (S-T) crossover from Mo^{IV}_{LS} to Mo^{IV}_{HS} has been proposed with breakthrough studies by the means of XAS and XMCD.[29-30]

Despite the fact that photomagnetic properties of numerous compounds based on octacyanometallate building blocks have been studied, most of the cases are constructed with cyanide ligand acting as the bridge.[1-12, 14-20] The formation of cyanide bridge can lead to complicated clusters or high dimensional coordination frameworks and make the quantitative interpretation of the photomagnetic mechanisms not easy. The simpler crystal structure can, in turn, facilitate the fundamental understanding of the photomagnetic mechanisms, which is essential for these systems. In particular, the S-T conversion could be in principle observed in mononuclear systems. Following this motivation, our study will focus on the mononuclear ionic compounds built from $[M(CN)_8]^{4-}$ (M = Mo, W) with only cyanide ligands acting as terminal ligands. With the expectation to reveal the impact of counterionic part on photomagnetic properties, simple cations will be incorporated.

In Table II. 1, we have summarized the ionic compounds built from $[M^{IV}(CN)_8]^{4-}$ with photomagnetic properties studied so far. To the best of our knowledge, only six mononuclear samples have been studied in the literature with quite diverse experimental conditions and attributions of the photomagnetic mechanisms. Because there is no systematic study for this type of simple complexes, we are motivated to dig further in this direction.

Table II. 1 The summary of reported photomagnetic mononuclear compounds based on $[M^{IV}(CN)_8]^{4-}$

Compound	$[M(CN)_8]^{4-}$ geometry	Before and after irradiation	Light source	Proposed mechanism	Ref.
$K_4[Mo(CN)_8]\cdot 2H_2O$	TDD	M: 0 to 0.06 Nβ at 10 K, 1 T	UV light	formation of $[Mo^{V}(CN)_8]^{3-}$	23
$[Ni(bipy)_3]_2[Mo(CN)_8]\cdot 12H_2O$	TDD	χT: 2.30 to 2.99 $cm^3\,K\,mol^{-1}$ at 10 K, 0.5 T	406-415 nm	formation of $[Mo^{V}(CN)_8]^{3-}$ and $[Ni^{II}(bipy)_2(bipy^{-})]^{+}$	28
$M^{I}[Co(bpy)_3][Mo(CN)_8]$ (M^{I} = alkali cations)	distorted SAPR	χT: 0.26 to 0.32 $cm^3\,K\,mol^{-1}$ at 10 K, 0.2 T	647 nm	MMCT	13
$(H_4cyclam)[Mo(CN)_8]\cdot 1.5H_2O$	SAPR	χT: 0 to 0.65 $cm^3\,K\,mol^{-1}$ at 10 K, 0.1 T	436 nm	S-T	31
$(H_4cyclam)[W(CN)_8]\cdot 1.5H_2O$	SAPR	χT: 0 to 0.25 $cm^3\,K\,mol^{-1}$ at 10 K, 0.1 T	436 nm	S-T	31
$\{[Cu(tren)]_2(\mu\text{-}tn)\}[Mo(CN)_8]\cdot 7\cdot 5H_2O$	SAPR	Not photoresponsive at 10 K, 1 T	405 nm/473 nm	--	32

SAPR and TDD abbreviations represent square antiprism, triangular dodecahedron, respectively.

In this chapter, we want to study several questions by changing the nature of cationic parts:

1. How does the coordination geometry of $[M(CN)_8]^{4-}$ influence the photomagnetic properties?

2. How does the cationic part influence the photomagnetic properties?
3. How do the wide existing intermolecular interactions and crystal packing influence the photomagnetic properties?

To achieve these goals, more evidences are demanded to resolve the underlying photomagnetic mechanism. More compounds need to be studied for their photomagnetic properties and corresponding mechanisms. Benefiting from the modular nature of the octacyanometallate system, various simple mononuclear compounds can be easily prepared by the judicious selection of the cationic components.

In this chapter, we report the study of inorganic ionic salts $A_4[M(CN)_8]\cdot xH_2O$ (A = alkali cations: Li^I, Na^I, K^I, Rb^I, Cs^I; M = Mo^{IV} and W^{IV}). The obtained samples are characterized by X-ray diffraction, UV-Vis spectroscopy, infrared (IR) spectroscopy, and photomagnetic measurement to understand the crucial role of different alkali cations.

II.2 Synthesis, characterizations and physical properties of $A_4[Mo(CN)_8]\cdot xH_2O$ (A = Alkali cations)

In recent years, it is worth to mention that a possible breakage of one Mo-CN bond with the formation of photo-induced Mo^{IV}_{HS} has been suggested by theoretical calculations.[33-34] Moreover, this photo-induced dissociation of M−CN bond has been reported in solution studies of octacyanometallate complexes.[35-39] However, there is no experimental evidence for this behavior in solid state. To gain more insights into this possible explanation, we want to study the most simple structural type $A_4Mo(CN)_8\cdot xH_2O$, with different alkali cations as the counter cations.

II.2.1 Investigation of $K_4[Mo(CN)_8]\cdot 2H_2O$ (1)

II.2.1.1 Investigation of $K_4[Mo(CN)_8]\cdot 2H_2O$ (1) in solid state

All the prepared compounds in this family are obtained by solution methods with $K_4Mo(CN)_8\cdot 2H_2O$ (**1**) as precursor. In this subsection, we will start our study with the well-known $K_4Mo(CN)_8\cdot 2H_2O$ for a detailed investigation. As shown in Figure II. 1, the Mo^{IV} is coordinated with eight terminal cyanide ligands. The negative charge of the $[Mo(CN)_8]^{4-}$ anion is balanced by potassium cations, constituting an ionic complex. In 2000, Rombaut et al. briefly reported that the photomagnetic studies of **1** is an irreversible process with UV light irradiation. A photooxidation from Mo^{4+} to Mo^{5+} was suggested to explain the photo-induced magnetic change.[23] In recent years, an alternative interpretation of singlet-triplet conversion on molybdenum center was proposed in a $MoZn_2$ complex[10] and in $(H_4cyclam)[Mo^{IV}(CN)_8]\cdot 1.5H_2O$ (cyclam = 1,4,8,11-tetraazacyclodecane),[31] which raises question for the exact photomagnetic mechanism for **1**. In this thesis, the objective is to study the photomagnetic properties of **1** in detail.

1 used in our studies has been prepared as following the procedure according to the literature.[40] We have employed a variety of characterization methods including Single Crystal X-ray diffraction (SXRD), powder X-ray diffraction (PXRD), thermogravimetric analysis (TGA), infrared spectra and UV-Vis spectra to confirm the purity of sample and to gain more information for **1** (see subsection II.5.2 Powder X-ray diffraction analysis, II.5.3 Optical measurements, II.5.4 IR spectra and II.5.5 Thermogravimetric analysis). The good agreement between single crystal and powder X-ray diffraction studies confirms the purity of the sample. The IR spectra and UV-Vis spectra are in line with the reported ones. Based on TGA, the experimental weight loss 7.12 % in the step before 100°C is consistent with the theoretical weight loss 7.26 % for two water molecules per formula unit.

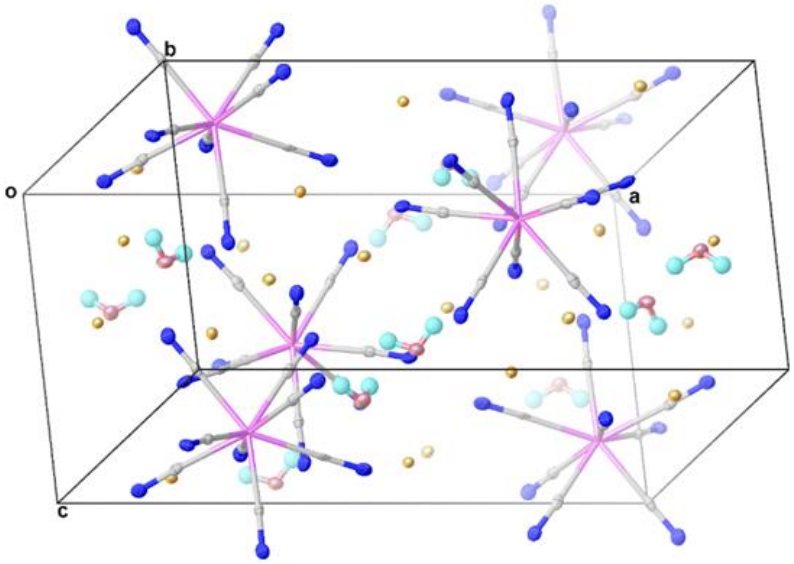

Figure II. 1 ORTEP diagram of crystal packing of **1** with 50 % ellipsoids possibility. (Pink for Mo, grey for C, blue for N, red for O, yellow for K and pale blue for H)

II.2.1.1.1 Photomagnetic studies of $K_4[Mo(CN)_8]\cdot 2H_2O$ (1)

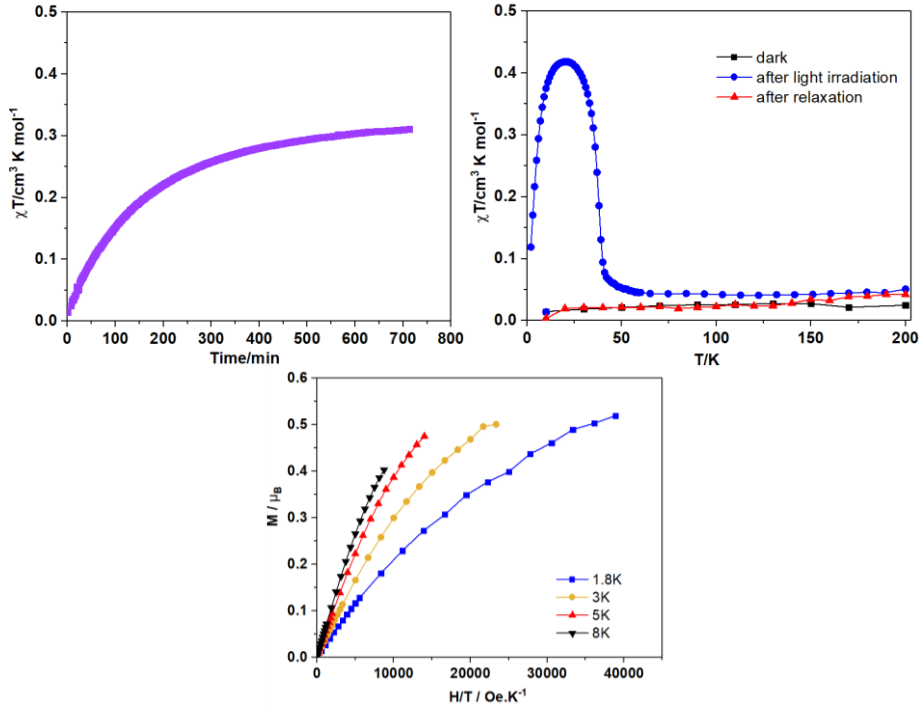

Figure II. 2 (Top left) Time dependence of the χT measured at 10 K, 1 T with 405 nm blue light irradiation. (Top right) χT = f(T) plots of **1** measured in the dark before any light irradiation, after 405 nm irradiation and after heating to 200 K. (Below) Reduced magnetizations at different temperatures (1.8 K, 3 K, 5 K and 8 K) in the photo-excited state.

Photomagnetic properties of **1** were studied in detail. As expected, the ground state of **1** is diamagnetic despite the temperature variation from 10 K to 200 K, which is in agreement with 2 electrons paired in the lowest-energy d_{x2-y2} orbital in TDD geometry. When **1** was irradiated with 405 nm at 10 K, the value of χT gradually increased from zero to 0.37 cm^3 mol^{-1} K after 11 hours of irradiation (Figure II. 2). Then the light was switched off after saturation, and low-temperature magnetizations and the temperature dependence of the χT from 2 K to 200 K have been measured. The non-superposed reduced magnetizations suggest

anisotropy in the photo-induced state. The thermal variation of the χT curve displays a complete relaxation around 65 K, temperature at which the compound recovers its diamagnetic state.

Then the photoreversibility was studied for **1** which has never been reported for mononuclear photomagnetic system involving $[Mo(CN)_8]^{4-}$ units. In the first step, a saturation of magnetic signal was obtained with continuous 405 nm blue light irradiation at 10 K (Figure II. 3). In the second step, a nearly complete light reversiblity was achieved by 650 nm red light irradiation. This full photoreversibilty with only 650 nm red light is unprecedent in the photomagnetic systems involving $[Mo(CN)_8]^{4-}$. To achieve the full reversibility, the reported photomagnetic systems involving Cu^{2+}-$[Mo(CN)_8]^{4-}$ demand a combined utilization of several wavelengths of 658-, 785-, and 840-nm light irradiation within the reverse-IT band ranging from 600 to 900 nm (λ_{max} = 710 nm).[15, 20]

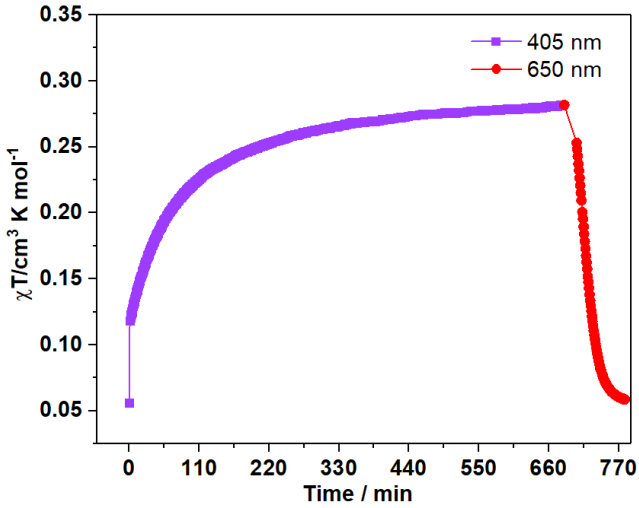

Figure II. 3 Time dependence of χT measured at 10 K, 1 T with continuous 405 nm blue light irradiation (violet line) and subsequent 650 nm light irradiation (red line). The discontinuous data at the beginning of the violet and red curves is due to bad centering of the sample at beginning and the heating effect of the 650 nm light.

II.2.1.1.2 Theoretical investigation of $K_4[Mo(CN)_8]\cdot 2H_2O$ (1)

To understand the photomagnetic behavior, in collaboration with the group of Prof. Coen de Graaf, theoretical calculations using the CASSCF/CASPT2 and TD-DFT approaches have been conducted for **1** to determine the excitation energies. The experimental UV-Vis spectra of **1** in solution and in solid state are nicely reproduced by the calculations (Figure II. 4 and Table II. 2). Notably, the lower energy transitions located at 430 and 360 nm are attributed to spin-forbidden transitions from the singlet ground state towards triplet excited states, in line with previous calculations.[41] At higher energy, the observed intense band at 240 nm is assigned to multiple spin-allowed excitations. In addition, the lowest triplet state is further calculated to map the energies and wavefunctions considering zero-field splitting coupling (Table II. 3).

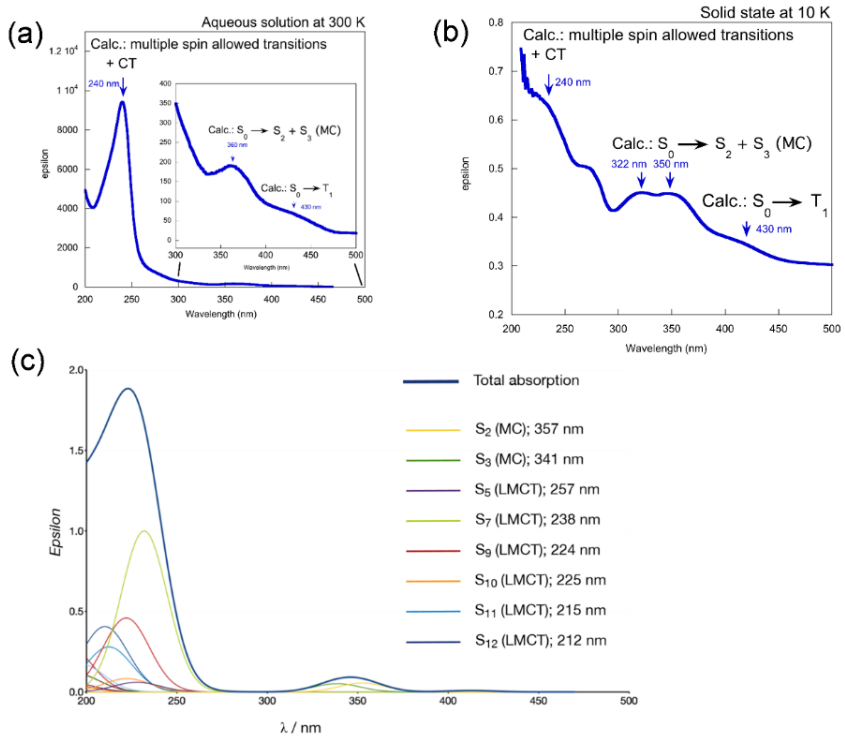

Figure II. 4 UV-Vis spectra for **1** in aqueous solution at 300 K (a) and in solid state at 10 K (b) compared with calculations from TD-DFT approach (see Table II. 2). Blue arrows indicate the position of the observed bands, and the numbers values indicate the calculated vertical excitations. (c) TD-DFT calculated spectrum where the thick blue line is the total absorption and the thinner colored lines are the individual contributions of each excitation as mentioned in the legend. S stands for singlet state and T stands for triplet state.

Table II. 2 Positions and assignments of all vertical excitations from theoretical calculations using CASPT2 approaches for metal-centered states of **1**.

State	**GS / nm**	**Oscillator strength**
S0	--	--
T1	429.6	1.7E-06
T1	429.1	5.4E-06
T1	429.0	8.4E-06
S1	381.6	2.7E-05
T2	357.0	4.0E-06
T2	355.5	<1.0e-7
T2	355.3	5.8E-06
T3	349.6	1.6E-06
T3	347.6	9.6E-07
T3	347.5	<1.0e-7
S2	322.5	8.4E-04
S3	316.0	5.7E-04
T4	263.1	4.5E-06
T4	263.1	3.9E-06
T4	263.0	5.0E-07
S4	256.3	5.7E-05

Table II. 3 Calculated Zero-field splitting parameters *D* and *E* (in cm^{-1}) and *g* values for the first excited triplet state of **1**.

	D	*E*	g_x	g_y	g_z
1	25.3	-2.8	1.793	1.819	1.946

II.2.1.1.3 Reflectivity studies of $K_4[Mo(CN)_8]\cdot 2H_2O$ (1)

To examine the photochromic properties, reflectivity measurements have been conducted for **1** (Figure II. 6). No significant spectral change has been observed for cooling or heating process between 300 K and 10 K, suggesting that this compound is stable with variation of temperature (Figure II. 6a and 6b). Useful information can be obtained by probing the change of absolute reflectivity after 5 min light irradiation with different wavelengths at 10 K. Interestingly, a new broad absorption around 650 nm was observed, when **1** was exposed to light within the 365-455 nm range at 10 K, indicating an important modification of the molybdenum center (Figure II. 6c and 6d). By comparison of the change of absolute reflectivity values at 650 nm after different light irradiation, 405 nm light is proved to be the most efficient wavelength. It is worth to mention that this important modification is not observed for light irradiation above 455 nm (Figure II. 6c). Then we performed 30 min irradiation with 405 nm light to access the spectrum of the photo-excited state that is stable with time at 10 K (Figure II. 6e and 5f).

Then the photoexcited sample was further heated, and the characteristic band of the photo-excited state at 650 nm started to disappear. This photoinduced signature vanished completely around 70 K, temperature at which the sample was fully relaxed (Figure II. 5). According to the results of the first set of theoretical calculations, the 405 nm excitation makes the lower-energy triplet state accessible.

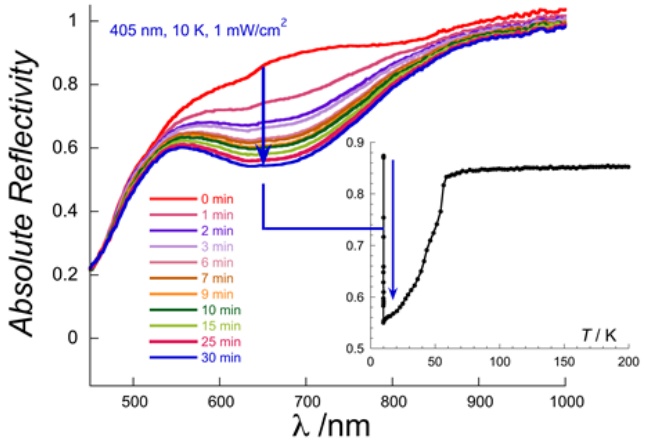

Figure II. 5 Reflectivity spectra of **1** versus time under 405 nm irradiation (1 mW/cm^2, 10 K). Inset: Temperature dependence of the absolute reflectivity at 650 nm (during the excitation (blue arrow) and after excitation in heating mode in the dark (dark points)).

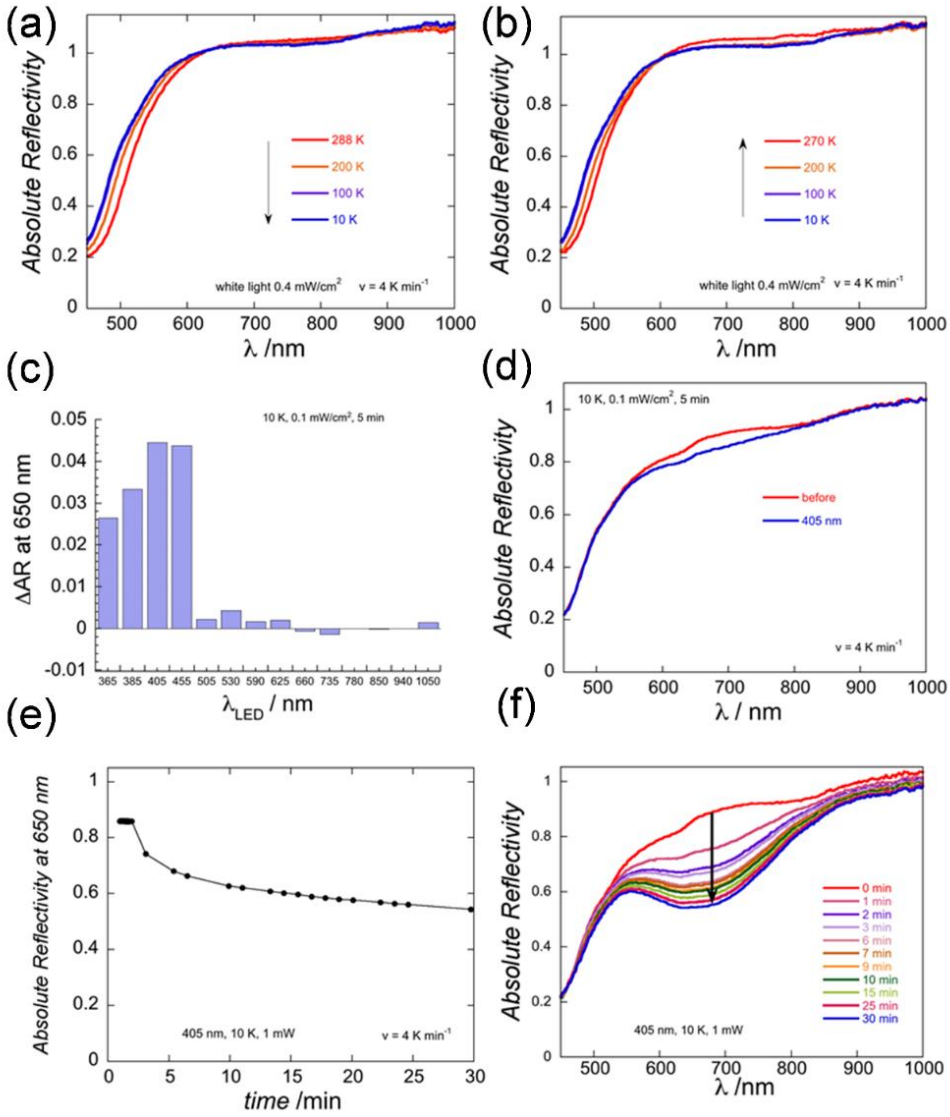

Figure II. 6 Reflectivity spectra for **1** in solid state. Reflectivity spectra for **1** when it is cooled (a) or heated (b) from 300 to 10 K. (c) When the compound was exposed at 10 K under specific wavelengths, the variation of the transition at 650 nm plotted against the wavelength applied. (d) When the compound was exposed with 405 nm light irradiation at 10 K, a new transition appears at 650 nm. (e) and (f) The photo-excited state that is stable with time has been realized at 10 K after one half-hour 405 nm light irradiation (i.e., the most efficient wavelength).

II.2.1.1.4 Photocrystallographic studies of $K_4[Mo(CN)_8]\cdot 2H_2O$ (1)

To gain more insights into the photoexcited state, photocrystallography at 10 K has been performed in collaboration with the group of Prof. Sébastien Pillet. Single crystal X-ray diffraction can provide reliable structural information for the metastable excited state. Upon exposure to 405 nm laser at 10 K, a clear color change from yellow to green was observed (Figure II. 7). The green color in photoinduced state is in agreement with the observation of the 650 nm band in the reflectivity spectra. Meanwhile, there was a detectable change of the cell parameters and we collected the whole set of data after 30 min exposure to light when the cell parameters were stabilized. The yellow color could be restored in relaxed state by heating to 70 K. The ground state, the photoinduced state and the relaxed state of **1** at 10 K are named as **1, 1*** and $\mathbf{1_{relax}}$, respectively.

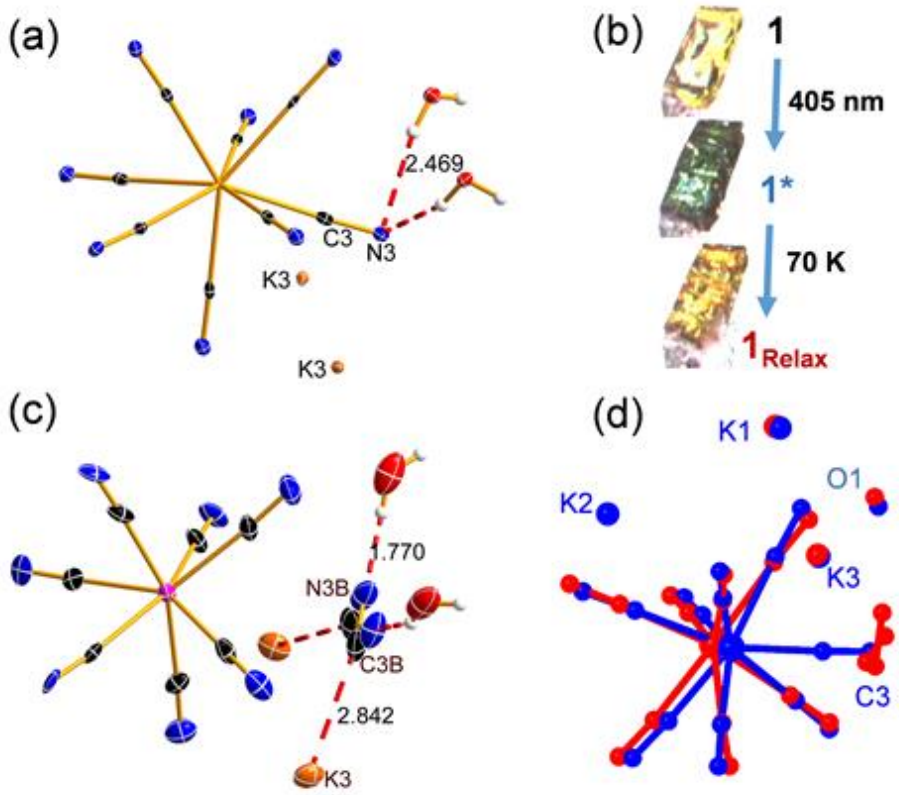

Figure II. 7 Crystal structures shown with 70 % probability thermal ellipsoids for **1** (a), **1*$_{PES}$** (c) with H bonding (red-dashed lines). (b) Crystal pictures for **1, 1*** and **1$_{relax}$** at 10 K. (d) Superposition of the relevant fragments for **1** (blue) and **1*$_{PES}$** (red).

The good crystallinity of **1, 1*** and **1$_{relax}$** allows to track the crystal structure modification in the photoinduced state and to check reversibility. The selected crystallography data are compiled in Table II. 4, Table II. 5, Table II. 6 and Table II. 7. After cooling down the sample to 10 K, there was no significant difference compared with the reported crystal structure at room temperature, except the expected thermal contraction. For **1, 1*** and **1$_{relax}$**, they are all crystallized in the same space group *Pnma* with the global crystal-packing description preserved. Importantly, **1*** clearly reveals a cell volume expansion with an increase of the *c* axis compared with **1**. The structure of **1*** possesses a coexistence of the ground state and the photo-excited state from which the structure of the photoinduced state has been derived and named as **1*$_{PES}$** hereafter. Based on the crystallographic data, the occupancy of **1*$_{PES}$** is around 53% due to a partial photoconversion.

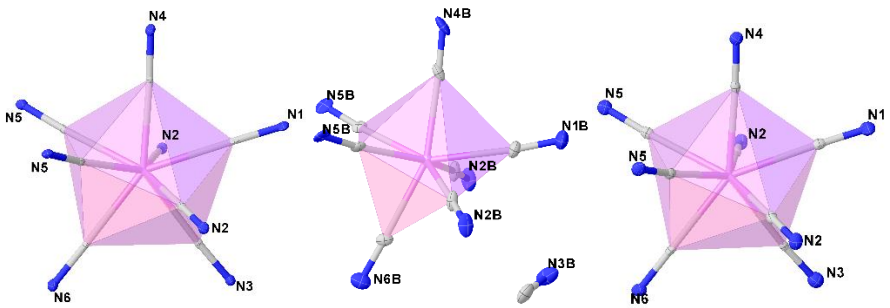

Figure II. 8 The coordination sphere of molybdenum for **1** (left), **1*$_{PES}$** (middle) and **1$_{Relax}$** (right).

The comparison of the coordination sphere of molybdenum for **1**, **1*$_{PES}$** and **1$_{relax}$** reveals spectacular modifications in the Mo environment (Figure II. 7 and Figure II. 8). **1*$_{PES}$** adopts a MoC_7 coordination sphere in an intermediate geometry between capped octahedron (COC) and capped trigonal prism (CTPR) with continuous shape measurement (CShM) values of 1.013 and 1.547, respectively. However, **1$_{relax}$** adopts the same MoC_8 coordination sphere as in **1**. Analysis of distortion parameters for **1** and **1$_{relax}$** reveals a triangular dodecahedron (TDD) geometry with CshM values of 0.250 and 0.244, respectively.[42]

Table II. 4 Selected distortion parameters (S, CShM) calculated from shape measurements, average bond lengths and bond angles for **1, 1*$_{PES}$** and **1$_{Relax}$**.

	1	**1*$_{PES}$**	**1$_{Relax}$**
S_{SAPR}	2.990	--	2.984
S_{TDD}	0.250	--	0.244
S_{COC}	--	1.013	--
S_{CTPR}	--	1.547	--
Mo-C $_{av.}$/Å	2.161	2.153	2.164
Mo-C-N $_{av.}$/°	177.5	176.4	177.2

S is continuous shape measurement (CShM) value. SAPR, TDD, COC and CTPR represent square antiprism, triangular dodecahedron, capped octahedron and capped trigonal prism, respectively.

The cleavage of the Mo-C3B bond in **1*$_{PES}$** is confirmed by its drastic elongation from 2.176(3) Å in **1** to 3.9632(2) Å in **1*$_{PES}$**, clearly showing that the C3B atom is not anymore linked to the molybdenum. The C3B-N3B bond distance of 1.123(7) Å indicates that the carbon-nitrogen triple bond is preserved. The C3-N3 ligand, that is sitting on a mirror plane in ground state, significantly shifts out of the mirror plane upon photo-excitation, being disordered over 2 symmetry-related positions. The superposition of relevant fragments for **1** and **1*$_{PES}$** shows that the Mo center moves in the opposite direction to the broken Mo-CN bond in the photoinduced state (Figure II. 7). The average Mo-C bond length for **1*$_{PES}$** is 2.153(4) Å, which is slightly shorter than the one found as 2.161(2) Å in **1**. The average Mo-C-N angle slightly changes from 177.5(2)° in **1** to 176.4(3)° in **1*$_{PES}$** (Table II. 4).

The hepta-coordinated complex $[Mo(CN)_7]^{3-}$, the detached CN^- anion and the K3 cations are stacking alternately in columns in *ac* plane (Figure II. 9). This probably explains the significant increase of *c* and *V* parameters in **1*$_{PES}$**.

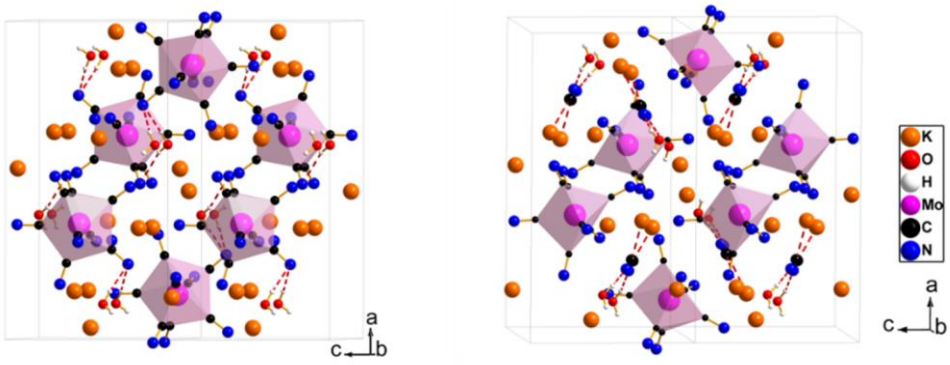

Figure II. 9 The crystal packing for **1** (Left) and **1*$_{PES}$** (Right).

Table II. 5 Crystal data, data collection, and refine parameters for **1**, **1*** and $\mathbf{1}_{relax}$.

	1	**1***	$\mathbf{1}_{Relax}$
Formula	$C_8H_4K_4MoN_8O_2$	$C_8H_4K_4MoN_8O_2$	$C_8H_4K_4MoN_8O_2$
$D_{calc.}$/g cm^{-3}	2.005	1.951	1.985
μ/mm^{-1}	1.827	1.778	1.809
Formula Weight/g mol^{-1}	496.53	496.53	496.53
T/K	10(2)	10(2)	10(2)
Crystal System	orthorhombic	orthorhombic	orthorhombic
Space Group	*Pnma*	*Pnma*	*Pnma*
a/Å	16.6310(3)	16.5760(9)	16.6686(12)
b/Å	11.4792(2)	11.4870(4)	11.5298(8)
c/Å	8.61746(18)	8.8786(6)	8.6459(6)
V/Å^3	1645.17(6)	1690.56(16)	1661.6(2)
Z	4	4	4
Z'	0.5	0.5	0.5
Wavelength/Å	0.71073	0.71073	0.71073
Radiation type	MoK$_a$	MoK$_a$	MoK$_a$
Q_{min}/°	2.449	2.457	2.444
Q_{max}/°	30.505	45.880	30.495
Measured Refl.	14222	25738	11813
Independent Refl.	2627	7529	2649
Reflections with I > 2(I)	2415	5324	2373
R_{int}	0.0523	0.0452	0.0448
Parameters	129	148	129
Restraints	0	16	0
Largest Peak	1.647	1.793	1.906
Deepest Hole	-2.218	-1.829	-0.707
GooF	1.187	1.068	1.076
wR_2 (all data)	0.1056	0.1152	0.0663
wR_2	0.0953	0.0966	0.0639
R_1 (all data)	0.0399	0.0796	0.0334
R_1	0.0352	0.0494	0.0284

Table II. 6 Selected bond lengths for **1**, **1*** $_{PES}$ and **1**$_{relax}$.

1	**Atoms**	**Length/Å**	**1*$_{PES}$**	**Atoms**	**Length/Å**	**1$_{Relax}$**	**Atoms**	**Length/Å**
Mo1	C1	2.153(3)	Mo1B	C1B	2.119(4)	Mo1	C1	2.157(3)
Mo1	C2	2.1492(18)	Mo1B	C2B	2.155(3)	Mo1	C2	2.1543(19)
Mo1	C3	2.176(3)	Mo1B	C4B	2.161(5)	Mo1	C3	2.181(3)
Mo1	C4	2.151(3)	Mo1B	C5B	2.154(3)	Mo1	C4	2.153(3)
Mo1	C5	2.1745(17)	Mo1B	C6B	2.171(4)	Mo1	C5	2.1760(19)
Mo1	C6	2.164(3)				Mo1	C6	2.159(3)
Average		2.161(10)	Average		2.153(4)	Average		2.164(11)
C1	N1	1.158(4)	C1B	N1B	1.159(6)	C1	N1	1.158(4)
C2	N2	1.156(2)	C2B	N2B	1.165(4)	C2	N2	1.160(2)
C3	N3	1.153(3)	C3B	N3B	1.123(7)	C3	N3	1.153(4)
C4	N4	1.155(4)	C4B	N4B	1.136(7)	C4	N4	1.161(4)
C5	N5	1.154(2)	C5B	N5B	1.141(4)	C5	N5	1.159(3)
C6	N6	1.157(4)	C6B	N6B	1.156(6)	C6	N6	1.161(4)
Average		1.155(3)	Average		1.148(5)	Average		1.159(3)

Table II. 7 Selected bond angles for **1**, **1*** $_{PES}$ and **1**$_{relax}$.

1	**Atoms**		**Angle/°**	**1*$_{PES}$**	**Atoms**		**Angle/°**	**1$_{Relax}$**	**Atoms**		**Angle/°**
Mo1	C1	N1	178.8(2)	Mo1B	C4B	N4B	177.3(4)	Mo1	C1	N1	177.8(2)
Mo1	C2	N2	177.74(16)	Mo1B	C5B	N5B	175.0(2)	Mo1	C2	N2	177.27(17)
Mo1	C3	N3	177.2(2)	Mo1B	C1B	N1B	175.6(4)	Mo1	C3	N3	175.7(2)
Mo1	C4	N4	176.80(19)	Mo1B	C6B	N6B	178.0(4)	Mo1	C4	N4	177.1(2)
Mo1	C5	N5	176.52(16)	Mo1B	C2B	N2B	176.9(3)	Mo1	C5	N5	176.39(17)
Mo1	C6	N6	178.7(2)					Mo1	C6	N6	179.7(2)
Average			177.5(11)	Average			176.4(3)	Average			177.2(10)

To explain the bond breakage of Mo-C3, we analyzed the hydrogen bonds in **1** with the help of the software PLATON[43] (Table II. 8). C3 and C5 atoms appear clearly involved in the crystal packing through hydrogen bonds interactions with nearby water molecules. However, the C3 atom is engaged into two hydrogen bonds and only one hydrogen bond for C5, which may be account for breakage of Mo-C3 under light irradiation (Figure II. 10).

The detached cyanide ligand is trapped in the crystal packing by potassium ions and water molecules. The nitrogen atoms of cyanide ligand N3B and water molecules form N3B···H-O hydrogen bonds. As shown in Figure II. 7 and Table II. 8, N3(B)…H distance has been drastically shortened from 2.469 Å to 1.770 Å after light irradiation, which indicates a much stronger H-bond interaction in **1*$_{PES}$**. The fingerprint analysis for the intermolecular interactions also confirms the large variation for H…N interaction (Figure II. 11). In parallel, the carbon atom of the cyanide ligand C3B interacts with the adjacent K3 cations.

The superposition of the crystal structures of **1** and **1**$_{relax}$ states confirms the full reversible process after thermal heating to 70 K (Figure II. 10), with all the crystallographic parameters fully restored (Table II. 4).

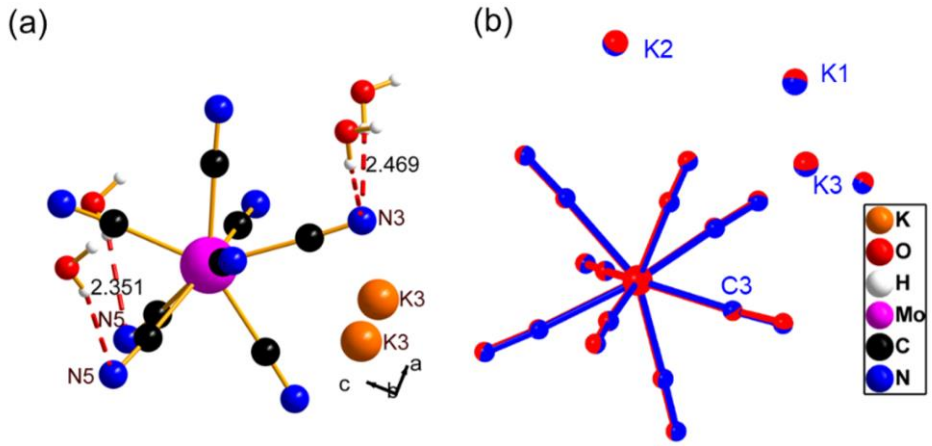

Figure II. 10 (a) The $[Mo(CN)_8]^{4-}$ complex in **1** with H bonding (red-dashed lines). (b) The superposition of crystal structure for **1** (in blue) and $\mathbf{1}_{relax}$ (in red). K1 and K2 atoms in (a) are omitted for clarity.

Table II. 8 H-bonds for the different states **1**, $\mathbf{1}^*_{PES}$ and $\mathbf{1}_{relax}$.

	Donor---H....Acceptor	D-H / Å	H...A / Å	D...A / Å	D-H...A / °
1	O(1)--H(1)..N(3)	0.79(3)	2.47(3)	3.182(2)	151(3)
	O(1)--H(2)..N(5)	0.79(3)	2.35(3)	3.120(2)	165(3)
$\mathbf{1}^*_{PES}$	O(1)--H(1)..N(3B)	0.7884(0)	1.77(0)	2.5062(1)	154.814(2)
	O(1)--H(1)..N(5B)	0.77(2)	2.40(3)	3.125 (3)	156(2)
$\mathbf{1}_{relax}$	O(1)--H(1)..N(3)	0.80(3)	2.53(3)	3.210(2)	143(3)
	O(1)--H(2)..N(5)	0.82(3)	2.31(3)	3.119(2)	169(3)

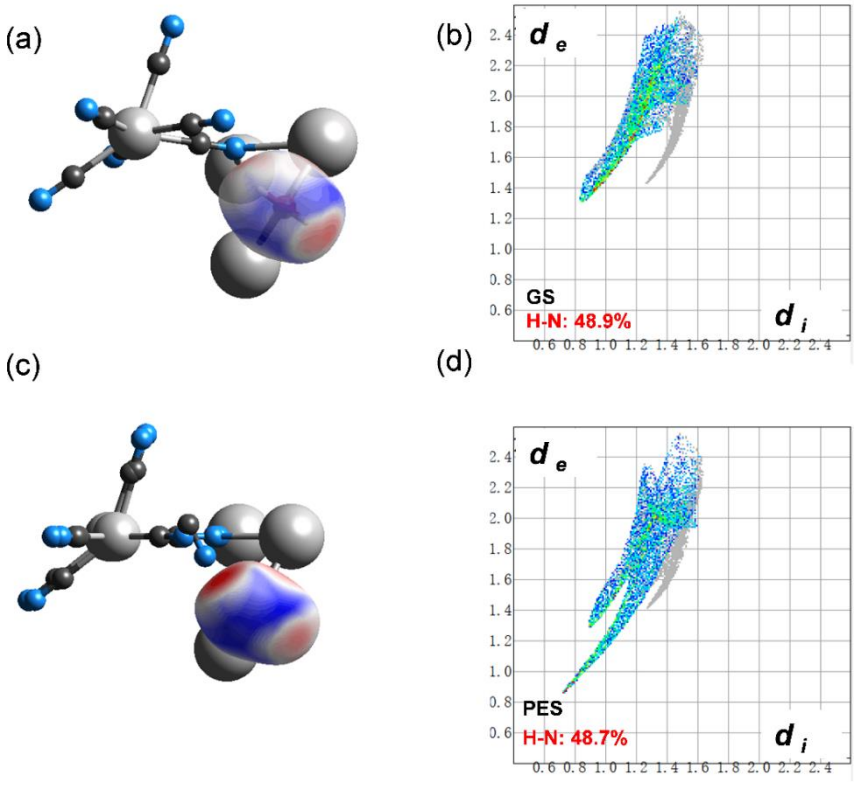

Figure II. 11 Fingerprints of the intermolecular interactions for H_2O molecule in **1** (a and b) and **1*** (c and d) from Single-Crystal X-ray Diffraction data. Grey zones represent all of the interactions and the blue zones account for the selected H…N interactions.

An optimized crystal structure was obtained for the lowest triplet state from periodic DFT, named as **1*$_{PEScal}$**. An examination of the coordination geometry in the photo-induced state shows that one cyanide ligand is leaving the coordination sphere of Mo center (Figure II. 12), which is in accordance with the previous calculations for $Cu^{II}/Mo^{IV}(CN)_8$ systems.[33-34]

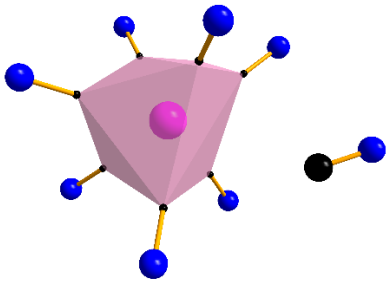

Figure II. 12 The calculated coordination geometry for Mo center in the photo-induced state **1*$_{PEScal}$**.

The superposition of the experimental structure **1*$_{PES}$** and **1*$_{PEScal}$** shows identical Mo coordination spheres in general, with the only difference coming from the disorder that affects the broken C3B-N3B part in **1*$_{PES}$** (Figure II. 13). Such discrepancy is not surprising since this disorder originates from the crystal packing symmetry, that is not taken into account in **1*$_{PEScal}$**.

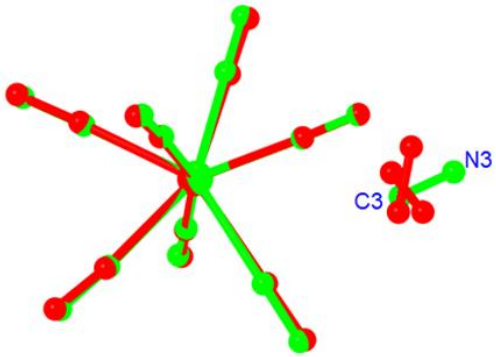

Figure II. 13 The superposition of Mo coordination spheres for **1*$_{PEScal}$** (in green) and **1*$_{PES}$** (in red).

II.2.1.1.5 Spectroscopic studies of $K_4[Mo(CN)_8]\cdot 2H_2O$ (1) at 10 K after excitation

To get more insights about the photoinduced state, we recorded UV-vis and IR spectra after 405 nm irradiation at 10 K (Figure II. 14 and Figure II. 15). The UV-vis spectrum shows a new transition around 350 nm and a broad absorption in the visible region that are consistent with reflectivity data, with both bands indicating the modifications of the Mo coordination. TD-DFT calculations attribute the broad absorption band to a LMCT absorption band from the detached cyanide to Mo (Table II. 9).

The IR spectrum recorded in the 2040-2160 cm^{-1} range corresponding to the cyanide asymmetric stretching reveals new features that can be tentatively attributed to the hepta-coordinated $Mo(CN)_7$ complex and to the detached cyanide at 2080 cm^{-1}.[44] A further thermal annealing at 100 K gives back UV-Vis and IR spectra, confirming again the full reversibility of the process.

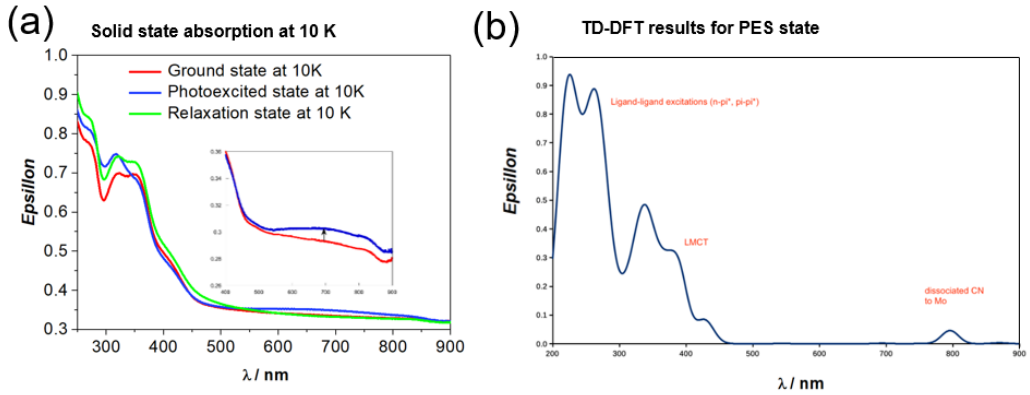

Figure II. 14 The evolution of UV-Vis spectra (a) for **1** with blue light irradiation at 10 K. (b) TD-DFT results based on **1*PES** crystal structure. Experimental detail for UV-Vis spectra: **1** was recrystallized on CaF_2 optical window. The sample was measured in transmission mode in a closed cycle He cryostat and photoexcited with 405 nm laser diode, followed by temperature increased to 100 K and decreased to 10 K.

Table II. 9 Comparison of the lowest singlet and triplet CASPT2 energies for metal-centered states in **1**, **1*PES**. These calculations have been obtained from experimental crystal structures of **1** and **1*PES**.

State	**1 / nm**	**State**	**1*PES / nm**
S0		T0	
T1	429.6	S1	1937.3
T1	429.1	S2	1771.2
T1	429.0	S3	837.7
S1	381.6	T1	310.0
T2	357.0	T2	306.9
T2	355.5	S4	278.6
T2	355.3	T3	276.8
T3	349.6	S5	270.7
T3	347.6	T4	263.2
T3	347.5	S6	244.5
S2	322.5	S7	236.6
S3	316.0	T5	236.2
T4	263.1	T6	232.6
T4	263.1	S8	221.8
T4	263.0	S9	219.1
S4	256.3		

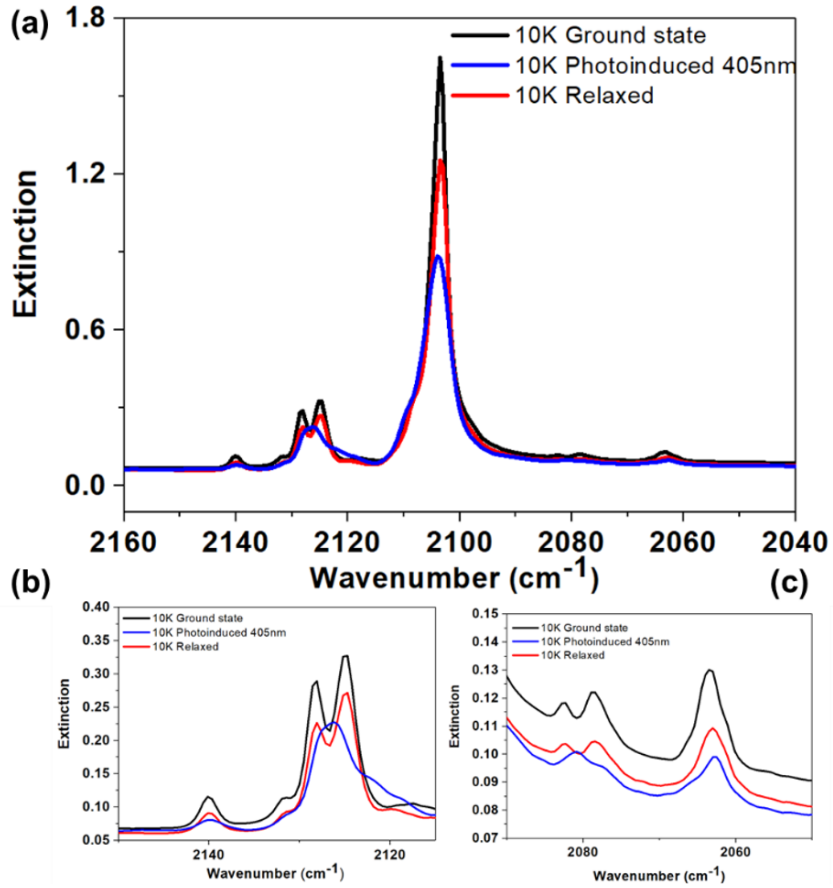

Figure II. 15 (a) The evolution of IR spectra for **1** with blue light irradiation at 10 K ranging from 2040 cm^{-1} to 2160 cm^{-1}. (b) The enlarged area ranging from 2100 cm^{-1} to 2160 cm^{-1}. (c) The enlarged area ranging from 2040 cm^{-1} to 2100 cm^{-1}. Experimental detail: **1** was recrystallized on CaF_2 optical window. The sample was measured in transmission mode in a closed cycle He cryostat and photoexcited with 405 nm 20 mW at 10 K, followed by temperature increased to 100 K and decreased to 10 K.

II.2.1.2 Further evidences of the $[Mo^{IV}(CN)_7]^{3-}$ complex from the photochemistry studies of $K_4[Mo^{IV}(CN)_8]\cdot 2H_2O$ (1) in solution

In collaboration with the group of Dawid Pinkowicz, we demonstrate the possible preparation of the $[Mo^{IV}(CN)_7]^{3-}$ complex as the sole Mo based photoproduct using a photochemical synthetic pathway with **1** as starting material. $[K(crypt\text{-}222)]_3[Mo^{IV}(CN)_7]\cdot 3CH_3CN$ (**2**) has been crystallized from an acetonitrile solution containing **1** in the presence of [2.2.2]cryptand after white light irradiation. The crystal structure of **2** has been determined as a $[Mo^{IV}(CN)_7]^{3-}$ anion charge balanced by three $[K(crypt\text{-}222)]^+$ in the asymmetric unit (Figure II. 16).

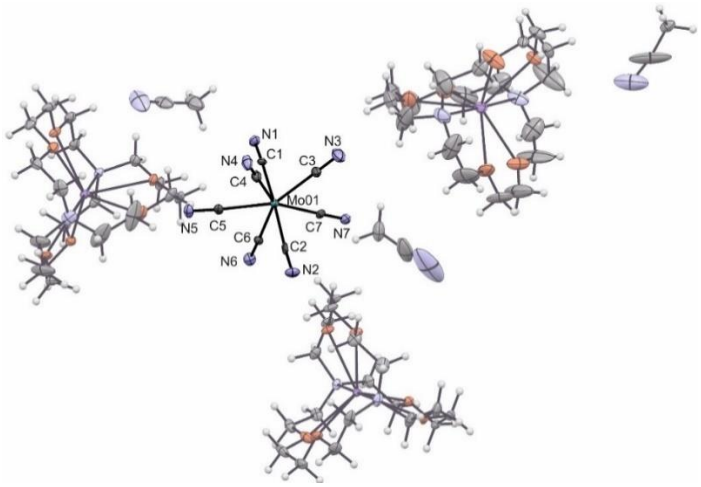

Figure II. 16 Asymmetric unit of $[K(crypt\text{-}222)]_3[Mo^{IV}(CN)_7]\cdot 3CH_3CN$ (**2**) with atom labeling scheme for the $[Mo^{IV}(CN)_7]^{3-}$ anion (thermal ellipsoids at 30 % probability).

The magnetic properties of **2** were studied and analyzed using the PHI software (Figure II. 17). They are nicely reproduced with the following parameters: g = 1.89(5), D = 20.6(1) cm^{-1}, and E = -1.4(8) cm^{-1}. These parameters are comparable with the parameters obtained for triplet state of **1** (Table II. 3). The significant anisotropy in **2** is in line with what we observed for the photoexcited state for **1**.

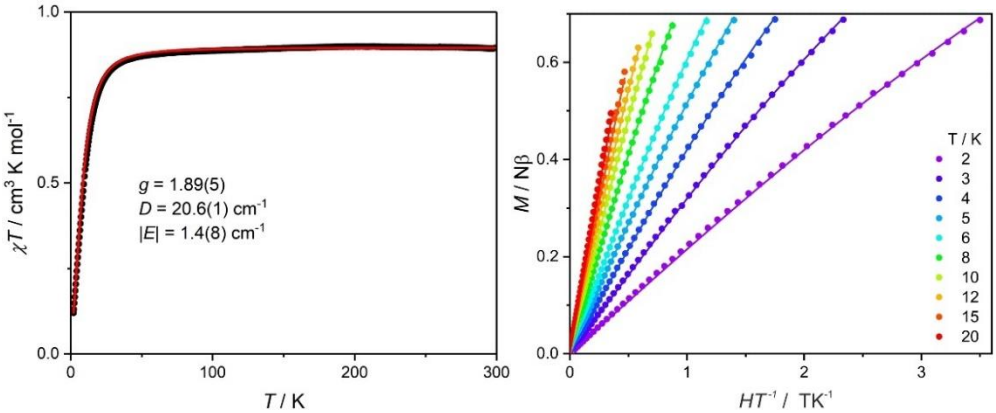

Figure II. 17 (Left) Experimental $\chi T(T)$ for $[K(crypt\text{-}222)]_3[Mo^{IV}(CN)_7]\cdot 3CH_3CN$ (**2**) recorded at 0.1 T external magnetic field (black points) and the best fit (red line) with the indicated parameters. (Right) Experimental M versus HT^{-1} curves recorded at the selected temperatures (points) and the best fits (solid lines). Both $\chi T(T)$ and $M(HT^{-1})$ were fitted simultaneously.

II.2.1.3 Discussions on the $K_4[Mo(CN)_8]\cdot 2H_2O$

To explain the bond breakage of Mo-CN, as suggested by theoretical calculations (Figure II. 18), the d orbital splitting patterns are significantly modified with the increasing of Mo-CN distance. The energy level of $4d_{x2-y2}$ and $4d_{z2}$ become close. Therefore, the ground state has an electronic configuration $(4d_{x2-y2})^2$, and the triplet state has an electronic configuration $(4d_{x2-y2})^1$ $(4d_{z2})^1$ (Figure II. 18). The d_{x2-y2} orbital is basically non-bonding. However, the $4d_{z2}$ orbital is slightly antibonding and it points on the other side directly to the C3≡N3 ligand (Figure II. 19). So this can explain why Mo-C3 is broken in the photoinduced state.

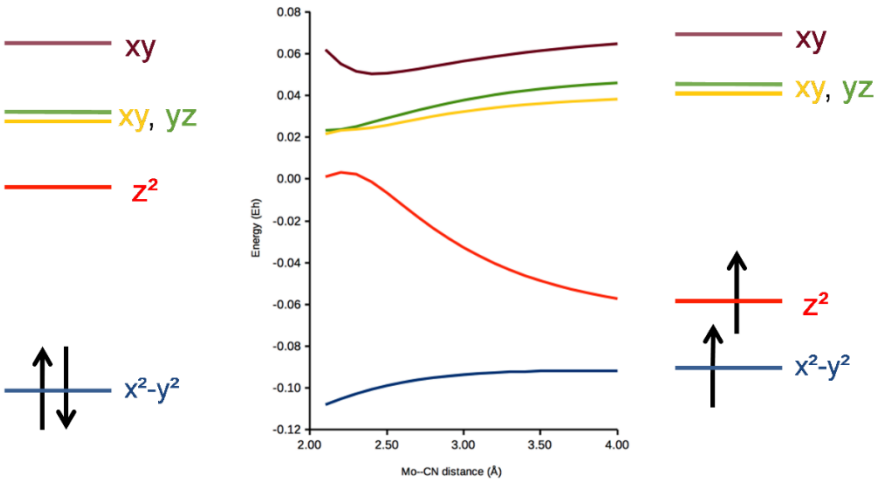

Figure II. 18 (Middle) The modification of d orbitals splitting patterns with increasing of Mo-CN distance based on theoretical calculations. The d-orbital splitting patterns in the ground state (Left) and in the photoexcited state (Right).

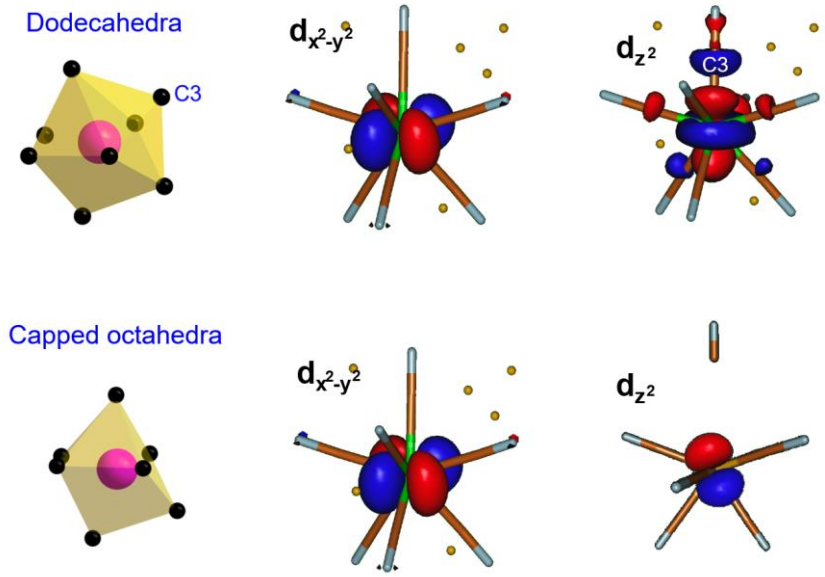

Figure II. 19 The coordination sphere for Mo center, d_{x2-y2} and d_{z2} orbital orientations for ground state (Top) and for photoinduced state (Below) based on calculations.

Given the good agreement between the results of photocrystallographic and the calculations, we consider that the observed photomagnetic properties for **1** are due to the population of a triplet state (S = 1). However, the obtained values (M_{sat} = 0.6 Nμ_B at 1.8 K and χT_{max} = 0.37 cm^3 mol^{-1} K at 20 K) are far from what are expected for a S = 1 (M_{sat} = 2 Nμ_B at 1.8 K and χT_{max} = 1 cm^3 mol^{-1} K assuming a Zeeman factor equal to 2). Attempts to reproduce these magnetic data by including zero-field splitting parameters and partial conversion of the triplet state at 1.8-20 K (temperature range for which the thermal relaxation is negligible) failed or led to overparameterization. However, as shown in Figure II. 20, the experimental photomagnetic properties agree well with theoretically expected magnetic response considering a 50 % photoconversion of triplet state with zero-field splitting parameters from theoretical calculation (Table II. 3).

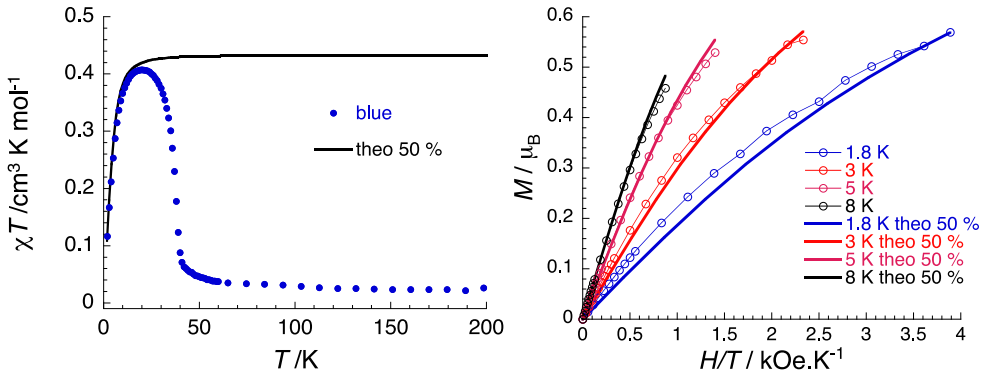

Figure II. 20 The comparison of experimental photomagnetic properties for **1** and theoretically expected magnetic response considering a 50 % photoconversion of triplet state.

Our results show experimentally and theoretically that the photomagnetism in **1** in solid state at 10 K is associated to the photodissociation of a Mo-CN bond. Specially, the photocrystallography data provides strong experimental proof for the results of theoretical calculation.

In the literature, several examples of photoinduced magnetism with large structural reorganizations are mainly based on photoisomerization of the ligands linked to Fe^{II},[45-46] or reversible formation or rupture of metal–ligand (O or N) bonds in 3d metal ions (Ni^{II}, Fe^{II} and Fe^{III}) complexes.[47-50] We observed for the first time a photomagnetic effect based on light-induced bond cleavage in the solid state for a 4d metal complex with the in-depth study of **1**.

Our intriguing findings for **1** in solid state prompt the preparation of new cyanide complexes with interesting magnetic properties in solution. The Mo-CN breakage with white light at room temperature in solution leads to the preparation of an unprecedented anisotropic $[Mo^{IV}(CN)_7]^{3-}$ complex, and the corresponding magnetic properties further support the formation of same species through light irradiation in solid state at 10 K.

The systematic investigations of **1**, as a ground-breaking result, unambiguously explain the formation of triplet state as the photodissociation of a Mo-CN bond. This encourages us to explore the effect of different alkali cations on the photomagnetic properties of $A_4[Mo(CN)_8]\cdot xH_2O$ (A = alkali cations, with A being other alkali cations than K^+).

II.2.2 Investigation of $Rb_4[Mo(CN)_8]\cdot 2H_2O$ (3)

$$K_4Mo(CN)_8\cdot 2H_2O + 2CdCl_2 \xrightarrow{H_2O} Cd_2Mo(CN)_8\cdot xH_2O\downarrow + 4KCl$$
$$Cd_2Mo(CN)_8\cdot xH_2O + 4RbOH \xrightarrow{H_2O} Rb_4Mo(CN)_8\cdot 2H_2O + 2Cd(OH)_2\downarrow$$

Scheme II 1 The approach followed to prepare the solution of $Rb_4[Mo(CN)_8]\cdot 2H_2O$ by replacement of potassium cation with rubidium cation.

Table II. 10 The reported ionic radius, *r*, of the alkali metal ions.[51]

Cation	Li^+	Na^+	K^+	Rb^+	Cs^+
Ionic radius/Å	0.69	1.02	1.38	1.49	1.70

There is a continuous increase of ionic radius for alkali cations from Li^+ to Cs^+, but the ionic radius for Rb^+ is close to K^+ (Table II. 10). To synthesize $Rb_4[Mo(CN)_8]\cdot 2H_2O$, a reported approach is followed as shown in Scheme II 1 (II.5.1 Synthesis).[13] In the first step, the precipitate of $Cd_2[Mo(CN)_8]\cdot xH_2O$ is isolated after the mixture of the aqueous solution of $K_4[Mo(CN)_8]\cdot 2H_2O$ and $CdCl_2$. Then the solution of $Rb_4[Mo(CN)_8]\cdot 2H_2O$ is obtained by double exchange reaction of rubidium hydroxide and $Cd_2[Mo(CN)_8]\cdot xH_2O$ complex after the filtration of the $Cd(OH)_2$ precipitate. The target crystals with good quality could be obtained by slow evaporation at room temperature.

The good agreement for the experimental powder X-ray diffraction pattern and the calculated one for **3**, indicates the purity of the synthesized batch (see subsection II.5.2

Powder X-ray diffraction analysis). UV-Vis spectra and infrared spectra (IR) show similarities for **1** and **3**. Regarding the results of thermogravimetric analysis (TGA), different with **1**, we observed clearly two steps before 200 °C for **3**. The first step corresponds to the loss of the two water molecules and the second step corresponds to the decomposition of the $Rb_4[Mo(CN)_8]$ (II.5.5 Thermogravimetric analysis).

II.2.2.1 Crystal structure of $Rb_4[Mo(CN)_8]\cdot 2H_2O$ (3)

3 is isostructural with **1** and crystalizes in the same space group *Pnma*. Due to the small differences of the ionic radius between K^+ and Rb^+ (Table II. 10 and Figure II. 21), there is a slight elongation of the cell parameters in **3**. For example, the *a* axis increases from 16.6310(3) Å for **1** to 17.0798(6) Å for **3** (Table II. 12**)**.

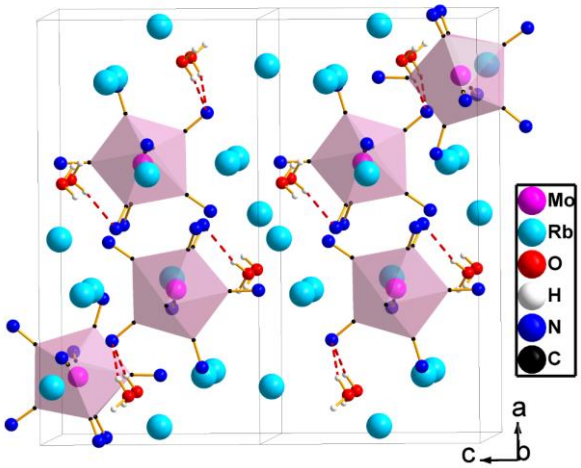

Figure II. 21 Crystal packing of **3** along *c* axis with the H bonds shown as red-dashed lines.

II.2.2.2 Photomagnetic studies of $Rb_4[Mo(CN)_8]\cdot 2H_2O$ (3)

As shown in Figure II. 22, the photomagnetic studies of **3** have been studied with the same procedure used for **1**. **3** shows a lot of similarities as **1** but with noticeable differences. Compared with **1**, **3** exhibits a more enhanced photomagnetic response using the same 405 nm light irradiation. The value of χT after light irradiation could reach 0.6 $cm^3\ mol^{-1}$ K for **3** compared with only 0.4 $cm^3\ mol^{-1}$ K for **1**. There is a significant magnetic anisotropy in photoexcited state for both **1** and **3**. Strikingly different with **1**, the thermal relaxation of the photogenerated state occurred in two distinct temperature regimes for **3**. The first step is similar with **1**, but shifts to higher temperature with the value of 65 K for **1** and 75 K for **3**. There is a clear plateau ranging from 20-50 K for **3**, which is not observed for **1**. A second relaxation step takes place around 250 K. The peculiar relaxation behavior for **3** suggests that there might be a coexistence of two different relaxation processes.

The photoreversibility with 650 nm light was also performed for **3**. Different with **1** which is nearly fully photoreversible with 650 nm light, only a small portion of paramagnetic signal has been decreased for **3** (Figure II. 23). Then we heated the compound after the 650 nm light irradiation to 300 K, indicating a one-step relaxation around 250 K which is comparable with the second relaxation step for the thermal relaxation curve. The fractional reversibility is another indication of the possible existence of two relaxation processes in **3**.

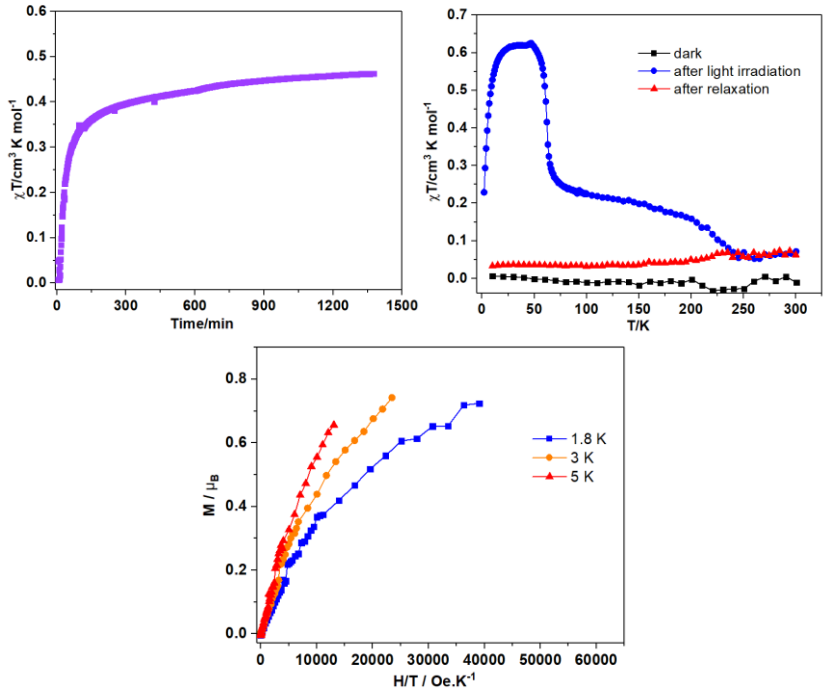

Figure II. 22 (Top left) Time dependence of the χT for **3** measured at 10 K, 1 T with continuous 405 nm blue light irradiation. (Top right) χT = f(T) plots of **3** measured in the dark before light irradiation, after 405 nm irradiation and after heating to 300 K. (Below) Reduced magnetizations at different temperatures (1.8 K, 3 K, 5 K) in the photo-excited state.

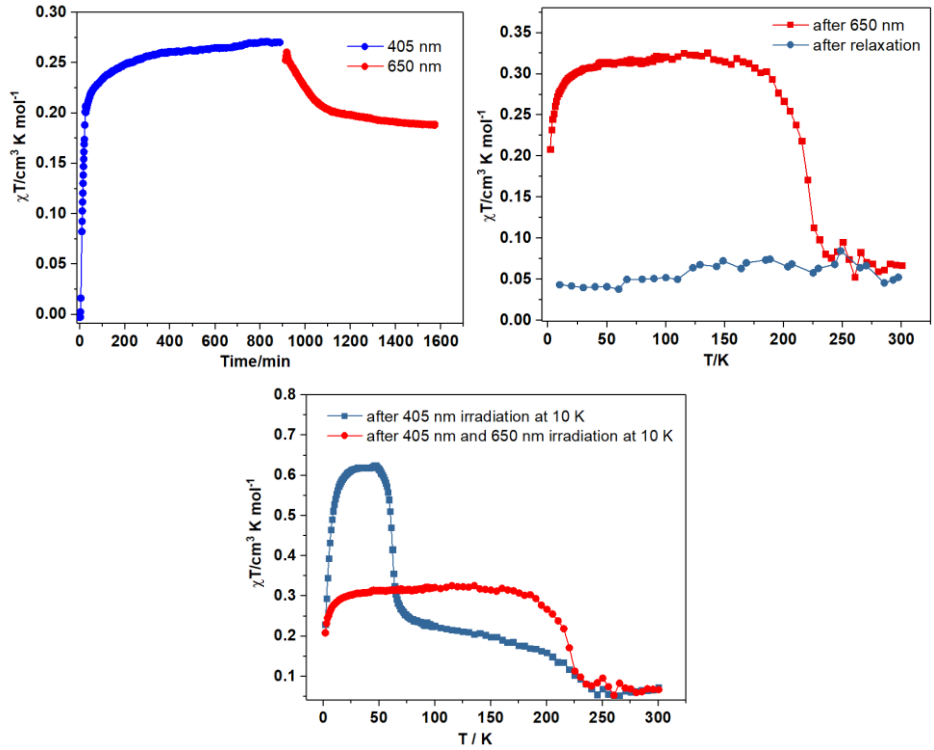

Figure II. 23 (Top left) Time dependence of the χT measured at 10 K, 1 T with continuous 405 nm blue light irradiation (blue) and then with 650 nm light irradiation (red). (Top right) χT = f(T) plots of **3** measured in the dark after 650 nm red light irradiation (red) and after heating to 300 K (blue). (Blow) The comparison of thermal relaxation curves after only 405 nm light irradiation and after 405 nm and 650 nm light irradiation.

II.2.2.3 Photocrystallographic studies of $Rb_4[Mo(CN)_8]\cdot 2H_2O$ (3)

In the similar way than for **1**, photocrystallography with 405 nm light irradiation at 10 K was also performed for **3** under same experimental conditions. The corresponding crystallographic data, selected bond lengths and angles and H-bonds are presented in Table II. 11, Table II. 12, Table II. 13, Table II. 14 and Table II. 15. The photoexcited structure **3*** also shows a coexistence of the ground state and the photo-excited state, but with much higher photoconversion rate 79 % for **3** than 53 % for **1**.

Similarly, the structure of the photoinduced state has been derived and named as $\mathbf{3^*_{PES}}$ hereafter. In Figure II. 24, the comparison of the coordination sphere of molybdenum for **3**, $\mathbf{3^*_{PES}}$ and $\mathbf{3_{Relax}}$ shows the similar striking modifications as **1**. $\mathbf{3^*_{PES}}$ reveals again a MoC_7 coordination with the rupture of Mo-C3 bond. The MoC_7 coordination sphere has an intermediate geometry between capped octahedron (COC) and capped trigonal prism (CTPR) with CShM values of 1.286 and 1.667, respectively. There is no noticeable difference between relaxed state at 75 K and ground state. Analysis of distortion parameters for **3** and $\mathbf{3_{relax}}$ both reveal a triangular dodecahedron (TDD) geometry with CShM values of 0.286 and 0.319, respectively.[42]

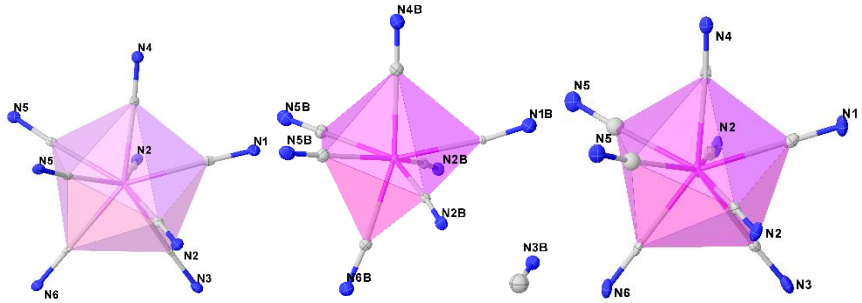

Figure II. 24 The coordination sphere of molybdenum for **3** (Left), $\mathbf{3^*_{PES}}$ (Middle) and $\mathbf{3_{Relax}}$ (Right).

Table II. 11 Selected cell parameters for the different states **1**, $\mathbf{1^*_{PES}}$, $\mathbf{1_{relax}}$, **3**, $\mathbf{3^*_{PES}}$ and $\mathbf{3_{relax}}$.

	1	$\mathbf{1^*_{PES}}$	$\mathbf{1_{Relax}}$
$\mathbf{S_{SAPR}}$	2.990	--	2.984
$\mathbf{S_{TDD}}$	0.250	--	0.244
$\mathbf{S_{COC}}$	--	1.013	--
$\mathbf{S_{CTPR}}$	--	1.547	--
Mo-C $_{av.}$/Å	2.161(10)	2.153(4)	2.164(11)
C-N $_{av.}$/Å	1.155(3)	1.148(5)	1.159(3)
Mo-C-N $_{av.}$/°	177.5(11)	176.4(3)	177.2(10)
$\mathbf{d_{Mo...Momin}}$**/Å**	7.53	--	--
	3	$\mathbf{3^*_{PES}}$	$\mathbf{3_{Relax}}$
$\mathbf{S_{SAPR}}$	3.015	--	3.038
$\mathbf{S_{TDD}}$	0.286	--	0.319
$\mathbf{S_{COC}}$	--	1.286	--
$\mathbf{S_{CTPR}}$	--	1.667	--
Mo-C $_{av.}$/Å	2.162(5)	2.160(13)	2.162(11)
C-N $_{av.}$/Å	1.159(6)	1.142(10)	1.152(14)
Mo-C-N $_{av.}$/°	177.5(4)	176.6(12)	177.5(9)
$\mathbf{d_{Mo...Momin}}$**/Å**	7.81	--	--

Table II. 12 Crystal data, data collection, and refine parameters for **3**, **3*** and $\mathbf{3_{Relax}}$.

Compound	**3**	**3***	$\mathbf{3_{Relax}}$
Formula	$MoRb_4N_8C_8H_4O_2$	$C_8H_4MoN_8O_2Rb_4$	$MoRb_4N_8C_8H_4O_2$
$D_{calc.}$/g cm^{-3}	2.556	2.460	2.569
μ/mm^{-1}	11.673	11.234	11.730
Formula Weight/g mol^{-1}	682.01	682.01	682.01
T/K	10(2)	10(2)	75(2)
Crystal System	orthorhombic	orthorhombic	orthorhombic
Space Group	*Pnma*	*Pnma*	*Pnma*
a/Å	17.0798(6)	16.8932(14)	17.0471(6)
b/Å	11.7589(5)	11.8018(13)	11.7485(5)
c/Å	8.8236(3)	9.2360(10)	8.8059(3)
V/Å^3	1772.13(12)	1841.4(3)	1763.63(12)
Z	4	4	4
Wavelength/Å	0.71073	0.71073	0.71073
Radiation type	MoK_a	MoK_a	MoK_a
Q_{min}/°	2.385	2.411	2.389
Q_{max}/°	30.501	32.919	30.504
Measured Refl.	14373	6720	8618
Independent Refl.	2832	2979	2807
Reflections with I > 2(I)	2583	1925	2136
R_{int}	0.0468	0.0690	0.0687
Parameters	129	224	124
Restraints	0	201	0
Largest Peak	1.002	1.783	5.972
Deepest Hole	-3.132	-2.902	-2.619
GooF	1.073	1.030	1.080
wR_2 (all data)	0.0932	0.1574	0.1704
wR_2	0.0909	0.1342	0.1573
R_1 (all data)	0.0374	0.0971	0.0884
R_1	0.0334	0.0576	0.0645

Table II. 13 Selected bond lengths for $[Mo^{IV}(CN)_8]^{4-}$ anion in **3**, **3*$_{PES}$** and **3$_{Relax}$**.

3	**Atoms**	**Length/Å**	**3*$_{PES}$**	**Atoms**	**Length/Å**	**3$_{Relax}$**	**Atoms**	**Length/Å**
Mo1	C1	2.159(6)	Mo1B	C1B	2.136(14)	Mo1	C1	2.158(12)
Mo1	C2	2.148(4)	Mo1B	C2B	2.135(13)	Mo1	C2	2.128(9)
Mo1	C3	2.172(6)	Mo1B	C4B	2.157(15)	Mo1	C3	2.191(12)
Mo1	C4	2.162(6)	Mo1B	C5B	2.193(11)	Mo1	C4	2.167(14)
Mo1	C5	2.174(4)	Mo1B	C6B	2.173(14)	Mo1	C5	2.181(8)
Mo1	C6	2.155(5)				Mo1	C6	2.163(13)
Average		2.162(5)	Average		2.160(13)	Average		2.162(11)
N1	C1	1.153(8)	N1B	C1B	1.15(2)	N1	C1	1.151(16)
N2	C2	1.164(5)	N2B	C2B	1.212(18)	N2	C2	1.179(11)
N3	C3	1.162(8)	N3B	C3B	1.11(3)	N3	C3	1.161(16)
N4	C4	1.150(8)	N4B	C4B	1.15(2)	N4	C4	1.133(17)
N5	C5	1.158(5)	N5B	C5B	1.064(16)	N5	C5	1.138(11)
N6	C6	1.162(7)	N6B	C6B	1.17(3)	N6	C6	1.136(17)
Average		1.159(6)	Average		1.142(10)	Average		1.152(14)

Table II. 14 Selected bond angles for $[Mo^{IV}(CN)_8]^{4-}$ anion in **3**, **3*$_{PES}$** and **3$_{Relax}$**.

3	**Atoms**		**Angle/°**	**3*$_{PES}$**	**Atoms**		**Angle/°**	**3$_{Relax}$**	**Atoms**		**Angle/°**
Mo1	C1	N1	177.7(5)	Mo1B	C1B	N1B	174.2(14)	Mo1	C1	N1	179.4(11)
Mo1	C2	N2	177.4(3)	Mo1B	C2B	N2B	176.0(9)	Mo1	C2	N2	177.3(8)
Mo1	C3	N3	177.7(5)	Mo1B	C4B	N4B	179.0(12)	Mo1	C3	N3	177.3(10)
Mo1	C4	N4	176.8(5)	Mo1B	C5B	N5B	177.8(12)	Mo1	C4	N4	175.9(10)
Mo1	C5	N5	176.4(3)	Mo1B	C6B	N6B	175.1(15)	Mo1	C5	N5	176.5(8)
Mo1	C6	N6	180.0(4)					Mo1	C6	N6	179.9(10)
Average			177.5(4)	Average			176.6(12)	Average			177.5(9)

Table II. 15 H-bonds for the different states **1**, **1*$_{PES}$**, **1$_{relax}$**, **3**, **3*$_{PES}$** and **3$_{relax}$**.

	Donor---H....Acceptor	D-H / Å	H...A / Å	D...A / Å	D-H...A / °
1	O(1)--H(1)..N(3)	0.79(3)	2.47(3)	3.182(2)	151(3)
	O(1)--H(2)..N(5)	0.79(3)	2.35(3)	3.120(2)	165(3)
1*$_{PES}$	O(1)--H(1)..N(3B)	0.7884(0)	1.77(0)	2.5062(1)	154.814(2)
	O(1)--H(1)..N(5B)	0.77(2)	2.40(3)	3.125 (3)	156(2)
1$_{relax}$ at 10 K	O(1)--H(1)..N(3)	0.80(3)	2.53(3)	3.210(2)	143(3)
	O(1)--H(2)..N(5)	0.82(3)	2.31(3)	3.119(2)	169(3)
3	O(1)--H(1)..N(3)	0.77	2.49	3.1790	149
	O(1)--H(2)..N(5)	0.79	2.35	3.1257	166
3*$_{PES}$	O(1)--H(1)..N(3B)	--	--	---	--
	O(1)--H(1)..N(5B)	0.82	2.37	3.1454	159
3$_{relax}$ at 75 K	O(1)--H(1)..N(3)	0.85	2.50	3.1882	138
	O(1)--H(2)..N(5)	0.85	2.32	3.1352	161

II.2.2.4 Discussions on the $Rb_4[Mo(CN)_8]\cdot 2H_2O$

Being isostructural with $K_4[Mo(CN)_8]\cdot 2H_2O$ (**1**), $Rb_4[Mo(CN)_8]\cdot 2H_2O$ (**3**) is a very interesting compound to study the influence of the size of alkali cation. Despite quite similar structure for these two compounds, **3** exhibits a surprisingly different relaxation behavior with two relaxation temperatures (~ 75 K and 250 K) and partial photoreversible behavior with 650 nm light. Interestingly, the light induced bond breakage of Mo-C3 bond is observed again at 10 K for **3**. The photoconversion rate (79 %) for **3** observed in photocrystallography is higher than **1** (53 %), correlating well with the photomagnetic result. This is supported by the comparison of the experimental photomagnetic properties and theoretically expected magnetic response considering a 75 % photoconversion of triplet state (Figure II. 25).

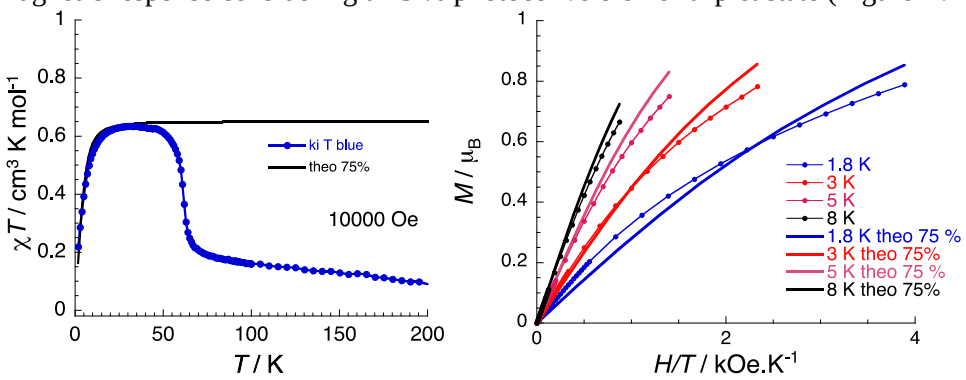

Figure II. 25 The comparison of experimental photomagnetic properties for **3** and theoretically expected magnetic response considering a 75 % photoconversion of triplet state with zero-field splitting parameters from theoretical calculation (Table II. 3).

Therefore, similar as **1**, the first relaxation step can be attributed as the photo-induced bond breakage of Mo-C bond. By analogy with nitrosyl (NO) system, the occurrence of isomerization cyanide ligand seems likely in the second relaxation step around 250 K for **3**.[52] Namely, the isomerization of broken cyanide bond may occur leading to the configuration of Mo-N≡C instead of the Mo-C≡N. In agreement with the observation for nitrosyl system, the relaxation of the Mo-N≡C metastable state may result a higher relaxation temperature.

However, the relaxation crystal structure of $\mathbf{3_{Relax}}$ at 75 K cannot offer experimental evidence for this isomerization of cyanide ligand, because C and N atoms are not able to be distinguished in Single Crystal X-ray diffraction. The relatively bigger size of Rb^+ compared with K^+ may lead to less dense crystal packing as shown by the minimum Mo…Mo distances 7.53 Å for **1** and 7.81 Å for **3** (Table II. 11). In case of **3**, the less dense crystal packing may provide enough space for the occurrence of isomerization of breakable cyanide ligand during thermal relaxation.

II.2.3 Investigation of $A_4[Mo(CN)_8]$ (A = Cs(4), Na(5), Li(6))

The ionic radius of alkali cations increases from Li^+ to Cs^+, and it is worth to further study the role of alkali cations in the crystal structure (Table II. 10). To synthesize $A_4[Mo(CN)_8]$ (A = alkali cations) (A = Cs(**4**), Na(**5**), Li(**6**)), a same approach is followed as shown in Scheme II 1 with rubidium cation substituted by target cations (II.5.1 Synthesis).[13]

However, the crystals of **4** and **5** are not stable because they absorb water easily from air atmosphere. This leads the discrepancy of the experimental powder X-ray diffraction patterns and the calculated one for **4**, and no successful powder X-ray diffraction pattern has been obtained for **5**. The low yield of **6** hinders the further characterizations. UV-Vis spectra of compounds $A_4[Mo(CN)_8]$ (A = Cs(**4**) and Na(**5**)) are very similar to each other (II.5.3 Optical measurements), with appearance of only the contributions of $[Mo(CN)_8]^{4-}$ complex. Even though **4** has different IR spectra than **1** and **3**, but the intense vibrations for cyanide ligand

fall in the same range around 2100 cm^{-1}, indicating that all the cyanide ligands are terminal (II.5.4 IR spectra). Moreover, the bands in *ν*(CN) region for **4** appear unusually broad and less resolved probably due to the contribution from different crystallographic independent Mo sites. No successful IR spectrum has been obtained for **5** because it is very easy to absorb water from air atmosphere.

II.2.3.1 Investigation of $Cs_{20}[Mo(CN)_8]_5 \cdot 7H_2O$ (4)

II.2.3.1.1 Crystal structure of $Cs_{20}[Mo(CN)_8]_5 \cdot 7H_2O$ (4)

Single-crystal X-ray diffraction analysis performed at 120 K reveals that **4** crystalizes in orthorhombic space group $Pna2_1$, therefore **4** is not isostructural with **1** and **3**. The crystal structure shows that $[Mo(CN)_8]^{4-}$ complexes are surrounded by Cs^+ and water molecules. The structural arrangement is constructed by the interaction between water molecules and terminal cyanide ligands of the octacyanidometalate(IV) moiety (Figure II. 26).

Table II. 16 and Table II. 17 present detailed crystallographic data and selected structural parameters for **4**. Different with **1** and **3** only containing one crystallographic independent Mo site, there are five crystallographic independent Mo sites in **4**. All the Mo sites in **4** are revealed to be more close to the square antiprism (SAPR) geometry with continuous shape measurement (CShM) values of 1.328(Mo1)/0.382(Mo2)/0.992(Mo3)/1.117(Mo4)/0.280(Mo5), respectively. The incorporation of Cs^+ leads to a different geometry for Mo sites than the triangular dodecahedron (TDD) geometry observed in **1** and **3**, proving that the geometry of Mo sites is easily influenced by the chemical environment.

For **4**, average bond distances of Mo-C and C-N are 2.18(3)/2.18(3)/2.16(3)/2.15(3)/2.16(3) Å and 1.15(4)/1.14(4)/1.15(4)/1.17(4)/1.17(4) Å, respectively, and the average Mo-C-N bond angles equal to 176(3)/176(3)/174(3)/177(3)/176(3)°. The minimum Mo…Mo distances are 8.56/7.73/7.83/7.83/7.50 Å, which are even longer than that for **3**.

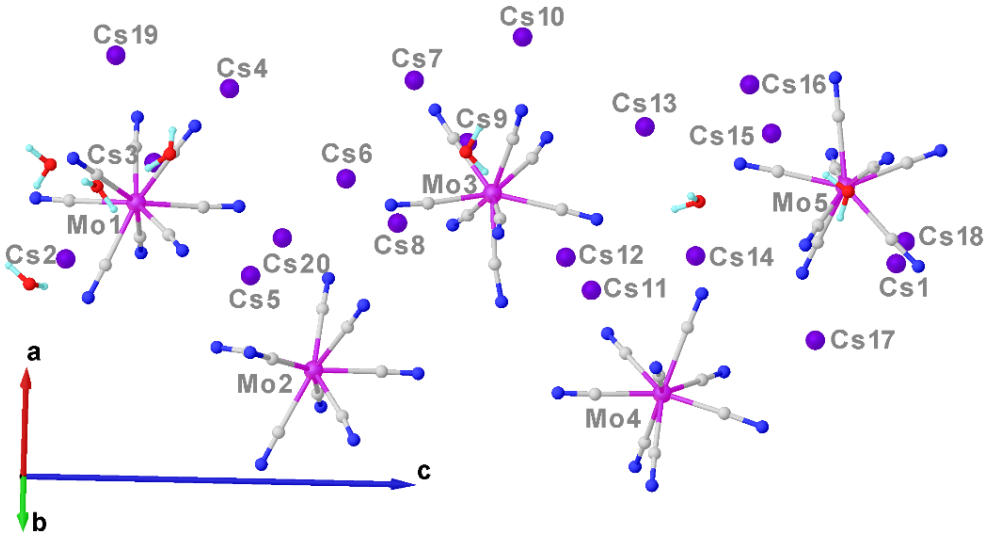

Figure II. 26 ORTEP diagram of molecule fragment of **4** with selected atoms labelling. Color codes: N, blue; C, grey; O, red; H, light blue; Cs, purple; Mo, pink.

Table II. 16 Crystal data, data collection, and refine parameters for **4**.

Compound	**4**
Formula	$Cs_{20}Mo_5C_{40}N_{40}O_7H_{14}$
$D_{calc.}$/g cm^{-3}	3.003
μ/mm^{-1}	8.264
Formula Weight/g mol^{-1}	4290.95
T/K	120(2)
Crystal System	orthorhombic
Space Group	$Pna2_1$
a/Å	18.0192(9)
b/Å	9.3369(5)
c/Å	56.412(3)
V/Å^3	9491.0(9)
Z	4
Z'	1
Wavelength/Å	0.71073
Radiation type	MoK_a
Q_{min}/°	2.211
Q_{max}/°	26.432
Measured Refl.	21544
Independent Refl.	10399
Reflections with I > 2(I)	10126
R_{int}	0.0215
Parameters	470
Restraints	1
Largest Peak	4.752
Deepest Hole	-3.412
GooF	1.066
wR_2 (all data)	0.1187
wR_2	0.1180
R_1 (all data)	0.0554
R_1	0.0540
Flack Parameter	0.040(8)
Hooft Parameter	0.040(9)
S_{SAPR}	1.328/0.382/0.992/1.117/0.280
S_{TDD}	1.384/2.019/1.543/1.303/1.871

S is continuous shape measurement (CShM) value. SAPR and TDD represent square antiprism and triangular dodecahedron, respectively.

Table II. 17 Selected bond lengths and angles for $[Mo^{IV}(CN)_8]^{4-}$ anion in **4**.

Atoms		**Length/Å**	**Atoms**		**Length/Å**	**Atoms**			**Angle/°**
Mo1	C1	2.21(4)	N1	C1	1.10(5)	N1	C1	Mo1	177(3)
Mo1	C2	2.18(3)	N2	C2	1.14(4)	N2	C2	Mo1	176(3)
Mo1	C3	2.19(3)	N3	C3	1.17(5)	N3	C3	Mo1	174(3)
Mo1	C4	2.18(3)	N4	C4	1.12(4)	N4	C4	Mo1	174(4)
Mo1	C5	2.16(3)	N5	C5	1.12(4)	N5	C5	Mo1	176(3)
Mo1	C6	2.17(4)	N6	C6	1.15(4)	N6	C6	Mo1	175(2)
Mo1	C7	2.13(3)	N7	C7	1.18(4)	N7	C7	Mo1	176(4)
Mo1	C8	2.18(3)	N8	C8	1.18(4)	N8	C8	Mo1	176(3)
Average		2.18(3)	Average		1.15(4)	Average			176(3)
Mo2	C9	2.22(5)	N9	C9	1.08(5)	N9	C9	Mo2	172(3)
Mo2	C10	2.19(3)	N10	C10	1.13(4)	N10	C10	Mo2	175(2)
Mo2	C11	2.14(4)	N11	C11	1.20(5)	N11	C11	Mo2	178(4)
Mo2	C12	2.19(3)	N12	C12	1.10(4)	N12	C12	Mo2	175(4)
Mo2	C13	2.21(3)	N13	C13	1.14(4)	N13	C13	Mo2	177(3)
Mo2	C14	2.15(4)	N14	C14	1.15(4)	N14	C14	Mo2	178(2)
Mo2	C15	2.17(3)	N15	C15	1.15(4)	N15	C15	Mo2	176(3)
Mo2	C16	2.14(2)	N16	C16	1.17(4)	N16	C16	Mo2	178(3)
Average		2.18(3)	Average		1.14(4)	Average			176(3)
Mo3	C17	2.19(3)	N17	C17	1.14(4)	N17	C17	Mo3	175(3)
Mo3	C18	2.16(3)	N18	C18	1.14(4)	N18	C18	Mo3	176(3)
Mo3	C19	2.11(4)	N19	C19	1.20(4)	N19	C19	Mo3	175(2)
Mo3	C20	2.17(2)	N20	C20	1.19(3)	N20	C20	Mo3	172(3)
Mo3	C21	2.17(2)	N22	C22	1.11(5)	N21	C21	Mo3	171(3)
Mo3	C22	2.19(4)	N21	C21	1.17(3)	N22	C22	Mo3	174(2)
Mo3	C23	2.16(3)	N23	C23	1.11(4)	N23	C23	Mo3	177(4)
Mo3	C24	2.16(3)	N24	C24	1.11(4)	N24	C24	Mo3	170(4)
Average		2.16(3)	Average		1.15(4)	Average			174(3)
Mo4	C25	2.17(3)	N25	C25	1.13(4)	N25	C25	Mo4	177(3)
Mo4	C26	2.17(3)	N26	C26	1.15(4)	N26	C26	Mo4	176(2)
Mo4	C27	2.12(5)	N27	C27	1.16(5)	N27	C27	Mo4	176(3)
Mo4	C28	2.19(3)	N28	C28	1.16(4)	N28	C28	Mo4	178(4)
Mo4	C29	2.18(3)	N29	C29	1.17(4)	N29	C29	Mo4	177(3)
Mo4	C30	2.05(4)	N30	C30	1.25(5)	N30	C30	Mo4	174(2)
Mo4	C31	2.18(3)	N31	C31	1.14(4)	N31	C31	Mo4	177(3)
Mo4	C32	2.17(3)	N32	C32	1.18(4)	N32	C32	Mo4	178(3)
Average		2.15(3)	Average		1.17(4)	Average			177(3)

(continue of Table II. 17)

Mo5	C33	2.12(5)	N33	C33	1.18(5)	N33	C33	Mo5	177(2)
Mo5	C34	2.17(3)	N34	C34	1.14(4)	N34	C34	Mo5	176(2)
Mo5	C35	2.16(3)	N35	C35	1.16(4)	N35	C35	Mo5	176(3)
Mo5	C36	2.16(4)	N36	C36	1.17(5)	N36	C36	Mo5	176(4)
Mo5	C37	2.16(3)	N37	C37	1.16(4)	N37	C37	Mo5	177(3)
Mo5	C38	2.14(4)	N38	C38	1.19(5)	N38	C38	Mo5	176(2)
Mo5	C39	2.18(3)	N39	C39	1.18(4)	N39	C39	Mo5	178(3)
Mo5	C40	2.15(2)	N40	C40	1.19(3)	N40	C40	Mo5	173(3)
Average		2.16(3)	Average		1.17(4)	Average			176(3)

II.2.3.1.2 Photomagnetic studies of $Cs_{20}[Mo(CN)_8]_5 \cdot 7H_2O$ (4)

The ground state of **4** is diamagnetic in agreement with 2 electrons paired in the lowest-energy d_{z2} orbital in SAPR geometry. When **4** was irradiated with 405 nm at 10 K, the value of χT reached 0.6 cm^3 mol^{-1} K after 42 hours of irradiation (Figure II. 27). The final photoconversion rate is comparable with **3**, but the duration of irradiation is longer than **1** and **3**. Then the light was switched off to measure low-temperature magnetizations and the temperature dependence of the χT from 2 K to 300 K. The non-superposed reduced magnetizations suggest anisotropy in the photo-induced state but the anisotropy appears much smaller than the ones found for **1** and **3**, because the curves at different temperatures are less separated. The shape of the thermal relaxation of the χT curve is somehow similar to **3**, but the appearance of two relaxation steps is not so evident and the fraction of the first step also becomes much smaller. Similarly to **3**, the complete relaxation is observed around 250 K.

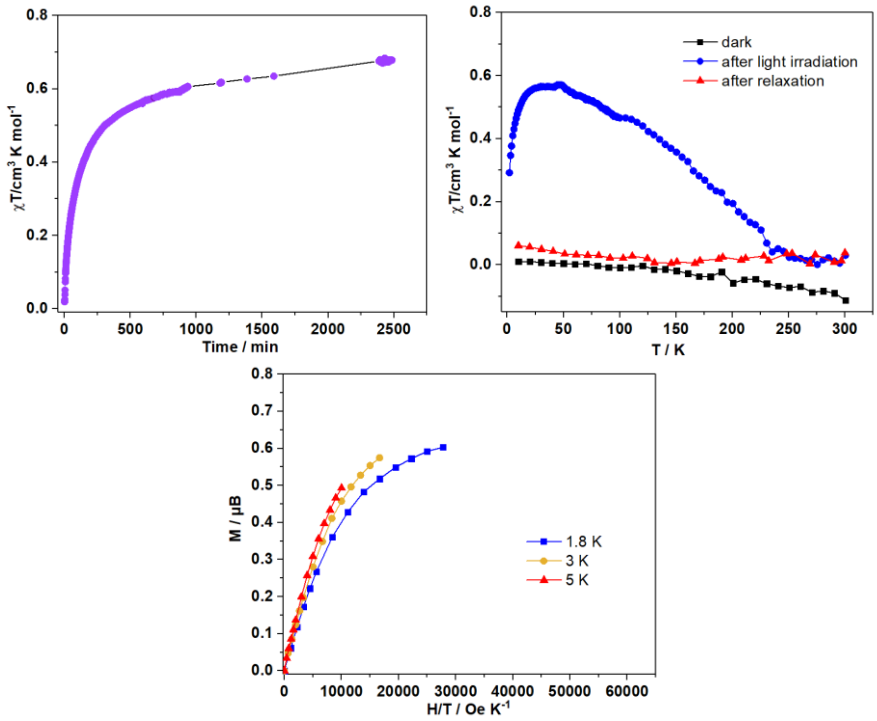

Figure II. 27 (Top left) Time dependence of the χT for **4** measured at 10 K, 1 T with continuous 405 nm blue light irradiation (The discontinuous curve is due to shutdown of magnetic field when the helium level was too low in the machine while the light irradiation at 10 K has been kept). (Top right) χT = f(T) plots of **4** measured in the dark before light irradiation, after 405 nm irradiation and after heating to 300 K. (Below) Reduced magnetizations at different temperatures (1.8 K, 3 K, and 5 K) in the photo-excited state.

II.2.3.1.3 Discussion on the $Cs_{20}[Mo(CN)_8]_5 \cdot 7H_2O$

The incorporation of Cs^+ can greatly affect crystal structure and the photomagnetic properties. Both the crystal structure and the coordination geometry of molybdenum are different with K^+ and Rb^+ compounds. The relaxation temperature at 250 K is similar to Rb^+ compound, but without a net first relaxation step around 65 K. The different photomagnetic behaviors for Cs^+ compound may be originated from the even less dense crystal structure, which provides more space for the occurence of isomerization of cyanide ligand.

II.2.3.2 Investigation of $Na_4[Mo(CN)_8] \cdot 4H_2O$ (5) and $Li_2K_2[Mo(CN)_8] \cdot 5H_2O$ (6)

The replacement of K^+ with Na^+ leads to the successful preparation of $Na_4[Mo(CN)_8] \cdot 4H_2O$ (**5**) (Table II. 22 and Table II. 23), but no significant photomagnetic effect has been observed. The reason may lie in quite dense crystal structure as shown by the minimum Mo…Mo distance around 6.58 Å, which is much smaller than previous described compounds. These short distances may prevent the Mo-CN bond breaking. The fully replacement of K^+ by Li^+ is not successful with only the preparation of $Li_2K_2[Mo(CN)_8] \cdot 5H_2O$ (**6**). No photomagnetic investigation has been performed for the partial K^+ substitution by Li^+ compound due to low yield. The detail for crystal structure and photomagnetic measurements for **5** and **6** is shown in supporting materials (II.5.6 Investigation of $Na_4[Mo(CN)_8] \cdot 4H_2O$ (**5**) and $Li_2K_2[Mo(CN)_8] \cdot 5H_2O$ (**6**)).

II.2.4 Discussions on the $A_4[Mo(CN)_8] \cdot xH_2O$ (A = Alkali cations)

Table II. 18 A summary of structural parameters and photomagnetic properties for $A_4[Mo(CN)_8] \cdot xH_2O$ (A = Alkali cations).

Compounds	**1**	**3**	**4**	**5**	**6**
T/K	10 K	10 K	120 K	150 K	150 K
S.G.	*Pnma*	*Pnma*	$Pna2_1$	*P*-1	$P2_1/n$
S_{SAPR}	2.990	3.015	1.328/0.382/0.992/1.117/0.280	0.359	2.060
S_{TDD}	0.250	0.286	1.384/2.019/1.543/1.303/1.871	1.858	0.349
Mo-C $_{av.}$/Å	2.161(10)	2.162(5)	2.18(3)/2.18(3)/2.16(3)/2.15(3)/2.16(3)	2.1599(11)	2.154(3)
C-N $_{av.}$/Å	1.155(3)	1.159(6)	1.15(4)/1.14(4)/1.15(4)/1.17(4)/1.17(4)	1.1522(15)	1.154(3)
Mo-C-N $_{av.}$/°	177.5(11)	177.5(4)	176(3)/176(3)/174(3)/177(3)/176(3)	176.10(10)	177.9(3)
$d_{Mo...Mo}$/Å	7.53	7.81	8.56/7.73/7.83/7.83/7.50	6.58	--
Photomagnetic properties	$\Delta\chi T$ = 0.37 cm^3 mol^{-1} K; T_{Relax} = 65 K	$\Delta\chi T$ = 0.6 cm^3 mol^{-1} K; T_{Relax} = 75 K and 250 K	$\Delta\chi T$ = 0.6 cm^3 mol^{-1} K; T_{Relax} = 250 K	--	--

(T_{Relax} = temperature for which the system is back to its initial state)

By investigation of the photomagnetic properties of $A_4[Mo(CN)_8] \cdot xH_2O$ ionic salts, fruitful insights have been gained for the photomagnetic mechanisms (Table II. 18).

1. The in-depth investigation of $K_4[Mo(CN)_8] \cdot 2H_2O$ provides a solid experimental proof for the observation of photoinduced triplet state of the Mo site with a bond breakage of one Mo-C bond. This unprecedent finding has been complemented by the results of theoretical calculation and the photochemical isolation of $[K(crypt\text{-}222)]_3[Mo^{IV}(CN)_7] \cdot 3CH_3CN$ in solution.
2. The replacement of K^+ with Rb^+ allows the conservation of the overall structure with nearly identical structural features. Importantly, the bond breakage of one Mo-C bond in photoexcited state is observed again for the Rb^+ compound. Despite their structural similarities, Rb^+ compound displays a thermal relaxation in two steps: the

first step is similar as K^+ compound around 65 K, and the second one occurs at 250 K. The isomerization of the Mo-CN for the removed cyanide ligand might explain the stepwise relaxation behavior.

3. The replacement of K^+ with Cs^+ drastically modifies the overall structure. The relaxation temperature for Cs^+ compound is also 250 K but without clear stepwise relaxation behavior as observed in Rb^+.
4. The replacement of K^+ with Na^+ also modifies the overall structure, accompanied with the loss of the photomagnetic properties.

The occurrence of bond breakage of Mo-C and/or isomerization of the broken cyanide ligand during relaxation probably needs free space in the structure. Our studies show a strong dependence of the photomagnetic effect with the nature of alkali cation. The reason may because of the bigger size of alkali cations such as Rb^+ and Cs^+, affording more free space in the structure. Further experimental evidences deriving from synchrotron X-ray radiation, IR spectra and UV-Vis spectra are needed to corroborate our hypothesis for the isomerization of cyanide ligand.

II.3 Studies of $A_4[W(CN)_8]\cdot xH_2O$ (A = K^+, Rb^+ and Cs^+)

The effect of alkali cation on photomagnetic properties has also been investigated for tungsten analogues. $K_4W^{IV}(CN)_8\cdot 2H_2O$ (**7**) has been synthesized successfully by following the procedure reported in the literature.[40] **RbW** (**8**) and **KCsW** (**9**) have been synthesized in an analogous way to the molybdenum analogues (Scheme II. 2). Despite numerous attempts, it is not possible to achieve the full replacement of K^+ by Cs^+.

$$K_4W(CN)_8\cdot 2H_2O + 2CdCl_2 \xrightarrow{H_2O} Cd_2W(CN)_8\cdot xH_2O\downarrow + 4KCl$$
$$Cd_2W(CN)_8\cdot xH_2O + 4RbOH \xrightarrow{H_2O} Rb_4W(CN)_8\cdot 2H_2O + 2Cd(OH)_2\downarrow$$

Scheme II. 2 The approach followed to prepare the solution of $Rb_4[W(CN)_8]\cdot H_2O$ by replacement of potassium cation with rubidium cation.

The good agreement for the experimental powder X-ray diffraction (PXRD) patterns and the calculated ones for **7**, suggests the phase purity of the synthesized batches (II.5 Supporting materials). While the experimental PXRD pattern is globally consistent with the calculated one for **8**, the unexpected peaks are probably due to the existence of another chiral form of crystals. As observed for molybdenum analogue, **9** is prone to absorb the water in air during the preparation of the powder X-ray diffraction sample, which results in the discrepancy between the experimental powder X-ray diffraction pattern and the theoretical one. UV-Vis spectra and Infrared spectra (IR) of compounds in this subsection are very similar with that for molybdenum analogue. There is a notable shifting to low cyanide stretching frequencies in IR spectra for tungsten analogues, probably caused by the back-donation of electrons from W^{4+} to unoccupied $2\pi^*$ orbitals of cyanide ligand.

The detail for crystal structure and photomagnetic measurements are shown in supporting materials (II.5.7 Investigation of $A_4[W(CN)_8]\cdot xH_2O$ (A = Alkali cations)). Unfortunately, **7**, **8** and **9** are not photomagnetic.

In Table II. 19, the coordination geometry for $[W(CN)_8]^{4-}$, average bond lengths and angles are summarized. Even $K_4W^{IV}(CN)_8\cdot 2H_2O$ (**7**) is isostructural with **1**, the average W-C bond length 2.157(4) Å at room temperature is shorter than that for **1** with 2.161(10) Å at 10 K. The reason may be that the ionic radius for Mo^{IV} and W^{IV} are quite close owing to the lanthanide contraction effect. The short W-C bond lengths might explain the absence of photomagnetic properties for tungsten analogues.

Table II. 19 Selected structural information for **7**, **8** and **9**.

Compounds	**7**	**8**	**9**
T/K	293(2)	150(2)	293(2)
S_{SAPR}	2.964	2.043	3.369/0.149/1.113
S_{TDD}	0.220	0.325	3.922/2.500/1.356
W-C $_{av.}$/Å	2.157(4)	2.159(10)	2.27(6)/2.17(4)/2.18(2)
C-N $_{av.}$/Å	1.148(5)	1.149(13)	1.06(9)/1.12(3)/1.13(3)
W-C-N $_{av.}$/°	177.6(4)	176.8(10)	170(7)/178(2)/176.8(2)

S is continuous shape measurement (CShM) value. SAPR and TDD represent square antiprism and triangular dodecahedron, respectively.

II.4 Conclusion and perspectives

Previous studies of photomagnetic properties of mononuclear systems involving $[Mo^{IV}(CN)_8]^{4-}$ are only limited to several cases. The understanding of photomagnetic mechanisms is not clearly established.

In this chapter, we focus on the study of the ionic salts in which the $[M^{IV}(CN)_8]^{4-}$ is compensated with different alkali cations. Remarkably, the photocrystallography studies at 10 K for K^+ and Rb^+ compounds unequivocally reveal the photoinduced dissociation of Mo-C bond for the photoinduced triplet state. We have shown that the incorporation of $[Mo^{IV}(CN)_8]^{4-}$ with different alkali cations (K^+, Rb^+, Cs^+ and Na^+) leads to different photomagnetic behaviors with markedly different relaxation temperatures. The increase of the size of the alkali cations results in the observation of higher relaxation temperatures.

We succeed to clarify several scientific problems by changing the alkali cation part:

1. The geometry of $[Mo(CN)_8]^{4-}$ is highly prone to be influenced by the chemical environment, while both TDD and SAPR geometries of $[Mo(CN)_8]^{4-}$ are photoresponsive.

2. The favorable intermolecular interaction and less dense crystal packing seem critical for the photomagnetic properties, but such conclusion needs further investigations.

3. The longer Mo-C bond length might facilitate the observation of the photomagnetic properties, as shown by the cleavage of longest Mo-C3 (2.176(3) Å) bond in the photoexcited state for $K_4[Mo(CN)_8]\cdot 2H_2O$.

4. Despite the similarities between Mo^{IV} and W^{IV} compounds, the ionic salts for which the anionic $[W^{IV}(CN)_8]^{4-}$ unit is compensated with different alkali cations are not photomagnetic.

For next steps, to gain more insights into the structure and photomagnetic property relationship for $[Mo^{IV}(CN)_8]^{4-}$, the exploration of other type of cations with judicious choice to change the spatial arrangement of photomagnetic $[M^{IV}(CN)_8]^{4-}$ and the cooperativity is highly demanded. We expect to understand how does $[Mo^{IV}(CN)_8]^{4-}$ exactly evolve upon light irradiation with direct evidences deriving from synchrotron X-ray radiation, IR spectra and UV-Vis spectra in the future. Further studies are also needed to understand why isostructural Mo and W compounds show very different photomagnetic behaviors.

II.5 Supporting materials

II.5.1 Synthesis

Preparation of KMo (1).

$K_4Mo^{IV}(CN)_8 \cdot 2H_2O$ (**1**) has been synthesized successfully by following the procedure according to the literature.[40]

Preparation of $[K(crypt\text{-}222)]_3[Mo^{IV}(CN)_7]\cdot 3CH_3CN$ (2).

The preparation of $[K(crypt\text{-}222)]_3[Mo^{IV}(CN)_7]\cdot 3CH_3CN$ (**2**) and all manipulations involving this compound were performed using the moisture and oxygen free glovebox system (Inert® PureLab HE).

$K_4[Mo^{IV}(CN)_8]\cdot 2H_2O$ (50 mg, 1.0 mmol) and Kryptofix®222 (160 mg, 4.25 mmol) were dissolved in 5 mL of dry CH_3CN in a 20 mL glass vial. The yellow solution was irradiated for 12 hours with a white LED light under an inert gas atmosphere (rigorous exclusion of oxygen is necessary). After that time the vial was placed inside a 100 mL glass jar filled with 50 mL of dry diethyl ether for the slow vapor diffusion crystallization. Colorless plate crystals of $[K(crypt\text{-}222)]_3[Mo^{IV}(CN)_7]\cdot 3CH_3CN$ (**2**) were obtained within one week. The crystals of $[K(crypt\text{-}222)]_3[Mo^{IV}(CN)_7]\cdot 3CH_3CN$ (**2**) are prone to partial desolvation.

Preparation of RbMo (3).

The preparation of $A_4[Mo^{IV}(CN)_8]$ has followed the reported approach.[13] First, $Cd_2[Mo^{IV}(CN)_8]\cdot xH_2O$ was prepared after the filtration of the mixture of the 3 mL solution $K_4Mo^{IV}(CN)_8]\cdot 2H_2O$ (150 mg, 3.0 mmol) and the 3 mL solution $CdCl_2$ (114 mg, 6.2 mmol).

Then we mixed the obtained $Cd_2[Mo^{IV}(CN)_8]\cdot xH_2O$ with 2 mL RbOH solution (143 mg, 1.4 mmol) and stirred it until all the yellow $Cd_2[Mo^{IV}(CN)_8]\cdot xH_2O$ changed to white $Cd(OH)_2$ precipitate. After filtration, the yellow solution was evaporated slowly at room temperature to get yellow bulk crystal of **3**.

Preparation of CsMo (4).

First, $Cd_2[Mo^{IV}(CN)_8]\cdot xH_2O$ was prepared after the filtration of the mixture of the 3 mL solution $K_4Mo^{IV}(CN)_8]\cdot 2H_2O$ (150 mg, 3.0 mmol) and the 3 mL solution $CdCl_2$ (114 mg, 6.2 mmol).

Then we mixed the obtained $Cd_2[Mo^{IV}(CN)_8]\cdot xH_2O$ with 2 mL CsOH solution (210 mg, 1.4 mmol) and stirred it until all the yellow $Cd_2[Mo^{IV}(CN)_8]\cdot xH_2O$ changed to white $Cd(OH)_2$ precipitate. After filtration, the yellow solution was evaporated slowly at room temperature to get yellow bulk crystal of **4**.

Preparation of NaMo (5).

First, $Cd_2[Mo^{IV}(CN)_8]\cdot xH_2O$ was prepared after the filtration of the mixture of the 3 mL solution $K_4Mo^{IV}(CN)_8]\cdot 2H_2O$ (150 mg, 3.0 mmol) and the 3 mL solution $CdCl_2$ (114 mg, 6.2 mmol).

Then we mixed the obtained $Cd_2[Mo^{IV}(CN)_8]\cdot xH_2O$ with 2 mL NaOH solution (57 mg, 1.43 mmol) and stirred it until all the yellow $Cd_2[Mo^{IV}(CN)_8]\cdot xH_2O$ changed to white $Cd(OH)_2$ precipitate. After filtration, the yellow solution was evaporated slowly at room temperature to get yellow bulk crystal of **5**.

Preparation of LiMo (6).

First, $Cd_2[Mo^{IV}(CN)_8]\cdot xH_2O$ was prepared after the filtration of the mixture of the 3 mL solution of $K_4Mo^{IV}(CN)_8]\cdot 2H_2O$ (150 mg, 3.0 mmol) and the 3 mL solution of $CdCl_2$ (114 mg, 6.2 mmol).

Then we mixed the obtained $Cd_2[Mo^{IV}(CN)_8]\cdot xH_2O$ with 2 mL LiOH solution (60 mg, 1.43 mmol) and stirred it until all the yellow $Cd_2[Mo^{IV}(CN)_8]\cdot xH_2O$ changed to white $Cd(OH)_2$ precipitate. After filtration, the yellow solution was evaporated slowly at room temperature to get yellow bulk crystal of **6**.

Preparation of KW (7), RbW (8) and KCsW (9).

KW (**7**) has been synthesized successfully by following the procedure according to the

literature.[40] **RbW** (**8**), **KCsW** (**9**) were synthesized in an analogous way to **RbMo** (**3**), **CsMo** (**4**), but with $K_4Mo^{IV}(CN)_8 \cdot 2H_2O$ replaced by $K_4W^{IV}(CN)_8 \cdot 2H_2O$.

II.5.2 Powder X-ray diffraction analysis

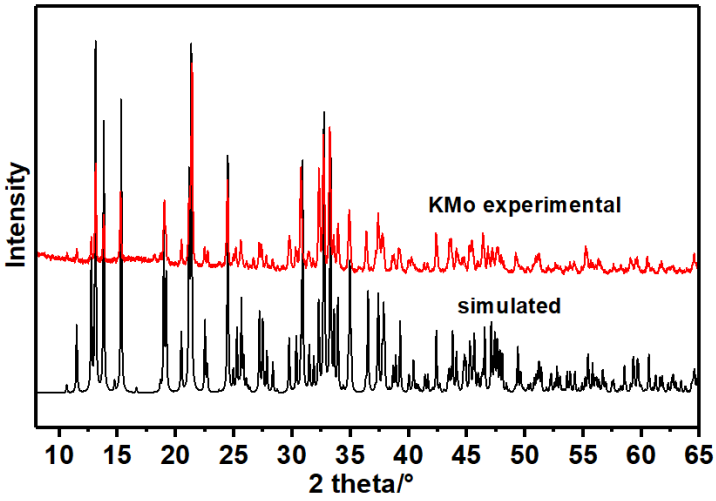

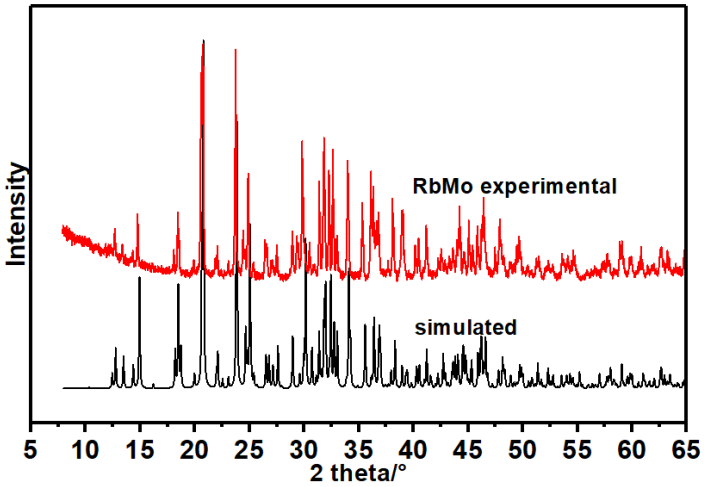

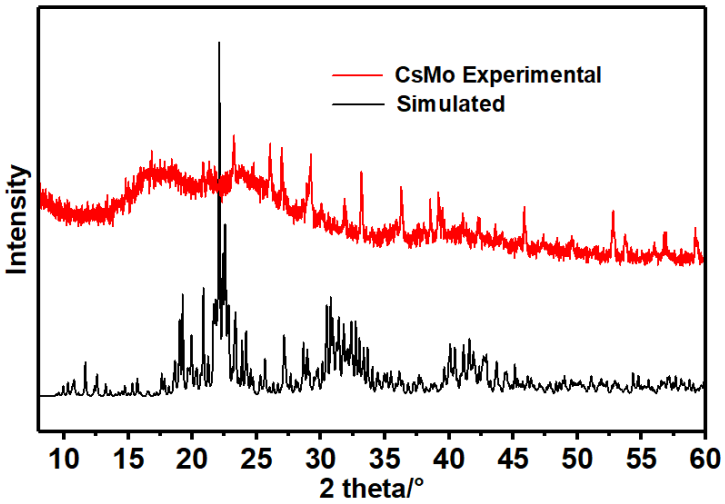

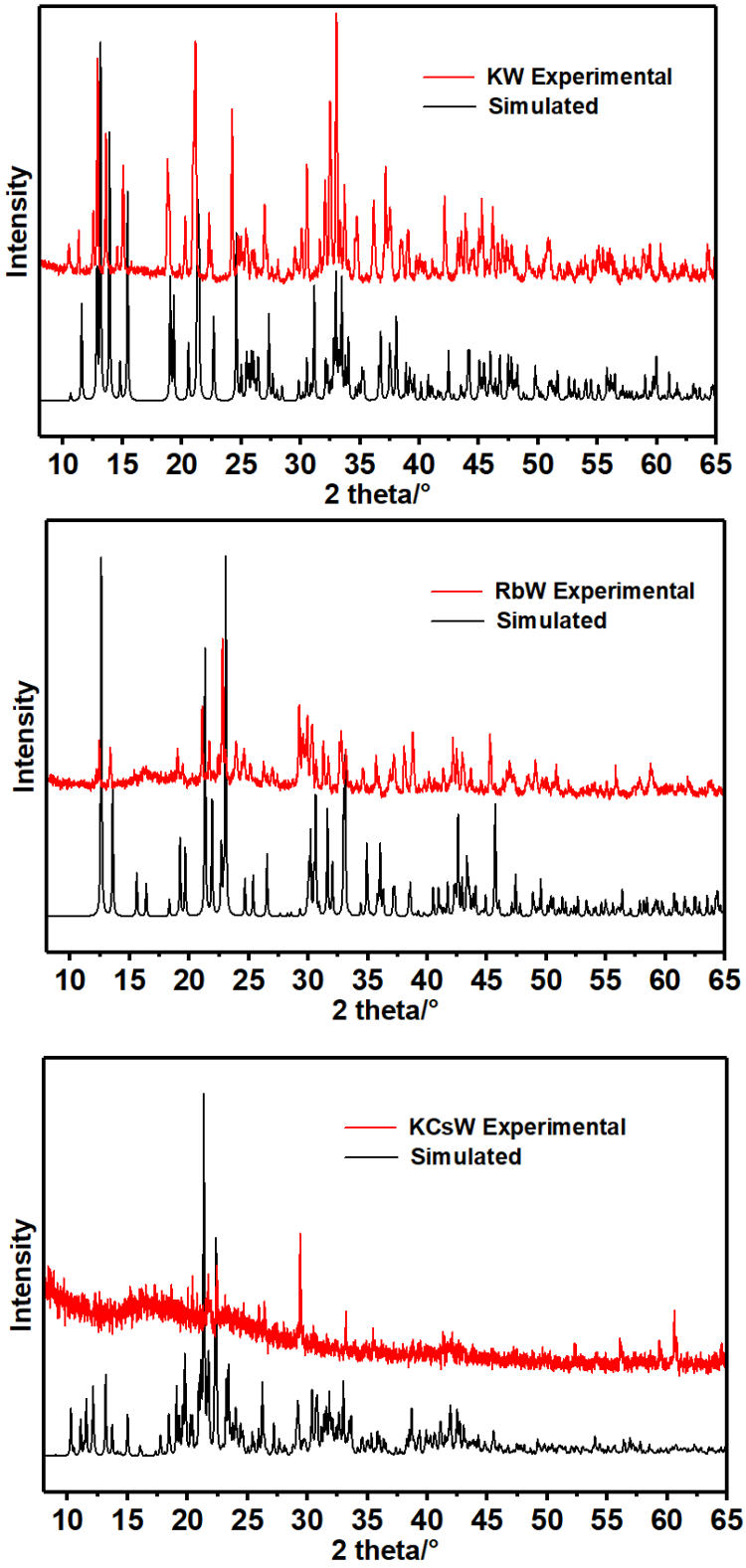
KW Experimental
Simulated
Intensity
10 15 20 25 30 35 40 45 50 55 60 65
2 theta/°
RbW Experimental
Simulated
Intensity
10 15 20 25 30 35 40 45 50 55 60 65
2 theta/°
KCsW Experimental
Simulated
Intensity
10 15 20 25 30 35 40 45 50 55 60 65
2 theta/°

II.5.3 Optical measurements

Table II. 20 The possible assignment of optical spectra according to literature.[53]

Region	Assignment
300-400 nm	LF bands of $[Mo(CN)_8]^{4-}$
450-600 nm	MMCT bands of Cu(II)–Mo(IV) pair
600-800 nm	d–d bands of Cu(II)

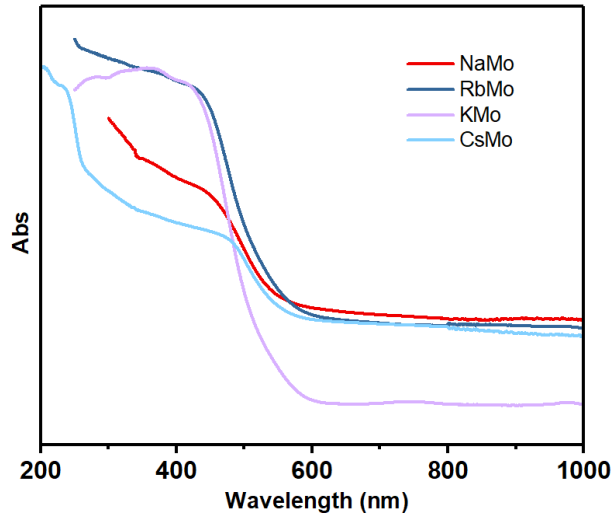

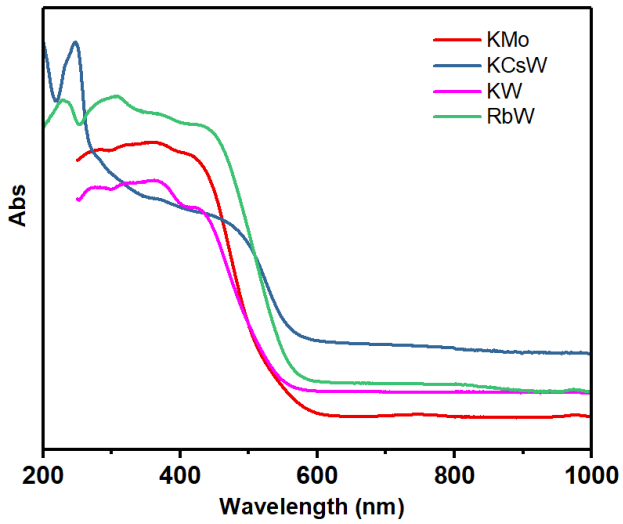

II.5.4 IR spectra

Table II. 21 Possible attribution of IR vibration according to literature.[53]

Region	Assignment
Broad peaks in the 3700 – 2500 cm^{-1}	ν(O–H) stretching bands of water molecules
sharp peaks in the 3000 – 2750 cm^{-1}	ν(C–H) and ν(N–H) vibrations
2200 – 2100 cm^{-1}	Stretching bands ν(C≡N) of cyanide
1700 – 400 cm^{-1}	ν(C=O) and ν(C–O) stretching band, δ(O–H) bending bands of water and several other bands: δ(H–C–H), ν(N–C) and ν(C–C)

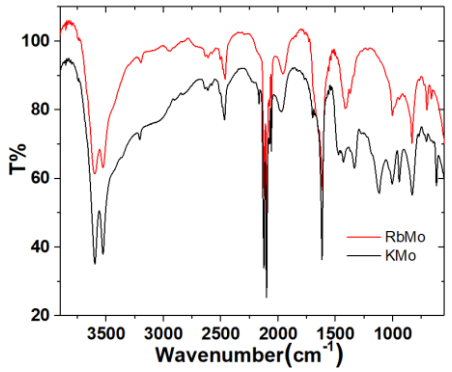
T%
Wavenumber(cm-1)
RbMo
KMo

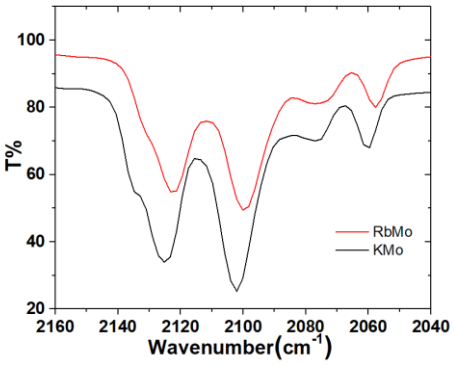
T%
Wavenumber(cm-1)
RbMo
KMo

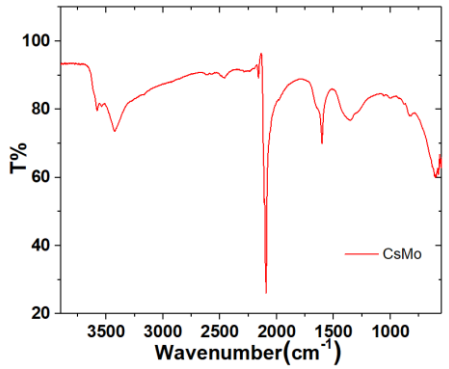
T%
Wavenumber(cm-1)
CsMo

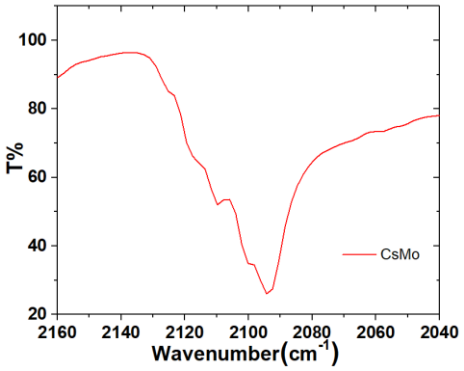
T%
Wavenumber(cm-1)
CsMo

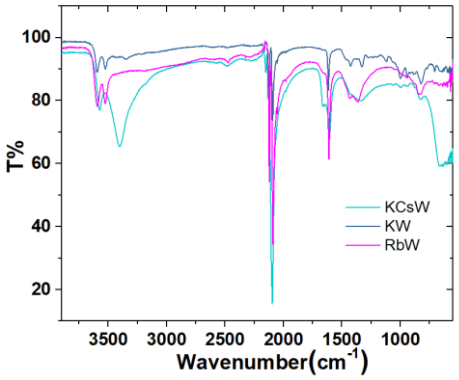
T%
Wavenumber(cm-1)
KCsW
KW
RbW

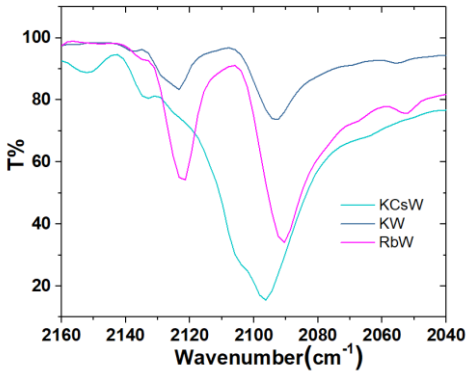
T%
Wavenumber(cm-1)
KCsW
KW
RbW

II.5.5 Thermogravimetric analysis

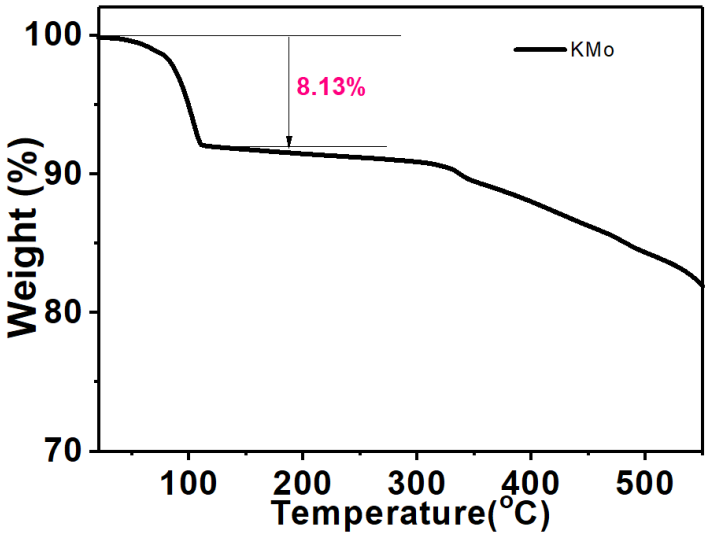

Theoretical weight loss of two water molecules per formula for **KMo** is 7.25%.

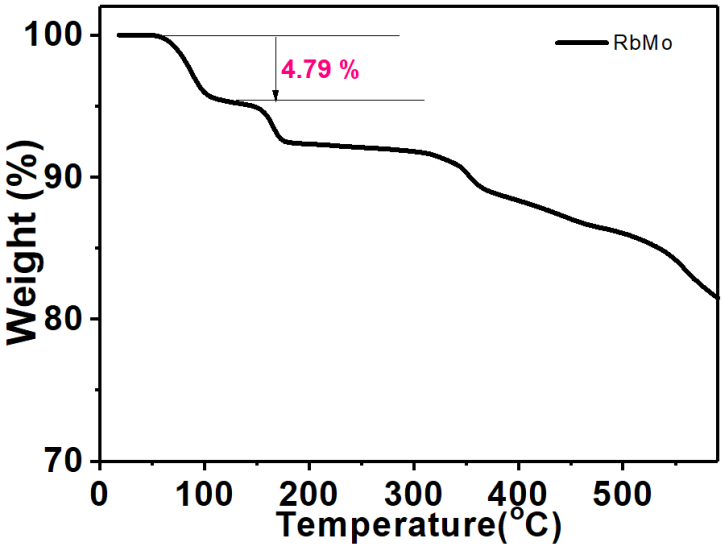

Theoretical weight loss of two water molecules per formula for **RbMo** is 5.28%.

II.5.6 Investigation of $Na_4[Mo(CN)_8]\cdot 4H_2O$ (5) and $Li_2K_2[Mo(CN)_8]\cdot 5H_2O$ (6)

II.5.6.1 Crystal structure of $Na_4[Mo(CN)_8]\cdot 4H_2O$ (5)

Table II. 22 Crystal data, data collection, and refine parameters for **5** and **6**.

Compound	**5**	**6**
Formula	$MoN_8Na_4O_4C_8H_8$	$C_8H_2K_2Li_2MoN_8O_5$
$D_{calc.}$/g cm^{-3}	1.830	1.713
μ/mm^{-1}	0.906	1.190
Formula Weight/g mol^{-1}	468.12	478.20
T/K	150(2)	150(2)
Crystal System	triclinic	monoclinic
Space Group	*P*-1	$P2_1/n$
a/Å	6.5766(3)	13.8700(10)
b/Å	9.0388(4)	9.1717(6)
c/Å	15.2863(7)	15.7372(10)
α/°	97.3760(10)	90
β/°	97.4710(10)	112.170(2)
γ/°	106.7380(10)	90
V/Å^3	849.54(7)	1853.9(2)
Z	2	4
Z'	1	1
Wavelength/Å	0.71073	0.71073
Radiation type	MoK_a	MoK_a
Q_{min}/°	2.390	1.672
Q_{max}/°	26.431	25.350
Measured Refl.	21028	23931
Independent Refl.	3478	3371
Reflections with I > 2(I)	3445	2541
R_{int}	0.0195	0.0397
Parameters	258	236
Restraints	0	0
Largest Peak	0.317	0.654
Deepest Hole	-0.367	-0.584
GooF	1.108	1.056
wR_2 (all data)	0.0306	0.0701
wR_2	0.0305	0.0665
R_1 (all data)	0.0117	0.0382
R_1	0.0116	0.0240
Flack Parameter	--	--
Hooft Parameter	--	--
S_{SAPR}	0.359	2.060
S_{TDD}	1.858	0.349

S is continuous shape measurement (CShM) value. SAPR and TDD represent square antiprism and triangular dodecahedron, respectively.

In **5**, crystal structure is determined as $[Mo(CN)_8]^{4-}$ complex surrounded by Na^+ and water molecules (Figure II. 28). The compound crystallizes in triclinic space group *P*-1, being different with the K^+ compound. The crystallographic data and selected bond lengths and angles are presented in Table II. 22 and Table II. 23. The Mo site is revealed to be more close to the square antiprism (SAPR) geometry with continuous shape measurement (CShM) value of 0.359. Average bond distances of Mo-C and C-N are 2.1599(11) and 1.1522(15) Å, respectively, and the average Mo-C-N bond angle equals to 176.10(10)°. The minimum Mo…Mo distance is 6.58 Å, which is much smaller than **1** and **3**.

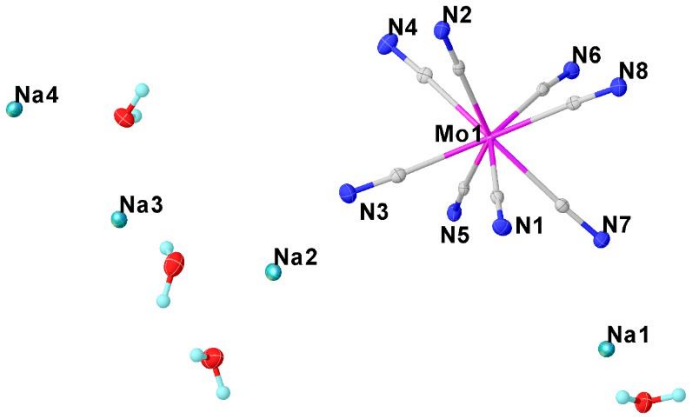

Figure II. 28 ORTEP diagram of molecule fragment of **5** with selected atoms labelling. Thermal ellipsoids of 50 % probability are shown.

Table II. 23 Selected bond lengths and angles for $[Mo^{IV}(CN)_8]^{4-}$ anion in **5**.

Atoms		**Length/Å**	**Atoms**		**Length/Å**		**Atoms**		**Angle/°**
Mo1	C1	2.1551(11)	N1	C1	1.1516(15)	N1	C1	Mo1	177.67(10)
Mo1	C2	2.1701(11)	N2	C2	1.1544(15)	N2	C2	Mo1	178.43(10)
Mo1	C3	2.1591(11)	N3	C3	1.1516(15)	N3	C3	Mo1	177.34(10)
Mo1	C4	2.1596(11)	C4	N4	1.1518(15)	N4	C4	Mo1	177.15(10)
Mo1	C5	2.1518(11)	N5	C5	1.1530(15)	N5	C5	Mo1	173.60(9)
Mo1	C6	2.1560(11)	N6	C6	1.1534(15)	N6	C6	Mo1	171.85(9)
Mo1	C7	2.1581(11)	N7	C7	1.1513(15)	N7	C7	Mo1	175.83(10)
Mo1	C8	2.1693(11)	N8	C8	1.1503(15)	N8	C8	Mo1	176.94(9)
Average		2.1599(11)	Average		1.1522(15)	Average			176.10(10)

II.5.6.2 Photomagnetic studies of $Na_4[Mo(CN)_8]\cdot 4H_2O$ (5)

When **5** was irradiated with 405 nm, the value of χT only increased from 0 to 0.025 cm^3 mol^{-1} K after 16 hours of irradiation (Figure II. 29). The saturation value of the paramagnetic signal is so small, which can be ignored. The temperature dependence of the χT for the photogenerated state from 2 K to 300 K has been measured. However, the rather small paramagnetic signal hinders the analysis of the photoexcited state components.

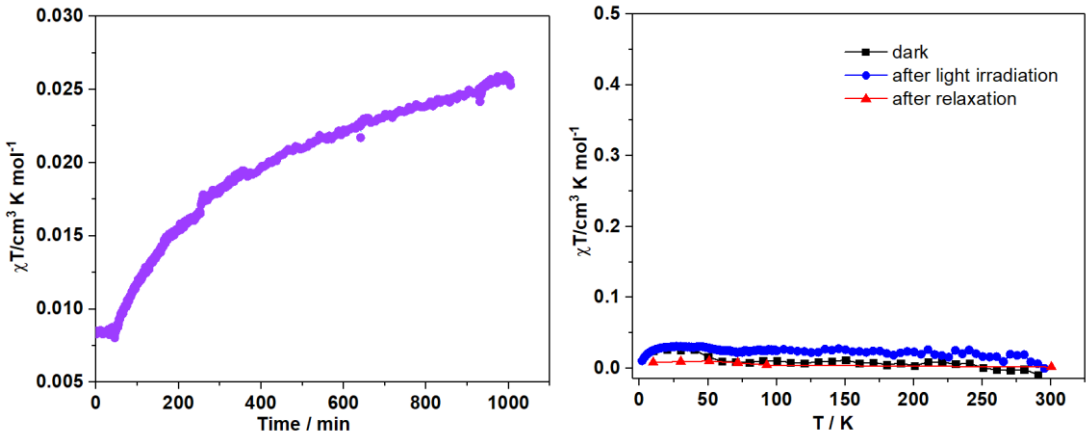

Figure II. 29 (Left) Time dependence of the χT for **5** measured at 10 K, 1 T with continuous 405 nm blue light irradiation. (Right) χT = f(T) plots of **5** measured in the dark before light irradiation, after 405 nm irradiation and after heating to 300 K.

II.5.6.3 Crystal structure of $Li_2K_2[Mo(CN)_8]\cdot 5H_2O$ (6)

In **6**, crystal structure determination reveals that one crystallographic independent $[Mo(CN)_8]^{4-}$ complex is surrounded by two Li^+, two K^+ and water molecules (Figure II. 30). **6** crystallizes in monoclinic space group $P2_1/n$. The crystallographic data and selected bond lengths and angles are presented in Table II. 22 and Table II. 24. The Mo site was revealed to be more close to triangular dodecahedron (TDD) geometry with continuous shape measurement (CShM) value of 0.349. Average bond distances of Mo-C and C-N are 2.154(3) and 1.154(3) Å, respectively, and the average Mo-C-N bond angle equals to 177.9(3)°. The low yield of **6** limits us to do further characterizations and photomagnetic test.

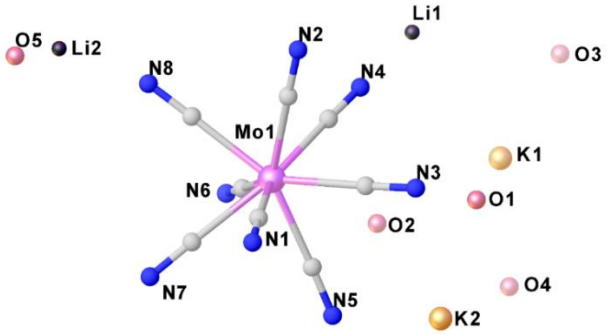

Figure II. 30 ORTEP diagram of molecule fragment of **6** with selected atoms labelling.

Table II. 24 Selected bond lengths and angles for $[Mo^{IV}(CN)_8]^{4-}$ anion in **6**.

Atoms		**Length/Å**	**Atoms**		**Length/Å**		**Atoms**		**Angle/°**
Mo1	C1	2.149(3)	C1	N1	1.155(3)	N1	C1	Mo1	176.1(3)
Mo1	C2	2.163(3)	C2	N2	1.156(3)	N2	C2	Mo1	175.1(2)
Mo1	C3	2.158(3)	C3	N3	1.152(3)	N3	C3	Mo1	178.4(2)
Mo1	C4	2.148(3)	N4	C4	1.150(4)	N4	C4	Mo1	178.3(2)
Mo1	C5	2.141(3)	C5	N5	1.157(4)	N5	C5	Mo1	178.2(2)
Mo1	C6	2.160(3)	C6	N6	1.153(3)	N6	C6	Mo1	179.6(3)
Mo1	C7	2.157(3)	C7	N7	1.152(3)	N7	C7	Mo1	178.3(3)
Mo1	C8	2.153(3)	N8	C8	1.153(3)	N8	C8	Mo1	179.0(3)
Average		2.154(3)	Average		1.154(3)	Average			177.9(3)

II.5.7 Investigation of $A_4[W(CN)_8]\cdot xH_2O$ (A = Alkali cations)

II.5.7.1 Crystal structure and photomagnetic measurements of $K_4[W(CN)_8]\cdot 2H_2O$ (7)

Single crystal X-ray studies reveal that **7** is isostructural with the corresponding analogue **1** (Figure II. 31). The average W-C bond length for **7** at room temperature is even significantly shorter than that for **1** at 10 K (Table II. 25 and Table II. 26).

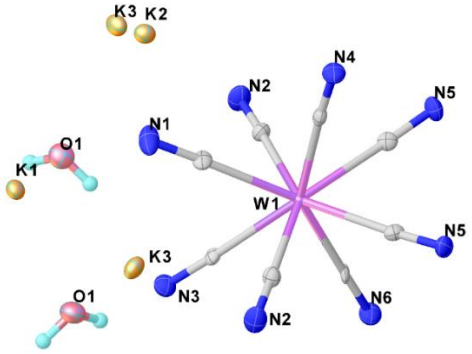

Figure II. 31 ORTEP diagram of molecule fragment of **7** with selected atoms labelling. Thermal ellipsoids of 50 % probability are shown.

Table II. 25 Selected bond lengths and angles for $[W^{IV}(CN)_8]^{4-}$ anion in **7**.

Atoms		Length/Å	Atoms		Length/Å	Atoms			Length/Å
W1	C1	2.148(5)	N1	C1	1.160(7)	N1	C1	W1	178.6(4)
W1	C2	2.140(3)	N2	C2	1.145(5)	N2	C2	W1	177.7(3)
W1	C3	2.171(5)	N3	C3	1.153(6)	N3	C3	W1	177.5(4)
W1	C4	2.154(5)	N4	C4	1.138(6)	N4	C4	W1	176.9(4)
W1	C5	2.174(3)	N5	C5	1.149(4)	N5	C5	W1	176.5(3)
W1	C6	2.151(4)	N6	C6	1.154(6)	N6	C6	W1	179.3(4)
Average		2.157(4)	Average		1.148(5)	Average			177.6(4)

The photomagnetic measurements has been realized for **7**. Drastically different with molybdenum analogue, **7** exhibits no photomagnetic effect (Figure II. 32).

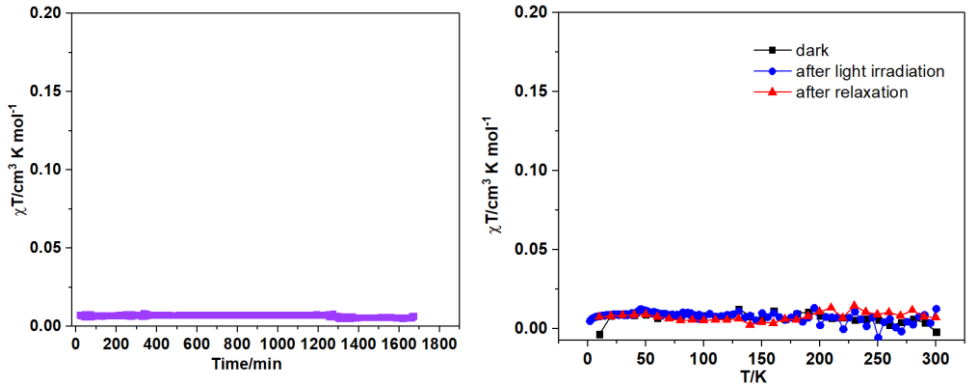

Figure II. 32 (Left) Time dependence of the χT for **7** measured at 10 K, 1 T with 405 nm blue light irradiation. (Right) χT = f(T) plots of **7** measured in the dark before light irradiation, after 405 nm irradiation and after heating to 300 K.

Table II. 26 Single crystal X-ray diffraction data and structure refinement parameters for $K_4[W(CN)_8]\cdot 2H_2O$ (**7**), $Rb_4[W(CN)_8]\cdot H_2O$ (**8**) and $K_6Cs_{16}[W(CN)_8]_5Cl_2\cdot 4H_2O$ (**9**).

Compound	**7**	**8**	**9**
Formula	$C_8H_4K_4N_8O_2W$	$C_8H_2N_8ORb_4W$	$C_{18}H_4ClCs_8K_3N_{18}O_2W_{2.5}$
$D_{calc.}$/g cm^{-3}	2.360	2.712	2.911
μ/mm^{-1}	8.052	16.787	11.905
T/K	293(2)	150(2)	293(2)
Crystal System	orthorhombic	tetragonal	monoclinic
Space Group	*Pnma*	$P4_32_12$	*C*2/*c*
a/Å	16.6310(3)	9.2271(8)	61.428
b/Å	11.4792(2)	9.2271(8)	9.295
c/Å	8.61746(18)	21.629(2)	18.107
α/°	90	90	90
β/°	90	90	106.14
γ/°	90	90	90
V/Å^3	1645.17(6)	1841.5(4)	9931.2
Z	4	4	8
Z'	0.5	0.5	1
Wavelength/Å	0.71073	0.71073	0.71073
Radiation type	MoK_a	MoK_a	MoK_a
Q_{min}/°	2.449	2.400	3.032
Q_{max}/°	30.773	25.026	25.681
Measured Refl.	47699	13738	107102
Independent Refl.	2680	1612	9423
Reflections with I > 2(I)	2522	1555	7420
R_{int}	0.0436	0.0376	0.0783
Parameters	129	107	508
Restraints	2	0	0
Largest Peak	0.995	1.704	3.032
Deepest Hole	-0.859	-0.920	-3.690
GooF	1.025	1.204	1.162
wR_2 (all data)	0.0568	0.0869	0.1774
wR_2	0.0554	0.0862	0.1688
R_1 (all data)	0.0226	0.0346	0.0916
R_1	0.0204	0.0331	0.0699
Flack Parameter	--	0.029(13)	--
Hooft Parameter	--	0.013(12)	--
S_{SAPR}	2.964	2.043	3.369/ 0.149/1.113
S_{TDD}	0.220	0.325	3.922/2.500/1.356

S is continuous shape measurement (CShM) value. SAPR and TDD represent square antiprism and triangular dodecahedron, respectively.

II.5.7.2 Crystal structure and photomagnetic measurements of $Rb_4[W(CN)_8]\cdot H_2O$ (8)

Single crystal X-ray studies revealed that **8** is not isostructural with the corresponding molybdenum analogue **3** with only one water molecule in the asymmetric unit (Figure II. 33). But **8** is very similar with **3** in terms of the building components. Instead of *Pnma* space group, **8** crystallizes in a chiral tetragonal space group $P4_32_12$. The average W-C bond length for **8** at 150 K is even significantly shorter than that for **3** at 10 K (Table II. 27).

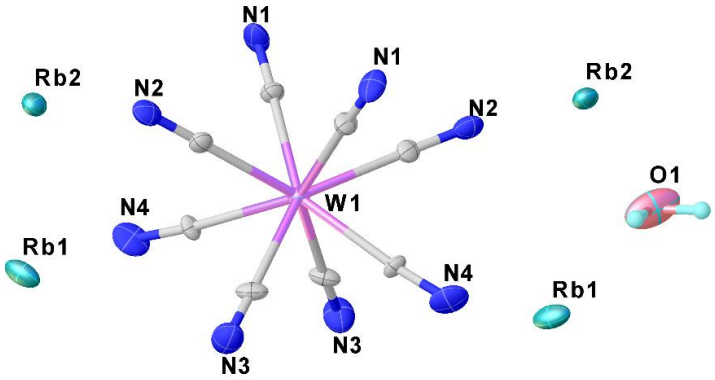

Figure II. 33 ORTEP diagram of molecule fragment of **8** with selected atoms labelling. Thermal ellipsoids of 50 % probability are shown.

Table II. 27 Selected bond lengths and angles for $[W^{IV}(CN)_8]^{4-}$ anion in **8**.

Atoms		**Length/Å**	**Atoms**		**Length/Å**		**Atoms**		**Angle/°**
W1	C1	2.158(9)	C1	N1	1.151(13)	N1	C1	W1	175.5(10)
W1	C2	2.158(11)	C2	N2	1.136(15)	N2	C2	W1	175.7(10)
W1	C3	2.171(9)	C3	N3	1.167(12)	N3	C3	W1	177.6(9)
W1	C4	2.150(9)	C4	N4	1.142(12)	N4	C4	W1	178.4(10)
Average		2.159(10)	Average		1.149(13)		Average		176.8(10)

The photomagnetic measurements have been realized for **8**. Drastically different with molybdenum analogue **3**, **8** exhibits no photomagnetic effect (Figure II. 34).

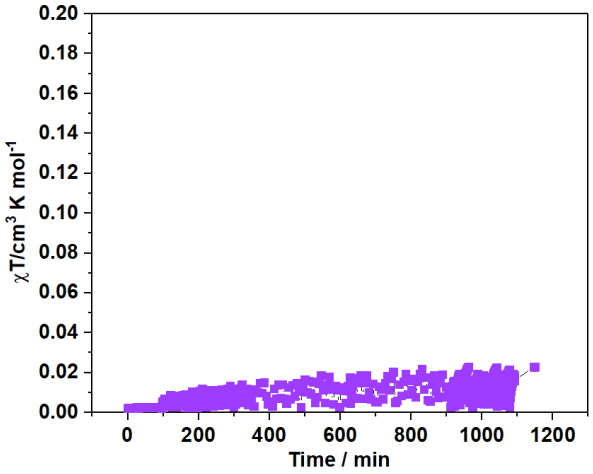

Figure II. 34 Time dependence of the χT for **8** measured at 10 K, 1 T with 405 nm blue light irradiation.

II.5.7.3 Crystal structure and photomagnetic measurements of $K_6Cs_{16}[W(CN)_8]_5Cl_2{\cdot}4H_2O$ (9)

As shown in Figure II. 35, crystal structure of **9** is revealed as $[W(CN)_8]^{4-}$ complex surrounded by K^+, Cs^+, Cl^- and water molecules. Despite the numerous attempts, the full substitution with Cs^+ could not be achieved. **9** is not isostructural with the corresponding analogue **4**. **9** crystallizes in monoclinic space group, *C2/c*, with chemical formula of $K_6Cs_{16}[W(CN)_8]_5Cl_2{\cdot}4H_2O$ (Table II. 26). The longest average W-C bond length is 2.27(6) Å, which is similar with the corresponding analogue **4** (Table II. 28).

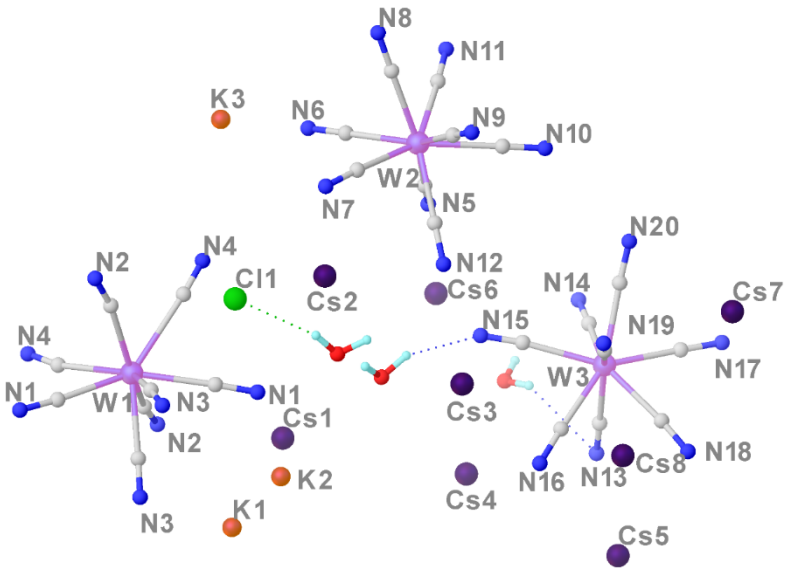

Figure II. 35 ORTEP diagram of molecule fragment of **9** with selected atoms labelling.

Photomagnetic measurements were also realized for **9**. Drastically different with molybdenum analogue, **9** exhibits clearly no photomagnetic effect (Figure II. 36).

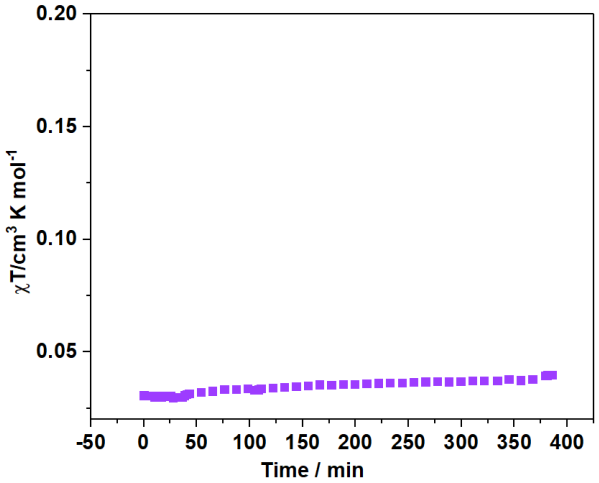

Figure II. 36 Time dependence of the χT for **9** measured at 10 K, 1 T with 405 nm blue light irradiation.

Table II. 28 Selected bond lengths and angles for $[W^{IV}(CN)_8]^{4-}$ anion in **9**.

Atoms		**Length/Å**	**Atoms**		**Length/Å**		**Atoms**		**Angle/°**
W1	C1	2.17(4)	C1	N1	1.11(5)	N1	C1	W1	175(4)
W1	C2	2.26(7)	C2	N2	1.08(8)	N2	C2	W1	169(6)
W1	C3	2.21(5)	C3	N3	1.02(7)	N3	C3	W1	168(6)
W1	C4	2.45(8)	C4	N4	1.04(14)	N4	C4	W1	169(10)
Average		2.27(6)	Average		1.06(9)		Average		170(7)
W2	C5	2.19(2)	C5	N5	1.09(3)	N5	C5	W2	176(2)
W2	C6	2.16(3)	C6	N6	1.15(3)	N6	C6	W2	178(3)
W2	C7	2.18(2)	C7	N7	1.10(3)	N7	C7	W2	175(3)
W2	C8	2.150(19)	C8	N8	1.13(3)	N8	C8	W2	179(3)
W2	C9	2.17(2)	C9	N9	1.10(3)	N9	C9	W2	178(2)
W2	C10	2.19(2)	C10	N10	1.11(3)	N10	C10	W2	179(2)
W2	C11	2.17(2)	C11	N11	1.14(3)	N11	C11	W2	177(2)
W2	C12	2.18(2)	C12	N12	1.13(3)	N12	C12	W2	179(2)
Average		2.17(4)	Average		1.12(3)		Average		178(2)
W3	C13	2.18(2)	C13	N13	1.07(3)	N13	C13	W3	177(2)
W3	C14	2.17(2)	C14	N14	1.17(3)	N14	C14	W3	177(2)
W3	C15	2.18(2)	C15	N15	1.10(3)	N15	C15	W3	174(2)
W3	C16	2.17(2)	C16	N16	1.15(3)	N16	C16	W3	177.4(19)
W3	C17	2.16(2)	C17	N17	1.15(3)	N17	C17	W3	177(2)
W3	C18	2.20(2)	C18	N18	1.13(3)	N18	C18	W3	175.1(19)
W3	C19	2.17(2)	C19	N19	1.12(3)	N19	C19	W3	179(2)
W3	C20	2.18(2)	C20	N20	1.11(3)	N20	C20	W3	178(2)
Average		2.18(2)	Average		1.13(3)		Average		176.8(2)

II.6 References

1. Korzeniak, T.; Sasmal, S.; Pinkowicz, D.; Nitek, W.; Pełka, R.; Czernia, D.; Stefańczyk, O.; Sieklucka, B., Chiral Photomagnets Based on Copper(II) complexes of 1,2-Diaminocyclohexane and Octacyanidomolybdate(IV) Ions. *Inorg. Chem.* **2020,** *59*, 5872-5882.
2. Arczyński, M.; Stanek, J.; Sieklucka, B.; Dunbar, K. R.; Pinkowicz, D., Site-Selective Photoswitching of Two Distinct Magnetic Chromophores in a Propeller-Like Molecule To Achieve Four Different Magnetic States. *J. Am. Chem. Soc.* **2019,** *141* (48), 19067-19077.
3. Stefanczyk, O.; Pelka, R.; Majcher, A. M.; Mathoniere, C.; Sieklucka, B., Irradiation Temperature Dependence of the Photomagnetic Mechanisms in a Cyanido-Bridged $Cu_2^{II}Mo^{IV}$ Trinuclear Molecule. *Inorg. Chem.* **2018,** *57* (14), 8137-8145.
4. Korzeniak, T.; Sasmal, S.; Pinkowicz, D.; Stefańczyk, O.; Sieklucka, B., Light-Induced Spin-State Switching of the Mo^{IV} Centre in Trinuclear $[Cu^{II}(diamine)_2]_2[Mo^{IV}(CN)_8]$ Molecules. *Eur. J. Inorg. Chem.* **2018,** *2018* (19), 2019-2025.
5. Korzeniak, T.; Sasmal, S.; Pinkowicz, D.; Sieklucka, B., The photomagnetic effect in 2-D cyanido-bridged coordination polymer $[Cu(aepa)]_{10}[Mo(CN)_8]_5{\cdot}30H_2O$. *New J. Chem.* **2018**.
6. Korzeniak, T.; Jankowski, R.; Kozieł, M.; Pinkowicz, D.; Sieklucka, B., Reversible Single-Crystal-to-Single-Crystal Transformation in Photomagnetic Cyanido-Bridged Cd_4M_2 Octahedral Molecules. *Inorg. Chem.* **2017,** *56* (21), 12914-12919.
7. Bridonneau, N.; Quatremare, P.; von Bardeleben, H. J.; Cantin, J.-L.; Pillet, S.; Bendeif, E.-E.; Marvaud, V., Direct Evidence of a Photoinduced Electron Transfer in Diluted "Molybdenum-Copper" Molecular Compounds. *Eur. J. Inorg. Chem.* **2017**, 370–377.
8. Bridonneau, N.; Chamoreau, L. M.; Gontard, G.; Cantin, J. L.; von Bardeleben, J.; Marvaud, V., A High-Nuclearity Metal-Cyanide Cluster $[Mo_6Cu_{14}]$ with Photomagnetic Properties. *Dalton Trans.* **2016,** *45* (23), 9412-9418.
9. Stefańczyk, O.; Majcher, A. M.; Rams, M.; Nitek, W.; Mathonière, C.; Sieklucka, B., Photo-induced magnetic properties of the $[Cu^{II}(bapa)]_2\,[Mo^{IV}(CN)_8]{\cdot}7H_2O$ molecular ribbon. *J. Mater. Chem. C* **2015,** *3* (33), 8712-8719.
10. Bridonneau, N.; Long, J.; Cantin, J. L.; Von Bardeleben, J.; Pillet, S.; Bendeif, E. E.; Aravena, D.; Ruiz, E.; Marvaud, V., First Evidence of Light-induced Spin Transition in Molybdenum(IV). *Chem. Commun.* **2015,** *51* (39), 8229-8232.
11. Xu, H.; Sato, O.; Li, Z.; Ma, J., A thermally reversible photoinduced magnetic trinuclear complex $[Cu_2(bpmen)_2][Mo^{IV}(CN)_8]{\cdot}8H_2O$. *Inorg. Chem. Commun.* **2012,** *15*, 311-313.
12. Zhang, W.; Sun, H. L.; Sato, O., Synthesis, characterization, and photoresponsive properties of a series of Mo(IV)-Cu(II) complexes. *Dalton Trans.* **2011,** *40* (12), 2735-2743.
13. Koziel, M.; Podgajny, R.; Kania, R.; Lebris, R.; Mathoniere, C.; Lewinski, K.; Kruczala, K.; Rams, M.; Labrugere, C.; Bousseksou, A.; Sieklucka, B., Series of $M^I[Co(bpy)_3][Mo(CN)_8].nH_2O$ (M^I = Li (1), K (2), Rb (3), Cs (4); n = 7-8) exhibiting reversible diamagnetic to paramagnetic transition coupled with dehydration-rehydration process. *Inorg. Chem.* **2010,** *49* (6), 2765-72.
14. Tokoro, H.; Nakagawa, K.; Nakabayashi, K.; Kashiwagi, T.; Hashimoto, K.; Ohkoshi, S. I., Photoreversible switching of magnetic coupling in a two-dimensional copper octacyanomolybdate. *Chem. Lett.* **2009,** *38* (4), 338-339.
15. Ohkoshi, S. I.; Tokoro, H.; Hozumi, T.; Zhang, Y.; Hashimoto, K.; Mathonière, C.; Bord, I.; Rombaut, G.; Verelst, M.; Cartier Dit Moulin, C.; Villain, F., Photoinduced Magnetization in Copper Octacyanomolybdate. *J. Am. Chem. Soc.* **2006,** *128* (1), 270-277.
16. Hozumi, T.; Hashimoto, K.; Ohkoshi, S. I., Electrochemical synthesis, crystal structure, and photomagnetic properties of a three-dimensional cyano-bridged copper-molybdenum complex. *J. Am. Chem. Soc.* **2005,** *127* (11), 3864-3869.
17. Rombaut, G.; Verelst, M.; Golhen, S.; Ouahab, L.; Mathonière, C.; Kahn, O., Structural and Photomagnetic Studies of Two Compounds in the System $Cu^{2+}/Mo(CN)_8^{4-}$:

From Trinuclear Molecule to Infinite Network. *Inorg. Chem.* **2001,** *40* (6), 1151-1159.
18. Rombaut, G.; Mathonière, C.; Guionneau, P.; Golhen, S.; Ouahab, L.; Verelst, M.; Lecante, P., Structural and photo-induced magnetic properties of M_2^{II} $[W^{IV}(CN)_8]\cdot xH_2O$ (M = Fe and x=8, Cu and x=5). Comparison with $Cu_2^{II}[Mo^{IV}(CN)_8]\cdot 7.5H_2O$. *Inorg. Chim. Acta* **2001,** *326* (1), 27-36.
19. Ohkoshi, S.-i.; Machida, N.; Zhong, Z. J.; Hashimoto, K., Photo-induced magnetization in copper(II) octacyanomolybdate(IV). *Synth.Met.* **2001,** *122* (3), 523-527.
20. Ohkoshi, S. I.; Machida, N.; Abe, Y.; Zhong, Z. J.; Hashimoto, K., Visible Light-Induced Reversible Photomagnetism in Copper(II) Octacyanomolybdate(IV). *Chem. Lett.* **2001,** (4), 312-313.
21. Herrera, J. M.; Marvaud, V.; Verdaguer, M.; Marrot, J.; Kalisz, M.; Mathonière, C., Reversible Photoinduced Magnetic Properties in the Heptanuclear Complex $[Mo^{IV}(CN)_2(CN\text{-}CuL)_6]^{8+}$: A Photomagnetic High-Spin Molecule. *Angew. Chem. Int. Ed.* **2004,** *43* (41), 5468-5471.
22. Arimoto, Y.; Ohkoshi, S. I.; Zhong, Z. J.; Seino, H.; Mizobe, Y.; Hashimoto, K., Photoinduced Magnetization in a Two-Dimensional Cobalt Octacyanotungstate. *J. Am. Chem. Soc.* **2003,** *125* (31), 9240-9241.
23. Rombaut, G.; Golhen, S.; Ouahab, L.; Mathonière, C.; Kahn, O., Structural and Photomagnetic Studies of a 1-D Bimetallic Chain $[Mn_2^{II}(L)_2(H_2O)][Mo^{IV}(CN)_8]\cdot 5H_2O$ (L = macrocycle): Analogy with the Photo-Oxidation of $K_4[Mo^{IV}(CN)_8]\cdot 2H_2O$. *J. Chem. Soc., Dalton Trans.* **2000,** (20), 3609-3614.
24. Ohkoshi, S. I.; Tokoro, H., Photomagnetism in Cyano-Bridged Bimetal Assemblies. *Acc. Chem. Res.* **2012,** *45* (10), 1749-1758.
25. Ozaki, N.; Tokoro, H.; Hamada, Y.; Namai, A.; Matsuda, T.; Kaneko, S.; Ohkoshi, S. I., Photoinduced Magnetization with a High Curie Temperature and a Large Coercive Field in a Co-W Bimetallic Assembly. *Adv. Funct. Mater* **2012,** *22* (10), 2089-2093.
26. Magott, M.; Reczyński, M.; Gaweł, B.; Sieklucka, B.; Pinkowicz, D., A photomagnetic sponge: high-temperature light-induced ferrimagnet controlled by water sorption. *J. Am. Chem. Soc.* **2018,** *140* (46), 15876-15882.
27. Mathonière, C.; Podgajny, R.; Guionneau, P.; Labrugere, C.; Sieklucka, B., Photomagnetism in Cyano-Bridged Hexanuclear Clusters $[Mn^{II}(bpy)_2]_4[M^{IV}(CN)_8]_2\cdot xH_2O$ (M = Mo, x= 14, and M = W, x= 9). *Chem. Mater.* **2005,** *17* (2), 442-449.
28. Korzeniak, T.; Mathonière, C.; Kaiba, A.; Guionneau, P.; Koziel, M.; Sieklucka, B., First example of photomagnetic effects in ionic pairs $[Ni(bipy)_3]_2[Mo(CN)_8]\cdot 12H2O$. *Inorg. Chim. Acta* **2008,** *361* (12-13), 3500-3504.
29. Brossard, S.; Volatron, F.; Lisnard, L.; Arrio, M. A.; Catala, L.; Mathoniere, C.; Mallah, T.; dit Moulin, C. C.; Rogalev, A.; Wilhelm, F.; Smekhova, A.; Sainctavit, P., Investigation of the Photoinduced Magnetization of Copper Octacyanomolybdates Nanoparticles by X-ray Magnetic Circular Dichroism. *J. Am. Chem. Soc.* **2012,** *134* (1), 222-228.
30. Arrio, M.-A.; Long, J. r. m.; Cartier dit Moulin, C.; Bachschmidt, A.; Marvaud, V. r.; Rogalev, A.; Mathonière, C.; Wilhelm, F.; Sainctavit, P., Photoinduced Magnetization on Mo Ion in Copper Octacyanomolybdate: An X-ray Magnetic Circular Dichroism Investigation. *J. Phys. Chem. C.* **2010,** *114* (1), 593-600.
31. Magott, M.; Stefanczyk, O.; Sieklucka, B.; Pinkowicz, D., Octacyanidotungstate(IV) Coordination Chains Demonstrate a Light-Induced Excited Spin State Trapping Behavior and Magnetic Exchange Photoswitching. *Angew. Chem. Int. Ed.* **2017,** *56* (43), 13283-13287.
32. Stefanczyk, O., doctoral dissertation, 2014.
33. Carvajal, M. A.; Reguero, M.; de Graaf, C., On the Mechanism of the Photoinduced Magnetism in Copper Octacyanomolybdates. *Chem. Commun.* **2010,** *46* (31), 5737-5739.
34. Carvajal, M. A.; Caballol, R.; de Graaf, C., Insights on the Photomagnetism in Copper Octacyanomolybdates. *Dalton Trans.* **2011,** *40* (28), 7295-303.
35. Szklarzewicz, J.; Matoga, D.; Niezgoda, A.; Yoshioka, D.; Mikuriya, M., Missing

Link in the Ligand-Field Photolysis of $[Mo(CN)_8]^{4-}$: Synthesis, X-ray Crystal Structure, and Physicochemical Properties of $[Mo(CN)_6]^{2-}$. *Inorg. Chem.* **2007,** *46* (23), 9531-9533.
36. Szklarzewicz, J.; Samotus, A.; Traverso, O.; Sostero, S., A Novel W^{V}-W^{IV} Reversible System: the Preparation and Characterization of $[W(CN)_6(phen)]^{2-}$ and $[W(CN)_6(phen)]^{-}$ Salts. *Polyhedron* **1994,** *13* (11), 1755-1762.
37. Sieklucka, B., Reactivity and Photoreactivity of Cyanocomplexes of the Transition Metals. *Prog. React. Kinet. and Mec.* **1999,** *24* (3), 165-221.
38. R.P.Mitra.; HariMohan, Tetracyano-oxo (hydroxo) complexes of Mo(IV): Their interconversion and relation to the primary photoaquation product of the $Mo(CN)_8^{4-}$ ion. *J. Inorg. Nucl. Chem.* **1974,** *36* (12), 3739-3743.
39. Adamson, A. W.; Perumareddi, J. R., Photochemistry of Aqueous Octacyanomolybdate(IV) Ion, $Mo(CN)_8^{-4}$. *Inorg. Chem.* **1965,** *4* (2), 247-249.
40. Szklarzewicz, J.; Matoga, D.; Lewiński, K., Photocatalytical Decomposition of Hydrazine in $K_4[Mo(CN)_8]$ Solution: X-ray Crystal Structure of $(PPh_4)_2[Mo(CN)_4O(NH_3)]\cdot 2H_2O$. *Inorg. Chim. Acta* **2007,** *360* (6), 2002-2008.
41. Hendrickx, M. F. A.; Mironov, V. S.; Chibotaru, L. F.; Ceulemans, A., Assignment of the Electronic Spectra of $[Mo(CN)_8]^{4-}$ and $[W(CN)_8]^{4-}$ by Ab Initio Calculations. *Inorg. Chem.* **2004,** *43* (10), 3142-3150.
42. Llunell, M.; Casanova, D.; Cirera, J.; Alemany, M.; Alvarez, S., SHAPE, v. 2.0; University of Barcelona: Barcelona, Spain **2010**.
43. Spek, A., Single-crystal structure validation with the program PLATON. *J. Appl. Crystallogr.* **2003,** *36* (1), 7-13.
44. Penneman, R. A.; Jones, L. H., Infrared Absorption Studies of Aqueous Complex Ions. II. Cyanide Complexes of Cu (I) in Aqueous Solution. *J. Chem. Phys.* **1956,** *24* (2), 293-296.
45. Zarembowitch, J.; Roux, C.; Boillot, M.-L.; Claude, R.; Itie, J.-P.; Polian, A.; Bolte, M., Temperature-, Pressure-and Light-Induced Electronic Spin Conversions in Transition Metal Complexes. *Mol. Cryst. Liq. Cryst. Sci. Technol., Sect. A* **1993,** *234* (1), 247-254.
46. Brachňaková, B.; Šalitroš, I., Ligand-driven Light-induced Spin Transition in Spin Crossover Compounds. *Chem. Pap.* **2018,** *72* (4), 773-798.
47. Nelson, S. M.; McIlroy, P. D.; Stevenson, C. S.; König, E.; Ritter, G.; Waigel, J., Quadridentate Versus Quinquedentate Coordination of Some N_5 and N_3O_2 Macrocyclic Ligands and an Unusual Thermally Controlled Quintet⇌ Singlet Spin Transition in an Iron(II) Comple. *J. Chem. Soc., Dalton Trans.* **1986,** (5), 991-995.
48. Guionneau, P.; Le Gac, F.; Kaiba, A.; Costa, J. S.; Chasseau, D.; Létard, J. F., A Reversible Metal-Ligand Bond Break Associated to a Spin-Crossover. *Chem. Commun.* **2007,** (36), 3723-3725.
49. Venkataramani, S.; Jana, U.; Dommaschk, M.; Sonnichsen, F. D.; Tuczek, F.; Herges, R., Magnetic Bistability of Molecules in Homogeneous Solution at Room temperature. *Science* **2011,** *331* (6016), 445-8.
50. Aguila, D.; Dechambenoit, P.; Rouzieres, M.; Mathoniere, C.; Clerac, R., Direct Crystallographic Evidence of the Reversible Photo-formation and Thermo-rupture of a Coordination Bond Inducing Spin-crossover Phenomenon. *Chem. Commun.* **2017,** *53* (84), 11588-11591.
51. Kubota, S.; Ozaki, S.; Onishi, J.; Kano, K.; Shirai, O., Selectivity on Ion Transport across Bilayer Lipid Membranes in the Presence of Gramicidin A. *Anal. Sci.* **2009,** *25* (2), 189-193.
52. Vorobyev, V.; Alferova, N. I.; Emelyanov, V. A., Infrared Detection with Temperature Sweep for Stability Determination of Ru-ON Metastable States. *Inorg. Chem.* **2019**.
53. Stefańczyk, O.; Ohkoshi, S.-i., Synthesis of Two-Dimensional Photomagnetic $K_4\{[Cu^{II}(ida)]_2[M^{IV}(CN)_8]\}\cdot 4H_2O$ (M^{IV} = Mo, W) Materials. *Inorg. Chem.* **2020,** *59* (7), 4292-4299.

Chapter III. Influence of coordination cations on photomagnetic properties of octacyanometallate-based ionic salts

III.1 Introduction

The investigation of inorganic ionic salts $A_4[M(CN)_8]\cdot xH_2O$ (A = Alkali cations: Li^I, Na^I, K^I, Rb^I, Cs^I; M = Mo or W) has shown that the nature of the alkali cations significantly influences the photomagnetic properties. An unusual bond breakage of Mo-CN has been discovered in the crystalline solid state after blue light irradiation at 10 K for the $K_4[MoCN_8]\cdot 2H_2O$ (**1**) and $Rb_4[MoCN_8]\cdot 2H_2O$ (**3**). To explore if this phenomenon can be extended to other Mo/W-based systems, we carry out in this chapter our research work to other discrete ionic compounds by incorporating different metal cations with blocking ligands. Additionally, the absence of photomagnetic properties in $A_4[W(CN)_8]\cdot xH_2O$ prompts us to explore other ionic salts based on the $[W(CN)_8]^{4-}$ unit.

When incorporated with Cu^{2+}, Mo^{4+} can be easily oxidized in Mo^{5+}. To rule out the possible MMCT mechanism, it is necessary to use M^{2+} cations which are difficult to be reduced in M^+, for example, Zn^{2+} and Cd^{2+}. In the literature, only two representative examples are reported with the incorporation of non-redox active cations: the trinuclear $[Zn(tren)]_2[Mo(CN)_8]$ complex and the hexanuclear $\{[Cd^{II}(bpy)_2]_4[Mo^{IV}(CN)_8]_2\}\cdot 10H_2O$ complex.[1-2] To further study new ionic salts involving $[Mo(CN)_8]^{4-}$, we first decide to explore coordination cations containing Zn^{2+} and Cd^{2+}. Besides, to explore if outer-sphere metal-to-metal charge transfer mechanism between Cu^{II} and $[Mo(CN)_8]^{4-}$ is possible, the incorporation of coordination cation containing Cu^{II} in ionic salts is also studied.

In this chapter, new ionic salts containing $[M(CN)_8]^{4-}$(M = Mo^{IV} and W^{IV}) have been prepared using coordination cations, $[Zn(en)_3]^{2+}$ and $[\{M'(tren)\}_3(\mu\text{-tren})]^{6+}$ (M' = Zn^{II}, Cd^{II} and Cu^{II}), built with ethylenediamine (noted hereafter en) and tris(2-aminoethyl)amine (noted hereafter tren) ligands, respectively. The introduction of coordination cations allows more possibilities for the crystal engineering and for the study of the relationship between the photomagnetic properties and the structural features (the coordination geometries, intermolecular interactions and crystal packing).

We herein present the studies of two main groups of ionic salts directed by coordination cations:

1. The synthesis, structural and magnetic characterizations of ionic salts $[Zn(en)_3]_2[M(CN)_8]\cdot xH_2O$ (M = Mo^{IV}, W^{IV}) with a well-known coordination cation $[Zn(en)_3]^{2+}$, built with en.

2. The synthesis, structural and magnetic characterizations of ionic salts $[\{M'(tren)\}\mu\text{-ren})]_2[M(CN)_8]_3\cdot xH_2O$ (M' = Zn^{II}, Cd^{II}, Cu^{II} for Mo^{IV} and Zn^{II} for W^{IV}) with a non-conventional bulky motif $[\{M'(tren)\}_3(\mu\text{-tren})]^{6+}$, built with tren.

III.2 Investigation of $[Zn(en)_3]_2[Mo(CN)_8]\cdot 5H_2O$ (10)

Yellow crystals for **10** are prepared by the addition of the aqueous solution containing both zinc chloride and en ligand to the aqueous solution of $K_4[Mo^{IV}(CN)_8]\cdot 2H_2O$ (III.6.1 Synthesis). The good agreement for the experimental powder X-ray diffraction pattern and the calculated one for **10**, indicates the absence of the starting materials for the synthesized batches (see subsection III.6.2 Powder X-ray diffraction analysis). UV-Vis spectra of **10** is similar with the ones for $A_4[Mo(CN)_8]$ (A = alkali cations) (III.6.3 Optical measurements) with only the contributions from $[Mo(CN)_8]^{4-}$. Infrared spectra (IR) bands for cyanide C-N stretching (2136, 2123, 2116, 2102, 2098 cm^{-1}) are at low wavenumbers, indicating that the cyanide ligands are terminal (III.6.4 IR spectra). Thermogravimetric analysis (TGA) for **10** shows that the weight loss for the first step is 11.5 %, which is close with theoretical weight loss for five water molecules 10.2 %. **10** is thermally stable with nearly no loss of solvent water before 340 K (III.6.5 Thermogravimetric analysis).

III.2.1 Crystal structure of $[Zn(en)_3]_2[Mo(CN)_8]\cdot 5H_2O$ (10)

10 crystallizes in monoclinic space group $P2_1/n$. The crystallographic data, selected bond lengths and angles are presented in Table III. 1, Table III. 2, Table III. 21 and Table III. 22. In the asymmetric unit, one crystallographic independent $[Mo^{IV}(CN)_8]^{4-}$ complex is charge balanced by two $[Zn(en)_3]^{2+}$, constituting an ionic salt where all the CN groups are terminal (Figure III. 1). The eight-coordinated Mo site is revealed to be closer to the square antiprism (SAPR) geometry with a minimum continuous shape measurement (CShM) value of 0.273. Average bond distances of Mo-C and C-N are 2.177(3) Å and 1.151(3) Å, respectively, and the average Mo-C-N bond angle equals to 178.7(2)°, which are similar with that for ionic salt $M^I[Co(bpy)_3][Mo(CN)_8]_3\cdot nH_2O$.[3] The shortest Mo…Mo distance is 9.48 Å, which is much longer than that for $Cs_{20}[Mo(CN)_8]_5\cdot 7H_2O$ (8.56 Å). The $[Zn(en)_3]^{2+}$ cation is formed by a Zn^{2+} coordinated to three en ligands by nitrogen atoms, adopting an octahedral geometry, for example, with CShM value of 1.043 for Zn1 site. Columns of $[Mo^{IV}(CN)_8]^{4-}$ complexes and water molecules are separated by $[Zn(en)_3]^{2+}$ cations along *c*-direction (Figure III. 2). The packing of the ionic components in the structure is dominated by wide-existing N-H…N≡C and O-H..N≡C hydrogen bondings formed by the interaction of $[Zn(en)_3]^{2+}$ or water molecules with $[Mo(CN)_8]^{4-}$ units, respectively.

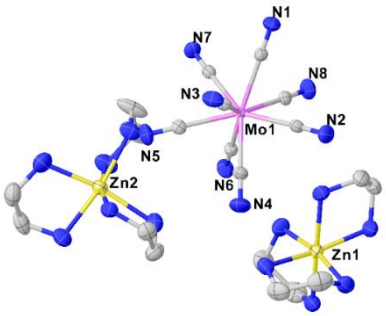

Figure III. 1 ORTEP diagram of asymmetric unit of **10** with selected atoms labelling. Thermal ellipsoids of 50 % probability are shown. Water molecules are omitted for clarity. Color codes: N, blue; C, grey; Zn, yellow; Mo, pink.

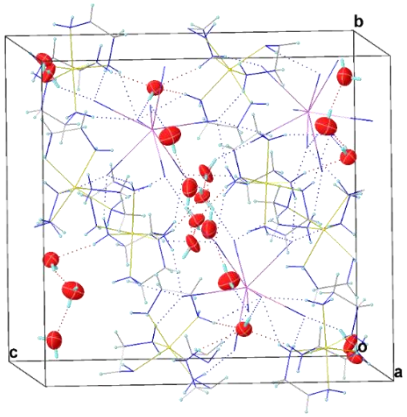

Figure III. 2 Packing structure of **10** with dashed lines as H-bonds**.** View on *bc* plane. Color codes: N, blue; C, grey; Zn, yellow; Mo, pink; O, red.

Table III. 1 Crystal data, data collection, and refine parameters for **10**.

Compound	**10**
Formula	$C_{20}H_{57}MoN_{20}O_5Zn_2$
$D_{calc.}$/g cm^{-3}	1.470
μ/mm^{-1}	1.560
F.W./g mol^{-1}	884.50
T/K	296(2)
Crystal System	monoclinic
Space Group	$P2_1/n$
a/Å	13.5621(6)
b/Å	16.6382(7)
c/Å	17.7348(8)
β/°	95.3510(10)
V/Å^3	3984.4(3)
Z	4
Z'	1
Wavelength/Å	0.71073
Radiation type	MoK$_a$
Q_{min}/°	1.682
Q_{max}/°	27.478
Measured Refl.	55724
Independent Refl.	9086
Reflections with I > 2(I)	7697
R_{int}	0.0343
Parameters	460
Restraints	0
Largest Peak	0.944
Deepest Hole	-0.823
GooF	1.214
wR_2 (all data)	0.0722
wR_2	0.0641
R_1 (all data)	0.0482
R_1	0.0354
S_{SAPR}	0.273
S_{TDD}	1.897

S is continuous shape measurement (CShM) value. SAPR and TDD represent square antiprism and triangular dodecahedron, respectively.

Table III. 2 Selected average bond lengths and angles for $[Mo^{IV}(CN)_8]^{4-}$ and $[Zn(en)_3]^{2+}$ in **10**.

	Length/Å		**Length/Å**		**Angle/°**
Average Mo1-C	2.177(3)	Average (Mo1-)C≡N	1.151(3)	Average Mo1-C≡N	178.7(2)
Average Zn1-N	2.202(3)	Average Zn2-N	2.204(3)		

III.2.2 Photomagnetic studies of $[Zn(en)_3]_2[Mo(CN)_8]\cdot 5H_2O$ (10)

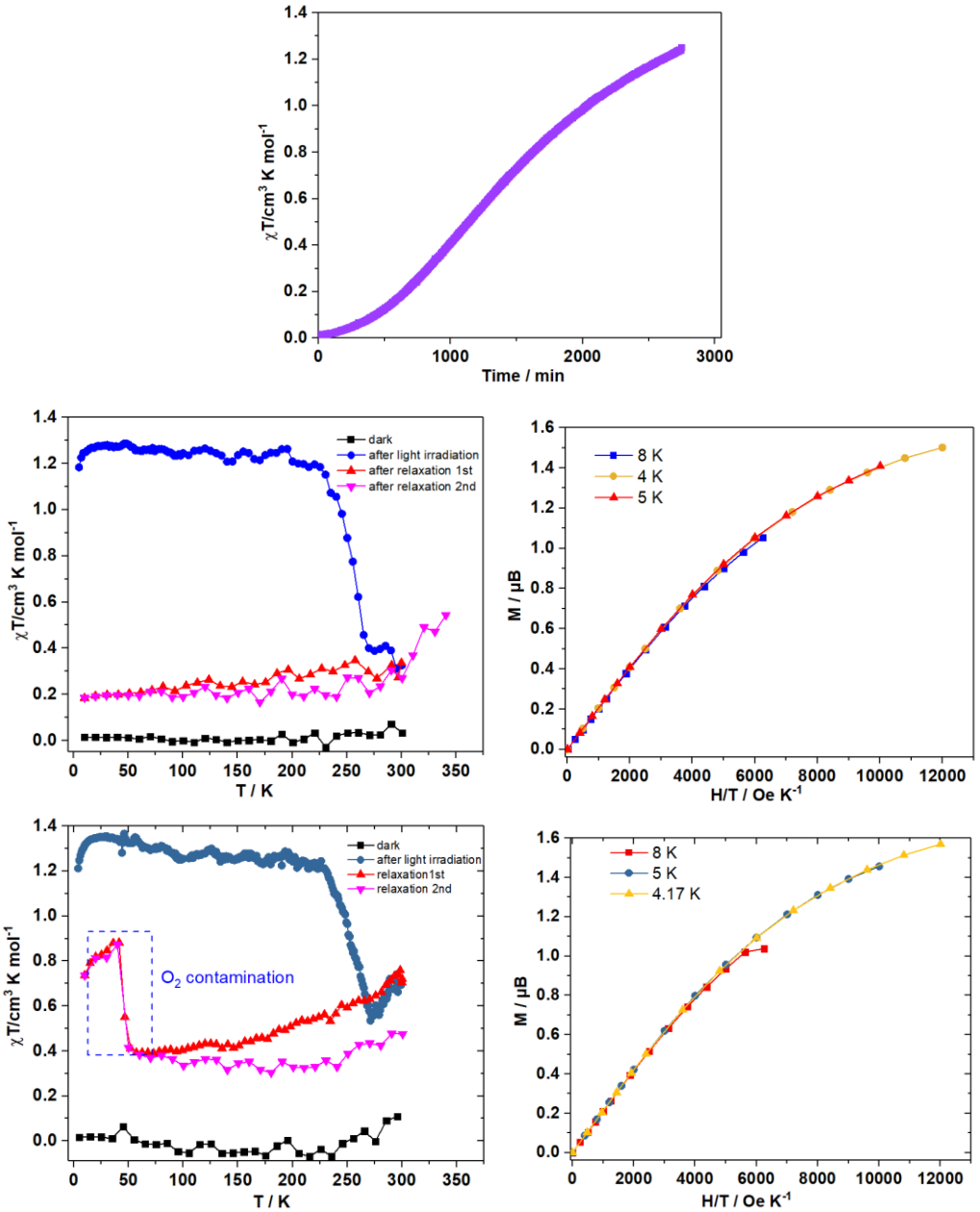

Figure III. 3 For the first set of photomagnetic experiment: (Top) Time dependence of the χT for **10** measured at 10 K, 1 T with continuous 405 nm blue light irradiation. (Middle left) χT = f(T) plots of **10** measured in the dark before any light irradiation, after 405 nm irradiation and after heating to 300 K or 340 K. (Middle right) Reduced magnetizations at different temperatures (4 K, 5 K and 8 K) in the photo-excited state.

For another set of photomagnetic experiment: (Below left) χT = f(T) plots of **10** measured in the dark before any light irradiation, after 405 nm irradiation and after heating to 300 K. The abnormal peak around 50 K is due to the O_2 contamination during measurement. (Below right) Reduced magnetizations at different temperatures (4.17 K, 5 K and 8 K) in the photo-excited state.

As expected, the ground state of **10** is diamagnetic as shown by the χT value close to 0 whatever the temperature is (Figure III. 3). When **10** was irradiated with 405 nm light at 10 K, the paramagnetic signal increased slowly at the beginning then quickly later. The rather long incubation time for nearly 500 mins looks like a nucleation growth process. The value of χT reached 1.2 cm^3 mol^{-1} K after 43 hours (Figure III. 3), but the signal is still not saturated even after this long time irradiation, which imposes difficulty for the analysis of the photoexcited state. After switched off the light, low-temperature magnetizations and the temperature dependence of the χT from 10 K to 300 K have been measured. The reduced magnetizations are nearly superposed, suggesting no anisotropy in the photo-induced state, which is consistent with the small decrease of χT at low temperature. These features are different with what observed for $K_4[Mo(CN)_8]\cdot 2H_2O$. The χT value is higher than what is expected for a S = 1 (χT_{max}= 1 cm^3 mol^{-1} K and M_{sat} = 2 $N\mu_B$ assuming a Zeeman factor equal to 2), but the M_{sat} value around 1.5 $N\mu_B$ is lower than expected. We performed another set of photomagnetic experiments that suggest this significant photomagnetic behavior is repeatable (Figure III. 3 below). The photo-induced state was stable up to around 225 K followed with a fast decrease and the relaxation finished with a residue of paramagnetic signal at 300 K. Based on the TGA data, we heated the compound at 340 K to see if higher temperature could eliminate the residue. But the residue with a χT value around 0.2 cm^3 mol^{-1} K was quite stable even after heated to 340 K.

III.2.3 Discussion on $[Zn(en)_3]_2[Mo(CN)_8]\cdot 5H_2O$ (10)

We have structurally and photomagnetically characterized the ionic compound **10**, which represents an unique example in this family with a non-redox active coordination cation $[Zn(en)_3]^{2+}$. The bigger size of $[Zn(en)_3]^{2+}$ than alkali cation leads to the $[Mo(CN)_8]^{4-}$ units be more separated with larger Mo…Mo distance. **10** exhibits significant photomagnetic properties. The χT values obtained suggest the formation of S =1 state. But the symmetry of the photoexcited state is different, because no significant magnetic anisotropy is obtained. The relaxation temperature around room temperature is also higher than that for $A_4[Mo(CN)_8]\cdot xH_2O$.

To explain why the photomagnetic properties are different with ones observed for $K_4[Mo(CN)_8]\cdot 2H_2O$ and $Rb_4[Mo(CN)_8]\cdot 2H_2O$, we can propose a role of the structure. We observe that **10** shows a less dense crystal packing, which can provide more space for the possible cleavage of Mo-CN bond. The reason for the too high χT value for the photoinduced state than what expected for triplet state maybe the loss of water molecules during the photomagnetic sample preparation with rigorous grinding. The discrepancy between χT and M_{sat} values for the photoexcited state also remains an unresolved issue requiring further investigations. There is a noticeable paramagnetic residue which is stable even after heated to 340 K, indicating that the photoexcited state is partially reversible when heated.

III.3 Studies of $[\{M'(tren)\}_3(\mu\text{-tren})]_2[Mo(CN)_8]_3\cdot$solv. (M' = Zn^{II}, Cd^{II}, Cu^{II}; tren = tris(2-amino)ethylamine) (11-13)

To check the possibility of incorporating even bulkier coordination cations than $[Zn(en)_3]^{2+}$, the assembly of $[\{M'(tren)\}_3(\mu\text{-tren})]^{n+}$ (M' = Zn^{II}, Cd^{II}, Cu^{II}; tren = tris(2-amino)ethylamine) and $[Mo(CN)_8]^{4-}$ moiety has been achieved. The utilization of tren ligand has been reported in several bridged systems based on $[Mo(CN)_8]^{4-}$, but not for non-bridged systems.[1, 4-6]

III.3.1 Studies of $[\{M'(tren)\}_3(\mu\text{-tren})]_2[Mo(CN)_8]_3\cdot$solv. (M' = Zn^{II} (11) and Cd^{II} (12); tren = tris(2-amino)ethylamine)

In this subsection, we have studied new ionic salts involving $[Mo(CN)_8]^{4-}$ and non-redox

active cations Zn^{2+}, Cd^{2+} and $[\{M'(tren)\}_3(\mu\text{-tren})]^{6+}$ (M' = Zn^{II} and Cd^{II}).

11 and **12** are obtained by mixing solutions containing 3d divalent metal cations M^{2+}, tren ligand and $[Mo(CN)_8]^{4-}$ anions following two different methods. Yellow crystals of **12** have been prepared by a layering method by the diffusion of an aqueous solution of $CdCl_2$ and tren ligand into the solution of $K_4Mo^{IV}(CN)_8]\cdot 2H_2O$, the two solutions being separated by a layer of methanol and water. **12** is soluble in the MeOH : H_2O (1:1) solution leading to only several crystals obtained. The low yield of **12** only allows us to characterize it by powder X-ray diffraction. **11** demonstrates similar solubility as **12**, and no crystal could be obtained for **11** with the layering technique. So **11** has been prepared with the one-pot synthesized method. By mixing the solution of $ZnCl_2$, tren ligand and $K_4Mo^{IV}(CN)_8]\cdot 2H_2O$, a clear yellow solution was obtained. Then a slow addition of about 1.5 mL methanol led to the formation of small amount of precipitate, which further transformed to a big amount of target yellow crystals of **11** after one night.

The experimental powder X-ray diffraction (PXRD) patterns are globally consistent with the SCXRD results, but the large unit-cells and the low symmetry involved make the PXRD almost mute in term of reliable information (see subsection III.6.2 Powder X-ray diffraction analysis). The comparison between **11** and **12** indicates that these two compounds are isostructural.

Infrared spectra (IR) for **11** shows the characteristics bands of the tren ligand at 1600, 1450, 1300, and 995 cm^{-1} (III.6.4 IR spectra). **11** also shows a broad band centered at 2098 cm^{-1}, the signature of terminal CN ligands coordinated to the Mo^{4+} by the C atoms. UV-Vis spectra of **11** is similar to that of $K_4[Mo(CN)_8]\cdot 2H_2O$ (III.6.3 Optical measurements).

III.3.1.1 Investigation of $[\{Zn(tren)\}_3(\mu\text{-tren})]_2[Mo(CN)_8]_3\cdot 18H_2O$ (11)

III.3.1.1a Crystal structure of $[\{Zn(tren)\}_3(\mu\text{-tren})]_2[Mo(CN)_8]_3\cdot 18H_2O$ (11)

11 is built from $[\{Zn(tren)\}_3(\mu\text{-tren})]^{6+}$ and $[Mo(CN)_8]^{4-}$ (Figure III. 4), and it crystallizes in the non-centrosymmetric space group *Cc*. The crystallographic data, selected bond lengths and angles are presented in Table III. 3, Table III. 5, Table III. 6, Table III. 23 and Table III. 24. Even though the standard criterion is expected for **11**, the crystal structure of **11** contains a high number of solvent molecules that are difficult to localize. Thus, it is hazardous to discuss in detail features that concern the solvent entities. The coordination metal ions are on the contrary well defined and can be further discussed.

$[\{Zn(tren)\}_3(\mu\text{-tren})]^{6+}$ cations found in **11**, all adopt the triangular bipyramidal geometry (TBPY), as indicated by the minimum continuous shape measurement (CShM) value observed for the TBPY geometry. For example, the minimum continuous shape measurement (CShM) value is 0.817 for Zn1 site (see Table III. 4). The coordination geometry of the Zn ions is close to the ones found in the reported trinuclear compound $MoZn_2$–tren.[1] The average bond distances of Zn-N are typical values for this system (see Table III. 6). The three Mo sites in **11** are also close to a square antiprism (SAPR) geometry as evidenced by the continuous shape measurement (CShM) values (Table III. 4). The selected bond lengths and angles for Mo sites are presented in Table III. 5. Average bond distances of Mo-C and C≡N are 2.174(13)/2.166(12)/2.179(12) and 1.139(12)/1.150(12)/1.132(12) Å, respectively. The average Mo-C≡N bond angles equal to 177.0(12)/177.7(15)/176.6(13)°. The shortest Mo…Mo distances are 9.48/9.46/9.46 Å, which are falling in the same range as the ones found in **10**.

Table III. 3 Crystal data, data collection, and refine parameters for **11**.

Compound / CCDC number	**11 / 2083836**
Formula	$Mo_3Zn_6C_{72}H_{180}N_{56}O_{18}$
$D_{calc.}$/g cm^{-3}	1.406
μ/mm^{-1}	4.036
Formula Weight/g mol^{-1}	2798.68
T/K	130(2)
Crystal System	monoclinic
Space Group	*Cc*
a/Å	32.1487(9)
b/Å	16.8699(3)
c/Å	25.4013(6)
β/°	106.487(3)
V/Å^3	13209.8(6)
Z	4
Z'	1
Wavelength/Å	1.54184
Radiation type	CuK$_a$
Q_{min}/°	2.867
Q_{max}/°	74.083
Measured Refl.	46339
Measured indep. Refl.	19947
Observed indep. Refl.	19214
R_{int}	0.0775
Parameters	1450
Restraints	2
Largest diff. Peak (e-.A^{-3})	1.7437
Deepest diff. Hole (e-.A^{-3})	-1.561
GooF (S)	1.042
wR_2 (all data)	0.2071
wR_2	0.2049
R_1 (all data)	0.0791
R_1	0.0769

Table III. 4 Continuous shape measurements (CShM) for metal ions in **11**.

Mo(CN)$_8$	**Mo1**	**Mo2**	**Mo3**
SAPR	**0.232**	**0.590**	**0.836**
TDD	2.106	1.567	1.372
JBTPR	2.245	1.907	1.819
BTPR	1.663	1.422	1.111

(continue of table III.4)

ZnN_5	Zn1	Zn2	Zn3	Zn4	Zn5	Zn6
TBPY	**0.817**	**0.773**	**1.076**	**0.771**	**0.814**	**0.760**
SPY	5.582	4.987	5.149	5.715	4.698	5.558
JTBPY	2.594	2.368	2.152	2.654	2.510	2.548

S : shape measure relatives to the square antiprism (SAPR), triangular dodecahedron (TDD), Johnson elongated triangular bipyramid (JBTPR) and biaugmented trigonal prism (BTPR) for $M(CN)_8$ unit; trigonal bipyramid (TBPY), spherical square pyramid (SPY) and Johnson trigonal bipyramid (JTBPY) for ZnN_5 unit. When the respective shape measure parameter equals zero, the real geometry coincides with the idealized one. For each site, the minimum calculated shape measure is given in violet.

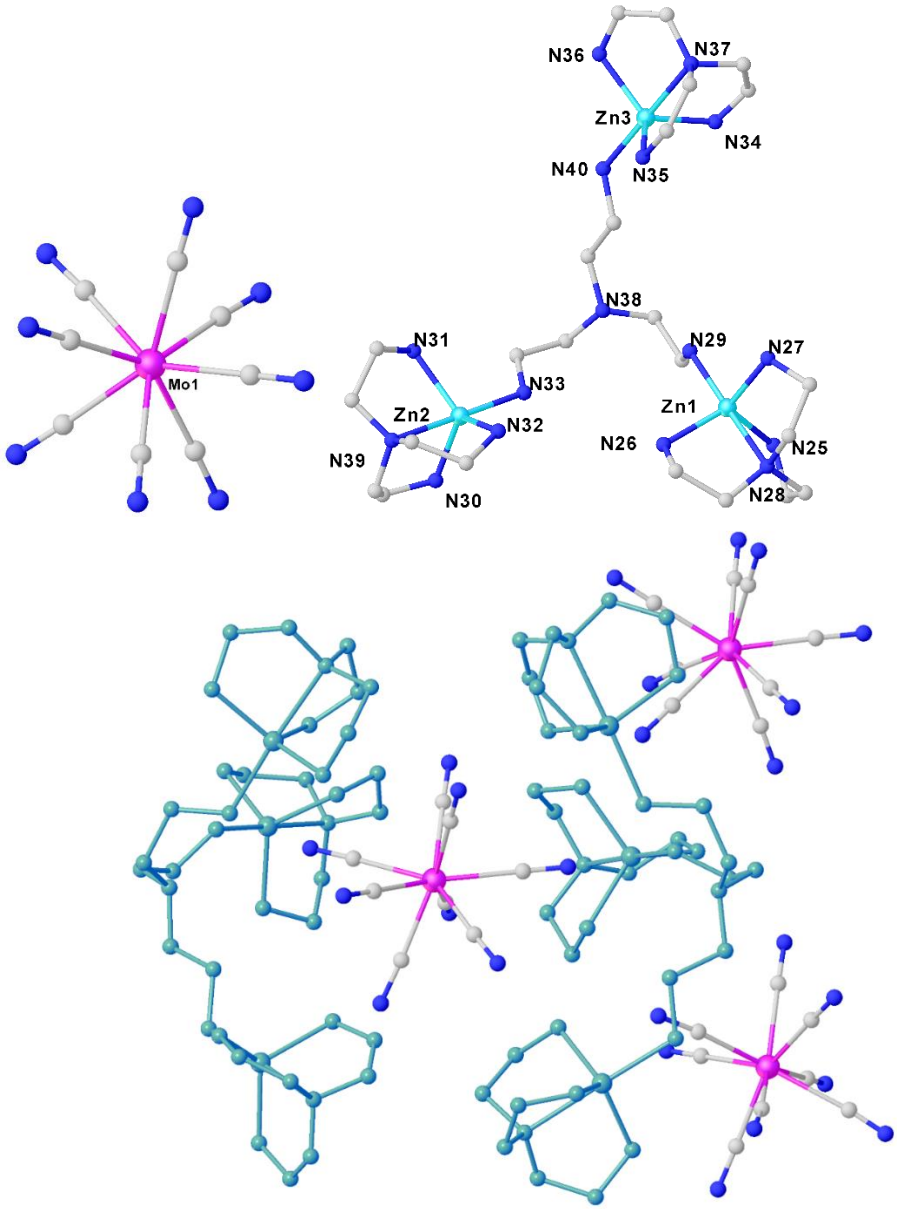

Figure III. 4 Selected $[Mo(CN)_8]^{4-}$ (Left), $[\{Zn(tren)\}_3(\mu\text{-tren})]^{6+}$ (Right) fragments of **11** and asymmetric unit of **11** (without solvent entities) with $[\{Zn(tren)\}_3(\mu\text{-tren})]^{6+}$ units in green (Below). Color codes: N, blue; C, grey; Zn, light blue; Mo, pink.

Table III. 5 Selected bond lengths and angles for $[Mo^{IV}(CN)_8]^{4-}$ anion in **11**.

	Length/Å		**Length/Å**		**Angle/°**
Average Mo1-C	2.174 (13)	Average (Mo1-)C≡N	1.139(12)	Average Mo1-C≡N	177.0(12)
Average Mo2-C	2.166(12)	Average (Mo2-)C≡N	1.150(12)	Average Mo2-C≡N	177.7(15)
Average Mo3-C	2.179(12)	Average (Mo3-)C≡N	1.132(12)	Average Mo3-C≡N	176.6(13)

Table III. 6 Selected bond lengths for $[\{Zn(tren)\}_3(\mu\text{-tren})]^{6+}$ cation in **11**.

	Length/Å		**Length/Å**		**Length/Å**
Average Zn1-N	2.130(12)	Average Zn2-N	2.132(12)	Average Zn3-N	2.111(14)
Average Zn4-N	2.124(12)	Average Zn5-N	2.128(11)	Average Zn5-N	2.138(11)

III.3.1.1b Photomagnetic studies of $[\{Zn(tren)\}_3(\mu\text{-tren})]_2[Mo(CN)_8]_3\cdot 18H_2O$ (11)

As **11** contains only diamagnetic metal ions $Zn^{2+}(3d^{10})$ and $Mo^{4+}(4d^2)$ in square antiprism geometry), the χT values measured in the dark are in agreement with the diamagnetic nature of the compound (Figure III. 5). Under light irradiation at 405 nm, the value of χT increased from 0 to 0.9 $cm^3\ mol^{-1}\ K$ after 38 hours of irradiation. The reduced magnetizations measured after the light excitation are not superimposed. This is consistent with a weak magnetic anisotropy in the photoinduced state. The saturation value of magnetization at 1.8 K was about 1.15 Nβ. A maximum value of χT product of 0.89 $cm^3\ mol^{-1}\ K$ was reached at 15 K. Then, the χT product decreased monotonously to reach 0.7 $cm^3\ mol^{-1}\ K$ at 240 K. Above this temperature, a faster decrease of the χT product was observed. At 300 K, the χT value reached 0.3 $cm^3\ mol^{-1}\ K$, well above the value obtained before the light irradiation. Finally, a new χT vs. T plot (relaxation curve) showed that the photo-induced process was not fully erased after a room temperature treatment. A clear remaining paramagnetic signal around 0.2 $cm^3\ mol^{-1}\ K$ was observed, which is also observed in **10**. This partial reversibility is also reported by Bridonneau et al. for trinuclear $[Zn(tren)]_2[Mo(CN)_8]$ based compound.[7]

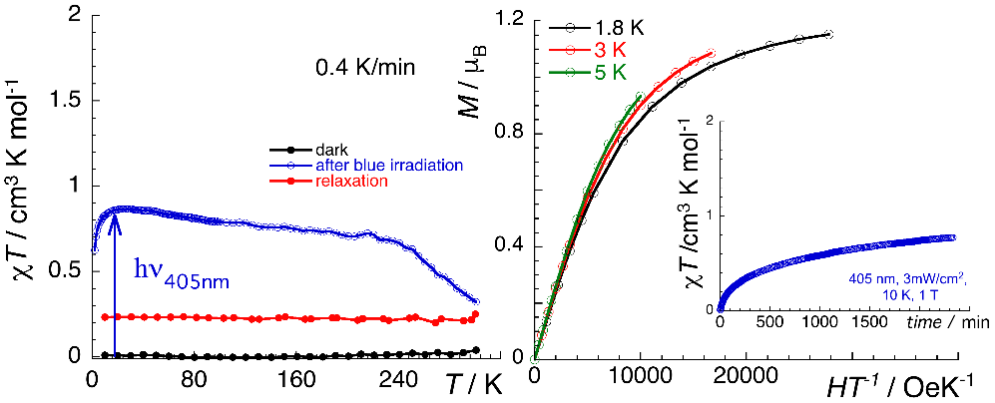

Figure III. 5 (Left) χT = f(T) plots of **11** measured in the dark before irradiation (dark points), after 405 nm irradiation (open blue points) and after reconditioning at 300 K (red points). (Right) Reduced magnetizations at different temperatures (1.8 K, 3 K and 5 K) in the photo-excited state of **11** (open points). (Insert: Time dependence of the χT for **11** measured at 10 K, with continuous irradiation of wavelength of 405 nm (3 mW/cm^2)).

III.3.1.2 Investigation of [{Cd(tren)}$_3$(μ-tren)]$_2$[Mo(CN)$_8$]$_3$·solv. (12)

III.3.1.2a Possible crystal structure of [{Cd(tren)}$_3$(μ-tren)]$_2$[Mo(CN)$_8$]$_3$·solv. (12)

Single crystal X-ray crystallographic analysis for **12** was not successful because of the poor quality of the crystals. But by the comparison of powder X-ray diffraction patterns with **11**, **12** has been revealed as isostructural with **11** (III.6.2 Powder X-ray diffraction analysis).

III.3.1.2b Photomagnetic studies of [{Cd(tren)}$_3$(μ-tren)]$_2$[Mo(CN)$_8$]$_3$·solv. (12)

The photomagnetic properties for **12** are similar with the ones of **11**. The population is slow (not saturate after 17h), with a maximum value of χT product of 0.45 cm^3 mol^{-1} K reached at 30 K. The non-superposed magnetization values also suggest a weak magnetic anisotropy in the photoinduced state. But we do not go further in the analysis because of the incomplete population of the photo-induced state. The shape of the relaxation curves are similar with the ones observed in **11** (Figure III. 6). A clear remaining of paramagnetic signal around 0.1 cm^3 mol^{-1} K was also observed for **12** after heating at 300 K.

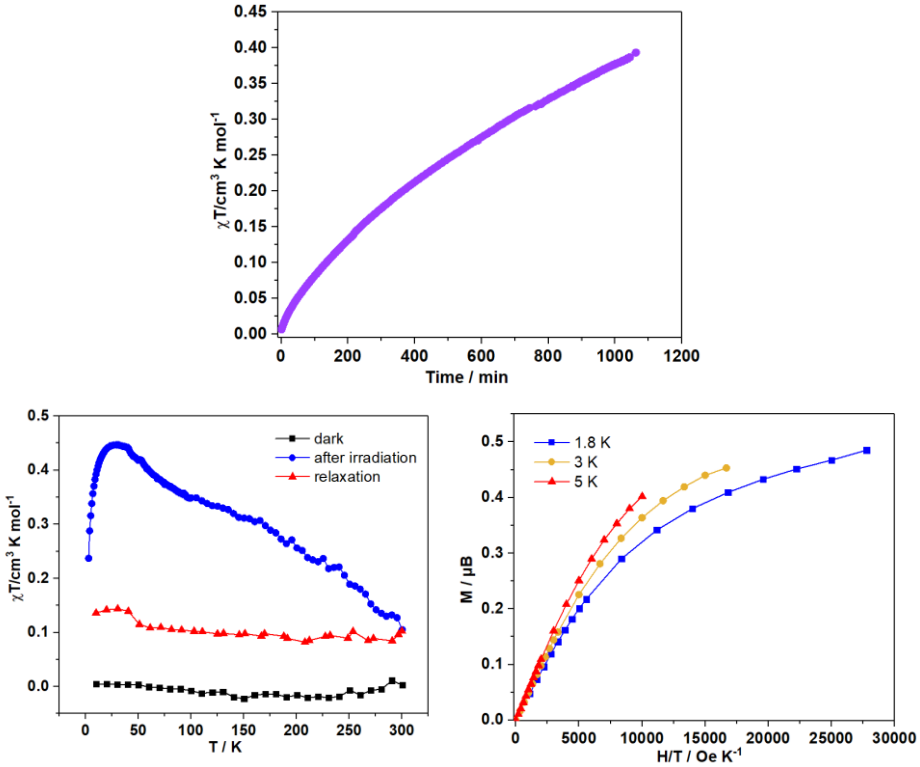

Figure III. 6 (Top) Time dependence of the χT for **12** measured at 10 K, 1 T with continuous 405 nm blue light irradiation. (Below left) χT = f(T) plots of **12** measured in the dark before any light irradiation, after 405 nm irradiation and after heating to 300 K. (Below right) Reduced magnetizations at different temperatures (1.8 K, 3 K and 5 K) in the photo-excited state.

III.3.2 Studies of $[\{Cu(tren)\}_3(\mu\text{-tren})]_2[Mo(CN)_8]_3\cdot 45H_2O\cdot 2CH_3OH$ (13)

Unlike Zn^{2+} and Cd^{2+} ions, Cu^{2+} ions can be easily reduced as Cu^{+} ions. To explore if outer-sphere metal-to-metal charge transfer mechanism between Cu^{II} and $[Mo(CN)_8]^{4-}$ is possible, the incorporation of coordination cation containing Cu^{II} in ionic salts is needed but barely reported in the literature. So in this subsection, the Zn^{II} or Cd^{II} ions are replaced by Cu^{II} to study an eventual outer-sphere metal-to-metal charge transfer mechanism.

Similarly with **12**, green crystals of **13** have been prepared by a layering method by the diffusion of an aqueous solution of $CuCl_2\cdot 2H_2O$ and tren ligand into the solution of $K_4Mo^{IV}(CN)_8]\cdot 2H_2O$, the two solutions being separated by a layer of methanol and water. While compared with **12**, **13** is less soluble in the MeOH : H_2O (1:1) solution leading to a large quantity of crystals obtained.

The drastic differences for Powder X-ray diffraction (PXRD) patterns between **11** and **13** indicate that these two compounds are crystallized in different space groups (see subsection III.6.2 Powder X-ray diffraction analysis).

Infrared spectra (IR) for **11** and **13** are very similar (III.6.4 IR spectra). These two compounds show the characteristic bands of the tren ligand at 1600, 1450, 1300, and 995 cm^{-1}. **11** and **13** both show a broad band centered at 2098 cm^{-1}, the signature of terminal CN ligands coordinated to the Mo^{4+} by the C atoms. These spectra indicate that **11** and **13** are ionic salts and that the chemical environment of the $[Mo(CN)_8]^{4-}$ anions are similar in these two compounds.

UV-Vis spectra of **13** is also similar to that of $K_4[Mo(CN)_8]\cdot 2H_2O$, while there is a broad absorption with maximum and shoulders at 877 and 657 nm for **13** (III.6.3 Optical measurements). These bands also appear in $[Cu(tren)]^{2+}$ complexes in square pyramidal geometry,[8] and suggest that the tren ligand acts in **13** as a tetradentate ligand for the Cu^{2+} ion. This means that a fifth ligand is necessary to assure the Cu^{2+} ion a bipyramid geometry. It is worth to note that for **13** no additional transition except the transitions observed in its precursors is observed, suggesting the absence of an outer-sphere charge transfer in Cu^{2+}/Mo^{4+} pairs in **13**.

III.3.2.1 Crystal structure of $[\{Cu(tren)\}_3(\mu\text{-tren})]_2[Mo(CN)_8]_3\cdot 45H_2O\cdot 2CH_3OH$ (13)

Single Crystal X-ray diffraction (SCXRD) analysis shows that **13** crystallizes in the monoclinic space group $P2_1/c$. The crystallographic data, selected bond lengths and angles are presented in Table III. 9, Table III. 10, Table III. 8, Table III. 25 and Table III. 26.

As shown by the crystallographic data in Table III. 8, the unit cell of **13** is very large leading to up to 323 atoms (without H atoms) which certainly puts this compound in the category of the giant unit-cell ones (V > 20000 $Å^3$). This makes the SCXRD crystal structure determination a challenge in itself. Similar with **11** and **12**, **13** is also constructed by the assembly of $[\{Cu(tren)\}_3(\mu\text{-tren})]^{6+}$ cations and $[Mo(CN)_8]^{4-}$ anions with no covalent bond between them. There are six $[Mo(CN)_8]^{4-}$ anions and four $[\{Cu(tren)\}_3(\mu\text{-tren})]^{6+}$ cations in the asymmetric unit (Figure III. 7). The very large number of solvent molecules in the asymmetric unit (> 40 water and/or methanol molecules) and the flexible arms for the $[\{Cu(tren)\}_3(\mu\text{-tren})]^{6+}$ cations cause structural disorder, which increases the difficulty in the crystal structure determination. Nevertheless, it is important to note that the crystal structure has been solved without ambiguity and is confirmed by the diffraction data investigation on several crystals from different batches. As a result, while the solvent part cannot be discussed in detail, the structural parameters and notably the 3D atomic coordinates for the anions and cations in **13** are on the contrary robust and can be discussed further. The packing diagram of **13** shows as a 2-D coordination polymer if considering the hydrogen bonds (Figure III. 8).

The $[\{Cu(tren)\}_3(\mu\text{-tren})]^{6+}$ is constructed by one μ-tren linked to three Cu sites, where each copper site is blocked by another tren ligand. Therefore, the tren ligands serve as a tetradentate ligand for the copper sites, and as a tridentate ligand to link the three different Cu sites contained in the trimetallic cation. To the best of our knowledge, this unusual trinuclear copper complex cation has been reported only in the crystal structure of $[Cu_3(tren)_4][Pt(CN)_4]_3 \cdot 2H_2O$.[9] The copper sites are in a similar chemical environment, indicating by very close average Cu-N bond lengths (Table III. 10). As indicated by the minimum continuous shape measurement (CShM) values, all the copper sites adopt triangular bipyramidal geometry, with exception for Cu9 site which corresponds to distorted square pyramidal geometry, in agreement with the UV-Vis spectra (Table III. 7). For instance, the minimum CShM value for Cu1 site is 0.420 corresponding to the triangular bipyramidal geometry and for Cu9 site is 1.491 corresponding to the square pyramidal geometry. The three copper sites in $[\{Cu(tren)\}_3(\mu\text{-tren})]^{6+}$ are arranged in the form of an irregular triangle, for example, with rather long Cu...Cu distances as 7.450, 7.542, 9.156 Å for Cu1...Cu2, Cu2...Cu3 and Cu1...Cu3 distances, respectively.

The $[Mo(CN)_8]^{4-}$ anion is stabilized by wide-numerous N-H…N≡C and O-H..N≡C hydrogen bondings formed by the interaction of $[\{Cu(tren)_3(\mu\text{-tren})]^{6+}$ or water molecules with $[Mo(CN)_8]^{4-}$ units, respectively. The selected bond lengths and angles for Mo sites are presented in Table III. 9. Average bond distances of Mo-C and C≡N are 2.179(10)/2.170(10)/2.176(14)/2.177(10)/2.153(13)/2.169(10) Å and 1.145(14)/1.141(14)/1.135(6)/1.137(13)/1.157(10)/1.138(14) Å, respectively, while the average Mo-C≡N bond angles equal to 177.0(10)/176.7(10)/175.9(12)/177.5(9)/176.8(13)/177.3(10)°. All the Mo sites reveal a geometry close to the square antiprism (SAPR) as evidenced by continuous shape measurement (CShM) analysis (Table III. 7). The minimum Mo…Mo distances are 9.65, 9.65, 9.77, 9.67, 9.80, 9.67 Å, which are much longer than the distance of 7.53 Å found in $K_4Mo^{IV}(CN)_8]\cdot 2H_2O$, but appear comparable to the values observed for $[Ni(bipy)_3]_2[Mo(CN)_8]\cdot 12H_2O$.[10]

Table III. 7 Continuous shape measurements (CShM) for metal ions in **13**.

$Mo(CN)_8$	**Mo1**	**Mo2**	**Mo3**	**Mo4**	**Mo5**	**Mo6**
SAPR	**0.218**	**0.254**	**0.535**	**0.230**	**0.652**	**0.321**
TDD	2.201	2.008	1.679	1.899	1.232	1.794
JBTPR	2.821	2.284	2.252	2.660	1.971	2.360
BTPR	2.220	1.709	1.649	2.077	1.384	1.738

CuN_5	**Cu1**	**Cu2**	**Cu3**	**Cu4**	**Cu5**	**Cu6**
TBPY	**0.420**	**0.377**	**0.904**	**0.540**	**0.368**	**0.443**
SPY	4.269	4.425	3.226	4.175	4.805	4.970
JTBPY	3.967	3.731	3.928	3.661	3.794	3.911
CuN_5	**Cu7**	**Cu8**	**Cu9**	**Cu10**	**Cu11**	**Cu12**
TBPY	**0.380**	**0.321**	2.225	**0.348**	**0.514**	**0.789**
SPY	4.975	4.832	**1.491**	5.009	4.016	3.401
JTBPY	3.966	3.639	4.730	3.705	4.016	3.977

S : shape measure relatives to the square antiprism (SAPR), triangular dodecahedron (TDD), Johnson elongated triangular bipyramid (JBTPR) and biaugmented trigonal prism (BTPR) for $M(CN)_8$ unit; trigonal bipyramid (TBPY), spherical square pyramid (SPY) and Johnson trigonal bipyramid (JTBPY) for CuN_5 unit. When the respective shape measure parameter equals zero, the real geometry coincides with the idealized one. For each site, the minimum calculated shape measure is given in violet.

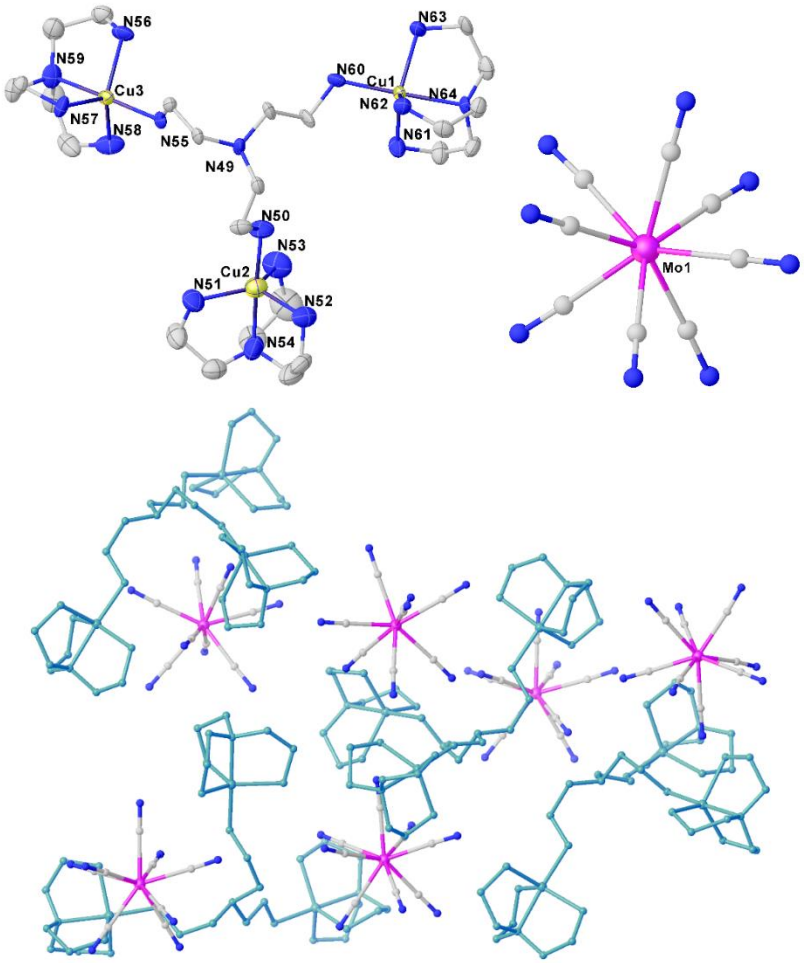

Figure III. 7 Selected fragments of $[\{Cu(tren)\}_3(\mu\text{-tren})]^{6+}$ (Left), $[Mo(CN)_8]^{4-}$ (Right) with partial atoms labelling and (Below) asymmetric unit of **13** (without solvent entities) viewed along *c* with $[\{Cu(tren)\}_3(\mu\text{-tren})]^{6+}$ units in green. Color codes: N, blue; C, grey; Cu, yellow; Mo, pink.

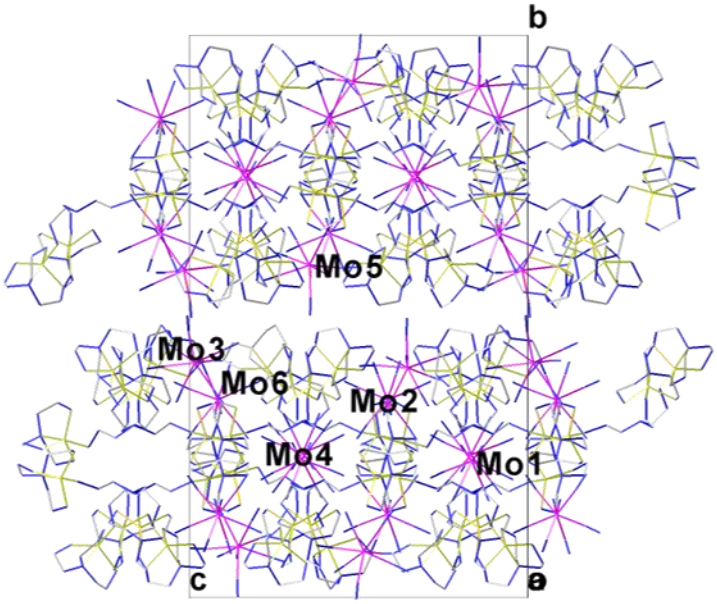

Figure III. 8 Packing diagram of **13** in *bc* planc, where the solvent molecules and hydrogen atoms are omitted for clarity.

Table III. 8 Crystal data, data collection, and refine parameters for **13**.

Compound / CCDC number	**13 / 2083835**
Formula	$Mo_6Cu_{12}C_{146}H_{386}N_{112}O_{47}$
$D_{calc.}$/g cm^{-3}	1.424
μ/mm^{-1}	4.121
Formula Weight/g mol^{-1}	5801.61
T/K	130(2)
Crystal System	monoclinic
Space Group	$P2_1/c$
a/Å	30.4150(4)
b/Å	37.1820(5)
c/Å	22.5401(2)
β/°	98.0410(10)
V/Å^3	25239.8(5)
Z	4
Z'	1
Wavelength/Å	1.54184
Radiation type	CuK_a
Q_{min}/°	2.309
Q_{max}/°	73.591
Measured Refl.	199397
Measured indep. Refl.	49550
Observed indep. Refl.	35018
R_{int}	0.0760
Parameters	2908
Restraints	0
Largest diff. Peak (e-.A^{-3})	19.876
Deepest diff. Hole (e-.A^{-3})	-2.959
GooF (S)	1.764
wR_2 (all data)	0.4624
wR_2	0.4298
R_1 (all data)	0.2056
R_1	0.1830

Table III. 9 Selected bond lengths and angles for $[Mo^{IV}(CN)_8]^{4-}$ anion in **13**.

	Length/Å		**Length/Å**		**Angle/°**
Average Mo1-C	2.179(10)	Average (Mo1-)C≡N	1.145(14)	Average Mo1-C≡N	177.0(10)
Average Mo2-C	2.170(10)	Average (Mo2-)C≡N	1.141(14)	Average Mo2-C≡N	176.7(10)
Average Mo3-C	2.176(14)	Average (Mo3-)C≡N	1.135(6)	Average Mo3-C≡N	175.9(12)
Average Mo4-C	2.177(10)	Average (Mo4-)C≡N	1.137(13)	Average Mo4-C≡N	177.5(9)
Average Mo5-C	2.153(13)	Average (Mo5-)C≡N	1.157(10)	Average Mo5-C≡N	176.8(13)
Average Mo6-C	2.169(10)	Average (Mo6-)C≡N	1.138(14)	Average Mo6-C≡N	177.3(10)

Table III. 10 Selected bond lengths for $[\{Cu(tren)\}_3(\mu\text{-tren})]^{6+}$ cation in **13**.

	Length/Å		**Length/Å**		**Length/Å**
Average Cu1-N	2.069(9)	Average Cu2-N	2.070(11)	Average Cu3-N	2.073(9)
Average Cu4-N	2.065(11)	Average Cu5-N	2.056(16)	Average Cu6-N	2.056(10)
Average Cu7-N	2.075(9)	Average Cu8-N	2.069(11)	Average Cu9-N	2.064(10)
Average Cu10-N	2.070(13)	Average Cu11-N	2.066(10)	Average Cu12-N	2.069(10)

III.3.2.2 Photomagnetic studies of $[\{Cu(tren)\}_3(\mu\text{-tren})]_2[Mo(CN)_8]_3\cdot 45H_2O\cdot 2CH_3OH$ (13)

As observed from the temperature dependence of the χT and low-temperature magnetizations in the dark (Figure III. 9 and Figure III. 10), **13** reveals a paramagnetic behaviour with a χT product equals at 0.80 $cm^3\ mol^{-1}\ K$ in agreement with two $Cu^{2+}(3d^9)$ ions of $S = 1/2$ (per Cu_2Mo units) with a Zeeman factor of $g = 2$ and one diamagnetic Mo^{4+} ion ($4d^2$ in square antiprism geometry). The superposition of the reduced magnetizations measured at 1.8, 3 and 5 K suggests the absence of magnetic anisotropy.

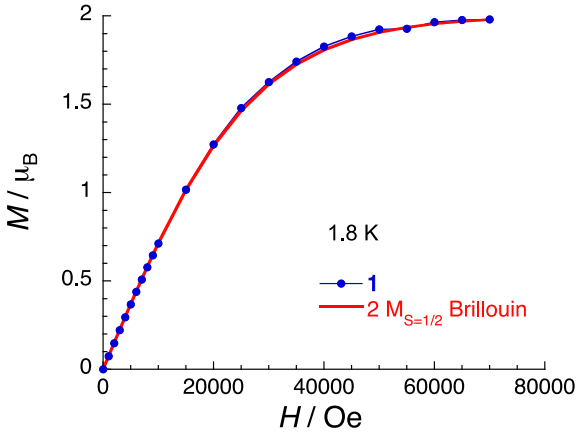

Figure III. 9 Fit of the magnetization of **13** at 1.8 K using Brillouin functions with $g = 2$.

When **13** was irradiated with a light of 405 nm, the value of χT at 10 K increased from 0.79 to 1.4 $cm^3\ mol^{-1}\ K$ after 25 hours of irradiation (Figure III. 11 Top left). Then the light was switched off, and low-temperature magnetizations at 1.8, 3 and 5 K have been measured (Figure III. 10). The saturation magnetization at 1.8 K was 3.09 Nβ significantly higher than the value of 2 Nβ found before irradiation. The non-superposed reduced magnetizations suggest anisotropy in the photo-induced state. This observation is clearly different in the ground state. The temperature dependence of the χT product from 2 K to 300 K has a similar shape than the χT vs. T plot of **11**. The temperature dependence of the χT from 2 K to 300 K first increased to reach a plateau at 1.67 $cm^3\ mol^{-1}\ K$ at 30 K. When compared with the χT product before irradiation, the χT value has increased with a maximum of 0.89 $cm^3\ mol^{-1}\ K$.

Then, the χT product slightly decreased monotonously to reach 1.43 cm^3 mol^{-1} K at 250 K. Above this temperature, a faster decrease of the χT product was observed. At 300 K, the χT value was back to the value obtained before the light irradiation. A new plot χT vs. T shows that the photo-induced process is reversible.

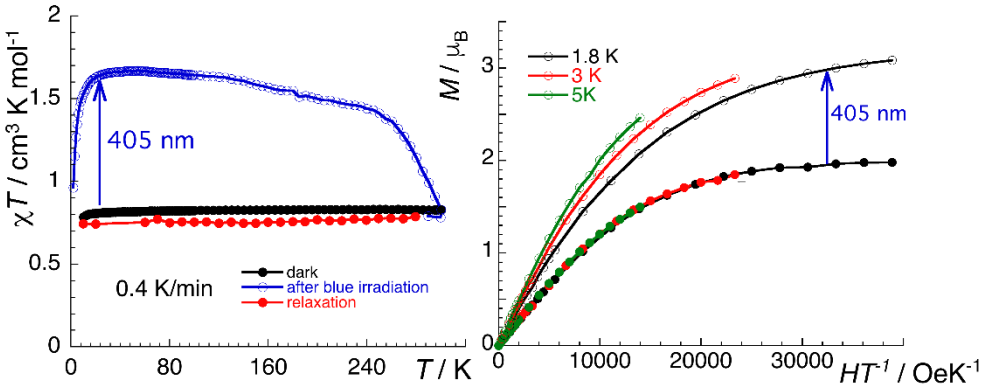

Figure III. 10 (Left) χT = f(T) plots of **13** measured in the dark before irradiation (dark points), after 405 nm irradiation (open blue points) and after an reconditioning to 300 K (red points). (Right) Reduced magnetizations at different temperatures (1.8 K, 3 K and 5 K) before irradiation (full points) and in the photo-excited state of **13** (open points).

As shown by the χT = f(T) plots, the photo-induced state seems stable at 100 K. Attempt to irradiate the **13** at 100 K with 405 nm light irradiation resulted in a small increase of χT from 0.75 to 0.95 cm^3 mol^{-1} K, which could be fully erased at 170 K (Figure III. 11). This indicates that the photo-induced state obtained at 100 K is less thermally stable than that obtained at 10 K.

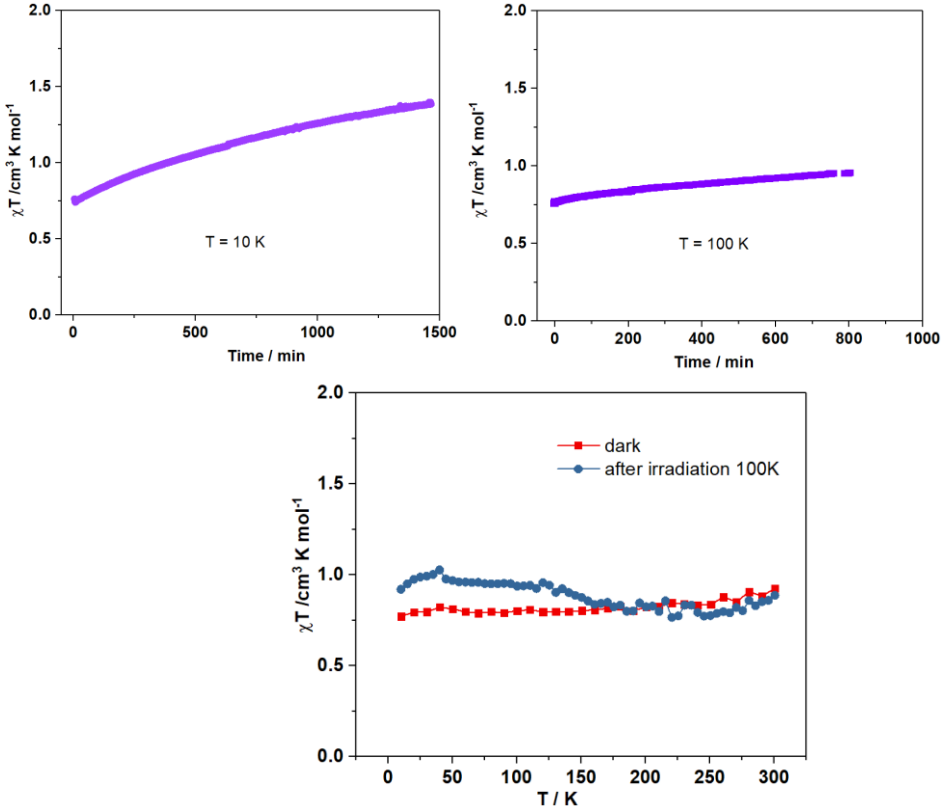

Figure III. 11 Time dependence of the χT for **13** measured at 10 K (Top left) and 100 K (Top right), 1 T with continuous 405 nm blue light irradiation, respectively. (Below) χT = f(T) plots of **13** measured in the dark before any light irradiation and after 405 nm irradiation at 100 K.

III.3.3 Discussion on $[\{M(tren)\}_3(\mu\text{-tren})]_2[Mo(CN)_8]_3\cdot solv.$ ($M = Zn^{II}$, Cd^{II}, Cu^{II}; tren = tris(2-amino)ethylamine) (11-13)

The three systems reported in this section are ionic salts and are based on large cations of formula of $[\{M'(tren)\}_3(\mu\text{-tren})]^{6+}$ containing 3d metal ions and $[M(CN)_8]^{4-}$ anions. **13** adopts a slightly different crystal packing than the ones found in **11** and **12** which are almost isostructural. But based on the vicinity of the coordination geometries of the metal ions in these three compounds, it is reasonable to compare their respective photomagnetic properties.

The three compounds reported in this work show a significant photomagnetic response. Some of the characteristics of their photo-induced states are common with the other photomagnetic systems based on $[M(CN)_8]^{4-}$ anions. First, the photo-induced states are formed at 10 K with a blue light irradiation. Second, they have also a high thermal stability, and the thermal relaxation of the photoinduced state occurs around room temperature.

Several mechanisms are proposed in the literature to explain the observed photomagnetic properties: metal-to-metal charge transfer (MMCT) or spin crossover (SCO) mechanisms. The metal-to-metal charge transfer is possible where the $[M(CN)_8]^{4-}$ units can be easily oxidized by the presence of easily reductive species, as for example Cu^{2+} ions. In this case, the presence of a metal-to-metal charge transfer transition (from Mo^{4+}-Cu^{2+} to Mo^{5+}-Cu^{+}) in optical spectra is the key feature of this mechanism. For the **13** of this study, no MMCT is observed in its optical spectrum in the range 200-1000 nm. Another indirect proof of the absence of MMCT mechanism for **13** is the comparison with the photomagnetic properties of **11** and **12**. In **11** and **12**, the Cu^{2+} ion has been substituted with Zn^{2+} and Cd^{2+} ions which cannot form easily Zn^{+} or Cd^{+} ions, thus excluding the MMCT mechanism.

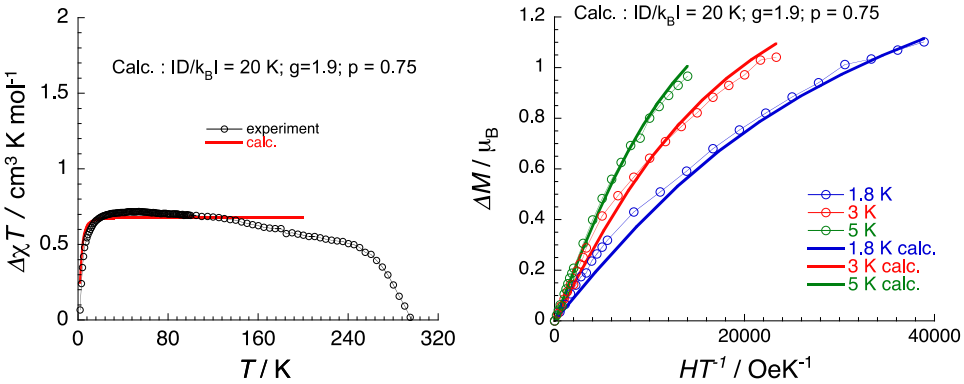

Figure III. 12 (Left) χT = f(T) plot of **13** obtained with the difference of χT before and after irradiation (open dark points). In red, theoretical model for the triplet state (see text). (Right) M = f(H/T) of the reduced magnetizations obtained with the difference of M before and after irradiation (open points) at different temperatures. In colored lines, theoretical models for the triplet state (see text).

The similarities of photomagnetic properties of **11** and **13** are nicely shown in Figure III. 12, showing by the photomagnetic difference curves of **13** where the Cu^{2+} contributions are removed by considering the difference of χT or M before and after irradiation. The resulted χT vs. T and M vs. H plots display a strong similarity with the plots of **11**. This suggests that the photomagnetic properties of **11** and **13** come from the $[Mo(CN)_8]^{4-}$ anions.

As mentioned in the introduction, this anion can display a SCO between a $S = 0$ state and a $S = 1$ state. In the chapter II, we have investigated the photo-induced singlet-triplet trapping in the $K_4[Mo(CN)_8]\cdot 2H_2O$ that is accompanied by a breaking of one Mo-CN bond in the crystalline state. To evaluate if this mechanism is active in **11**, **12** and **13**, we have tested the hypothesis of the photo-induced formation of the triplet state. Because the photomagnetic properties of **11** and **12** are not fully reversible, we have only analyzed the magnetic data of **13** after the removal of the Cu^{2+} contributions (Figure III. 12). The triplet state has been computed using the anisotropy parameters calculated in the $K_4[Mo(CN)_8]\cdot 2H_2O$, namely $|D/k_B| = 20$ K and $g = 1.9$. To simulate correctly the properties of **13**, we have also used a partial population of the triplet state at 75 % (p = 0.75). The Figure III. 12 shows the good

reproducibility of the experimental data at low temperature (T < 120 K) considering the triplet state. At higher temperatures, relaxation that is not considered in the theoretical model probably occurs, and leads to discrepancies with the experiment. This comparative analysis suggests a singlet-triplet trapping mechanism centered on the $[Mo(CN)_8]^{4-}$ anions in **11**, **12** and **13**.

III.4 Studies of octacyanotungstate based ionic salts with coordination cations

Yellow crystals of $[Zn(en)_3]_2[W(CN)_8]\cdot 5H_2O$ (**14**) and $[\{Zn(tren)\}_3(\mu\text{-tren})]_2[W(CN)_8]_3\cdot 17H_2O$ (**15**) are synthesized in an analogous way to the molybdenum analogues.

The good agreement for the experimental powder X-ray diffraction patterns and the calculated ones for **14** and **15**, indicates the isostructural character with molybdenum analogues (**10** and **11**, respectively) (III.6.2 Powder X-ray diffraction analysis). UV-Vis spectra and Infrared spectra (IR) for **14** and **15** are also very similar with that for molybdenum analogues (III.6.3 Optical measurements and III.6.4 IR spectra). Notably, the cyanide vibration band appears at 2091 cm^{-1} for **15**, in agreement with the coordination of the terminal CN to the W^{4+} by the C atoms, but shifting a bit to lower wavenumbers compared to the molybdenum analogue at 2098 cm^{-1}.

III.4.1 Investigation of $[Zn(en)_3]_2[W(CN)_8]\cdot 5H_2O$ (14)

The crystal structure of **14** has been determined and it is isostructural with **10**, with the substitution of $[Mo(CN)_8]^{4-}$ by $[W(CN)_8]^{4-}$. However, **14** exhibits no photomagnetic effect with 405 nm light irradiation at 10 K (see subsection III.6.6 Crystal structure and photomagnetic measurements of $[Zn(en)_3]_2[W(CN)_8]\cdot 5H_2O$ (**14**)).

III.4.2 Investigation of $[\{Zn(tren)\}_3(\mu\text{-tren})]_2[W(CN)_8]_3\cdot 17H_2O$ (15)

III.4.2.1 Crystal structure of $[\{Zn(tren)\}_3(\mu\text{-tren})]_2[W(CN)_8]_3\cdot 17H_2O$ (15)

The crystallographic data of **15** is given in Table III. 12. It adopts the same unit-cell and space group as **11**, and atomic positions are very close in these two structures. The crystal structure of **15** is therefore similar to **11** with the replacement of $[Mo(CN)_8]^{4-}$ anions by $[W(CN)_8]^{4-}$ anions. Crystal structure criteria of **15** are even slightly better than for **11**. The asymmetric unit of **15** is given in Figure III. 13, whereas the selected bond lengths and angles are reported in Table III. 13, Table III. 14, Table III. 29 and Table III. 30. All the $[W(CN)_8]^{4-}$ anions adopt the SAPR geometry and Zn sites adopt TBPY geometry as evidenced by the minimum CShM values shown in Table III. 11. The shortest W…W distances are 9.40/9.45/9.40 Å.

It is worth to note that the crystal packing for **15** is quite different from that of **13** (Figure III. 14). **13** and **15** exhibit as two-dimensional and three-dimensional coordination polymers if considering the hydrogen bonds, respectively.

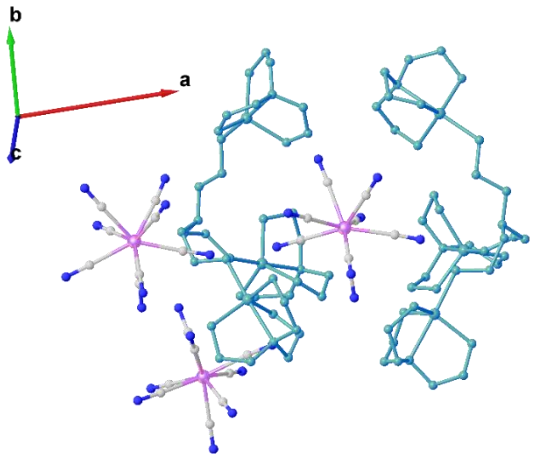

Figure III. 13 Asymmetric unit of **15** in *ab* plane with $[\{Zn(tren)\}_3(\mu\text{-tren})]^{6+}$ units in green.

Table III. 11 Continuous shape measurements (CShM) for metal ions in **15**.

$W(CN)_8$	**W1**	**W2**	**W3**
SAPR	**0.969**	**0.295**	**0.532**
TDD	1.110	1.922	1.781
JBTPR	1.868	2.104	1.934
BTPR	1.151	1.540	1.355

ZnN_5	**Zn1**	**Zn2**	**Zn3**	**Zn4**	**Zn5**	**Zn6**
TBPY	**0.792**	**0.916**	**0.742**	**0.976**	**0.852**	**0.889**
SPY	5.393	4.487	5.890	4.707	4.803	5.930
JTBPY	2.514	2.535	2.449	2.285	2.290	2.413

S: shape measure relatives to the square antiprism (SAPR), triangular dodecahedron (TDD), Johnson elongated triangular bipyramid (JBTPR) and biaugmented trigonal prism (BTPR) for $M(CN)_8$ unit; trigonal bipyramid (TBPY), spherical square pyramid (SPY) and Johnson trigonal bipyramid (JTBPY) for ZnN_5 unit. When the respective shape measure parameter equals zero, the real geometry coincides with the idealized one. For each site, the minimum calculated shape measure is given in violet.

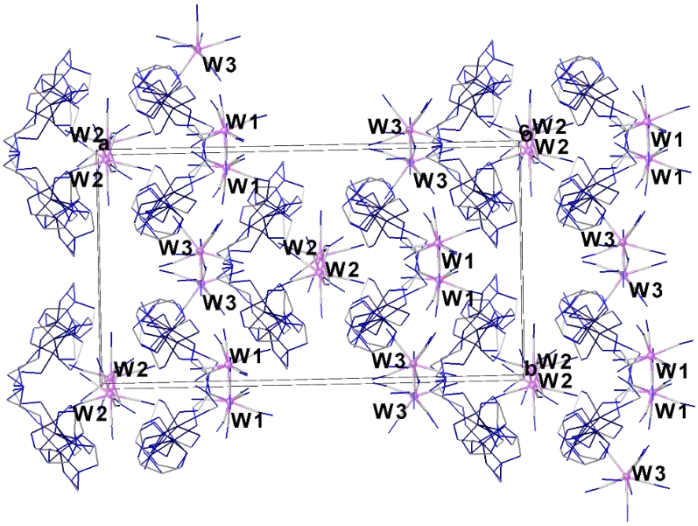

Figure III. 14 Packing diagram of **15**, where the solvent molecules and hydrogen atoms are omitted for clarity.

Table III. 12 Single crystal X-ray diffraction data and structure refinement parameters for $[\{Zn(tren)\}_3(\mu\text{-}tren)]_2[W(CN)_8]_3\cdot 17H_2O$ (**15**)

Compound / CCDC number	**15 / 2083837**
Formula	$W_3Zn_6C_{72}H_{178}N_{56}O_{17}$
$D_{calc.}$/g cm^{-3}	1.537
μ/mm^{-1}	3.760
Formula Weight/g mol^{-1}	3044.39
T/K	150(2)
Crystal System	monoclinic
Space Group	*Cc*
a/Å	31.8599(9)
b/Å	16.9574(3)
c/Å	25.3107(6)
β/°	106.013(3)
V/Å^3	13143.8(6)
Z	4
Z'	1
Wavelength/Å	0.71073
Radiation type	MoK$_a$
Q_{min}/°	1.701
Q_{max}/°	26.733
Measured Refl.	151852
Measured indep. Refl.	27860
Observed indep. Refl.	22758
R_{int}	0.0796
Parameters	1438
Restraints	20
Largest diff. Peak (e-.A^{-3})	1.938
Deepest diff. Hole (e-.A^{-3})	-1.187
GooF (S)	1.018
wR_2 (all data)	0.0959
wR_2	0.0894
R_1 (all data)	0.0574
R_1	0.0397

Table III. 13 Selected bond lengths and angles for $[W^{IV}(CN)_8]^{4-}$ anion in **15**.

	Length/Å		**Length/Å**		**Angle/°**
AverageW1-C	2.168(12)	Average (W1-)C≡N	1.145(14)	Average W1-C≡N	177.7(11)
AverageW2-C	2.165(12)	Average (W2-)C≡N	1.153(14)	Average W2-C≡N	177.3(10)
AverageW3-C	2.172(12)	Average (W3-)C≡N	1.147(14)	Average W3-C≡N	178.2(11)

Table III. 14 Selected bond lengths for $[\{Zn(tren)\}_3(\mu\text{-tren})]^{6+}$ cation in **15**.

	Length/Å		**Length/Å**		**Length/Å**
Average Zn1-N	2.124(8)	Average Zn2-N	2.115(8)	Average Zn3-N	2.128(9)
Average Zn4-N	2.117(12)	Average Zn5-N	2.135(9)	Average Zn6-N	2.121(9)

III.4.2.2 Photomagnetic measurements for $[\{Zn(tren)\}_3(\mu\text{-tren})]_2[W(CN)_8]_3\cdot 17H_2O$ (15)

As evidenced above, **11** and **15** exhibit very similar crystal structures, but they contain a different octacyanometalate anion, though in the same geometry. As shown by the magnetic properties of **15** in Figure III. 15, **15** is a diamagnetic compound in agreement with the diamagnetic configuration of two $Zn^{2+}(3d^{10})$ ions and the one $W^{4+}(5d^2$ in square antiprism geometry) ion, with χT values measured in the dark close to 0. Under light irradiation at 405 nm, the value of χT increased from 0 to reach 0.49 cm^3 mol^{-1} K after 30 hours of irradiation. But the magnetic signal is still far from saturation which limits us to further analyze the photoexcited state. The reduced magnetizations measured after the light excitation are almost superimposed, consistent with a negligible magnetic anisotropy in the photoinduced state. A clear saturation of magnetization at 1.8 K was observed at the value of 0.51 Nβ. The temperature dependence of the χT product from 2 K to 300 K is of similar shape than the χT vs. T plots of **11** and **12**. For **15**, a plateau was observed with a maximum value of 0.66 cm^3 mol^{-1} K around 50 K. Then, a small decrease was observed to reach 0.4 cm^3 mol^{-1} K at 200 K. Above this temperature, a faster decrease of the χT product was observed, and the χT value was back to 0 at 250 K, suggesting that the compound was back in its diamagnetic ground state. This was also confirmed by a new χT vs. T plot measured after the light excitation and thermal heating of the sample.

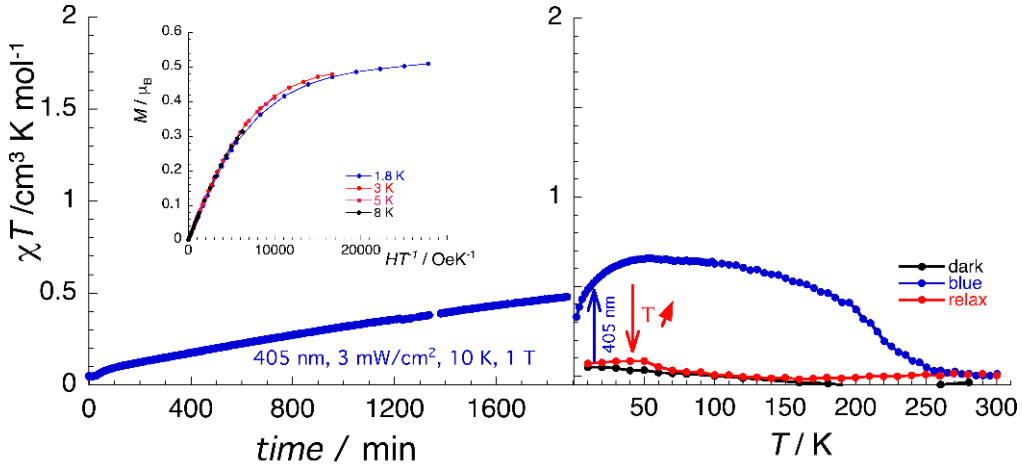

Figure III. 15 (Left) Time dependence of the χT product of **15** during 405 nm light irradiation. (Inset : Reduced magnetizations at different temperatures (1.8 K, 3 K, 5 K and 8 K) in the photo-excited state of **15**) (Right) χT = f(T) plots of **15** measured in the dark before any light irradiation, after 405 nm light irradiation and after reconditioning to 300 K.

III.4.3 Discussion on $[Zn(en)_3]_2[W(CN)_8]\cdot 5H_2O$ (14) and $[\{Zn(tren)\}_3(\mu\text{-tren})]_2[W(CN)_8]_3\cdot 17H_2O$ (15)

In this section, being analogous with molybdenum analogues, we have been able to obtain two new ionic salts containing the 5d $[W(CN)_8]^{4-}$ anion. The $[Mo(CN)_8]^{4-}$ anion is known to be involved in several polynuclear compounds exhibiting photomagnetic properties. On the opposite, despite the similarity of electronic configuration between $W^{IV}(5d^2_{LS})$ and $Mo^{IV}(4d^2_{LS})$ in ground state, only few examples of photomagnetic systems based on the

$[W(CN)_8]^{4-}$ complex have been reported [11-13] and most of cases of the tungsten analogues are reported as not photoresponsive. So it is not surprising that **14** is confirmed as being not photomagnetic in this study.

The photomagnetic properties of the two Zn-based compounds **11** and **15** are similar but **15** displays a lower photoconversion rate than **11**, as shown by the lower observed values in the χT vs. T and M vs. H/T plots. By analogy with **11**, the observed behaviour can be interpreted as a spin crossover from low spin $S = 0$ to high spin $S = 1$ for a $5d^2$ complex. Compared to other systems containing the $[W^{IV}(CN)_8]^{4-}$ units, the photoexcited state of **15** has a significant magnetic response, even at 200 K. This feature shows that the photo-induced state in **15** has a lifetime much higher than that observed in 3d spin crossover metal ions exhibiting the LIESST phenomenon.

III.5 Conclusion and perspectives

In this chapter, a series of new ionic salts based on $[M^{IV}(CN)_8]^{4-}$ charge balanced with coordination cations, $\{Zn(en)_3\}^{2+}$ and $[\{M'(tren)\}_3(\mu\text{-tren})]^{6+}$ ($M' = Cu^{II}$, Zn^{II}, Cd^{II}), have been studied (Table III. 15). Remarkably, we have shown that the incorporation of $[Mo^{IV}(CN)_8]^{4-}$ with $\{Zn(en)_3\}^{2+}$ and $[\{M'(tren)\}_3(\mu\text{-tren})]^{6+}$ cations leads to an important photomagnetic response with a high thermal stability (above 200 K). Importantly, by comparative study of zinc analogue, we proposed that the singlet-triplet conversion mechanism is operative for $[\{Cu(tren)\}_3(\mu\text{-tren})]_2[Mo(CN)_8]_3\cdot 45H_2O\cdot 2CH_3OH$ (**13**), instead of outer-sphere metal-to-metal charge transfer between Cu^{2+} and Mo^{4+}.

The tungsten analogue $[Zn(en)_3]_2[W(CN)_8]\cdot 5H_2O$ (**14**) is not photomagnetic. However, a significant photomagnetic effect is confirmed for $[\{Zn(tren)\}_3(\mu\text{-tren})]_2[W(CN)_8]_3\cdot 17H_2O$ (**15**). So the discrete building block of $[W^{IV}(CN)_8]^{4-}$ can be photoresponsive, but the structural factors that dominate the photomagnetic properties are not clear. This is quite an interesting result because the photoexcited state of **15** has a significant magnetic response, even at 200 K.

To check if these photo-induced changes are also accompanied with a M-CN bond breaking as already reported in the $K_4[Mo^{IV}(CN)_8]\cdot 2H_2O$, other measurements are necessary such as photocrystallography at low temperature. These compounds containing $[\{M'(tren)\}_3(\mu\text{-tren})]^{6+}$ cations are not the best candidates for that because of their huge solvent content, but it is worth to perform photocrystallography studies for compounds containing $\{Zn(en)_3\}^{2+}$. IR studies for sample after light irradiation as well as further magnetization studies are needed to investigate the irreversible parts for **10**, **11** and **12**. For time constraints of this phD thesis, these studies will be performed later. To further explain the structure and photomagnetic property relationship in ionic compounds built with $[M(CN)_8]^{4-}$ anions, the exploration of other type of cations to modify the spatial arrangement of photomagnetic-active $[Mo^{IV}(CN)_8]^{4-}$ is still necessary. To reveal the uncommon photomagnetic phenomena for photoresponsive $[W^{IV}(CN)_8]^{4-}$, theoretical calculations are necessary as well as the preparation of new compounds based on this anion.

Table III. 15 The comparsion of selected structral parameters for compounds studied in this chapter.

Compound	**10**	**11**	**13**	**15**
T/K	296(2)	130(2)	130(2)	150(2)
S_{SAPR}	0.273	0.232-0.836	0.218-0.652	0.295-0.969
Mo-C $_{av.}$/Å	2.177(3)	2.166(12)-2.179(12)	2.153(13)-2.179(10)	2.165(12)-2.172(12)
C-N $_{av.}$/Å	1.151(3)	1.132(12)-1.150(12)	1.135(6)-1.157(10)	1.145(14)-1.153(14)
Mo-C-N $_{av.}$/°	178.7(2)	176.6(13)-177.7(15)	175.9(12)-177.5(9)	177.3(10)- 178.2(11)
$d_{Mo\ldots Mo}$/Å	9.48	9.46-9.48	9.65-9.80	9.40-9.45
Photomagnetic properties	$\Delta\chi T$ = 1.2 cm^3 mol^{-1} K, T_{Relax} = 300 K, partial relaxation (χT = 0.2 cm^3 mol^{-1} K)	$\Delta\chi T$ = 0.89 cm^3 mol^{-1} K, T_{Relax} = 300 K, partial relaxation (χT = 0.2 cm^3 mol^{-1} K)	$\Delta\chi T$ = 0.89 cm^3 mol^{-1} K, T_{Relax} = 300 K, full relaxation	$\Delta\chi T$ = 0.66 cm^3 mol^{-1} K, T_{Relax} = 250 K, full relaxation

III.6 Supporting materials

III.6.1 Synthesis

$K_4[Mo^{IV}(CN)_8]\cdot 2H_2O$ and $K_4[W^{IV}(CN)_8]\cdot 2H_2O$ have been synthesized successfully by following the procedure according to the literature.[14]

Preparation of ZnenMo (10).

First, we mixed 2 mL solution of $ZnCl_2$ (36.6 mg, 2.6 mmol) with 500 mg solution of en ligand. **10** was prepared by adding slowly of the above mixture solution to 1 mL solution of $K_4[Mo^{IV}(CN)_8]\cdot 2H_2O$ (50 mg, 1.0 mmol) avoid shaking. The yellow crystals of **10** would appear immediately.

Preparation of ZntrenMo (**11**)

In the first step, we mixed a 2 mL solution of $ZnCl_2$ (30.0 mg, 2.2 mmol) with 240 mg solution of tren ligand. The above mixture solution was added slowly to 1 mL solution of $K_4[Mo^{IV}(CN)_8]\cdot 2H_2O$ (50 mg, 1.0 mmol) avoid shaking. Then 1.5 mL of MeOH was slowly added, and yellow crystals of **11** were obtained after one night.

Preparation of CdtrenMo (12).

12 was prepared by a layering technique. A mixture solution of 3 mL solution $CdCl_2$ (119 mg, 6.5 mmol) and 250 mg of tren ligand was diffused through 20 mL MeOH : H_2O (1:1) into the bottom 1 mL solution of $K_4[Mo^{IV}(CN)_8]\cdot 2H_2O$ (163 mg, 3.3 mmol). Yellow crystals of **12** would appear after one week of slow diffusion.

Preparation of CutrenMo (**13**)

13 was also prepared by a layering technique. A mixture of 3 mL solution $CuCl_2\cdot 2H_2O$ (35.7 mg, 2.0 mmol) and 528 mg of tren ligand was diffused through 20 mL MeOH : H_2O (1:1) solution into the bottom 1 mL solution of $K_4[Mo^{IV}(CN)_8]\cdot 2H_2O$ (100 mg, 2.0 mmol). Green crystals of **11** would appear after one week of slow diffusion.

Preparation of ZnenW (14).

Similarly to **10**, first, we mixed 2 mL solution of $ZnCl_2$ (36.6 mg, 2.6 mmol) with 500 mg solution of en ligand. **14** was prepared by adding slowly of the above mixture solution to 1 mL solution of $K_4[W^{IV}(CN)_8]\cdot 2H_2O$ (58 mg, 1.0 mmol) to avoid rapid mixture. The yellow crystals of **14** were obtained immediately.

Preparation of ZntrenW (**15**)

Similarly to **11**, we first mixed a 2 mL solution of $ZnCl_2$ (30.0 mg, 2.2 mmol) with 240 mg solution of the tren ligand. The above mixture solution was added slowly to 1 mL solution of $K_4[W^{IV}(CN)_8]\cdot 2H_2O$ (58 mg, 1.0 mmol) avoid shaking. Then 1.5 mL of MeOH was slowly added, and yellow crystals of **15** were obtained after one night.

III.6.2 Powder X-ray diffraction analysis

Compound **10** $[Zn(en)_3]_2[Mo(CN)_8]\cdot 5H_2O$

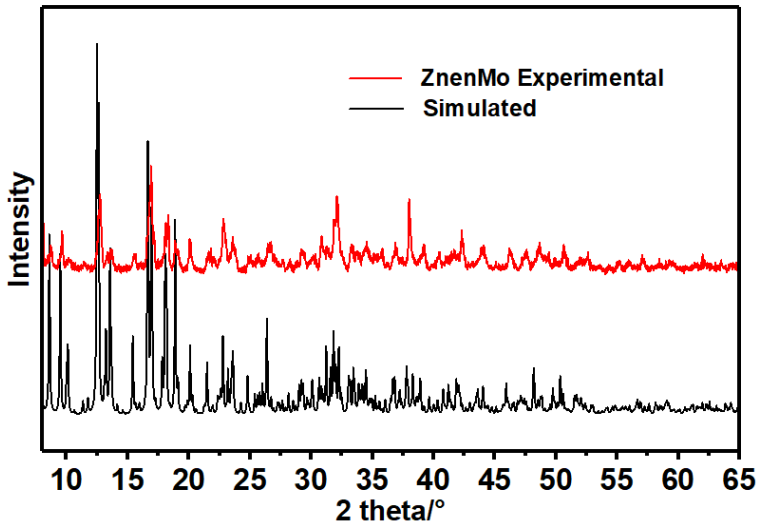

Compound **11** $[\{Zn(tren)\}_3(\mu\text{-tren})]_2[Mo(CN)_8]_3\cdot 18H_2O$

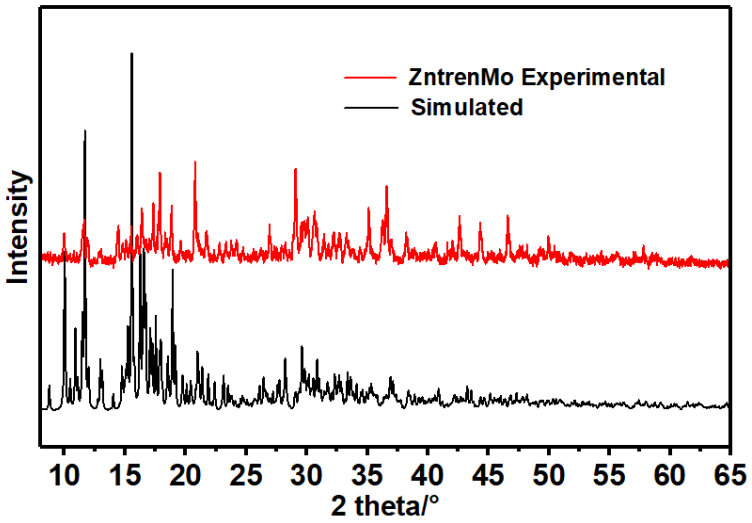

Compound **12** $[\{Cd(tren)\}_3(\mu\text{-tren})]_2[Mo(CN)_8]_3\cdot solv.$

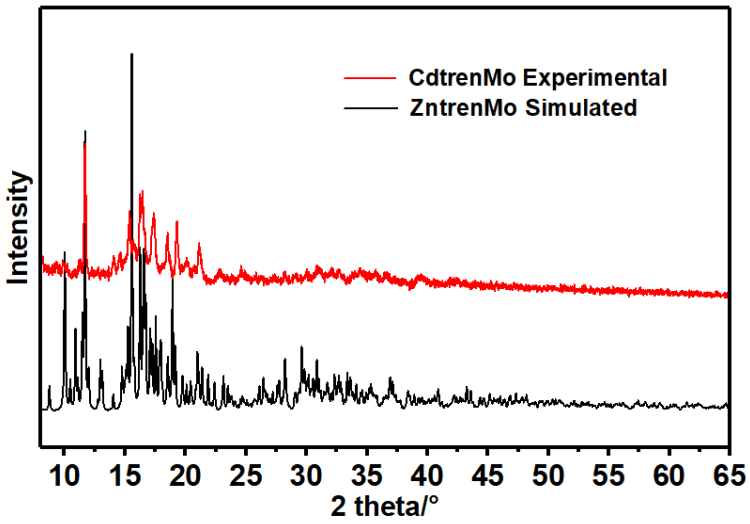

Compound **13** $[\{Cu(tren)\}_3(\mu\text{-tren})]_4[Mo(CN)_8]_6\cdot 45H_2O\cdot 2CH_3OH$

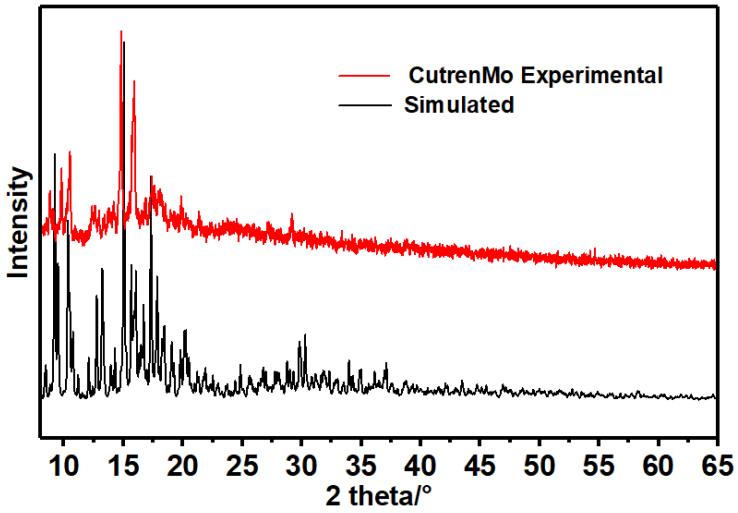

Compound **14** $[Zn(en)_3]_2[W(CN)_8]\cdot 5H_2O$

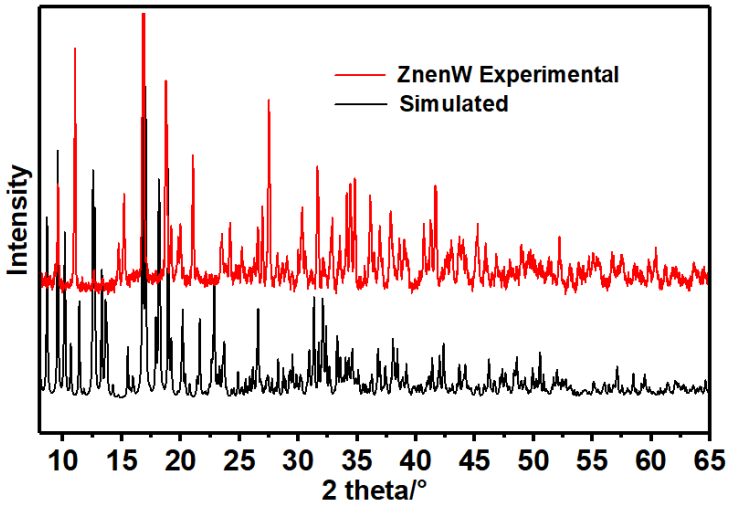

Compound **15** $[\{Zn(tren)\}_3(\mu\text{-tren})]_2[W(CN)_8]_3\cdot 17H_2O$

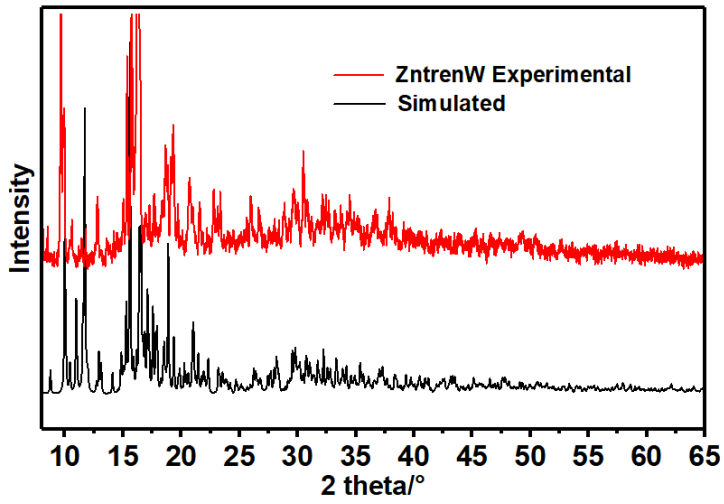

III.6.3 Optical measurements

Table III. 16 The data of optical spectra comparison with reported compounds.

Compounds	Wavelength / nm
$K_4[Mo(CN)_8]\cdot 2H_2O$[15]	430, 368, 308 (Mo ligand field transitions)
$[Cu(tren)(NH_3)][ClO_4]_2$[8]	872, 643
$[\{Cu(tren)\}_3(\mu\text{-tren})]_4[Mo(CN)_8]_6\cdot 45H_2O\cdot 2CH_3OH$ **13**	877, 657, 430, 306
$[\{Zn(tren)\}_3(\mu\text{-tren})]_2[Mo(CN)_8]_3\cdot 18H_2O$ **11**	430, 356
$K_4[W(CN)_8]\cdot 2H_2O$[15]	435, 370, 303 (W ligand field transitions)
$[\{Zn(tren)\}_3(\mu\text{-tren})]_2[W(CN)_8]_3\cdot 17H_2O$ **15**	445, 300

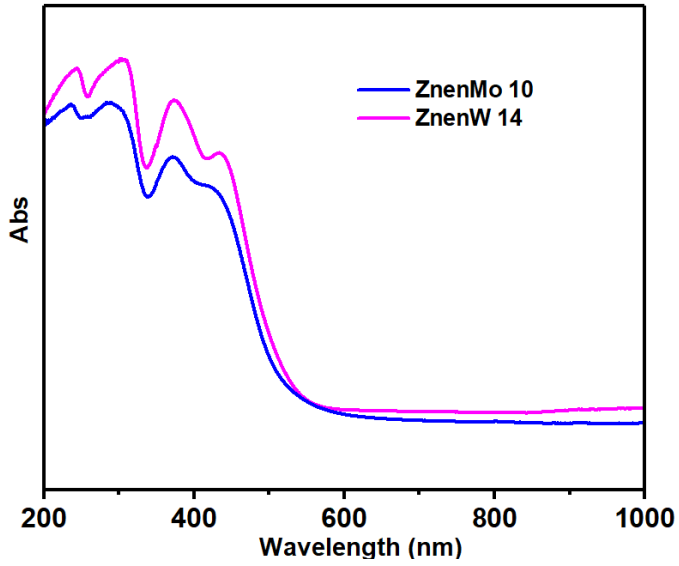

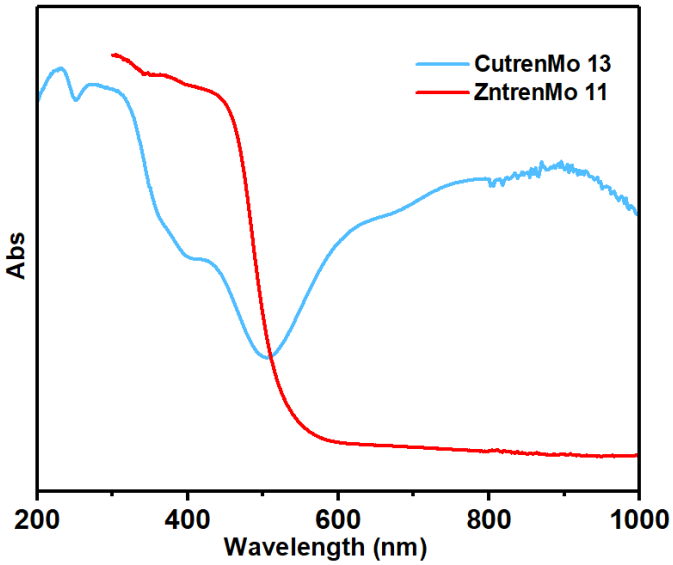

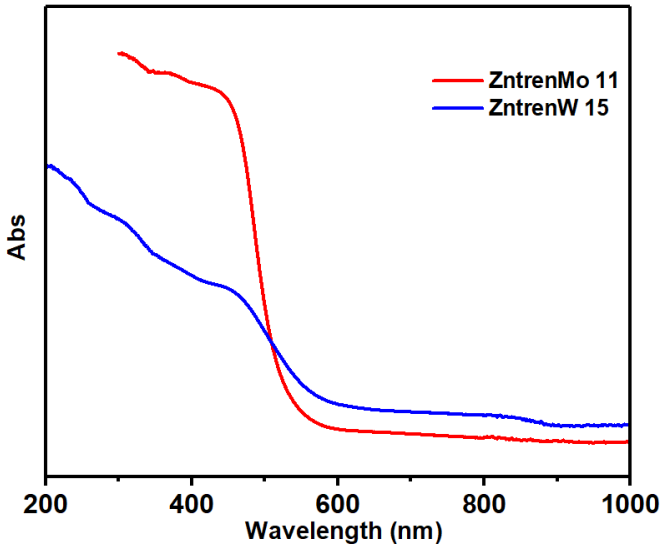

III.6.4 IR spectra

Table III. 17 Possible attribution of IR vibration according to literature.[16]

Region	Assignment
Broad peaks in the 3700 – 3000 cm^{-1}	ν(O–H) stretching bands of water molecules
Sharp peaks in the 3000 – 2750 cm^{-1}	ν(C–H) and ν(N–H) vibrations of the tren ligand
2200 – 2100 cm^{-1}	Stretching bands ν(C≡N) of cyanide group
1700 – 600 cm^{-1}	δ(O–H) bending bands of water and several other bands from the tren ligand: δ(H–C–H), ν(N–C) and ν(C–C)

Table III. 18 The summary of $\tilde{\nu}_{CN}$ stretching bands observed for the compounds involved in this section.

Compounds	$\tilde{\nu}_{CN}$ stretching bands / cm^{-1}
$K_4Mo(CN)_8 \cdot 2H_2O$	2160, 2123, 2100, 2059
$[\{Cu(tren)\}_3(\mu\text{-tren})]_4[Mo(CN)_8]_6 \cdot 45H_2O \cdot 2CH_3OH$ (**13**)	2098
$[\{Zn(tren)\}_3(\mu\text{-tren})]_2[Mo(CN)_8]_3 \cdot 18H_2O$ (**11**)	2098
$K_4W(CN)_8 \cdot 2H_2O$	2168, 2125, 2093, 2056
$[\{Zn(tren)\}_3(\mu\text{-tren})]_2[W(CN)_8]_3 \cdot 17H_2O$ (**15**)	2091
$[Zn(en)_3]_2[Mo(CN)_8] \cdot 5H_2O$ (**10**)	2136, 2123, 2116, 2102
$[Zn(en)_3]_2[W(CN)_8] \cdot 5H_2O$ (**14**)	2137, 2119, 2114, 2094

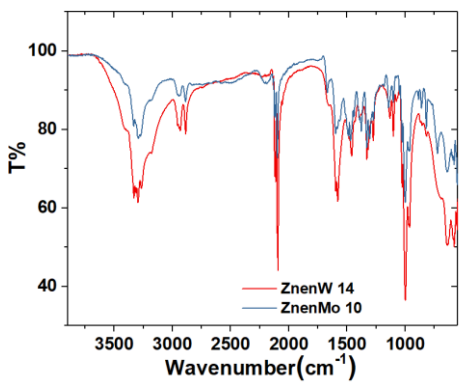

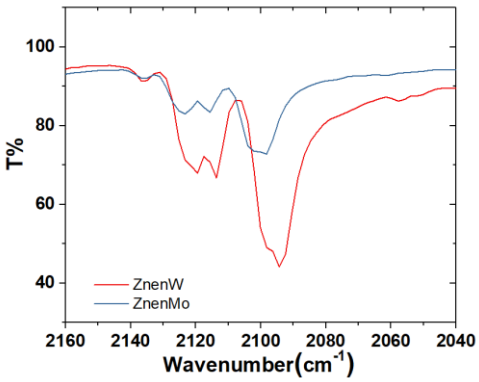

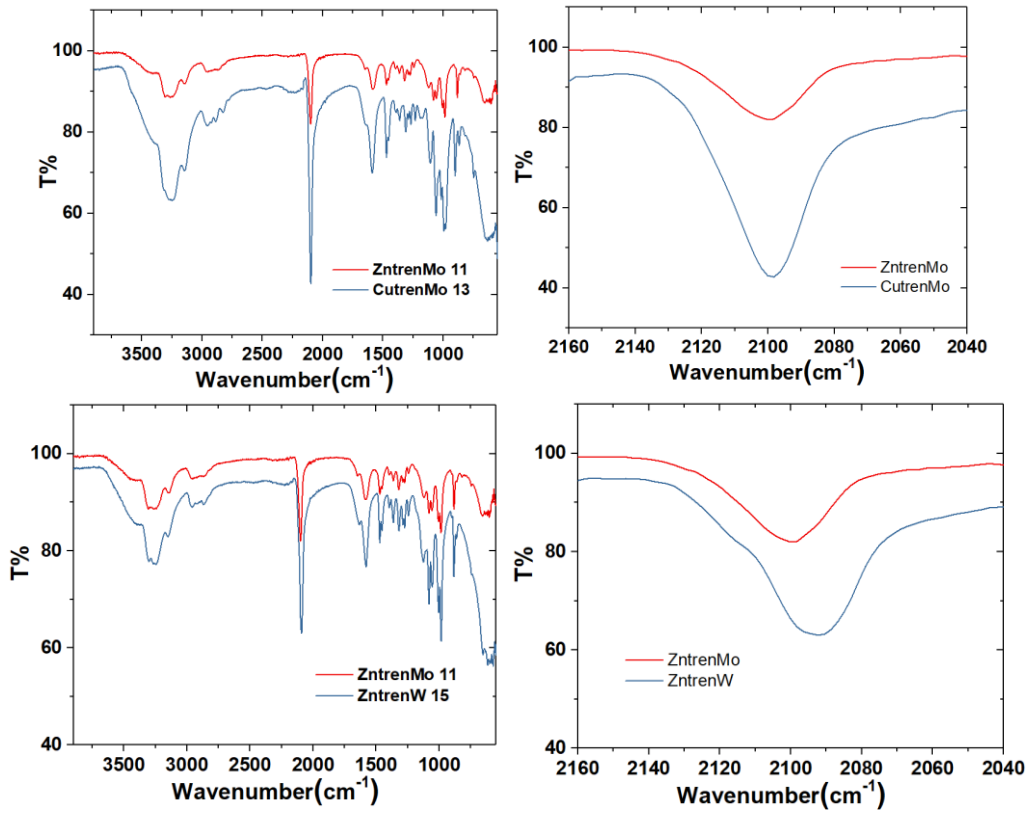

III.6.5 Thermogravimetric analysis

Compound **10** $[Zn(en)_3]_2[Mo(CN)_8]\cdot 5H_2O$

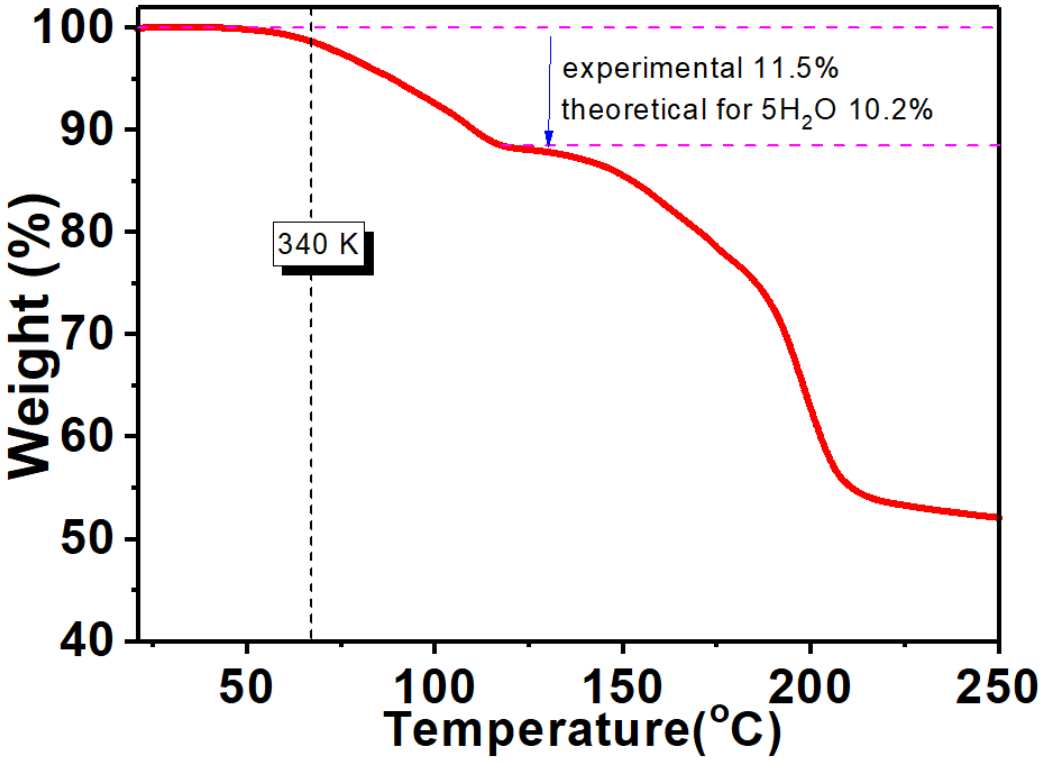

III.6.6 Crystal structure and photomagnetic measurements of $[Zn(en)_3]_2[W(CN)_8]\cdot 5H_2O$ (14)

Single crystal X-ray studies reveal that **14** is isostructural with the corresponding molybdenum analogue (**10**). (Table III. 20 and Figure III. 16) However, the average W-C and C-N distances are also significantly decreased for **14** (Table III. 19, Table III. 27 and Table III. 28).

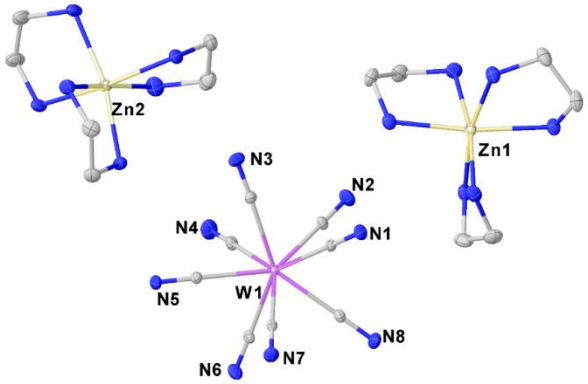

Figure III. 16 ORTEP diagram of molecule fragment of **14** with selected atoms labelling. Thermal ellipsoids of 50 % probability are shown. Color codes: N, blue; C, grey; Zn, light yellow; Mo, pink.

Table III. 19 Selected average bond lengths and angles for $[W^{IV}(CN)_8]^{4-}$ and $[Zn(en)_3]^{2+}$ in **14**.

	Length/Å		**Length/Å**		**Angle/°**
Average W1-C	2.171(4)	Average (W1-)C≡N	1.142(6)	Average W1-C≡N	178.7(2)
Average Zn1-N	2.192(4)	Average Zn2-N	2.194(4)		

Time dependent photomagnetic measurements were also performed with **14**. Drastically different with molybdenum analogue, **14** showed clearly no photomagnetic effect with 5 hours of 405 nm light irradiation at 10 K (Figure III. 17).

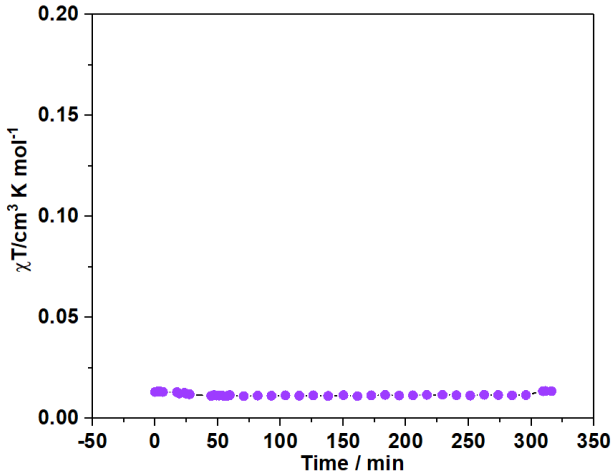

Figure III. 17 Time dependence of the χT for **14** measured at 10 K, 1 T with continuous 405 nm blue light irradiation.

Table III. 20 Single crystal X-ray diffraction data and structure refinement parameters for **14**.

Compound	**14**
Formula	$C_{20}H_{52}N_{20}O_5WZn_2$
$D_{calc.}$/g cm^{-3}	1.636
μ/mm^{-1}	4.190
Formula Weight/g mol^{-1}	967.40
T/K	296(2)
Crystal System	monoclinic
Space Group	$P2_1/n$
a/Å	13.4564(6)
b/Å	16.5881(7)
c/Å	17.6669(8)
β/°	95.1630(10)
V/Å^3	3927.5(3)
Z	4
Z'	1
Wavelength/Å	0.71073
Radiation type	MoK$_a$
Q_{min}/°	1.954
Q_{max}/°	27.481
Measured Refl.	93571
Independent Refl.	9000
Reflections with I > 2(I)	8020
R_{int}	0.0292
Parameters	455
GooF	1.334
wR_2 (all data)	0.0945
wR_2	0.0865
R_1 (all data)	0.0412
R_1	0.0344
S_{SAPR}	0.268
S_{TDD}	1.918

S is continuous shape measurement (CShM) value. SAPR and TDD represent square antiprism and triangular dodecahedron, respectively.

III.6.7 Annex

Table III. 21 Selected bond lengths and angles for $[Mo^{IV}(CN)_8]^{4-}$ anion in **10**.

Atoms		**Length/Å**	**Atoms**		**Length/Å**		**Atoms**		**Angle/°**
Mo1	C1	2.180(3)	N1	C1	1.152(3)	N1	C1	Mo1	179.5(2)
Mo1	C2	2.179(3)	N2	C2	1.155(3)	N2	C2	Mo1	178.5(2)
Mo1	C3	2.180(3)	N3	C3	1.156(3)	N3	C3	Mo1	177.6(3)
Mo1	C4	2.171(3)	C4	N4	1.147(4)	N4	C4	Mo1	178.9(3)
Mo1	C5	2.169(3)	C5	N5	1.143(3)	N5	C5	Mo1	179.0(2)
Mo1	C6	2.179(3)	C6	N6	1.150(3)	N6	C6	Mo1	178.9(2)
Mo1	C7	2.183(3)	N7	C7	1.158(3)	N7	C7	Mo1	179.1(2)
Mo1	C8	2.172(3)	N8	C8	1.146(3)	N8	C8	Mo1	178.1(3)
Average		2.177(3)	Average		1.151(3)	Average			178.7(2)

Table III. 22 Selected bond lengths and angles for $[Zn(en)_3]^{2+}$ anion in **10**.

Atoms		**Length/Å**	**Atoms**		**Length/Å**
Zn1	N14	2.203(3)	Zn2	N20	2.193(3)
Zn1	N11	2.234(3)	Zn2	N16	2.217(3)
Zn1	N9	2.240(3)	Zn2	N19	2.220(3)
Zn1	N10	2.158(3)	Zn2	N17	2.214(3)
Zn1	N13	2.191(3)	Zn2	N18	2.204(3)
Zn1	N12	2.186(3)	Zn2	N15	2.174(3)
Average		2.202(3)	Average		2.204(3)

Table III. 23 Selected bond lengths and angles for $[Mo^{IV}(CN)_8]^{4-}$ anion in **11**.

Atoms		**Length/Å**	**Atoms**		**Length/Å**		**Atoms**		**Angle/°**
Mo1	C1	2.168(14)	N1	C1	1.164(19)	N1	C1	Mo1	176.6(12)
Mo1	C2	2.180(11)	N2	C2	1.112(16)	N2	C2	Mo1	176.2(13)
Mo1	C3	2.181(13)	N3	C3	1.129(18)	N3	C3	Mo1	175.2(13)
Mo1	C4	2.178(16)	N4	C4	1.14(2)	N4	C4	Mo1	175.2(16)
Mo1	C5	2.157(12)	N5	C5	1.136(17)	N5	C5	Mo1	179.8(16)
Mo1	C6	2.206(14)	N6	C6	1.11(2)	N6	C6	Mo1	178(2)
Mo1	C7	2.175(12)	N7	C7	1.144(17)	N7	C7	Mo1	178.7(12)
Mo1	C8	2.144(13)	N8	C8	1.18(2)	N8	C8	Mo1	176.6(15)
Average		2.174 (13)	Average		1.139(12)	Average			177.0(12)

(continue of Table III. 23)

Mo2	C9	2.153(13)	N9	C9	1.150(18)	N9	C9	Mo2	177.1(11)
Mo2	C10	2.199(9)	N10	C10	1.126(16)	N10	C10	Mo2	177.2(13)
Mo2	C11	2.146(14)	N11	C11	1.14(2)	N11	C11	Mo2	178.8(17)
Mo2	C12	2.200(10)	N12	C12	1.156(19)	N12	C12	Mo2	178.9(16)
Mo2	C13	2.147(14)	N13	C13	1.18(2)	N13	C13	Mo2	177.9(18)
Mo2	C14	2.160(12)	N14	C14	1.148(19)	N14	C14	Mo2	176.9(14)
Mo2	C15	2.187(12)	N15	C15	1.116(19)	N15	C15	Mo2	178.2(14)
Mo2	C16	2.133(14)	N16	C16	1.18(2)	N16	C16	Mo2	176.3(17)
Average		2.166(12)	Average		1.150(12)	Average			177.7(15)
Mo3	C17	2.164(12)	N17	C17	1.177(19)	N17	C17	Mo3	175.8(13)
Mo3	C18	2.176(16)	N18	C18	1.13(2)	N18	C18	Mo3	178.1(14)
Mo3	C19	2.178(13)	N19	C19	1.128(19)	N19	C19	Mo3	175.0(14)
Mo3	C20	2.146(14)	N20	C20	1.151(19)	N20	C20	Mo3	178.3(13)
Mo3	C21	2.21(2)	N21	C21	1.10(3)	N21	C21	Mo3	176(2)
Mo3	C22	2.216(12)	N22	C22	1.075(19)	N22	C22	Mo3	177.9(19)
Mo3	C23	2.160(14)	N23	C23	1.20(2)	N23	C23	Mo3	174.2(13)
Mo3	C24	2.178(12)	N24	C24	1.095(19)	N24	C24	Mo3	177.6(14)
Average		2.179(12)	Average		1.132(12)	Average			176.6(13)

Table III. 24 Selected bond lengths for $[\{Zn(tren)\}_3(\mu\text{-tren})]^{6+}$ cation in **11**.

Atoms		**Length/Å**	**Atoms**		**Length/Å**		**Atoms**	**Length/Å**
Zn1	N25	2.095(14)	Zn2	N30	2.081(11)	Zn3	N34	2.015(19)
Zn1	N26	2.075(14)	Zn2	N31	2.081(13)	Zn3	N35	2.02(2)
Zn1	N27	2.084(11)	Zn2	N32	2.065(13)	Zn3	N36	2.055(16)
Zn1	N28	2.294(12)	Zn2	N33	2.119(10)	Zn3	N37	2.272(16)
Zn1	N29	2.101(11)	Zn2	N39	2.315(13)	Zn3	N40	2.193(19)
Average		2.130(12)	Average		2.132(12)	Average		2.111(14)
Zn4	N41	2.070(11)	Zn5	N46	2.077(11)	Zn6	N51	2.113(12)
Zn4	N42	2.077(11)	Zn5	N47	2.082(11)	Zn6	N52	2.102(11)
Zn4	N43	2.103(12)	Zn5	N48	2.073(10)	Zn6	N53	2.063(12)
Zn4	N44	2.259(12)	Zn5	N49	2.301(12)	Zn6	N54	2.311(11)
Zn4	N45	2.110(12)	Zn5	N50	2.105(10)	Zn6	N55	2.101(10)
Average		2.124(12)	Average		2.128(11)	Average		2.138(11)

Table III. 25 Selected bond lengths and angles for $[Mo^{IV}(CN)_8]^{4-}$ anion in **13**.

Atoms		**Length/Å**	**Atoms**		**Length/Å**	**Atoms**			**Angle/°**
Mo1	C1	2.166(10)	N1	C1	1.176(15)	N1	C1	Mo1	177.8(9)
Mo1	C2	2.192(9)	N2	C2	1.143(14)	N2	C2	Mo1	174.4(10)
Mo1	C3	2.187(8)	N3	C3	1.131(14)	N3	C3	Mo1	177.8(10)
Mo1	C4	2.175(11)	N4	C4	1.139(15)	N4	C4	Mo1	178.5(9)
Mo1	C5	2.185(9)	N5	C5	1.139(14)	N5	C5	Mo1	175.7(9)
Mo1	C6	2.165(11)	N6	C6	1.153(14)	N6	C6	Mo1	177.0(10)
Mo1	C7	2.185(9)	N7	C7	1.131(14)	N7	C7	Mo1	178.4(9)
Mo1	C8	2.178(9)	N8	C8	1.145(14)	N8	C8	Mo1	176.7(10)
Average		2.179(10)	Average		1.145(14)	Average			177.0(10)
Mo2	C9	2.178(10)	N9	C9	1.118(15)	N9	C9	Mo2	177.5(11)
Mo2	C10	2.169(10)	N10	C10	1.140(14)	N10	C10	Mo2	179.0(9)
Mo2	C11	2.158(10)	N11	C11	1.153(14)	N11	C11	Mo2	175.4(8)
Mo2	C12	2.169(9)	N12	C12	1.137(13)	N12	C12	Mo2	176.2(9)
Mo2	C13	2.173(9)	N13	C13	1.147(13)	N13	C13	Mo2	177.1(10)
Mo2	C14	2.154(10)	C14	N14	1.152(16)	N14	C14	Mo2	177.8(11)
Mo2	C15	2.194(9)	N15	C15	1.138(14)	N15	C15	Mo2	174.9(9)
Mo2	C16	2.165(9)	N16	C16	1.145(14)	N16	C16	Mo2	175.7(9)
Average		2.170(10)	Average		1.141(14)	Average			176.7(10)
Mo3	C17	2.196(14)	C17	N17	1.11(2)	N17	C17	Mo3	177.6(14)
Mo3	C18	2.184(13)	C18	N18	1.14(2)	N18	C18	Mo3	176.0(14)
Mo3	C19	2.169(13)	N19	C19	1.107(18)	N19	C19	Mo3	177.2(13)
Mo3	C20	2.186(14)	N20	C20	1.12(2)	N20	C20	Mo3	177.1(15)
Mo3	C21	2.173(16)	C21	N21	1.11(2)	N21	C21	Mo3	175.4(19)
Mo3	C22	2.166(14)	N22	C22	1.17(2)	N22	C22	Mo3	173(2)
Mo3	C23	2.153(14)	N23	C23	1.194(19)	N23	C23	Mo3	177.7(14)
Mo3	C24	2.177(15)	C24	N24	1.13(2)	N24	C24	Mo3	173(2)
Average		2.176(14)	Average		1.135(6)	Average			175.9(12)
Mo4	C25	2.147(13)	C25	N25	1.162(18)	N25	C25	Mo4	176.2(11)
Mo4	C26	2.204(10)	N26	C26	1.121(14)	N26	C26	Mo4	174.8(9)
Mo4	C27	2.176(9)	N27	C27	1.154(14)	N27	C27	Mo4	178.0(9)
Mo4	C28	2.163(10)	N28	C28	1.152(14)	N28	C28	Mo4	178.4(9)
Mo4	C29	2.174(10)	N29	C29	1.136(14)	N29	C29	Mo4	179.1(10)
Mo4	C30	2.161(8)	N30	C30	1.145(14)	N30	C30	Mo4	179.7(10)
Mo4	C31	2.196(14)	C31	N31	1.11(2)	N31	C31	Mo4	178(2)
Mo4	C32	2.198(9)	N32	C32	1.119(15)	N32	C32	Mo4	175.7(12)
Average		2.177(10)	Average		1.137(13)	Average			177.5(9)

(continue of Table III. 25)

Mo5	C33	2.137(14)	C33	N33	1.18(2)	N33	C33	Mo5	175.5(18)
Mo5	C34	2.160(14)	N34	C34	1.16(2)	N34	C34	Mo5	177.7(15)
Mo5	C35	2.127(11)	N35	C35	1.170(17)	N35	C35	Mo5	178.0(13)
Mo5	C36	2.176(12)	N36	C36	1.122(17)	N36	C36	Mo5	176.6(14)
Mo5	C37	2.114(14)	N37	C37	1.181(18)	N37	C37	Mo5	177.0(10)
Mo5	C38	2.194(13)	N38	C38	1.13(2)	N38	C38	Mo5	177.8(15)
Mo5	C39	2.172(10)	N39	C39	1.162(17)	N39	C39	Mo5	178.5(13)
Mo5	C40	2.144(13)	C40	N40	1.15(2)	N40	C40	Mo5	173(3)
Average		2.153(13)	Average		1.157(10)	Average			176.8(13)
Mo6	C41	2.175(10)	N41	C41	1.134(14)	N41	C41	Mo6	177.8(11)
Mo6	C42	2.160(10)	C42	N42	1.149(16)	N42	C42	Mo6	178.6(13)
Mo6	C43	2.172(9)	N43	C43	1.129(14)	N43	C43	Mo6	176.3(9)
Mo6	C44	2.172(10)	N44	C44	1.146(13)	N44	C44	Mo6	174.9(9)
Mo6	C45	2.174(9)	N45	C45	1.134(14)	N45	C45	Mo6	179.2(11)
Mo6	C46	2.176(11)	N46	C46	1.131(15)	N46	C46	Mo6	178.2(10)
Mo6	C47	2.154(10)	N47	C47	1.140(14)	N47	C47	Mo6	175.7(8)
Mo6	C48	2.170(10)	N48	C48	1.138(14)	N48	C48	Mo6	177.7(9)
Average		2.169(10)	Average		1.138(14)	Average			177.3(10)

Table III. 26 Selected bond lengths for $[\{Cu(tren)\}_3(\mu\text{-tren})]^{6+}$ cation in **13**.

Atoms		**Length/Å**	**Atoms**		**Length/Å**		**Atoms**	**Length/Å**
Cu1	N64	2.045(8)	Cu2	N50	1.993(9)	Cu3	N55	2.022(9)
Cu1	N60	1.984(9)	Cu2	N54	2.068(12)	Cu3	N57	2.148(9)
Cu1	N62	2.104(9)	Cu2	N52	2.129(11)	Cu3	N56	2.046(9)
Cu1	N61	2.091(9)	Cu2	N51	2.059(11)	Cu3	N59	2.082(10)
Cu1	N63	2.120(8)	Cu2	N53	2.101(12)	Cu3	N58	2.066(10)
Average		2.069(9)	Average		2.070(11)	Average		2.073(9)
Cu4	N66	2.020(9)	Cu5	N80	2.027(14)	Cu6	N72	2.020(8)
Cu4	N75	2.082(9)	Cu5	N79	2.170(16)	Cu6	N68	2.000(10)
Cu4	N74	2.113(10)	Cu5	N78	2.024(19)	Cu6	N69	2.067(12)
Cu4	N76	2.064(10)	Cu5	N67	1.998(14)	Cu6	N71	2.171(10)
Cu4	N73	2.048(18)	Cu5	N77	2.060(18)	Cu6	N70	2.024(12)
Average		2.065(11)	Average		2.056(16)	Average		2.056(10)

(continue of Table III. 26)

Cu7	N10	2.034(8)	Cu8	N95	2.000(10)	Cu9	N94	2.027(9)
Cu7	N98	2.099(10)	Cu8	N10	2.076(10)	Cu9	N108	2.096(9)
Cu7	N96	2.008(9)	Cu8	N10	2.117(10)	Cu9	N107	2.136(11)
Cu7	N97	2.105(9)	Cu8	N10	2.085(12)	Cu9	N105	2.035(12)
Cu7	N99	2.131(11)	Cu8	N10	2.066(13)	Cu9	N106	2.027(11)
Average		2.075(9)	Average		2.069(11)	Average		2.064(10)
Cu10	N84	2.014(11)	Cu11	N83	1.981(8)	Cu12	N82	2.000(10)
Cu10	N11	2.049(10)	Cu11	N85	2.116(8)	Cu12	N90	2.140(9)
Cu10	N11	2.076(12)	Cu11	N86	2.104(10)	Cu12	N92	2.076(10)
Cu10	N10	2.117(16)	Cu11	N88	2.048(9)	Cu12	N89	2.073(9)
Cu10	N11	2.093(14)	Cu11	N87	2.081(16)	Cu12	N91	2.058(13)
Average		2.070(13)	Average		2.066(10)	Average		2.069(10)

Table III. 27 Selected bond lengths and angles for $[W^{IV}(CN)_8]^{4-}$ anion in **14**.

Atoms		**Length/Å**	**Atoms**		**Length/Å**		**Atoms**		**Angle/°**
W1	C1	2.180(4)	N1	C1	1.138(5)	N1	C1	W1	179.5(4)
W1	C2	2.167(4)	N2	C2	1.150(6)	N2	C2	W1	178.5(4)
W1	C3	2.171(4)	N3	C3	1.148(6)	N3	C3	W1	177.5(4)
W1	C4	2.170(4)	C4	N4	1.133(6)	N4	C4	W1	179.0(5)
W1	C5	2.173(4)	C5	N5	1.132(5)	N5	C5	W1	178.4(4)
W1	C6	2.177(4)	C6	N6	1.143(6)	N6	C6	W1	179.1(4)
W1	C7	2.168(4)	N7	C7	1.147(6)	N7	C7	W1	179.1(4)
W1	C8	2.162(4)	N8	C8	1.147(6)	N8	C8	W1	177.9(4)
Average		2.171(4)	Average		1.142(6)		Average		178.6(4)

Table III. 28 Selected bond lengths and angles for $[Zn(en)_3]^{2+}$ anion in **14**.

Atoms		**Length/Å**	**Atoms**		**Length/Å**
Zn1	N14	2.182(4)	Zn2	N20	2.180(4)
Zn1	N11	2.223(4)	Zn2	N16	2.211(4)
Zn1	N9	2.233(4)	Zn2	N19	2.209(4)
Zn1	N10	2.152(4)	Zn2	N17	2.197(4)
Zn1	N13	2.184(4)	Zn2	N18	2.199(4)
Zn1	N12	2.179(4)	Zn2	N15	2.169(5)
Average		2.192(4)	Average		2.194(4)

Table III. 29 Selected bond lengths and angles for $[W^{IV}(CN)_8]^{4-}$ anion in **15**.

Atoms		**Length/Å**	**Atoms**		**Length/Å**	**Atoms**			**Angle/°**
W1	C1	2.144(11)	N1	C1	1.158(14)	N1	C1	W1	177.8(10)
W1	C7	2.166(11)	N7	C7	1.139(13)	N7	C7	W1	177.7(9)
W1	C6	2.150(11)	N6	C6	1.167(14)	N6	C6	W1	177.7(10)
W1	C2	2.172(12)	N2	C2	1.154(14)	N2	C2	W1	179.1(10)
W1	C3	2.161(11)	C3	N3	1.137(14)	N3	C3	W1	179.3(11)
W1	C4	2.200(12)	N4	C4	1.117(14)	N4	C4	W1	179.0(12)
W1	C8	2.198(12)	N8	C8	1.133(14)	N8	C8	W1	174.8(10)
W1	C5	2.155(13)	N5	C5	1.155(15)	N5	C5	W1	175.8(14)
Average		2.168(12)	Average		1.145(14)	Average			177.7(11)
W2	C10	2.151(11)	C10	N10	1.134(13)	N10	C10	W2	178.3(9)
W2	C9	2.162(11)	N9	C9	1.146(13)	N9	C9	W2	178.0(10)
W2	C13	2.176(12)	N13	C13	1.153(14)	N13	C13	W2	175.3(9)
W2	C15	2.149(12)	N15	C15	1.169(14)	N15	C15	W2	176.4(9)
W2	C11	2.143(11)	N11	C11	1.163(13)	N11	C11	W2	178.0(11)
W2	C16	2.179(12)	N16	C16	1.151(13)	N16	C16	W2	175.3(10)
W2	C14	2.168(12)	C14	N14	1.163(14)	N14	C14	W2	178.8(11)
W2	C12	2.192(11)	N12	C12	1.143(14)	N12	C12	W2	178.3(10)
Average		2.165(12)	Average		1.153(14)	Average			177.3(10)
W3	C20	2.163(11)	C20	N20	1.119(13)	N20	C20	W3	179.5(10)
W3	C22	2.176(13)	N22	C22	1.158(15)	N22	C22	W3	179.0(10)
W3	C18	2.117(12)	C18	N18	1.174(14)	N18	C18	W3	177.8(11)
W3	C23	2.155(12)	N23	C23	1.192(15)	N23	C23	W3	177.2(12)
W3	C19	2.193(11)	N19	C19	1.147(13)	N19	C19	W3	177.5(9)
W3	C21	2.202(13)	N21	C21	1.113(14)	N21	C21	W3	177.3(11)
W3	C17	2.179(12)	N17	C17	1.144(14)	N17	C17	W3	179.6(12)
W3	C24	2.188(13)	N24	C24	1.127(15)	N24	C24	W3	178.0(12)
Average		2.172(12)	Average		1.147(14)	Average			178.2(11)

Table III. 30 Selected bond lengths for $[\{Zn(tren)\}_3(\mu\text{-tren})]^{6+}$ cation in **15**.

Atoms		**Length/Å**	**Atoms**		**Length/Å**	**Atoms**		**Length/Å**
Zn1	N28	2.113(8)	Zn2	N36	2.308(8)	Zn3	N56	2.299(9)
Zn1	N51	2.061(8)	Zn2	N33	2.081(9)	Zn3	N54	2.083(9)
Zn1	N49	2.081(8)	Zn2	N35	2.042(9)	Zn3	N53	2.076(8)
Zn1	N52	2.283(9)	Zn2	N27	2.080(8)	Zn3	N26	2.110(8)
Zn1	N50	2.080(9)	Zn2	N34	2.063(8)	Zn3	N55	2.070(9)
Average		2.124(8)	Average		2.115(8)	Average		2.128(9)
Zn4	N48	2.295(12)	Zn5	N57	2.107(8)	Zn6	N61	2.295(9)
Zn4	N45	2.097(11)	Zn5	N43	2.060(9)	Zn6	N59	2.060(8)
Zn4	N47	2.020(14)	Zn5	N42	2.090(9)	Zn6	N38	2.122(8)
Zn4	N39	2.146(12)	Zn5	N44	2.351(9)	Zn6	N58	2.034(10)
Zn4	N46	2.028(13)	Zn5	N41	2.067(10)	Zn6	N60	2.095(10)
Average		2.117(12)	Average		2.135(9)	Average		2.121(9)

III.7 References

1. Bridonneau, N.; Long, J.; Cantin, J. L.; Von Bardeleben, J.; Pillet, S.; Bendeif, E. E.; Aravena, D.; Ruiz, E.; Marvaud, V., First Evidence of Light-induced Spin Transition in Molybdenum(IV). *Chem. Commun.* **2015,** *51* (39), 8229-8232.
2. Korzeniak, T.; Jankowski, R.; Kozieł, M.; Pinkowicz, D.; Sieklucka, B., Reversible Single-Crystal-to-Single-Crystal Transformation in Photomagnetic Cyanido-Bridged Cd_4M_2 Octahedral Molecules. *Inorg. Chem.* **2017,** *56* (21), 12914-12919.
3. Koziel, M.; Podgajny, R.; Kania, R.; Lebris, R.; Mathoniere, C.; Lewinski, K.; Kruczala, K.; Rams, M.; Labrugere, C.; Bousseksou, A.; Sieklucka, B., Series of $M^I[Co(bpy)_3][Mo(CN)_8].nH_2O$ (M^I = Li (1), K (2), Rb (3), Cs (4); *n* = 7-8) exhibiting reversible diamagnetic to paramagnetic transition coupled with dehydration-rehydration process. *Inorg. Chem.* **2010,** *49* (6), 2765-72.
4. Herrera, J. M.; Marvaud, V.; Verdaguer, M.; Marrot, J.; Kalisz, M.; Mathonière, C., Reversible Photoinduced Magnetic Properties in the Heptanuclear Complex $[Mo^{IV}(CN)_2(CN\text{-}CuL)_6]^{8+}$: A Photomagnetic High-Spin Molecule. *Angew. Chem. Int. Ed.* **2004,** *43* (41), 5468-5471.
5. Zhang, W.; Sun, H. L.; Sato, O., Synthesis, characterization, and photoresponsive properties of a series of Mo(IV)-Cu(II) complexes. *Dalton Trans.* **2011,** *40* (12), 2735-2743.
6. Zhang, W.; Sun, H. L.; Sato, O., A one-dimensional homochiral Mo(iv)-Cu(ii) coordination polymer: Spontaneous resolution and photoresponsive properties. *CrystEngComm.* **2010,** *12* (12), 4045-4047.
7. Bridonneau, N.; Quatremare, P.; von Bardeleben, H. J.; Cantin, J.-L.; Pillet, S.; Bendeif, E.-E.; Marvaud, V., Direct Evidence of a Photoinduced Electron Transfer in Diluted "Molybdenum-Copper" Molecular Compounds. *Eur. J. Inorg. Chem.* **2017**, 370–377.
8. Duggan, M.; Ray, N.; Hathaway, B.; Tomlinson, G.; Brint, P.; Pelin, K., Crystal structure and electronic properties of ammine[tris(2-aminoethyl)amine]copper(II) diperchlorate and potassium penta-amminecopper(II) tris(hexafluorophosphate). *J. Chem. Soc., Dalton Trans.* **1980,** (8), 1342-1348.
9. P. Y. Shek, I.; Lau, T.-C.; Wong, W.-T.; Zuo, J.-L., A novel trinuclear copper(II) complex bridged by tren: $[Cu_3(tren)_4][Pt(CN)_4]_3{\cdot}2H_2O$. *New J. Chem.* **1999,** *23* (11), 1049-1050.
10. Korzeniak, T.; Mathonière, C.; Kaiba, A.; Guionneau, P.; Koziel, M.; Sieklucka, B., First example of photomagnetic effects in ionic pairs $[Ni(bipy)_3]_2[Mo(CN)_8]{\cdot}12H2O$. *Inorg. Chim. Acta* **2008,** *361* (12-13), 3500-3504.
11. Magott, M.; Stefanczyk, O.; Sieklucka, B.; Pinkowicz, D., Octacyanidotungstate(IV) Coordination Chains Demonstrate a Light-Induced Excited Spin State Trapping Behavior and Magnetic Exchange Photoswitching. *Angew. Chem. Int. Ed.* **2017,** *56* (43), 13283-13287.
12. Magott, M.; Reczyński, M.; Gaweł, B.; Sieklucka, B.; Pinkowicz, D., A photomagnetic sponge: high-temperature light-induced ferrimagnet controlled by water sorption. *J. Am. Chem. Soc.* **2018,** *140* (46), 15876-15882.
13. Rombaut, G.; Mathonière, C.; Guionneau, P.; Golhen, S.; Ouahab, L.; Verelst, M.; Lecante, P., Structural and photo-induced magnetic properties of $M_2^{II}[W^{IV}(CN)_8]{\cdot}xH_2O$ (M = Fe and x=8, Cu and x=5). Comparison with $Cu_2^{II}[Mo^{IV}(CN)_8]{\cdot}7.5H_2O$. *Inorg. Chim. Acta* **2001,** *326* (1), 27-36.
14. Szklarzewicz, J.; Matoga, D.; Lewiński, K., Photocatalytical Decomposition of Hydrazine in $K_4[Mo(CN)_8]$ Solution: X-ray Crystal Structure of $(PPh_4)_2[Mo(CN)_4O(NH_3)]{\cdot}2H_2O$. *Inorg. Chim. Acta* **2007,** *360* (6), 2002-2008.
15. Perumareddi, J. R.; Liehr, A. D.; Adamson, A. W., Ligand Field Theory of Transition Metal Cyanide Complexes. Part I. The Zero, One and Two Electron or Hole Configurations. *J. Am. Chem. Soc.* **1963,** *85* (3), 249-259.
16. Stefańczyk, O.; Ohkoshi, S.-i., Synthesis of Two-Dimensional Photomagnetic $K_4\{[Cu^{II}(ida)]_2[M^{IV}(CN)_8]\}{\cdot}4H_2O$ (M^{IV} = Mo, W) Materials. *Inorg. Chem.* **2020,** *59* (7), 4292-4299.

Chapter IV. Photomagnetic studies of cyanido-bridged complexes based on $[M(CN)_8]^{4-}$

IV.1 Introduction

In chapters II and III, we have investigated a series of ionic salts to understand the photomagnetic mechanisms based on the isolated $[M^{IV}(CN)_8]^{4-}$ units (M = Mo or W) when the cyanide ligands are terminal. We have revealed an unusual light-induced bond breakage concomitant with a spin-triplet (S-T) state trapping in $K_4[Mo(CN)_8]\cdot 2H_2O$ (**1**) and $Rb_4[Mo(CN)_8]\cdot 2H_2O$ (**3**). As shown in chapter I, we have seen that the majority of photomagnetic $[Mo(CN)_8]$-based compounds contain cyanide bridges. Our first thought is that the Mo-CN bond breaking cannot be reversible when cyanide ligands are engaged as bridges. To explore if the unusual bond-breaking is general, it is interesting to study the photomagnetic compounds based on $[M^{IV}(CN)_8]^{4-}$ units where the cyanide ligands are engaged in bridges.

In this chapter, we will study cyanido-bridged complexes, in which cyanides of Mo site are involved in bridges with firstly diamagnetic Cd^{II} ions and secondly Cu^{II} ions. The incorporation of diamagnetic Cd^{II} will help in the realization or not of the S-T mechanism in bridged systems. Previously, S-T mechanism was confirmed for 3D-$Cs^{I}_2Cu^{II}_7[Mo^{IV}(CN)_8]_4\cdot 6H_2O$ (**CsCuMo**) nanoparticles, in which all cyanide groups are engaged as bridges, by the results of X-ray Absorption Spectroscopy and X-ray magnetic circular dichroism (see details in chapter I).[1] Later, a coexistence of MMCT and S-T mechanisms was reported in the trinuclear $[Cu^{II}(enpnen)]_2[Mo^{IV}(CN)_8]\cdot 6.75H_2O$ (enpnen = N,N'-bis(2-aminoethyl)-1,3-propanediamine), with two out of eight cyanide groups are engaged as bridges.[2] Despite the photomagnetic properties have been widely observed for Cu^{II}-$[Mo^{IV}(CN)_8]^{4-}$ bridged systems,[2-7] the unambiguous understanding for the S-T and/or MMCT processes needs further studies. In this chapter, to further explore Cu^{II}-$[Mo^{IV}(CN)_8]^{4-}$ bridged systems, our efforts include:

i. The study of inorganic Cu^{II}-$[M^{IV}(CN)_8]^{4-}$ system, where Cu^{II} is not blocked by organic ligands.
ii. The study of inorganic-organic hybrid Cu^{II}-$[Mo^{IV}(CN)_8]^{4-}$ system, where Cu^{II} is blocked by the well-known bidentate ligand, ethylenediamine (en).

IV.2 Synthesis, characterization and physical properties of bridged complexes based on the Cd^{II}-$[Mo^{IV}(CN)_8]^{4-}$ pair

Hexanuclear $\{[Cd^{II}(bpy)_2]_4[Mo^{IV}(CN)_8]_2\}\cdot 10H_2O$ (bpy = bipyridine) is the only reported cyanido-bridged complex based on Cd^{II}-$[Mo^{IV}(CN)_8]^{4-}$ pair, in which four cyanide ligands of each Mo site participate in bridges with Cd^{II} ions.[8] In this subsection, a three dimensional network $Cd_2[Mo(CN)_8]\cdot 8H_2O$ (**16**), with all cyanides bridging to Cd^{II} ions, has been obtained and characterized structurally and photomagnetically.

16 is prepared as the first intermediate in the synthesis of $A_4[Mo^{IV}(CN)_8]$ (A = alkali cations) (see chapter II in experimental section II.5.1 and IV.6.1 Synthesis). The experimental powder X-ray diffraction pattern is generally consistent with the calculated one, even if there is unknown impurity which is probably generated during the fast precipitation (IV.6.2 Powder X-ray diffraction analysis). UV-Vis spectra of **16** is similar with that for $A_4[Mo(CN)_8]$ (A = alkali cations) (IV.6.3 Optical measurements). Infrared spectra (IR) for cyanide vibration region is informative, because the formation of cyanide bridges restraints the vibrations of cyanide ligand, and hence increases cyanide stretching frequency.[9] The cyanide stretching frequency for **16** shows an unique peak at 2135 cm^{-1}, which is higher in energy than the non-bridged systems, indicating the formation of only cyanide bridges in the crystal structure (IV.6.4 IR spectra).

IV.2.1 Investigation of $Cd_2[Mo(CN)_8]\cdot 8H_2O$ (16)

IV.2.1.1 Crystal structure of $Cd_2[Mo(CN)_8]\cdot 8H_2O$ (16)

Single crystal X-ray diffraction studies show that **16** is featuring a three dimensional network, which has a similar topology as $M^{II}_2[Mo^{IV}(CN)_8]\cdot nH_2O$ (M = Mn, Fe, Co, Ni, Cu).[10-13] However, the structural characteristics are quite different as illustrated for average Mo-C-N bond angles, M^{II}-N and M^{II}…Mo bond Lengths (Table IV. 1). Among this series of compounds, the light-induced magnetization is only reported for $Cu^{II}_2[Mo^{IV}(CN)_8]\cdot nH_2O$.[4]

16 crystallizes in the tetragonal *I*4/*mcm* space group (Table IV. 2). The asymmetric unit contains one Cd site and one Mo site (Figure IV. 1). The Mo site is revealed to have nearly an ideal square antiprism (SAPR) geometry, as shown by a CShM value of 0.131 for this geometry. Average bond distances of Mo-C and C-N bonds are 2.158(3) Å and 1.146(5) Å, respectively, and the average Mo-C-N bond angle equals to 178.4(3)°. All cyanide ligands of Mo site are engaged in bridges with Cd sites.

Each Cd site is coordinated by four cyanide bridges from Mo site in equatorial position and two water molecules in axial position, forming an octahedral geometry as shown by a CShM value of 0.323 for this geometry. Cd-N bond length equals to 2.311(3) Å and Cd-O bond lengths equal to 2.278(7) and 2.439(8) Å, respectively (Table IV. 3).

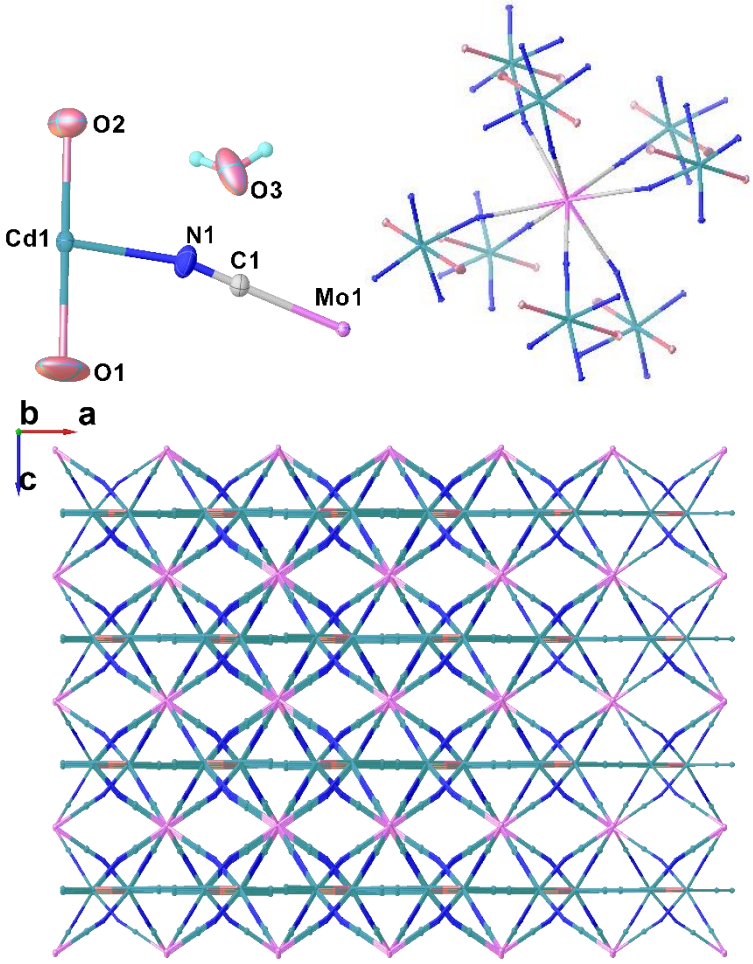

Figure IV. 1 (Top left) ORTEP diagram of the asymmetric unit of **16** with selected atoms labelling. (Top right) Molecule fragment highlighting the coordination environment of Mo site. (Below) The crystal packing in *ac* plane. Thermal ellipsoids of 50 % probability are shown. Color codes: N, blue; C, grey; Cd, green; Mo, pink; O, red; H, light blue.

Table IV. 1 Comparison of selected structural parameters in $M^{II}_2[Mo^{IV}(CN)_8]\cdot nH_2O$.

Compound	**Average Mo-C-N Angle/°**	**M^{II}-N Length/Å**	**M^{II}…Mo Length/Å**	**Ref.**
$Cu_2[Mo(CN)_8]\cdot 4H_2O$	177.06(15)	1.9702(15)	5.22	[12]
$Fe_2[Mo(CN)_8]\cdot 8H_2O$	163.6(15)	2.222(10)	5.38	[13]
$Cd_2[Mo(CN)_8]\cdot 8H_2O$	178.4(3)	2.311(3)	5.57	This study

Table IV. 2 Single crystal X-ray diffraction data and structure refinement parameters for $Cd_2[Mo(CN)_8]\cdot 8H_2O$ (**16**).

Compound	**16**
Formula	$C_8H_{16}Cd_2MoN_8O_8$
$D_{calc.}$/g cm^{-3}	2.798
μ/mm^{-1}	5.741
Formula Weight/g mol^{-1}	201.84
T/K	296(2)
Crystal System	tetragonal
Space Group	*I*4/*mcm*
a/Å	11.9268(3)
c/Å	13.4745(4)
V/Å^3	1916.73(11)
Z	4
Wavelength/Å	0.71073
Radiation type	MoK_a
Q_{min}/°	2.415
Q_{max}/°	28.264
Measured Refl.	21444
Independent Refl.	667
Reflections with I > 2(I)	571
R_{int}	0.0374
Parameters	42
Largest Peak	0.886
Deepest Hole	-0.843
GooF	1.326
wR_2 (all data)	0.0640
wR_2	0.0489
R_1 (all data)	0.0265
R_1	0.0193
S_{SAPR}	0.131
S_{TDD}	2.627

S is continuous shape measurement (CShM) value. SAPR and TDD represent square antiprism and triangular dodecahedron, respectively.

Table IV. 3 Selected bond lengths and angles in **16**.

Atoms		Length/Å	Atoms		Length/Å	Atoms			Angle/°
Mo1	C1	2.158(3)	N1	C1	1.146(5)	N1	C1	Mo1	178.4(3)
Cd1	N1	2.311(3)				C1	N1	Cd1	163.8(3)
Cd1	O2	2.278(7)							
Cd1	O1	2.439(8)							

IV.2.1.2 Photomagnetic measurements for $Cd_2[Mo(CN)_8]\cdot 8H_2O$ (16)

16 is diamagnetic before light irradiation as expected with only Cd^{2+} ($4d^{10}$, $S = 0$) and Mo^{4+} ($4d^2$, $S = 0$) ions. There was a gradual increase of χT with 405 nm light irradiation for 7 h, with χT product increasing from 0 to around 0.14 $cm^3\ mol^{-1}\ K$ (Figure IV. 2). The photomagnetic effect is less pronounced than in the molecular compound $\{[Cd^{II}(bpy)_2]_4[Mo^{IV}(CN)_8]_2\}\cdot 10H_2O$.[8] For $\{[Cd^{II}(bpy)_2]_4[Mo^{IV}(CN)_8]_2\}\cdot 10H_2O$, the χT product increases from 0 to around 0.52 $cm^3\ mol^{-1}\ K$ with 24 hours light irradiation.

The light-induced χT vs. T plot showed a small increase when temperature increased from 2 K to 25 K (blue curve in Figure IV. 2). A maximum χT value of 0.15 $cm^3\ mol^{-1}\ K$ was reached at 25 K. Then, the χT product decreased monotonously to reach around 0 $cm^3\ mol^{-1}\ K$ at 240 K. The temperature dependent of the χT product from 2 K to 300 K has a similar shape as the χT vs. T plot of $\{[Cd^{II}(bpy)_2]_4[Mo^{IV}(CN)_8]_2\}\cdot 10H_2O$. Finally, a new χT vs. T plot (red curve in Figure IV. 2) showed that the photo-induced state was fully erased after a room temperature treatment.

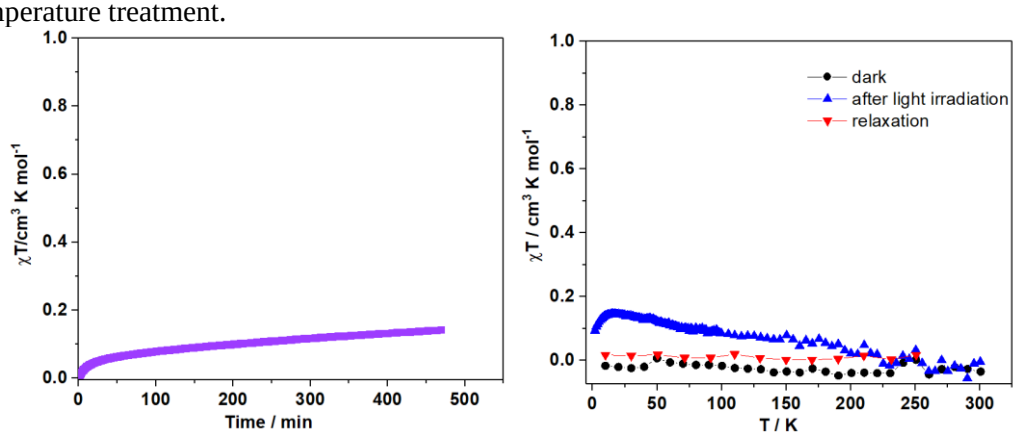

Figure IV. 2 (Left) Time dependence of the χT for **16** measured at 10 K, 1 T with continuous 405 nm blue light irradiation. (Right) $\chi T = f(T)$ plots of **16** measured in the dark before any light irradiation, after 405 nm irradiation and after heating to 300 K.

IV.2.2 Discussion on $Cd_2[Mo(CN)_8]\cdot 8H_2O$ (16)

16 has been structurally and photomagnetically studied, as the first three dimensional network with all cyanide bridges of Mo site linked to Cd^{2+} ions. The photomagnetic effect is weaker than the previous studied ionic salts in this thesis and the reported molecular compound $\{[Cd^{II}(bpy)_2]_4[Mo^{IV}(CN)_8]_2\}\cdot 10H_2O$. The observed effect may be due to surface effects induced by light irradiation. This suggests that the photomagnetic effect of the $[Mo^{IV}(CN)_8]^{4-}$ unit is very weak when all cyanides are acting as bridges in a three dimensional network. In **16**, MMCT is highly unprobable (due to the formation of unstable Cd^{+}). The fact that **16** is not significantly photomagentic is an important result, because the significant photomagnetic properties observed in $Cu_2[Mo(CN)_8]\cdot xH_2O$ may be due to a MMCT between Mo^{4+} and Cu^{2+} ions.

IV.3 Synthesis, characterization and physical properties of bridged complexes based on the Cu^{I}/Cu^{II}-$[M^{IV}(CN)_8]^{4-}$ pair

The inorganic copper(II)-octacyanidomolybdate(IV) based three-dimensional (3-D) networks show interesting photoinduced spontaneous magnetization,[7] as illustrated for $Cu_2[Mo(CN)_8]\cdot xH_2O$ (**$CuMo_{preci.}$**), $Cs^{I}_2Cu^{II}_7[Mo^{IV}(CN)_8]_4\cdot 6H_2O$ (**CsCuMo**) and $Rb^{I}_{3/2}Cu^{II}_7[Mo^{IV}(CN)_8]_{31/8}\cdot 12H_2O$ (**RbCuMo**).[4-7, 14-16] However, the sample studied for $Cu_2[Mo(CN)_8]\cdot xH_2O$ was precipitated with poor crystallinity from solution,[6] while $Cs^{I}_2Cu^{II}_7[Mo^{IV}(CN)_8]_4\cdot 6H_2O$ and $Rb^{I}_{3/2}Cu^{II}_7[Mo^{IV}(CN)_8]_{31/8}\cdot 12H_2O$ were electrochemically prepared in solution by reduction of $[Mo^{V}(CN)_8]^{3-}$ to $[Mo^{IV}(CN)_8]^{4-}$ to form crystalline materials.[5] The poor crystallinity of $Cu_2[Mo(CN)_8]\cdot xH_2O$ renders it difficult for the understanding of the structure-photomagnetic properties relationship.

At the beginning of its discovery, the photomagnetic effect in Cu^{II}-$Mo^{IV}(CN)_8$ systems was interpreted as light-induced metal-to-metal charge transfer (MMCT) (Scheme IV. 1), as proposed by Henning et al. in solution[17] and in analogy with Prussian Blue analogues $Co/Fe(CN)_6$.[18]

For the MMCT mechanism, the $Cu^{II}(3d^9)$-$Mo^{IV}(4d^2)$ pair is converted in $Cu^{I}(3d^{10})$-$Mo^{V}(4d^1)$ pair under light irradiation. As the compounds contain more Cu^{2+} than Mo^{4+}, the ferromagnetic interaction between photogenerated Mo^{V} and remaining Cu^{II} can explain the photomagnetic effect (Scheme IV. 1a). The number of spin remains unchanged with MMCT process. The increase of magnetization has been explained by ferromagnetic interactions, but the saturation magnetization is identical before and after irradiation. However, the increase of the saturation magnetization after light irradiation has been observed in some compounds.[2, 19-20] Moreover, spin crossover on the Mo ion from singlet state to triplet state (S-T) has been revealed by the results of X-ray absorption spectroscopy and X-ray magnetic circular dichroism, which has also been recently confirmed in ionic compounds (see chapter II).[21] S-T mechanism can explain well the increase of the total spin number which is generated during the transition from Mo^{IV} ($4d^2_{LS}$, S = 0) state to Mo^{IV} ($4d^2_{HS}$, S = 1) state and finally the increase of saturation magnetization (Scheme IV. 1b). Only in one compound $[Cu^{II}(enpnen)]_2[Mo^{IV}(CN)_8]\cdot 6.75H_2O$ (enpnen = N,N'-bis(2-aminoethyl)-1,3-propanediamine), coexistence of MMCT and S-T mechanisms was clearly proved, with two out of eight cyanide groups engaged as bridges.[2]

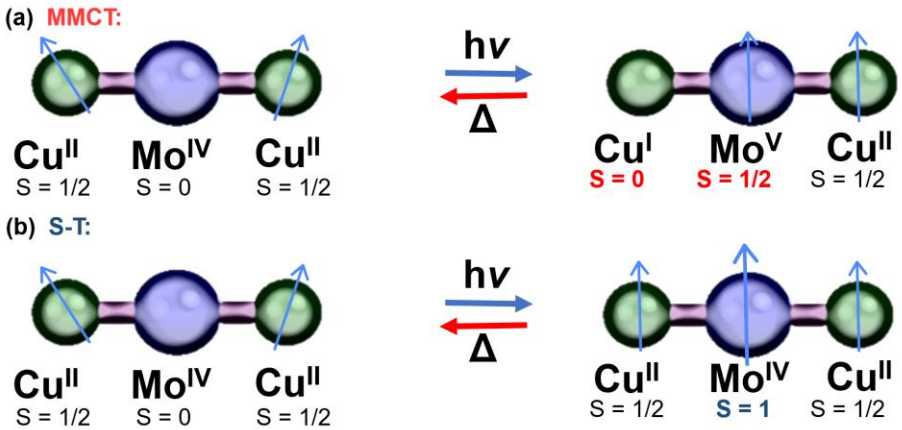

Scheme IV. 1 Schematic illustration of (a) light-induced metal-to-metal charge transfer (MMCT) and (b) singlet-triplet (S-T) transition in Cu^{II}-$[Mo^{IV}(CN)_8]$ system.

Considering the few illustrations of photomagnetic properties in inorganic copper (II)-octacyanidometallate (IV) system, new studies of novel photomagnetic inorganic copper (II)-octacyanidometallates (IV) are desirable for understanding the photomagnetic mechanisms. Having this in mind, it is interesting to investigate new crystalline copper-

octacyanidometallate compounds where all or some cyanides are acting as bridges.

In this chapter, we have studied three novel copper-octacyanidometallate compounds: $KCu^{I}Cu^{II}[Mo^{IV}(CN)_8]\cdot 3H_2O$ (**17**) and $K_2Cu^{I}_3(\mu\text{-}CN)[M^{IV}(CN)_8]\cdot 4H_2O$ (M= Mo for **18**, M= W for **19**). These compounds form cyanide-bridged Cu^{I}/Cu^{II}-$[M^{IV}(CN)_8]^{4-}$ based three-dimensional networks with K^+ ions and H_2O molecules in close contact.

17 and **18** are successfully synthesized by the slow diffusion of the aqueous solution of $CuCl_2\cdot 2H_2O$ through a water layer into the aqueous solution of $K_4Mo(CN)_8\cdot 2H_2O$ inside a straight tube under room temperature and 80 ℃, respectively (Scheme IV. 2 and IV.6.1 Synthesis). Also, if we heat the **17** within the mother solution at 80 ℃, yellow crystals of **18** have alternatively been obtained as confirmed by the color change from purple to yellow (Figure IV. 3). Besides, dark purple precipitate $Cu_2[Mo(CN)_8]\cdot xH_2O$ (denoted as **CuMo$_{preci.}$**), the reported photomagnet,[4] has been prepared as a reference sample by adding dropwise the aqueous solution $CuCl_2\cdot 2H_2O$ into the aqueous solution of $K_4Mo(CN)_8\cdot 2H_2O$.[6]

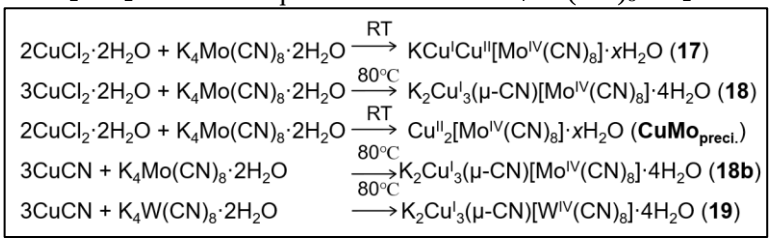

Scheme IV. 2. The reaction scheme for **17**, **18**, **CuMo$_{preci.}$**, **18b** and **19**.

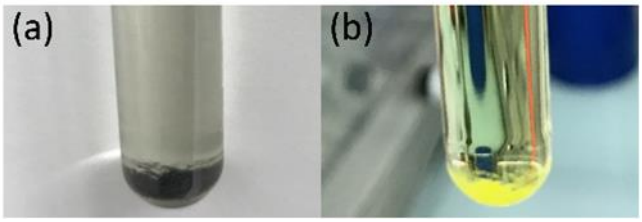

Figure IV. 3 Crystals of **17** (a) and **18** (b) in mother liquor. **18** has been obtained by heating solution (a) at 80 ℃.

The experimental Powder X-ray Diffraction (PXRD) patterns generally agree with the calculated ones for **17** and **18**. This indicates that the powder compound and the single crystals are corresponding to the same compound (IV.6.2 Powder X-ray diffraction analysis). There are several unexpected peaks for the experimental PXRD pattern for **17** may due to the bad quality of the single crystal data.

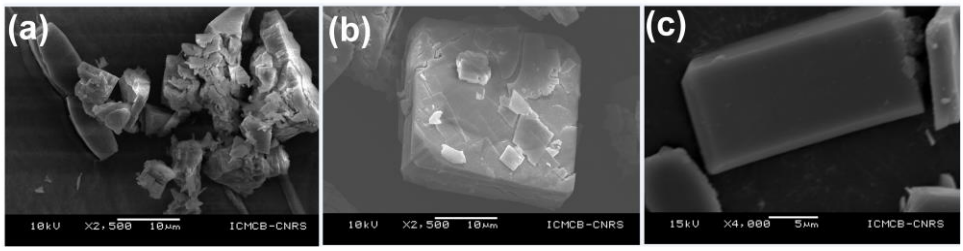

Figure IV. 4 The SEM images for (a) **CuMo$_{preci.}$**, (b) **17** and (c) **18**.

The Scanning Electron Microscopy (SEM) images show that the crystals of **18** have well-defined edges, while it is not the case for **CuMo$_{preci.}$** and **17** (Figure IV. 4). Based on the analysis of Energy-dispersive X-ray spectroscopy (EDX), the characteristic spectra for K, Cu and Mo elements are detected for **17** and **18**, while only Cu and Mo elements are detected for **CuMo$_{preci.}$** (Figure IV. 5). Based on the comparison of the UV-Vis spectra between these two compounds, additional medium intense bands in 500-510 nm range are observed for **17**, which is in good agreement with the existence of a MMCT band for the Cu^{II}-NC-Mo linkage (IV.6.3 Optical measurements).[6, 22] The spectra of **18** are quite similar to the spectra of $K_4Mo(CN)_8\cdot 2H_2O$ which only exhibits the MLCT and spin-allowed transitions of the $[Mo^{IV}(CN)_8]^{4-}$ units. These results are consistent with the crystal colors shown in Figure IV. 3.

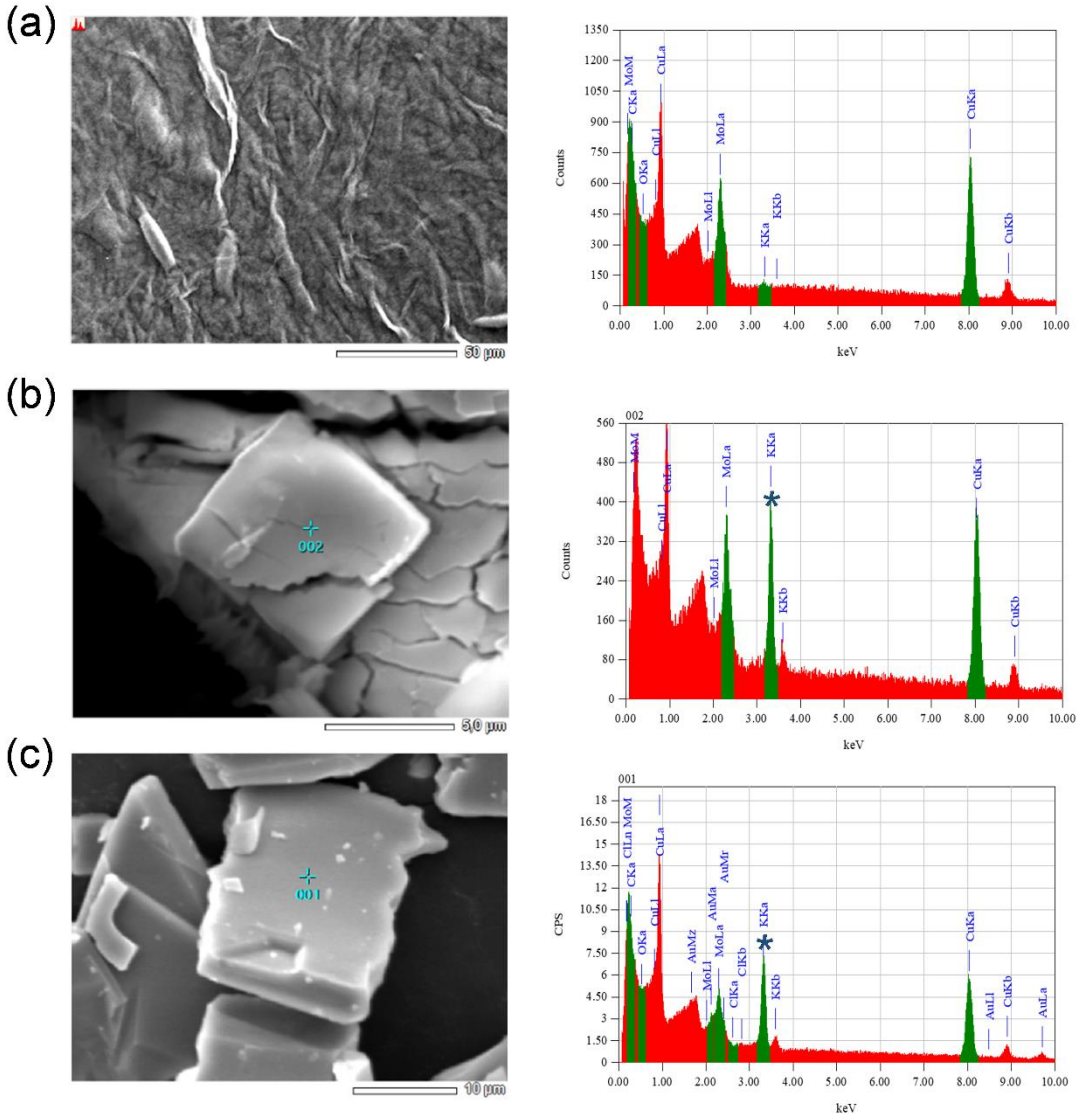

Figure IV. 5 The SEM images and corresponding EDS results for **CuMo$_{preci.}$**(a), **17** (b) and **18** (c), with * indicating the presence of K element.

The presence of Cu^{I} for both **17** and **18** based on the single crystal X-ray diffraction results confirms the occurrence of the metal-to-metal charge transfer in solution. The Cu^{I} is successfully captured during crystallization, and the synthesis at higher temperature can facilitate the metal-to-metal charge transfer process during the synthesis. To understand how Cu^{I} ions are formed, we performed an Electron Paramagnetic Resonance (EPR) study for the analysis of the mother solution of **18** (Figure IV. 6). The mother solution of **18** was found to be more colored (yellow) than the one for **17** that is almost colorless. We suspect that the yellow color might derive from the Mo^{V} released during the formation of Cu^{I} through a MMCT process in the Cu^{II}-$[Mo^{IV}(CN)_8]^{4-}$ pair. This is suggested by a EPR signal with a *g* value of 1.92. The *g* value observed could be ascribed to paramagnetic Mo^{V} (S = 1/2), even if the obtained *g* value is a bit lower for a Mo^{V} ion.[23] The EPR signal is quite weak, probably because most of the Mo^{V} ions have been further reduced in Mo^{IV} during the reaction.

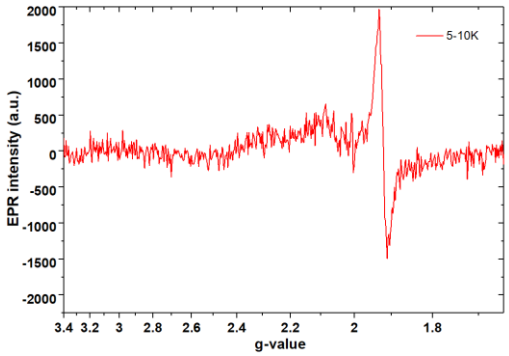

Figure IV. 6 EPR spectra for the concentrated mother solution of **18**.

The analysis of IR spectra in the 2000-2200 cm^{-1} range show two bands at 2161 cm^{-1}, 2129 cm^{-1} for **17** and 2129 cm^{-1}, 2042 cm^{-1} for **18**, respectively (IV.6.4 IR spectra). The vibration around 2161 cm^{-1} can be attributed to Cu^{II}-NC-Mo linkage which is consistent with the reported value for $Cu_2[Mo(CN)_8]\cdot xH_2O$.[22] The shared peak 2129 cm^{-1} between **17** and **18** could be assigned to the Cu^{I}-NC-Mo linkage. The peak at 2042 cm^{-1} for **18** could be assigned to the disordered cyanide ligand N|C≡N|C.

18 can be obtained by reacting at least three weeks in a 80 ℃ oven to observe a complete color change from violet to goldish yellow. However, the replacement of $K_4[Mo(CN)_8]\cdot 2H_2O$ by $K_4[W(CN)_8]\cdot 2H_2O$ cannot lead to the same tungsten analogue as **18** (PXRD patterns see with IV.6.2 Powder X-ray diffraction analysis). Thus, the MMCT process if any is not efficient in solution for Cu^{II}-W^{IV}.

Furthermore, we have succeeded to prepare **18** in one day directly using $Cu^{I}CN$ as a starting material. $Cu^{I}CN$ is not soluble in water which is safer by avoiding the hazardous solubility of the cyanide ions (Scheme IV2). So the synthesis is a solid to solid conversion which leads to tiny crystals not suitable for SXRD. But the successful preparation of **18** can be confirmed by the PXRD results (IV.6.2 Powder X-ray diffraction analysis). The product prepared in this approach is labeled **18b**. This alternative pathway is also working for the tungsten analogue. The comparison of PXRD patterns of this tungsten product and the calculated one from **18** suggests that the tungsten product is isostructural with **18** (IV.6.2 Powder X-ray diffraction analysis). So a tungsten analogue $K_2Cu^{I}_3(\mu\text{-}CN)W(CN)_8\cdot 4H_2O$ (**19**) was successfully obtained. Besides, UV-Vis and IR results also confirm the successful preparation of both **18b** and **19** (see subsection： IV.6.3 Optical measurements and IV.6.4 IR spectra). However, an unexpected peak at 1416 cm^{-1} is observed for the IR spectra of **18**, probably due to the slightly unknown structural difference between **18** and **18b**.

IV.3.1 Investigation of $KCu^{I}Cu^{II}[Mo(CN)_8]\cdot 3H_2O$ (17)

IV.3.1.1 Crystal structure of $KCu^{I}Cu^{II}[Mo(CN)_8]\cdot 3H_2O$ (17)

17 contains a mixed valence of copper, Cu^{I} and Cu^{II}, with the chemical formula $KCu^{I}Cu^{II}[Mo^{IV}(CN)_8]\cdot 3H_2O$. It possesses a relatively poor crystal structure criteria with large R_1 value 11.21 % and the structure has to be solved with the "twin" strategy. Nevertheless, it is important to note that the global structure for **17** has been solved without ambiguity and it is generally consistent with the PXRD, IR, UV-Vis and magnetic data.

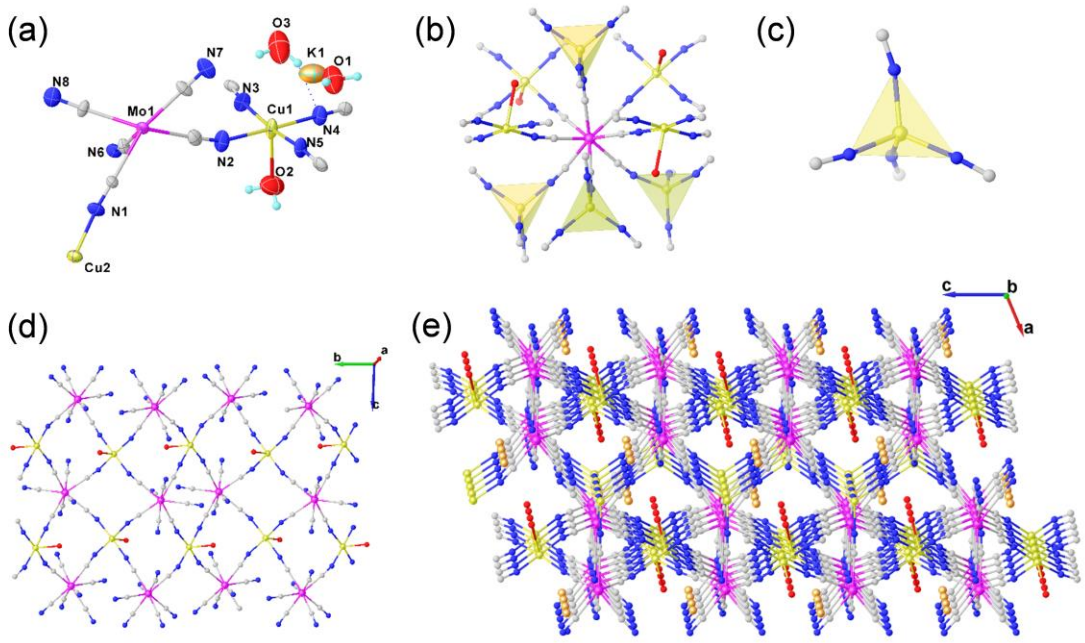

Figure IV. 7 (a) ORTEP diagram of the asymmetric unit of **17** with selected atoms labelling. Thermal ellipsoids of 50 % probability are shown. (b) Molecule fragment highlights the coordination environment of Mo site. (c) $[Cu^{I}(N{\equiv}C)_4]^{3-}$ building block connects the wavery layer fragment (d) to form the three dimensional network (e). Solvent water molecules are omitted for clarity.

17 crystallizes in the space group $P2_1/c$ with unit cell parameters: a = 9.5167(6) Å, b = 12.3167(7) Å, c = 14.8688(11) Å, β = 112.561(5) ° and V = 1609.46(19) Å^3 (Table IV. 4). Selected structural parameters for **17** are listed in Table IV. 5. It has one Mo^{IV} site, one Cu^{II} site, one Cu^{I} site and one K^+ in the asymmetric unit (Figure IV. 7a). The $[Mo(CN)_8]^{4-}$ anion for **17** is revealed as square antiprism (SAPR) geometry with the CShM value of 0.342 in this geometry (Table IV. 4). The average Mo-C bond length is 2.158(15) Å and the average C≡N distance is 1.13(6) Å. The $[Mo^{IV}(CN)_8]^{4-}$ complex is linked with four square pyramidal $[Cu^{II}(H_2O)(NC)_4]^{2-}$ and four tetrahedral $[Cu^{I}(NC)_4]^{3-}$ by the eight cyanide bridges (Figure IV. 7b). The square-pyramidal coordination sphere for Cu^{II} is formed by one axial H_2O with Cu-O distance of 2.412(15) Å and four equatorial nitrogen atoms deriving from the cyanide ligands with an average Cu−N length of 1.966(12) Å. The tetrahedral coordination sphere for Cu^{I} is formed by four nitrogen atoms deriving from cyanide ligands with an average Cu-N length of 2.008(14) Å, which is slightly longer than that for Cu^{II}. Notably, the corresponding Cu^{I}–N≡C (162.8(13)°) is more bent than Cu^{II}–N≡C (165.8(14)°). It's worth to mention that the tetrahedral geometry is in agreement with the Cu^{I} oxidation state.[5]

K^+ cations are in close contact with the Cu sites which also play a significant role in the construction of three dimensional network. However, to make the structure description easier, our focus will be put on the Cu-NC-Mo skeleton by considering K^+ just as counter cation.

For **17**, the square-pyramidal $[Cu^{II}(H_2O)(NC)_4]^{2-}$ units are connected by $[Mo(CN)_8]^{4-}$ anions to form a wavery plane which is similar with $Cs^{I}[\{Co^{II}(3\text{-cyanopyridine})_2\}\{W^{V}(CN)_8\}]\cdot H_2O$[24] and $Ag_4(NH_3)_5Mo(CN)_8\cdot 1.5H_2O$[25] (Figure IV. 7d). The wavery plane is constructed by edge-sharing Mo_2Cu_2 rhombus polyhedra with water ligands pointing to the vertical direction. The planes are further linked by tetrahedron Cu^{I} along the a axis to form three dimensional network with K^+ and H_2O in close contact (Figure IV. 7c and e).

So the crystal structure of **17** is a three dimensional network containing a mixed valence of copper, Cu^{I} and Cu^{II}, with K^+ and H_2O in close contact.

Table IV. 4 Single crystal X-ray diffraction data and structure refinement parameters for $KCu^{I}Cu^{II}[Mo(CN)_8]\cdot 3H_2O$ (**17**)

Compound	**17**
Formula	$C_{16}H_{12}Cu_4K_2Mo_2N_{16}O_6$
$D_{calc.}$/g cm^{-3}	2.201
μ/mm^{-1}	11.957
Formula Weight/g mol^{-1}	1066.71
T/K	293(2)
Crystal System	monoclinic
Space Group	$P2_1/c$
a/Å	9.5167(6)
b/Å	12.3167(7)
c/Å	14.8688(11)
β/°	112.561(5)
V/Å^3	1609.46(19)
Z	2
Wavelength/Å	1.54184
Radiation type	CuK_a
Q_{min}/°	4.823
Q_{max}/°	67.068
Measured Refl.	2858
Independent Refl.	2858
Reflections with I > 2(I)	2522
R_{int}	0.051
Parameters	216
Restraints	0
Largest Peak	9.507
Deepest Hole	-3.656
GooF	1.635
wR_2 (all data)	0.3513
wR_2	0.3463
R_1 (all data)	0.1169
R_1	0.1121
S_{SAPR}	0.342
S_{TDD}	1.564

S is continuous shape measurement (CShM) value. SAPR and TDD represent square antiprism and triangular dodecahedron, respectively.

Table IV. 5 Selected bond lengths and angles for **17**.

Atoms		**Length/Å**	**Atoms**		**Length/Å**	**Atoms**			**Angle/°**
Mo1	C1	2.170(14)	N1	C1	1.13(2)	N1	C1	Mo1	176.4(13)
Mo1	C2	2.165(16)	N2	C2	1.10(2)	N2	C2	Mo1	176.6(15)
Mo1	C3	2.140(16)	N3	C3	1.13(2)	N3	C3	Mo1	177.0(13)
Mo1	C4	2.134(14)	N4	C4	1.16(2)	N4	C4	Mo1	176.6(14)
Mo1	C5	2.149(16)	N5	C5	1.14(2)	N5	C5	Mo1	175.5(14)
Mo1	C6	2.176(13)	N6	C6	1.111(18)	N6	C6	Mo1	171.6(12)
Mo1	C7	2.167(15)	N7	C7	1.15(2)	N7	C7	Mo1	178.3(14)
Mo1	C8	2.160(13)	N8	C8	1.140(19)	N8	C8	Mo1	176.6(14)
Average		2.158(15)	Average		1.13(6)	Average			176.1(14)
Cu1	N2	1.982(13)				C2	N2	Cu1	161.3(15)
Cu1	N3	1.973(11)				C3	N3	Cu1	168.1(12)
Cu1	N4	1.931(12)				C4	N4	Cu1	168.3(13)
Cu1	N5	1.976(12)				C5	N5	Cu1	165.4(14)
Average		1.966(12)				Average			165.8(14)
Cu1	O2	2.412(15)				C1	N1	Cu2	166.1(13)
Cu2	N1	1.989(13)				C6	N6	Cu2	160.4(12)
Cu2	N6	2.033(12)				C7	N7	Cu2	166.8(14)
Cu2	N7	1.968(17)				C8	N8	Cu2	157.7(14)
Cu2	N8	2.042(15)							
Average		2.008(14)				Average			162.8(13)

IV.3.1.2 Photomagnetic measurements for $KCu^{I}Cu^{II}[Mo(CN)_8]\cdot 3H_2O$ (17)

The magnetic properties of **17** in the ground state (Figure IV. 8) show a paramagnetic signal, with a χT value reaching 0.45 cm^3 K mol^{-1}, which agrees with the contribution from one spin 1/2 of the copper(II) center ($3d^9$) with g = 2.19.

The 405 nm excitation light source is chosen for the photomagnetic experiment, because it has been efficient for both MMCT and S-T processes.[2] When **17** was irradiated with a light of 405 nm, the χT product increased to 0.79 cm^3 mol^{-1} K after 23 hours of irradiation (Figure IV. 8). Then the photo-induced state has been studied.

The temperature dependence of the χT from 2 K to 300 K first increased to reach a maximum at 0.81 cm^3 mol^{-1} K at 12 K, but the χT variation is much weaker than that for $Cu_2[Mo(CN)_8]\cdot xH_2O$ which shows an increase from 0.78 to 3.10 cm^3 mol^{-1} K.[11] Then, the χT product decreased monotonously and the χT value was back to the value obtained before the light irradiation around 200 K. The temperature dependence of the χT product from 2 K to 300 K has a similar shape than $Cu_2[Mo(CN)_8]\cdot xH_2O$,[4] The rapid decrease for **17** around 20 K is usually understood as ferromagnetic interaction between Cu^{II} and Mo^{V} generated from the MMCT process. A new plot χT vs. T shows that the photo-induced process is reversible.

It is hard to conclude if S-T mechanism is operative or not in **17**. Usually when the S-T mechanism is active, the χT vs. T plot displays either a round maximum or a plateau (see chapter II, III), which is not observed here. Compared to the reference compound $Cu^{II}_2[Mo^{IV}(CN)_8]\cdot xH_2O$, the increase of χT in **17** is smaller. Based on these observations, we propose that MMCT is active in **17**.

$$KCu^{I}Cu^{II}[Mo^{IV}_{LS}(CN)_8]\cdot 3H_2O(\mathbf{17}) \underset{T}{\overset{h\nu}{\rightleftharpoons}} KCu^{I}_{1+x}Cu^{II}_{1-x}[Mo^{IV}_{1-x}Mo^{V}_{x}(CN)_8]\cdot 3H_2O$$

Scheme IV. 3 The photomagnetic mechanism of **17**.

If the MMCT is complete, the following photo-induced phase will be obtained, $KCu^{I}_2[Mo^{V}(CN)_8]\cdot 3H_2O$. This phase would contain only S = 1/2 coming from the photogenerated Mo^{V}, and thus would exhibit a χT value around 0.375 $cm^3\ mol^{-1}\ K$. In **17**, the obtained χT value reaches a maximum value of 0.8 $cm^3\ mol^{-1}\ K$. Therefore, the only explanation for **17** is a partial MMCT with the proposed formula (Scheme IV. 3). Finally, the ferromagnetic interaction between the remaining (1-*x*)Cu^{II} and the photogenerated *x*Mo^{V} can explain the increase of χT product, with *x* as a partial conversion rate.

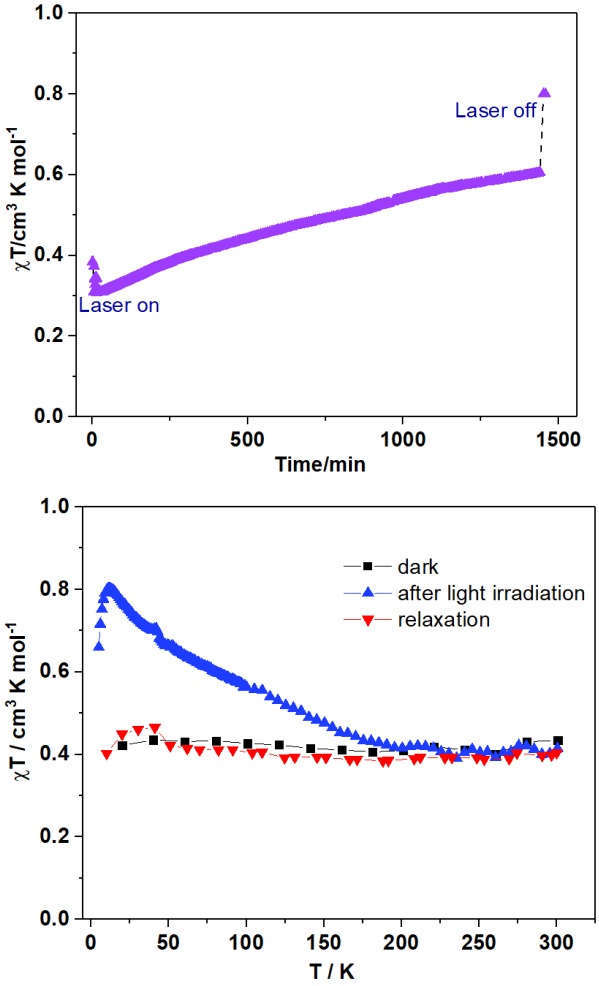

Figure IV. 8 (Top) Time dependence of the χT for **17** measured at 10 K, 1 T with continuous 405 nm blue light irradiation. (Below) χT = f(*T*) plots of **17** measured in the dark before any light irradiation, after 405 nm irradiation and after heating to 300 K.

IV.3.2 Investigation of $K_2Cu^{I}_3(\mu\text{-}CN)[Mo(CN)_8]\cdot 4H_2O$ (18)

IV.3.2.1 Crystal structure of $K_2Cu^{I}_3(\mu\text{-}CN)[Mo(CN)_8]\cdot 4H_2O$ (18)

Different to **17**, **18** contains only one valence state of copper, Cu^{I}. The chemical formula for **18**, $K_2Cu^{I}_3(\mu\text{-}CN)[Mo^{IV}(CN)_8]\cdot 4H_2O$, is different than **17** ($KCu^{I}Cu^{II}[Mo^{IV}(CN)_8]\cdot 3H_2O$), with different K/Mo (1/1 for **17** and 2/1 for **18**) and Cu/Mo (2/1 for **17** and 3/1 for **18**) ratios. **18** crystallizes in space group *Cmcm* with the unit cell parameters *a* = 8.7320(2) Å, *b* = 25.0144(5) Å, *c* = 9.1059(2) Å and *V* = 1988.96(7) $Å^3$ (Table IV. 6). Selected structural parameters for **18** are listed in Table IV. 7. **18** has one Mo^{IV} site, two Cu^{I} sites and two K^+ ions in the asymmetric unit (Figure IV. 9a).

The $[Mo(CN)_8]^{4-}$ anion in **18** is revealed as a square antiprism (SAPR) based on the CShM value 0.419 in this geometry (Table IV. 6). Average Mo-C and C≡N bond lengths are equal to 2.151(4) and 1.143(5) Å, respectively.

One $[Mo^{IV}(CN)_8]^{4-}$ complex is linked to four single $[Cu^{I}(N{\equiv}C)_4]^{3-}$ and two $[Cu_2^{I}(N{\equiv}C)_2(N|C \equiv N|C)_2]_2^{6-}$ tetramers through eight cyanide bridges (Figure IV. 9b). The average angle for Mo-C-N which further connected to the copper tetramer (175.4(3)°) is acuter than the ones connected to the single Cu^{I} (177.3(4)°).

In the structure one cyanide ligand N4|C4≡N4|C4 (violet atoms in Figure IV. 9) is disordered with a co-occupancy by nitrogen and carbon atoms with a ratio of 50 % for each. This kind of structural disorder has also been reported in CuCN[26] and AuCN.[27] However, the bond length for disordered cyanide ligand is revealed to be short with a value of 1.114(9) Å. This disordered cyanide ligand N|C≡N|C is not linked to molybdenum atom. This can be explained by a possible cleavage of Mo-CN cyanide ligand during the MMCT process in solution.[28-31] This disordered cyanide ligand connects edge-sharing tetrahedrons $[Cu_2^{I}(N{\equiv}C)_2(N|C{\equiv}N|C)_2]^{3-}$ to form mesh-like chains (Figure IV. 9c).

The single $[Cu^{I}(N{\equiv}C)_4]^{3-}$ unit is constructed by one Cu^{I} and four cyanide ligands with an average Cu-N length of 1.989(4) Å and an average Cu-N≡C bond angle of 177.0(4)°, respectively. The $[Cu_2^{I}(N \equiv C)_2(N|C \equiv N|C)_2]_2^{6-}$ tetramer possesses average Cu-N and Cu-N|C lengths of 1.959(3) Å and 2.154(3) Å, respectively. The average bond angle in the tetramer for Cu-N|C≡N|C (142.96(7)°) is acuter than single Cu−N≡C (160.7(3)°).

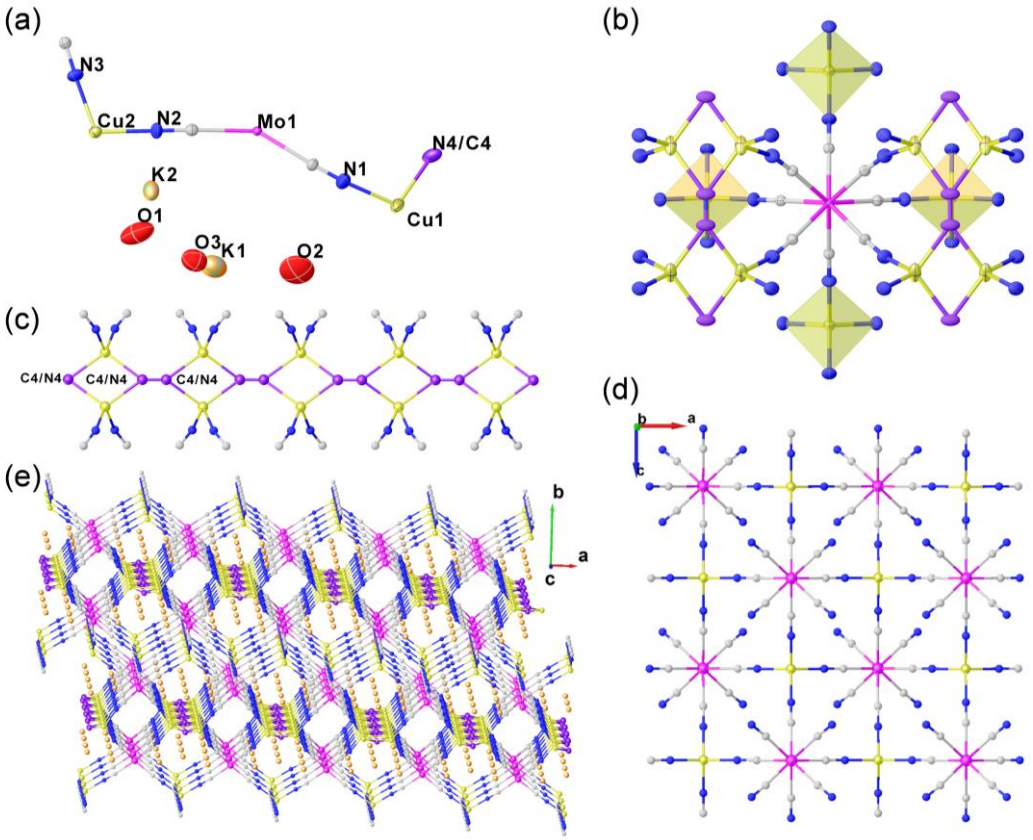

Figure IV. 9 (a) ORTEP diagram of the asymmetric unit of **18** with selected atoms labelling. (b) Molecule fragment highlights the coordination environment of Mo site. Thermal ellipsoids of 50 % probability are shown. (c) The mesh-like Cu chain connects the wavery layer fragment (d) to form the three dimensional network (e). Solvent water molecules are omitted for clarity.

For **18**, a statistical disorder exists between K^+ and H_2O with a ratio of 50 % for each. Again, to make the structure description easier, we will also consider K^+ just as a counter cation. Tetrahedral $[Cu^{I}(N{\equiv}C)_4]^{3-}$ units are connected by $[Mo(CN)_8]^{4-}$ anions to form wavery planes as in **17** (Figure IV. 9d). The mesh-like chains as shown in Figure IV. 9c act as

conjunctions to connect the aforementioned wavery layer to form a 3-D framework (Figure IV. 9e).

Table IV. 6 Single crystal X-ray diffraction data and structure refinement parameters for $K_2Cu^{I}_3(\mu\text{-}CN)[Mo(CN)_8]\cdot 4H_2O$ (**18**)

Compound	**18**
Formula	$C_9Cu_3K_2MoN_9O_4H_8$
$D_{calc.}$/g cm^{-3}	2.214
μ/mm^{-1}	4.233
Formula Weight/g mol^{-1}	662.94
T/K	120(2)
Crystal System	orthorhombic
Space Group	*Cmcm*
a/Å	8.7320(2)
b/Å	25.0144(5)
c/Å	9.1059(2)
V/Å^3	1988.96(7)
Z	4
Wavelength/Å	0.71073
Radiation type	MoK_a
Q_{min}/°	2.471
Q_{max}/°	26.391
Measured Refl.	23295
Independent Refl.	1161
Reflections with I > 2(I)	1085
R_{int}	0.0296
Parameters	82
Restraints	0
Largest Peak	1.111
Deepest Hole	-1.121
GooF	1.094
wR_2 (all data)	0.0648
wR_2	0.0632
R_1 (all data)	0.0271
R_1	0.0246
S_{SAPR}	0.419
S_{TDD}	1.965

S is continuous shape measurement (CShM) value. SAPR and TDD represent square antiprism and triangular dodecahedron, respectively.

Table IV. 7 Selected bond lengths and angles for **18**.

Atoms		Length/Å	Atoms		Length/Å	Atoms			Angle/°
Mo1	C1	2.152(3)	N1	C1	1.143(4)	N1	C1	Mo1	175.4(3)
Mo1	C2	2.147(4)	N2	C2	1.145(5)	N2	C2	Mo1	176.4(3)
Mo1	C3	2.152(4)	N3	C3	1.142(6)	N3	C3	Mo1	178.2(4)
Average		2.151(4)	Average		1.143(5)	Average			176.4(3)
Cu1	N1	1.959(3)	N4	C4	1.114(9)	C1	N1	Cu1	160.7(3)
Cu1	N4	2.154(3)				C4	N4	Cu1	142.96(7)
Cu2	N2	1.994(4)				C2	N2	Cu2	179.7(3)
Cu2	N3	1.983(4)				C3	N3	Cu2	174.3(4)
Average		1.989(4)				Average			177.0(4)

IV.3.2.2 Photomagnetic measurements for $K_2Cu^I_3(\mu\text{-}CN)[Mo(CN)_8]\cdot 4H_2O$ (18)

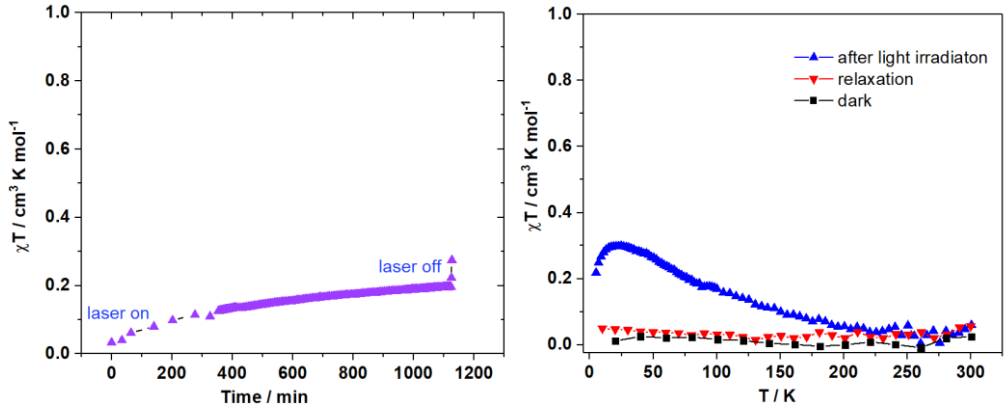

Figure IV. 10 (Left) Time dependence of the χT for **18** measured at 10 K, 1 T with continuous 405 nm blue light irradiation. (Right) χT = f(T) plots of **18** measured in the dark before any light irradiation, after 405 nm irradiation and after heating to 300 K.

In contrast with **17**, a fully diamagnetic behavior is observed for **18**, as it contains only diamagnetic metal ions $Cu^+(3d^{10}, S = 0)$ and $Mo^{4+}(4d^2, S = 0)$ in square antiprism geometry (Figure IV. 10).

Time dependence of the χT product was also recorded with 405 nm light excitation at 10 K for **18**. The photomagnetic response for **18** is less significant than **17**, with $\Delta\chi T$ = 0.4 cm^3 K mol^{-1} for **17** after 23 hours of irradiation and $\Delta\chi T$ = 0.3 cm^3 K mol^{-1} for **18** upon light exposure around 20 hours.

Then the temperature-dependent χT plot for **18** also followed an increase of the χT product at low temperature when the temperature was increasing and then a monotonous decrease up to 220 K. Different with the sharp shape for the χT-T plots for **17**, the photo-induced χT curve for **18** is smoother, which is similar with **Cd_4Mo_2** demonstrating the S-T mechanism.[8] A plateau in the range of 15-30 K is observed for **18** which demonstrates a relatively long lifetime for the photoexcited state of **18**. Above 220 K, the χT values showed no clear difference with the values before irradiation, indicating that an initial state was restored by the thermal heating.

The scenario is simple for **18** which contains non-redox active Cu^I. Similar as **Cd_4Mo_2**, only S-T mechanism occurs in **18**. The photoconversion rate is around 30 % if we do not take into account of magnetic anisotropy of Mo^{IV} high spin ($4d^2$ high spin, S = 1, χT = 1 cm^3 K mol^{-1}). The uncomplete conversion might be explained by the rigidity of the three-dimensional network with all cyanides are bridges. The photomagnetic effect is more significant for **18** than **16**, probably because the structure of **18** is more flexible to

accommodate the structural change associated to S-T process.

Based on the comparison with the photomagnetic properties described in **16**, **17** and **18**, we propose that **17** involves MMCT mechanism, while **16** and **18** involve S-T mechanism.

IV.3.3 Investigation of $K_2Cu^I_3(\mu\text{-}CN)[W(CN)_8]\cdot 4H_2O$ (19)

IV.3.3.1 Crystal structure of $K_2Cu^I_3(\mu\text{-}CN)[W(CN)_8]\cdot 4H_2O$ (19)

Single crystal X-ray crystallographic analysis for **19** were not successful because of the tiny size of the crystals. But by the comparison of powder X-ray diffraction patterns with **18**, **19** has been revealed to be isostructural with **18** (IV.6.2 Powder X-ray diffraction analysis). **19** is then a 3D network containing diamagnetic Cu^I centers and diamagnetic W^{IV} centers.

IV.3.3.2 Photomagnetic measurements for $K_2Cu^I_3(\mu\text{-}CN)[W(CN)_8]\cdot 4H_2O$ (19)

The same photoirradiation experiment was performed with **19** and no photomagnetic effect was observed (Figure IV. 11).

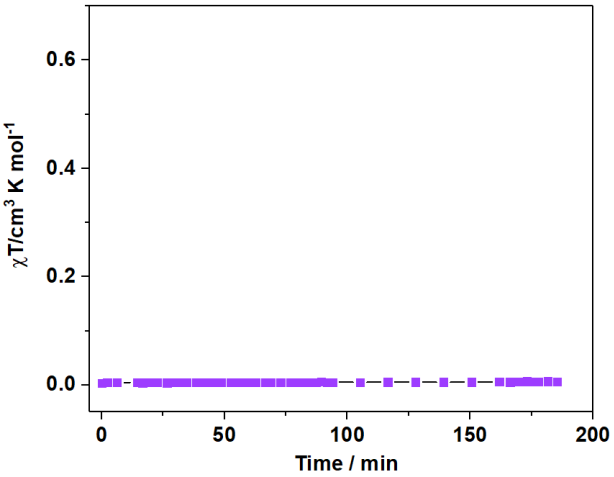

Figure IV. 11 Time dependence of the χT for **19** measured at 10 K, 1 T with 405 nm blue light irradiation.

IV.3.4 Discussion on $KCu^ICu^{II}[Mo(CN)_8]\cdot 3H_2O$ (17) and $K_2Cu^I_3(\mu\text{-}CN)[M(CN)_8]\cdot 4H_2O$ (M = Mo for (18), M = W for (19))

17 is the rare example of octacyanidometallate-based 3-D network containing Cu^I/Cu^{II} cations.[5, 7] It is well-known that Cu^{II} can be easily reduced in Cu^I and Mo^{IV} can be easily oxidized in Mo^V. The $[Mo^{IV}(CN)_8]^{4-}$ can be generated by the reduction of $[Mo^V(CN)_8]^{3-}$ by electrocrystallization for $Cs^I_2Cu^{II}_7[Mo^{IV}(CN)_8]_4\cdot 6H_2O$.[5] But there is no system that contains mixed valency of Cu (Cu^I and Cu^{II}) species at the same time. In this study, we isolate a mixed-valence Cu^I/Cu^{II}-Mo^{IV} compound, with the generation of the reduced Cu^I by MMCT process in solution where Mo^{IV} is involved. By increasing the synthesis temperature, **18** containing only Cu^I species is obtained. Under the same experimental conditions, tungsten analogues cannot be obtained. In parallel, **18b** and the corresponding tungsten analogue (**19**) have been successfully prepared with another approach by the direct utilization of Cu^ICN as a starting material.

For the photomagnetic studies, **17** is the unique three-dimensional network with the coexistence of mixed-valence states Cu^{II}/Cu^I. **18** and **19** represent unique examples incorporating Cu^I ion with $[M^{IV}(CN)_8]^{4-}$ anions.

Based on the comparison of the photomagnetic properties, we can propose that **17** might involve MMCT mechanism, while **18** involves S-T mechanism. The final exclusion of S-T mechanism for **17** needs further studies, such as magnetization studies to observe or not the increase of the total magnetization after light irradiation. For limited access of experiments,

these measurements were not performed in this thesis and will be done in the near future.

In conclusion, the presence of Cu^{I} in **17** and **18** indicates a MMCT process during synthesis. Three novel inorganic three-dimensional octacyanidometallate based coordination networks: $KCu^{I}Cu^{II}[Mo(CN)_8]\cdot xH_2O$ (**17**), $K_2Cu^{I}_3(\mu\text{-}CN)[M(CN)_8]\cdot 4H_2O$ (M= Mo for **18**, M= W for **19**) have been prepared with different coordination geometries around Cu^{II} and Cu^{I} ions. Both **17** and **18** are photomagnetic. Unlike its molybdenum analogues, the $[W^{IV}(CN)_8]^{4-}$ building block is again not photomagnetic in **19**.

As **18** is showing a S-T process, we tried a photocrystallography experiment at 10 K: a single crystal of **18** was exposed to a light of 405 nm during 30 mins. We observed an increase for the cell parameters from a = 8.6792(2) Å, b = 25.2704(5) Å, c = 8.9949(2) Å, V = 1972.82(7) $Å^3$ in the ground state to a = 8.7215(2) Å, b = 25.1730(5) Å, c = 9.0058(2) Å, V = 1977.20(7) $Å^3$ in the photoexcited state. However, the crystal structure of this photoexcited state has been revealed as not significantly different with the ground state. We can explain this by a possible isomerization of the cyanide ligand in the photoexcited state and/or by a low photoconversion with all cyanide groups in bridges.

IV.4 Synthesis, characterization and physical properties of bridged complexes based on the $[Cu^{II}(en)_x]$-$[Mo^{IV}(CN)_8]^{4-}$ pair

Different polyamines have been widely used to coordinate Cu^{II} in the construction of Cu^{2+}-$[Mo(CN)_8]^{4-}$ cyanide-bridged molecular compounds, but the understanding of the structure-property relationship of such materials is still unclear.[19, 32-33] In this subsection, 2D-$Cu(en)_2]_2[Mo(CN)_8]$ (**20**) and 3D-$[Cu(en)]_3[Cu(en)_2]_2[Mo(CN)_8]_{2.5}\cdot 2MeOH\cdot 5H_2O$ (**21**) based on the simple bidentate diamine, ethylenediamine, have been studied.

The purple crystals of **20** are obtained immediately by slow addition of methanol into the mixture of the solution of $CuCl_2$, ethylenediamine ligand and $K_4Mo^{IV}(CN)_8]\cdot 2H_2O$. However, purple crystals of **21** are prepared by the slow diffusion of the aqueous solution of $CuCl_2\cdot 2H_2O$ and ethylenediamine ligand into aqueous solution of $K_4Mo^{IV}(CN)_8\cdot 2H_2O$ in straight tube, but the amount of ethylenediamine ligand is reduced compared with **20** (IV.6.1 Synthesis).

The good agreement for the experimental powder X-ray diffraction pattern and the calculated one for **20**, indicates the successful preparation of the corresponding crystal (IV.6.2 Powder X-ray diffraction analysis). UV-Vis spectrum of **20** shows a broad absorption band from 300 nm to 800 nm without clear maxima, which indicates the probable observation of both d-d Cu ligand field transitions and charge transfer band for Cu^{2+}/Mo^{4+} pairs (IV.6.3 Optical measurements). Infrared (IR) spectrum for cyanide vibration regions are 2116, 2090 and 2050 cm^{-1} for **20**, which are the typical values for a system with terminal cyanides (IV.6.4 IR spectra). The frequencies observed are lower than that expected for bridging cyanide ligands, probably due to the rather long Cu-N bond distance (2.748 Å) in the cyanide bridges. Thermogravimetric analysis (TGA) show that **20** is stable up to 130 °C, thus there is no presence of solvents in the structure (III.6.5 Thermogravimetric analysis).

For **21**, no general characterization study has been conducted for the batch we synthesized because of the low yield. But this crystal structure and the characterization of **21** have been reported in the literature.[34] The reported infrared spectra for cyanide vibration regions are 2104, 2115, 2143 and 2159 cm^{-1}. The latter two frequencies 2143 and 2159 cm^{-1} can be attributed to bridging cyanide groups, because they are higher in energy than that of $K_4Mo^{IV}(CN)_8\cdot 2H_2O$ (2060-2125 cm^{-1}), suggesting the formation of cyanide bridges. A clear metal-to-metal charge transfer band in the UV-Vis spectrum located at 530 nm also indicates a metal-to-metal charge transfer from Mo^{IV} to Cu^{II} for **21**.

IV.4.1 Investigation of $[Cu(en)_2]_2[Mo(CN)_8]$ (20)

IV.4.1.1 Crystal structure of $[Cu(en)_2]_2[Mo(CN)_8]$ (20)

The crystal structure of **20** has been reported by Zhan et al., as a two-dimensional cyanido-bridged coordination polymer with no solvent in the structure (Table IV. 12 and Figure IV. 12).[35] Even if this compound has been reported, neither the physical characterizations nor the photomagnetic properties have been studied for this compound in the literature, which have been realized in this thesis.

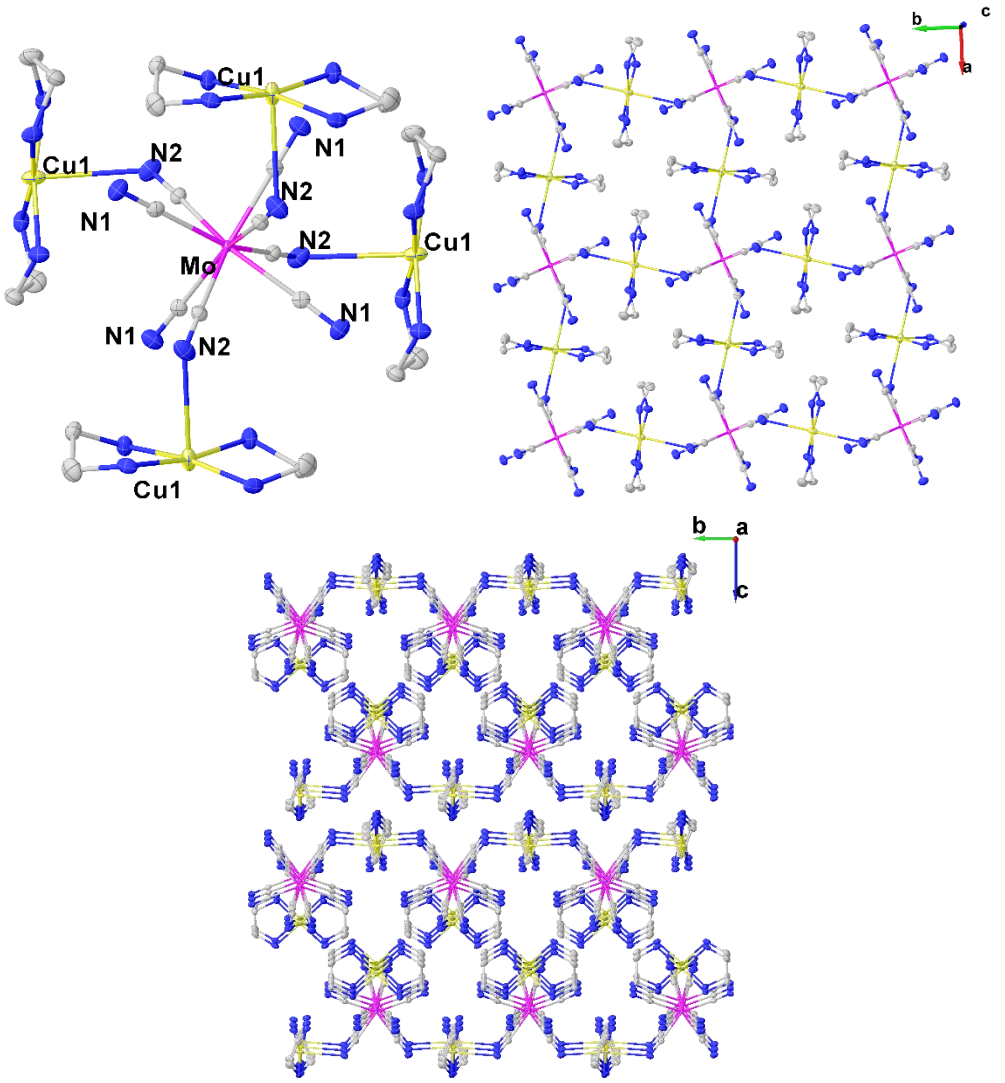

Figure IV. 12 (Top left) ORTEP diagram of molecular fragment of **20** for the coordination environment of Mo site with selected atoms labelling. (Top right) The single layer structure view along *c* axis. (Below) Four layers packed along *c* axis. Thermal ellipsoids of 50 % probability are shown.

Here we recall the important structural parameters of **20**. The Mo site adopts an almost idealized triangular dodecahedron (TDD) geometry as shown by the CShM value of 0.111 in this geometry. Four cyanide groups of Mo site form bridges with four Cu1 sites and the other four cyanides are terminal. The Cu1 sites in elongated octahedral geometry are coordinated to four nitrogen atoms from two en ligands in equatorial position and two cyanides from the neighboring molybdeum site in axial positions. The axial Cu1-N bond length around 2.7 Å is much more elongated than the equatorial ones which are around 2.0 Å (Table IV. 10). The axial bond angle for Cu-N≡C is around 119.175° which is severely deviated from linear. The layer is constructed by square-like eight member rings and the layers are packed by ABAB mode along *c* axis.

IV.4.1.2 Photomagnetic measurements for $[Cu(en)_2]_2[Mo(CN)_8]$ (20)

As observed from the temperature dependent of the χT product in the dark (Figure IV. 13), **20** reveals a paramagnetic behaviour with a χT value equals at 0.85 cm^3 mol^{-1} K, in agreement with two $Cu^{2+}(3d^9)$ ions of S = 1/2 (per Cu_2Mo units) with a Zeeman factor of g = 2.13 and one diamagnetic $Mo^{4+}(4d^2$ in square antiprism geometry) ion.

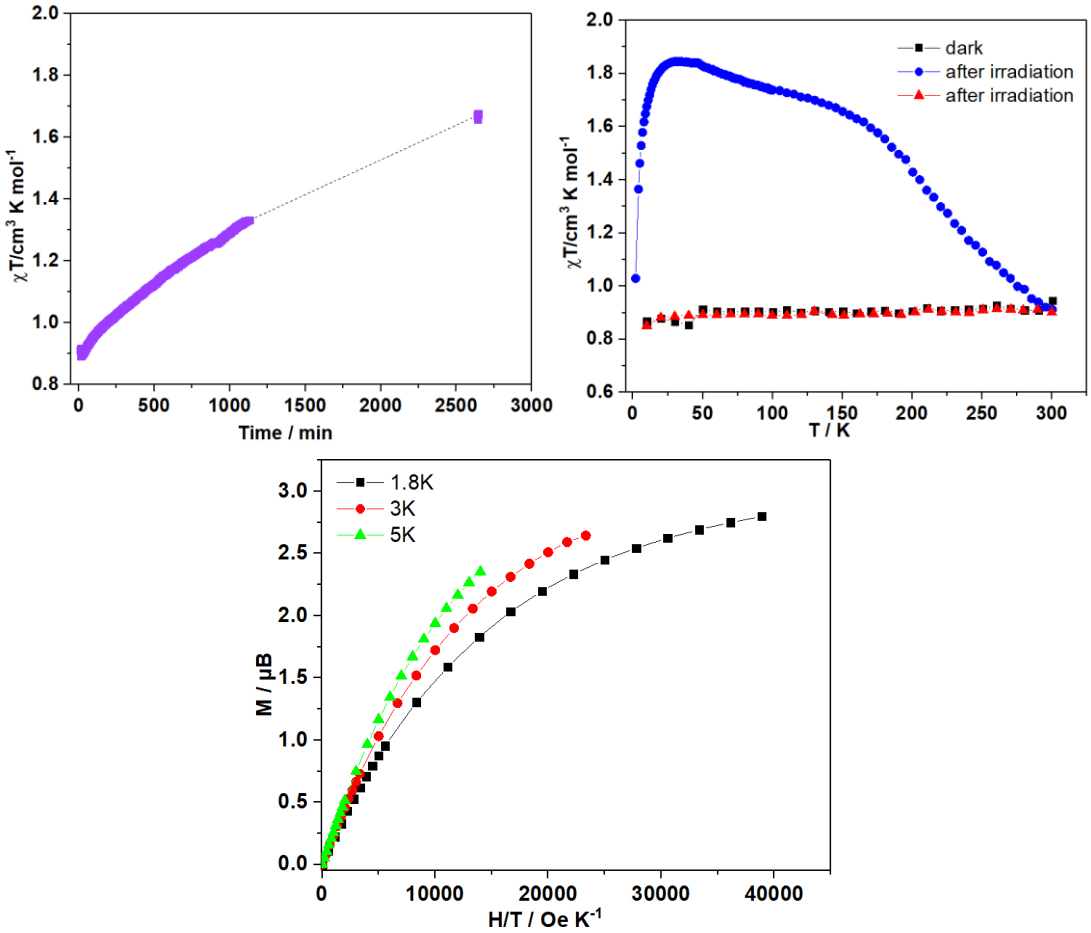

Figure IV. 13 (Top left) Time dependence of the χT for **20** measured at 10 K, 1 T with continuous 405 nm blue light irradiation (The discontinuous curve is due to shutdown of magnetic field when the helium level was too low in SQUID magnetometer, while the light irradiation at 10 K has been kept). (Top right) χT = f(T) plots of **20** measured in the dark before any light irradiation, after 405 nm irradiation and after heating to 300 K. (Below) Reduced magnetizations at different temperatures (1.8 K, 3 K, and 5 K) in the photo-excited state.

When **20** was irradiated with a light of 405 nm, the χT product increased from 0.89 to 1.68 cm^3 mol^{-1} K after 44 hours of irradiation. The curve is not continuous due to the shutdown of the magnetic field when the helium level was too low in SQUID magnetometer, while the light irradiation at 10 K has been kept. Then the light was switched off, and low-temperature magnetizations at 1.8, 3 and 5 K have been measured. The saturation magnetization at 1.8 K is 2.78 Nβ significantly higher than the expected value of 2 Nβ for two $Cu^{2+}(3d^9)$ ions before irradiation. The non-superposed reduced magnetizations suggest anisotropy in the photo-induced state.

Then the temperature dependence of the χT product from 2 K to 300 K first increased to reach a plateau at 1.85 cm^3 mol^{-1} K at 30 K. When compared with the χT product before irradiation, the χT value drastically increased, reaching a maximum difference of 0.94 cm^3 mol^{-1} K. Then, the χT product slightly decreased monotonously to reach 1.60 cm^3 mol^{-1} K at 170 K. Above this temperature, a faster decrease of the χT product was observed. At 300 K, the χT value was back to the value obtained before the light irradiation. The temperature dependence of the χT product from 2 K to 300 K has a similar shape than the χT vs. T plot of

13, suggesting that only the spin change of Mo^{IV} site is accounted for the strong photomagnetic effect for both compounds (Figure IV. 13). A new plot χT vs. T shows that the photo-induced process is reversible.

IV.4.2 Investigation of $[Cu(en)]_2[Cu(en)_2]_2[Mo(CN)_8]_2 \cdot 2MeOH \cdot 5H_2O$ (21)

IV.4.2.1 Crystal structure of $[Cu(en)]_2[Cu(en)_2]_2[Mo(CN)_8]_2 \cdot 2MeOH \cdot 5H_2O$ (21)

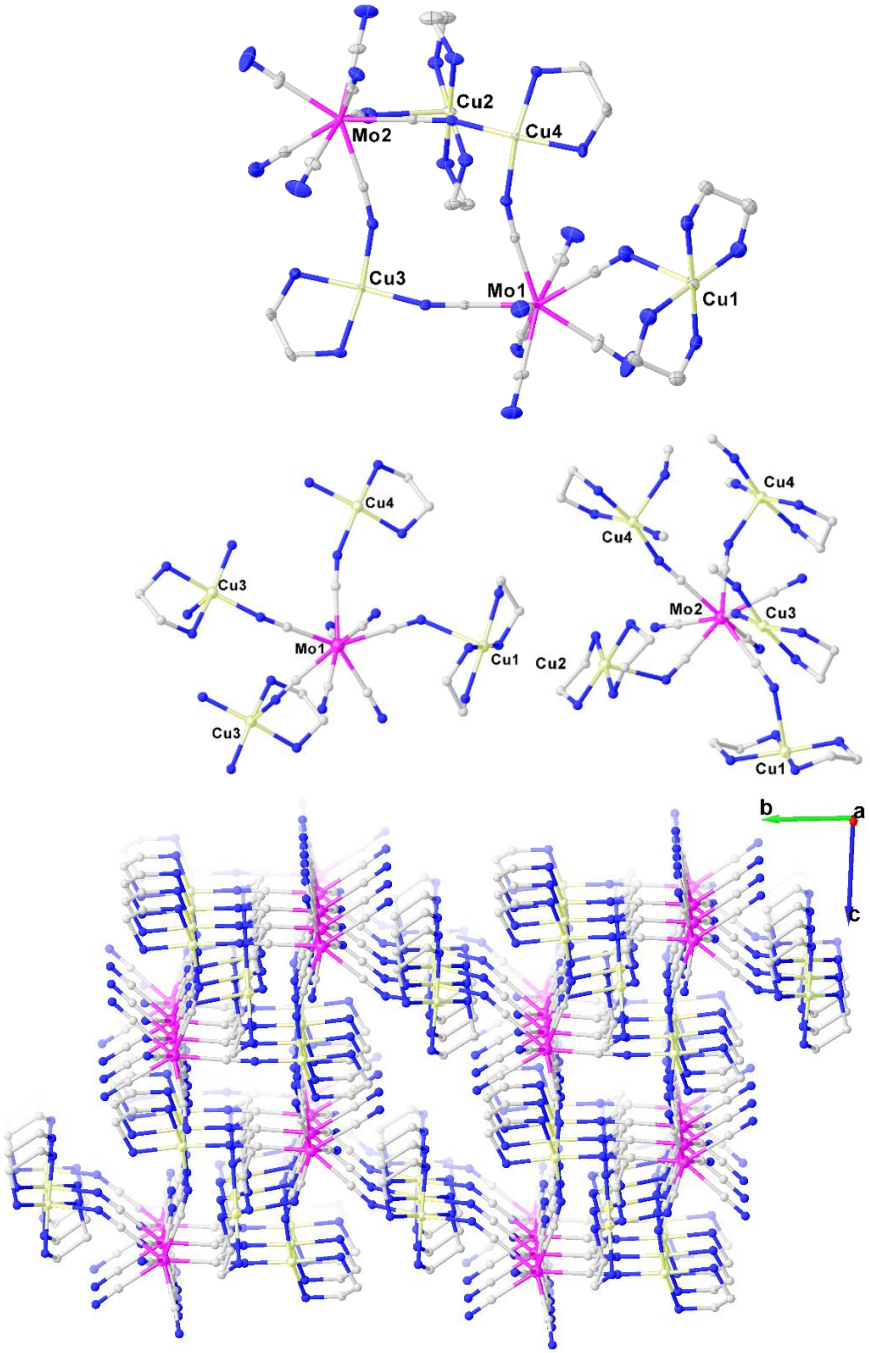

Figure IV. 14 (Top) ORTEP diagram of asymmetric unit of **21** with selected atoms labelling. Thermal ellipsoids of 50 % probability are shown. (Middle) The coordination environments for Mo1 and Mo2 sites. (Below) View of the three-dimensional network of **21** along the *a* axis. Non-coordinated solvent molecules are omitted for clarity.

The crystal structure of this type of three-dimensional cyanido-bridged bimetallic coordination polymer has been reported for $\{[Cu(en)_2][Cu(en)][Mo(CN)_8]\}_n \cdot 4nH_2O$.[34] Both this compound and **21** adopt triclinic space group *P*-1. The main difference between $[Cu(en)_2][Cu(en)][Mo(CN)_8]\}_n \cdot 4nH_2O$ and **21** is that **21** accommodates two types of solvents MeOH and H_2O. This results a slight difference in the cell parameters and the asymmetric unit. The *a* axis has been elongated from 9.0820(11) Å in the reported compound to 17.9756(16) Å in **21** (Table IV. 11 and Table IV. 12). But the same neutral three-dimensional cyanido-bridged bimetallic network is adopted by these two compounds if the solvent is ignored (Figure IV. 14 below).

X-ray diffraction studies show that the asymmetric unit of **21** contains two [Cu(en)], two $[Cu(en)_2]$ and two $[Mo(CN)_8]^{4-}$ units. The asymmetric unit is also doubled than the reported compound which consists one [Cu(en)], two halfves $[Cu(en)_2]$ and one $[Mo(CN)_8]^{4-}$ (Figure IV. 14 top). Four cyanides of Mo1 site are bridged with one Cu1 site, two Cu3 sites and one Cu4 site. Five cyanides of Mo2 site form bridges with one Cu1 site, one Cu2 site, one Cu3 site and two Cu4 sites (Figure IV. 14 middle). The Cu1 and Cu2 sites are coordinated to four nitrogen atoms from two en ligands and two cyanides from the neighboring molybdeum site, forming an elongated octahedral geometry. However, Cu3 and Cu4 sites are coordinated to two nitrogen atoms from the en ligand and three cyanides from the neighboring molybdeum site, forming a square pyramidal environment geometry.

III.4.2.2 Photomagnetic measurements for $[Cu(en)]_2[Cu(en)_2]_2[Mo(CN)_8]_2 \cdot 2MeOH \cdot 5H_2O$ (21)

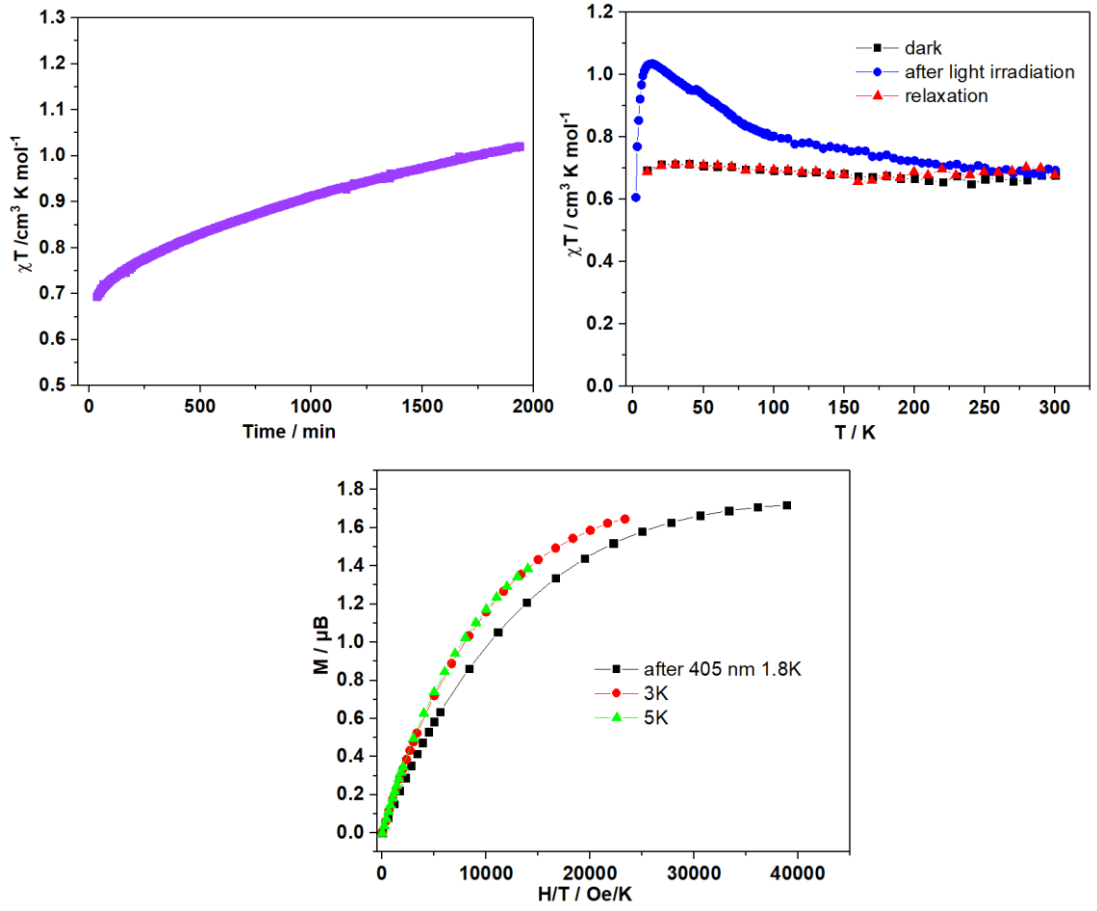

Figure IV. 15 (Top left) Time dependence of the χT product for **21** measured at 10 K, 1 T with continuous 405 nm blue light irradiation. (Top right) χT = f(T) plots of **21** measured in the dark before any light irradiation, after 405 nm irradiation and after heating to 300 K. (Below) Reduced magnetizations at different temperatures (1.8 K, 3 K and 5 K) in the photo-excited state.

The photomagnetic studies for **21** are very different with **20** (Figure IV. 15). When **21** was irradiated with a light of 405 nm, the χT product only increased from 0.70 to 1.02 cm^3 mol^{-1} K after 32 hours of irradiation. The $\Delta\chi T = \chi T_{after} - \chi T_{before}$ equals 0.32 cm^3 mol^{-1} K which is much smaller than $\Delta\chi T$ = 0.89 cm^3 mol^{-1} K found for **20**.

Then the light was switched off, and low-temperature magnetizations at 1.8, 3 and 5 K have been measured. The reduced magnetizations do not show any clear magnetic anisotropy in the photo-induced state. Different with **20**, the temperature dependent curve for the photoexcited state shows a clear peak at 13 K, which is similar to **17**. Above 13 K, the fast decrease of χT product when temperature was increasing can be explained by the ferromagnetic interaction between the photogenerated Mo^V and the Cu^{II} remained after light irradiation, suggesting a metal-to-metal charge transfer photomagnetic mechanism.[2] The fully reversible behavior after thermal relaxation at 300 K was also observed for **21**.

IV.4.3 Discussion on $[Cu(en)_2]_2[Mo(CN)_8]$ (20) and $[Cu(en)]_2[Cu(en)_2]_2[Mo(CN)_8]_2 \cdot 2MeOH \cdot 5H_2O$ (21)

Using ethylenediamine ligand as blocking ligand for Cu^{2+} ions, 2D-$Cu(en)_2]_2[Mo(CN)_8]$ (**20**) and 3D-$[Cu(en)]_2[Cu(en)_2]_2[Mo(CN)_8]_2 \cdot 2MeOH \cdot 5H_2O$ (**21**) are studied. Similar with **13**, only a S-T mechanism is proposed for **20**. The S-T mechanism is compatible with the presence of non-bridged CN groups which allows structural rearrangement as those shown in chapter II. The absence of MMCT process for **20** is probably due to the rather long Cu-N length which is around 2.748 Å. For **21**, a light-induced metal-to-metal charge transfer (MMCT) is proposed and it is not easy to conclude the existence of S-T mechanism because of the weak photomagnetic effect.

IV.5 Conclusion and perspectives

In this chapter, a series of compounds are reported with different dimensionalities and with different number of cyanide ligands engaging as bridges (Table IV. 8). The diamagnetic compound $Cd_2[Mo(CN)_8] \cdot 8H_2O$ (**16**), as the first three dimensional network with all cyanide bridges of Mo site linked to Cd^{2+} ions, has been structurally and photomagnetically studied. The photomagnetic effect is weak and much smaller than the previous studied ionic salts in this thesis and the reported molecular compound $\{[Cd^{II}(bpy)_2]_4[Mo^{IV}(CN)_8]_2\} \cdot 10H_2O$. This suggests that the photomagnetic effect of the $[Mo^{IV}(CN)_8]^{4-}$ unit is very weak when all cyanides are acting as bridges in a three dimensional network, where MMCT can be ruled out.

The studies of the inorganic 3-D copper(II)-octacyanidomolybdate(IV) compounds, $KCu^ICu^{II}Mo(CN)_8 \cdot 3H_2O$ (**17**) and $K_2Cu^I_3(\mu\text{-}CN)Mo(CN)_8 \cdot 4H_2O$ (**18**), show that the metal-to-metal charge transfer process occurs during synthesis in solution and this process is facilitated by increasing the synthesis temperature. The photomagnetic properties for **17** confirm the presence of MMCT mechanism. The photomagnetic properties of **18** suggest that only S-T effect is observed for **18** as all the cyanide groups of $[Mo(CN)_8]^{4-}$ are engaged in bridges with Cu^I. Unlike molybdenum, the $[W^{IV}(CN)_8]^{4-}$ building block is proved to be not photomagnetic in $K_2Cu^I_3(\mu\text{-}CN)W(CN)_8 \cdot 4H_2O$ (**19**).

We have also structurally and photomagnetically studied copper (II)-octacyanidomolybdate(IV) bridged complexes, $[Cu(en)_2]_2[Mo(CN)_8]$ (**20**) and $[Cu(en)]_2[Cu(en)_2]_2[Mo(CN)_8]_2 \cdot 2MeOH \cdot 5H_2O$ (**21**). Similar with **13**, only S-T mechanism is proposed for **20.** The rather long Cu-N≡C distance in **20** may render less probable the MMCT process. Similar with **17**, a metal-to-metal charge transfer (MMCT) mechanism is confirmed for **21**, and the S-T mechanism is not evident (Figure IV. 16). It is worth to mention that all the photomagnetic properties of the compounds reported in this section (even weak) are all reversible.

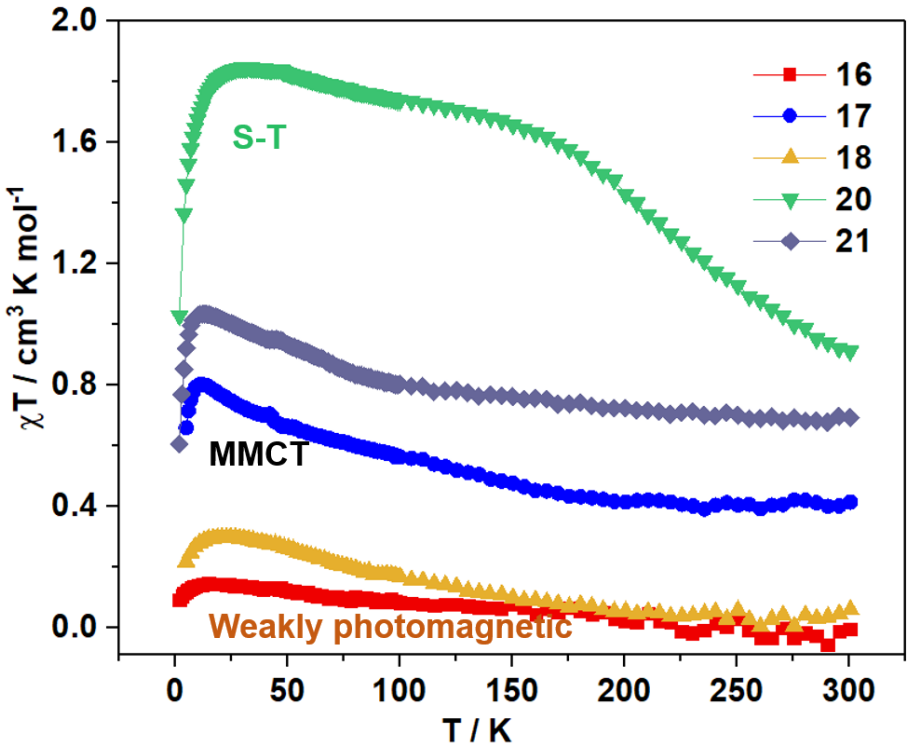

Figure IV. 16 The comparison of χT = f(T) plots of **16**, **17**, **18**, **20** and **21** measured after 405 nm irradiation.

In conclusion, we provide proofs for the existence of MMCT process both in solution and in solid state for copper(II)-octacyanidomolybdate(IV) system. We confirm the possible presence of MMCT process when cyanide ligands are linked to Cu^{2+}, but it is not clear for the contribution of S-T mechanism for such system. To clarify the contributions of MMCT and S-T mechanisms in copper(II)-octacyanidomolybdate(IV) bridged systems, photomagnetic studies of other simple molecular compounds with low nuclearity are still necessary. This will help the understanding the influence of structural characteristics (such as Mo-C≡N bond angles, Cu-N≡C bond angles and Cu-N bond distances and the geometry of molybdenum site or copper site).

Table IV. 8 The summary of structural characteristics for the compounds involved in this chapter.

Compound	**Formula**	**Bridged cyanide groups per Mo site**	**Proposed mechanism**
16	3D-$Cd_2[Mo(CN)_8]\cdot 8H_2O$	8	weak
17	3D-$KCu^{I}Cu^{II}[Mo(CN)_8]\cdot 3H_2O$	8	MMCT
18	3D-$K_2Cu^{I}_3(\mu\text{-}CN)[Mo(CN)_8]\cdot 4H_2O$	8	weak
19	3D-$K_2Cu^{I}_3(\mu\text{-}CN)[W(CN)_8]\cdot 4H_2O$	8	none
20	2D-$[Cu(en)_2]_2[Mo(CN)_8]$	4	S-T
21	3D-$[Cu(en)]_2[Cu(en)_2]_2[Mo(CN)_8]_2\cdot 2MeOH\cdot 5H_2O$[34]	4 for Mo1 and 5 for Mo2	MMCT

IV.6 Supporting materials

IV.6.1 Synthesis

Preparation of $Cd_2[Mo(CN)_8]\cdot 8H_2O$ (16).

The preparation of **16** is as described during the synthesis of $A_4[Mo^{IV}(CN)_8]$ (A = alkali cations). **16** was prepared as precipitate by mixing the 3 mL solution $K_4[Mo^{IV}(CN)_8]\cdot 2H_2O$ (150 mg, 3.0 mmol) and the 3 mL solution $CdCl_2$ (114 mg, 6.2 mmol). The crystal which is suitable for Single-Crystal X-Ray Diffraction (SCXRD) analysis was obtained by the slow diffusion by water in a H tube by placing these two solutions into two different arms.

Preparation of $KCu^{I}Cu^{II}Mo(CN)_8\cdot 3H_2O$ (17).

Single crystals for **17** were obtained by slow diffusion at room temperature in a straight tube, by diffusing 1 mL aqueous solution of $CuCl_2\cdot 2H_2O$ (17.0 mg, 1 mmol) into 1mL aqueous solution of $K_4[Mo^{IV}(CN)_8]\cdot 2H_2O$ (50 mg, 1.0 mmol) with 20 mL H_2O as buffer layer. Dark purple crystals for **17** were obtained after one month.

Preparation of $K_2Cu^{I}_3(\mu\text{-}CN)Mo(CN)_8\cdot 4H_2O$ (18).

Single crystals for **18** were obtained by an analogous way as **17** but with slow diffusion at 80 ℃ in oven. Yellow crystals for **18** were obtained after one month.

Preparation of $K_2Cu^{I}_3(\mu\text{-}CN)Mo(CN)_8\cdot 4H_2O$ (18b).

Tiny yellow crystals for **18b** were obtained by direct reaction at 80 ℃ in a small vial by mixing 2 mL aqueous solution $K_4[Mo^{IV}(CN)_8]\cdot 2H_2O$ (25 mg, 0.5 mmol) and CuCN (18 mg, 2 mmol).

Preparation of $K_2Cu^{I}_3(\mu\text{-}CN)W(CN)_8\cdot 4H_2O$ (19).

Tiny yellow crystals for **19** were obtained by direct reaction at 80 ℃ in a small vial by mixing 2 mL aqueous solutions $K_4[W^{IV}(CN)_8]\cdot 2H_2O$ (30 mg, 0.5 mmol) and CuCN (18 mg, 2 mmol).

Preparation of $[Cu(en)_2]_2[Mo(CN)_8]$ (20).

First, 2 mL aqueous solution of $CuCl_2$ (17.0 mg, 1 mmol) was mixed with 60 mg solution of ethylenediamine ligand. Then a violet solution was prepared by adding slowly of the above mixture solution to 1 mL aqueous solution of $K_4[Mo^{IV}(CN)_8]\cdot 2H_2O$ (26 mg, 0.5 mmol) with shaking. Then after slowly addition of about 1 mL MeOH without shaking, the square purple crystals of **20** would appear immediately.

Preparation of $[Cu(en)]_2[Cu(en)_2]_2[Mo(CN)_8]_2\cdot 2MeOH\cdot 5H_2O$ (21).

Single crystals for **21** were obtained by slow diffusion at room temperature in a straight tube. The layer on the top was a mixture of 2 mL aqueous solution of $CuCl_2\cdot 2H_2O$ (17.6 mg, 1 mmol) and 5 mg ethylenediamine ligand. The buffer layer was 20 mL MeOH : H_2O = 1 : 1. The bottom layer was 1 mL aqueous solution of $K_4[Mo^{IV}(CN)_8]\cdot 2H_2O$ (26 mg, 0.5 mmol). Purple needle crystals for **21** were obtained after two weeks.

IV.6.2 Powder X-ray diffraction analysis

$Cd_2[Mo(CN)_8]\cdot 8H_2O$ (16) with blue stars indicating unknown impurities

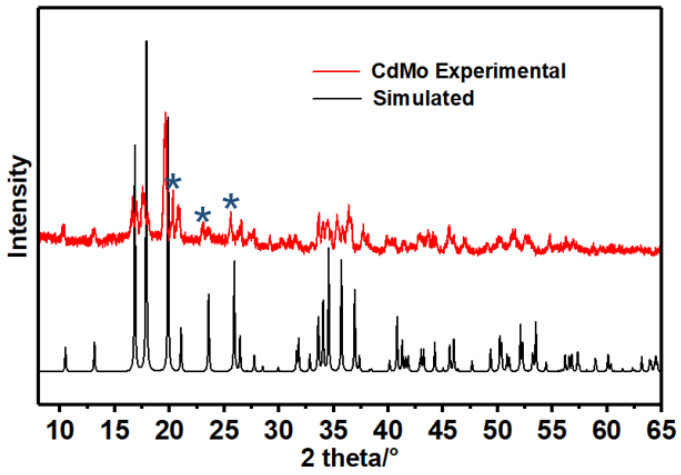

$KCu^{I}Cu^{II}[Mo(CN)_8]\cdot 3H_2O$ (17) with blue stars indicating unknown impurities

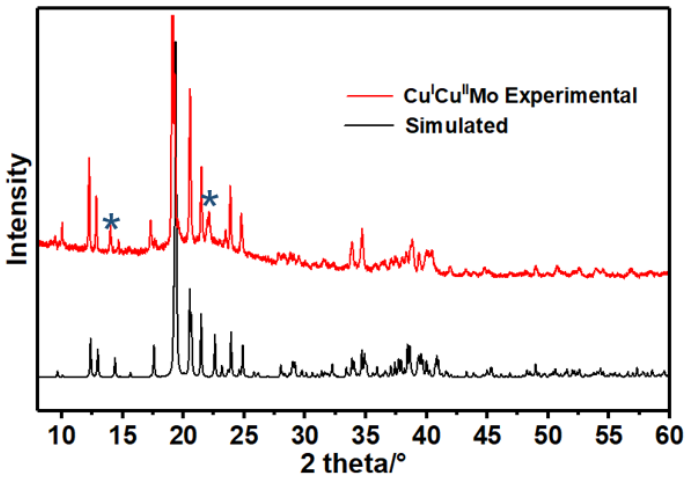

$K_2Cu^{I}_3(\mu\text{-}CN)[Mo(CN)_8]\cdot 4H_2O$ (18)

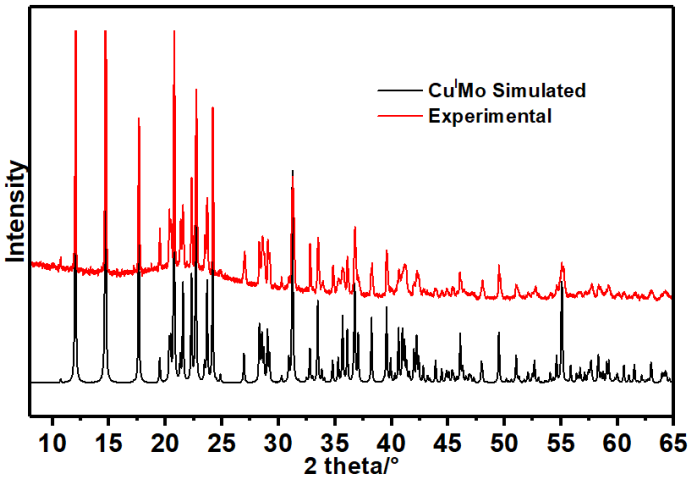

$Cu_2[W(CN)_8]\cdot 5H_2O$ prepared with same approach as **18**.[14]

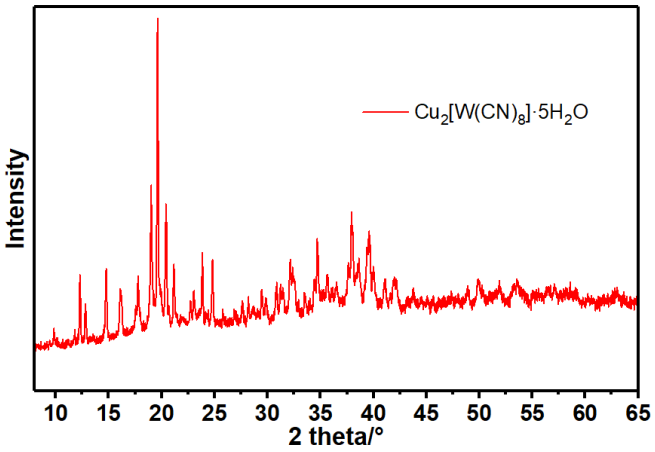

$K_2Cu^I_3(\mu\text{-}CN)[Mo(CN)_8]\cdot 4H_2O$ (18b) prepared with CuCN as starting material

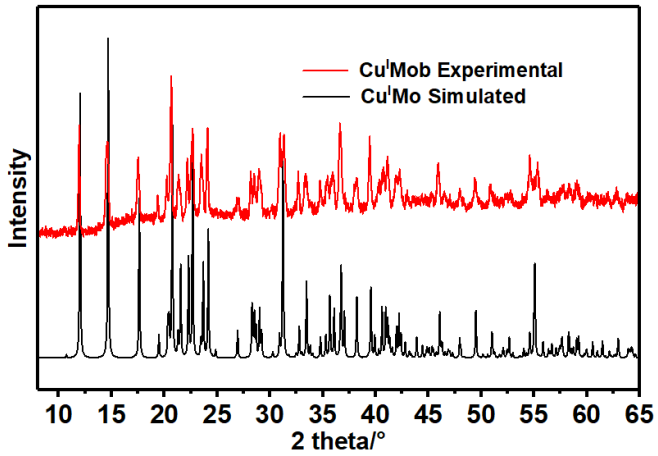

The experimental $K_2Cu^I_3(\mu\text{-}CN)[W(CN)_8]\cdot 4H_2O$ (19) and simulated $K_2Cu^I_3(\mu\text{-}CN)[Mo(CN)_8]\cdot 4H_2O$ (18)

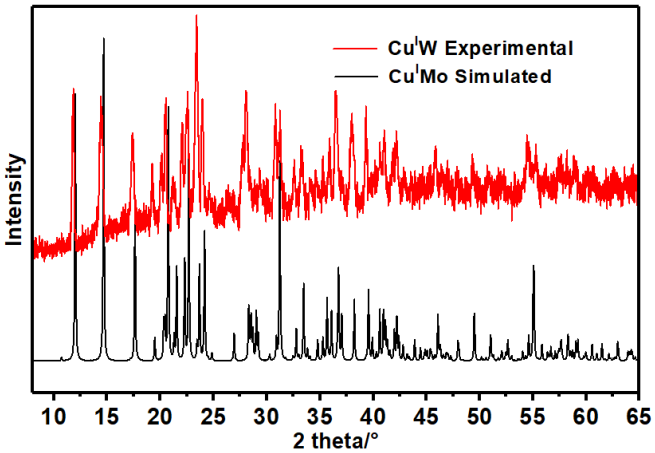

$[Cu(en)_2]_2[Mo(CN)_8]$ (20)

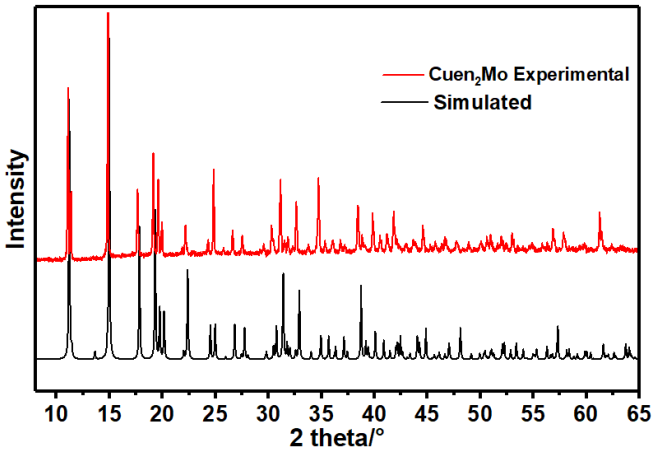

IV.6.3 Optical measurements

The comparison between $Cd_2[Mo(CN)_8]\cdot 8H_2O$ (16) and $K_4[Mo(CN)_8]\cdot 2H_2O$ (1):

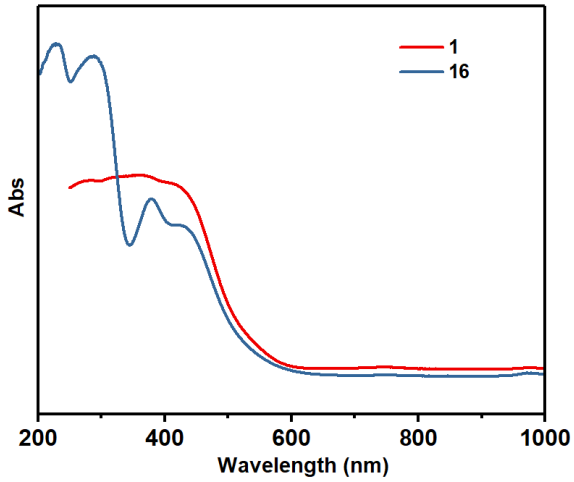

The comparison of $KCu^{I}Cu^{II}[Mo(CN)_8]\cdot 3H_2O$ (17), $K_2Cu^{I}_3(\mu\text{-}CN)[Mo(CN)_8]\cdot 4H_2O$ (18) and $K_2Cu^{I}_3(\mu\text{-}CN)[Mo(CN)_8]\cdot 4H_2O$ (18b)

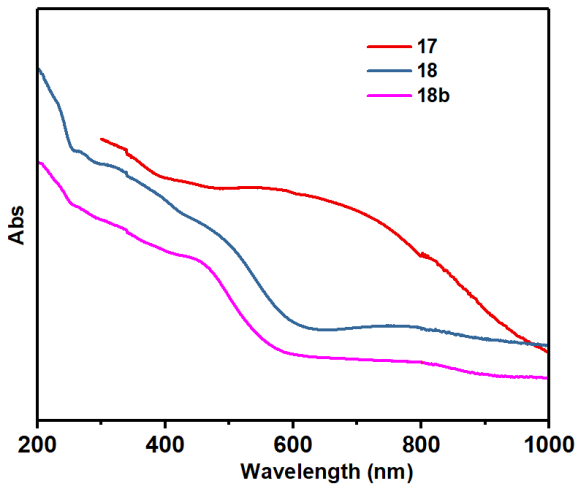

The comparison of $K_2Cu^I_3(\mu\text{-}CN)[Mo(CN)_8]\cdot 4H_2O$ (18b) and $K_2Cu^I_3(\mu\text{-}CN)[W(CN)_8]\cdot 4H_2O$ (19)

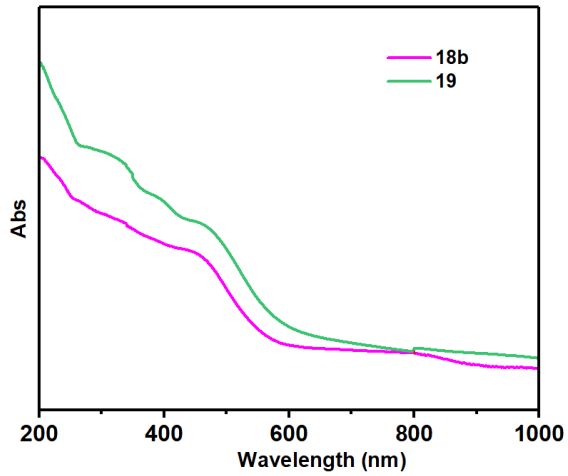

$[Cu(en)_2]_2[Mo(CN)_8]$ (20)

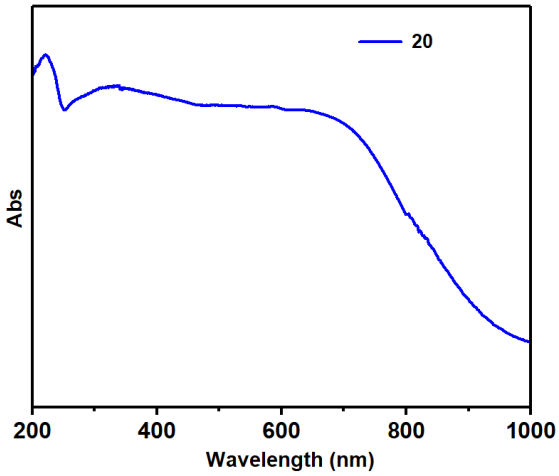

IV.6.4 IR spectra

Table IV. 9 The summary of $\tilde{\nu}_{CN}$ stretching bands observed for the compounds involved in this thesis.

Compound	Formula	$\tilde{\nu}_{CN}$ stretching bands / cm^{-1}
1	$K_4[Mo(CN)_8]\cdot 2H_2O$	**2125**, **2102**, 2076, 2060
3	$Rb_4[Mo(CN)_8]\cdot 2H_2O$	**2122**, **2100**, 2075, 2057
4	$Cs_{20}[Mo(CN)_8]_5\cdot 7H_2O$	**2094**
7	$K_4[W(CN)_8]\cdot 2H_2O$	**2123**, 2092, 2056
8	$Rb_4[W(CN)_8]\cdot H_2O$	**2121**, 2090, 2052
9	$K_6Cs_{16}[W(CN)_8]_5Cl_2\cdot 4H_2O$	**2096**
10	$[Zn(en)_3]_2[Mo(CN)_8]\cdot 5H_2O$	**2136**, 2123, 2116, 2102
11	$[\{Zn(tren)\}_3(\mu\text{-tren})]_2[Mo(CN)_8]_3\cdot 18H_2O$	**2100**
13	$[\{Cu(tren)\}_3(\mu\text{-tren})]_4[Mo(CN)_8]_6\cdot 45H_2O\cdot 2CH_3OH$	**2098**
14	$[Zn(en)_3]_2[W(CN)_8]\cdot 5H_2O$	**2137**, 2119, 2114, 2094
15	$[\{Zn(tren)\}_3(\mu\text{-tren})]_2[W(CN)_8]_3\cdot 17H_2O$	**2092**
16	$Cd_2[Mo(CN)_8]\cdot 8H_2O$	**2135***
17	$KCu^{I}Cu^{II}[Mo(CN)_8]\cdot 3H_2O$	**2160***, 2129*
18	$K_2Cu^{I}_3(\mu\text{-CN})[Mo(CN)_8]\cdot 4H_2O$	**2129***, 2042*
19	$K_2Cu^{I}_3(\mu\text{-CN})[W(CN)_8]\cdot 4H_2O$	**2123***, 2040*
20	$[Cu(en)_2]_2[Mo(CN)_8]$	**2116**, 2090, 2050
21	$[Cu(en)]_2[Cu(en)_2]_2[Mo(CN)_8]_2\cdot 2MeOH\cdot 5H_2O$[34]	**2159***, 2143*, 2115, 2104

*These frequencies are ascribed to the bridging cyanide ligands.

$Cd_2[Mo(CN)_8]\cdot 8H_2O$ (16):

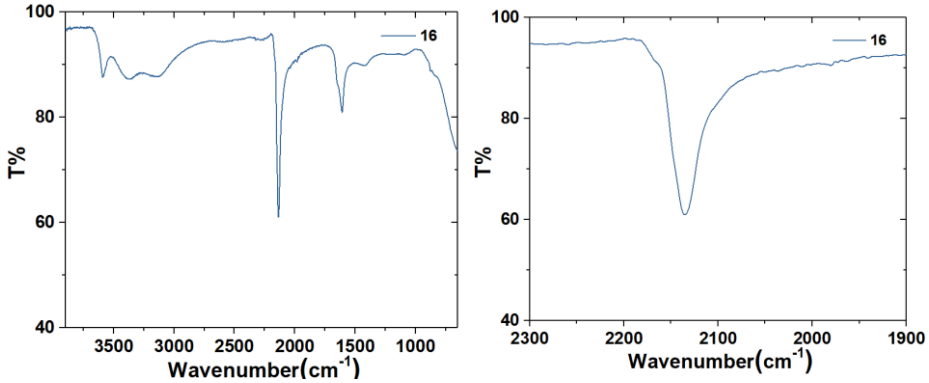

The comparison of $KCu^{I}Cu^{II}[Mo(CN)_8]\cdot 3H_2O$ (17), $K_2Cu^{I}_3(\mu\text{-}CN)[Mo(CN)_8]\cdot 4H_2O$ (18) and $Cu^{II}_2[Mo(CN)_8]\cdot xH_2O$ ($Cu^{II}Mo$)

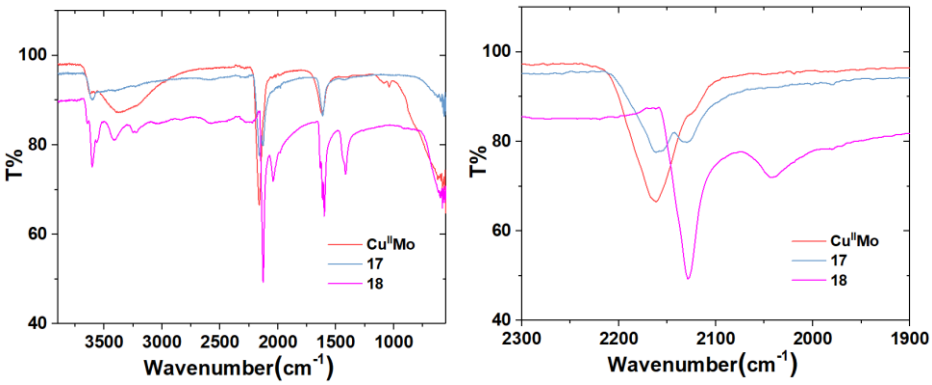

The comparison of $K_2Cu^{I}_3(\mu\text{-}CN)[Mo(CN)_8]\cdot 4H_2O$ (18), $K_2Cu^{I}_3(\mu\text{-}CN)[Mo(CN)_8]\cdot 4H_2O$ (18b) and $K_2Cu^{I}_3(\mu\text{-}CN)[W(CN)_8]\cdot 4H_2O$ (19)

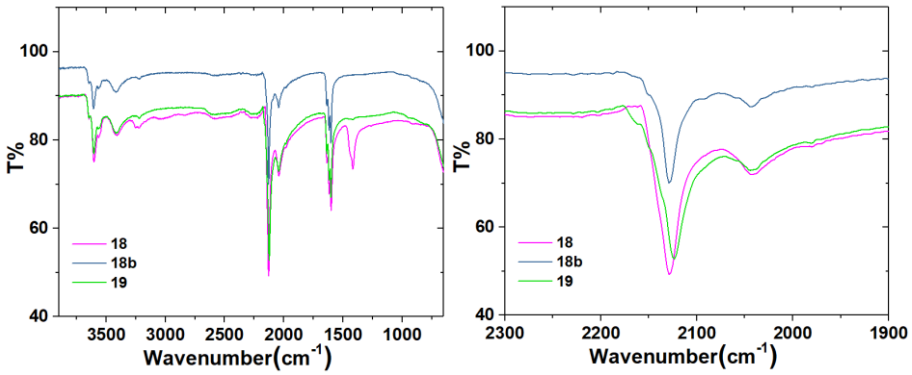

$[Cu(en)_2]_2[Mo(CN)_8]$ (20)

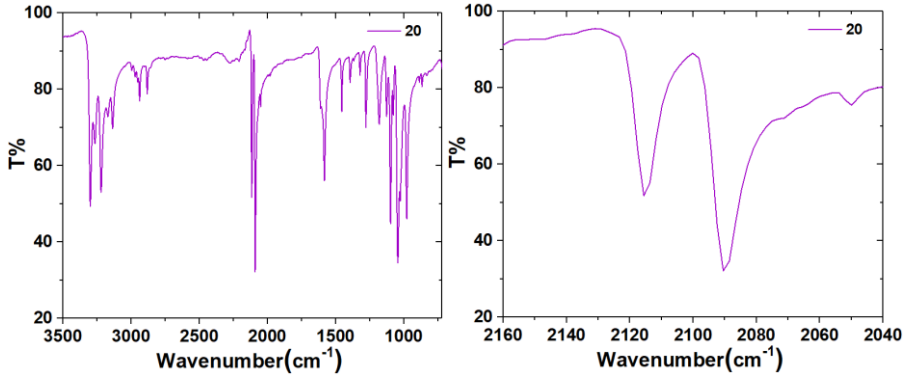

IV.6.5 Thermogravimetric analysis

$[Cu(en)_2]_2[Mo(CN)_8]$ (20)

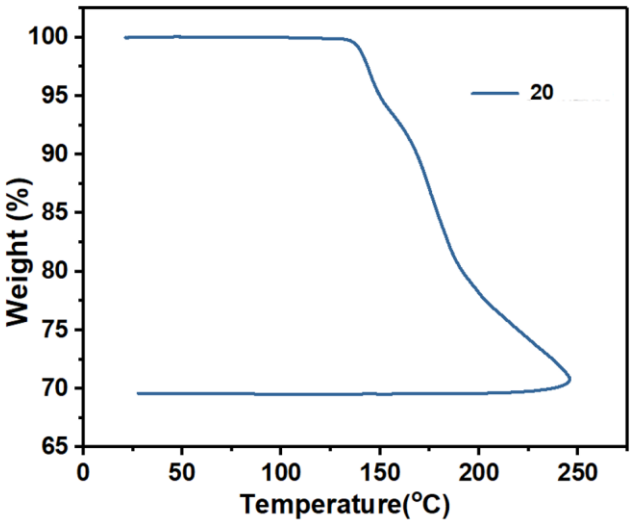

IV.6.6 Crystallographic data for $[Cu(en)_2]_2[Mo(CN)_8]$ (20) and $[Cu(en)]_2[Cu(en)_2]_2[Mo(CN)_8]_2 \cdot 2MeOH \cdot 5H_2O$ (21)

Table IV. 10 Selected bond lengths and angles for **20**.

Atoms		**Length/Å**	**Atoms**		**Length/Å**	**Atoms**			**Angle/°**
Mo	C1	2.154(3)	N1	C1	1.156(4)	N1	C1	Mo	177.5(3)
Mo	C2	2.176(3)	C2	N2	1.148(4)	N2	C2	Mo	177.2(3)
Average		2.165(3)	Average		1.152(4)	Average			177.4(3)
Cu1	N2	2.748				C2	N2	Cu1	119.175
Cu1	N3	2.004(3)				C3	N3	Cu1	108.67(19)
Cu1	N4	2.009(3)				C4	N4	Cu1	108.3(2)

Table IV. 11 Selected bond lengths and angles for **21**.

Atoms		**Length/Å**	**Atoms**		**Length/Å**	**Atoms**			**Angle/°**
Mo1	C1	2.160(3)	N1	C1	1.145(4)	N1	C1	Mo1	174.7(3)
Mo1	C2	2.158(4)	C2	N2	1.151(5)	N2	C2	Mo1	178.8(4)
Mo1	C3	2.156(4)	C3	N3	1.142(5)	N3	C3	Mo1	177.6(4)
Mo1	C4	2.167(3)	N4	C4	1.150(5)	N4	C4	Mo1	177.5(3)
Mo1	C5	2.161(3)	N5	C5	1.148(4)	N5	C5	Mo1	175.2(3)
Mo1	C6	2.150(3)	N6	C6	1.151(4)	N6	C6	Mo1	178.5(3)
Mo1	C7	2.158(3)	N7	C7	1.146(5)	N7	C7	Mo1	177.6(3)
Mo1	C8	2.164(3)	N8	C8	1.152(4)	N8	C8	Mo1	175.8(3)
Average		2.159(3)	Average		1.148(5)	Average			177.0(3)

(continue of Table IV. 11)

Mo2	C21	2.168(3)	C21	N21	1.147(5)	N21	C21	Mo2	179.1(3)
Mo2	C22	2.154(4)	C22	N22	1.147(5)	N22	C22	Mo2	178.9(4)
Mo2	C23	2.160(3)	N23	C23	1.148(4)	N23	C23	Mo2	176.8(3)
Mo2	C24	2.165(4)	C24	N24	1.145(5)	N24	C24	Mo2	178.5(3)
Mo2	C25	2.158(3)	N25	C25	1.151(4)	N25	C25	Mo2	178.4(3)
Mo2	C26	2.159(3)	N26	C26	1.152(5)	N26	C26	Mo2	176.1(3)
Mo2	C27	2.150(3)	N27	C27	1.151(4)	N27	C27	Mo2	174.6(3)
Mo2	C28	2.155(4)	N28	C28	1.152(5)	N28	C28	Mo2	177.7(3)
Average		2.159(3)	Average		1.149(5)	Average			177.5(3)
Cu1	N2	2.511(3)	Cu3	N6	1.994(3)	C2	N2	Cu1	132.0(3)
Cu1	N13	2.026(3)	Cu3	N9	2.013(3)	C26	N26	Cu2	125.4(3)
Cu1	N14	2.021(4)	Cu3	N10	2.019(3)	C6	N6	Cu3	161.7(3)
Cu1	N15	2.012(3)	Cu3	N27	1.985(3)	C27	N27	Cu3	157.6(3)
Cu1	N16	2.018(3)	Cu3	N5	2.222(3)	C1	N1	Cu4	159.1(3)
						C25	N25	Cu4	165.0(3)
Cu2	N17	2.026(3)	Cu4	N11	2.020(3)	C23	N23	Cu4	151.2(3)
Cu2	N18	2.012(3)	Cu4	N12	2.018(3)				
Cu2	N19	2.026(3)	Cu4	N1	1.992(3)				
Cu2	N20	2.023(3)	Cu4	N25	1.993(3)				
Cu2	N26	2.553(3)	Cu4	N23	2.206(3)				

Table IV. 12 Single crystal X-ray diffraction data and structure refinement parameters for $[Cu(en)_2]_2[Mo(CN)_8]$ (**20**) and $[Cu(en)]_2[Cu(en)_2]_2[Mo(CN)_8]_2 \cdot 2MeOH \cdot 5H_2O$ (**21**).

Compound	**20**	**Compound**	**21**
Formula	$C_{16}H_{32}Cu_2MoN_{16}$	Formula	$C_{30}H_{56}Cu_4Mo_2N_{28}O_7$
$D_{calc.}$/g cm^{-3}	1.709	$D_{calc.}$/g cm^{-3}	1.740
μ/mm^{-1}	2.126	μ/mm^{-1}	2.137
Formula Weight/g mol^{-1}	671.59	Formula Weight/g mol^{-1}	1367.06
T/K	120(2)	*T*/K	293(2)
Crystal System	tetragonal	Crystal System	triclinic
Space Group	$P4_2/n$	Space Group	*P*-1
a/Å	9.1875(4)	*a*/Å	9.7331(8)
b/Å	9.1875(4)	*b*/Å	15.5918(14)
c/Å	15.4636(6)	*c*/Å	17.9756(16)
α/°	90	α/°	85.525(10)
β/°	90	*β*/°	81.422(8)
γ/°	90	*γ*/°	75.459(7)
V/Å^3	1305.28(12)	V/Å^3	2608.7(4)
Z	2	*Z*	2
Z'	0.25	*Z'*	1
Wavelength/Å	0.71073	Wavelength/Å	0.71073
Radiation type	MoK_a	Radiation type	MoK_a
Q_{min}/°	2.634	Q_{min}/°	3.033
Q_{max}/°	26.455	Q_{max}/°	27.500
Measured Refl.	7673	Measured Refl.	54973
Independent Refl.	1351	Independent Refl.	11948
Reflections with I > 2(I)	1294	Reflections with I > 2(I)	9033
R_{int}	0.0206	R_{int}	0.0464
Parameters	80	Parameters	654
Restraints	0	Restraints	0
Largest Peak	0.608	Largest Peak	1.815
Deepest Hole	-0.476	Deepest Hole	-1.583
GooF	1.265	GooF	1.037
wR_2 (all data)	0.0707	wR_2 (all data)	0.1173
wR_2	0.0701	wR_2	0.1041
R_1 (all data)	0.0282	R_1 (all data)	0.0613
R_1	0.0270	R_1	0.0397
S_{SAPR}	2.881	S_{SAPR}	0.612/0.502
S_{TDD}	0.111	S_{TDD}	1.003/1.215

S is continuous shape measurement (CShM) value. SAPR and TDD represent square antiprism and triangular dodecahedron, respectively.

IV.7 References

1. Brossard, S.; Volatron, F.; Lisnard, L.; Arrio, M. A.; Catala, L.; Mathoniere, C.; Mallah, T.; dit Moulin, C. C.; Rogalev, A.; Wilhelm, F.; Smekhova, A.; Sainctavit, P., Investigation of the Photoinduced Magnetization of Copper Octacyanomolybdates Nanoparticles by X-ray Magnetic Circular Dichroism. *J. Am. Chem. Soc.* **2012,** *134* (1), 222-228.
2. Stefanczyk, O.; Pelka, R.; Majcher, A. M.; Mathoniere, C.; Sieklucka, B., Irradiation Temperature Dependence of the Photomagnetic Mechanisms in a Cyanido-Bridged $Cu_2^{II}Mo^{IV}$ Trinuclear Molecule. *Inorg. Chem.* **2018,** *57* (14), 8137-8145.
3. Bridonneau, N.; Quatremare, P.; von Bardeleben, H. J.; Cantin, J.-L.; Pillet, S.; Bendeif, E.-E.; Marvaud, V., Direct Evidence of a Photoinduced Electron Transfer in Diluted "Molybdenum-Copper" Molecular Compounds. *Eur. J. Inorg. Chem.* **2017**, 370–377.
4. Ohkoshi, S. I.; Tokoro, H.; Hozumi, T.; Zhang, Y.; Hashimoto, K.; Mathonière, C.; Bord, I.; Rombaut, G.; Verelst, M.; Cartier Dit Moulin, C.; Villain, F., Photoinduced Magnetization in Copper Octacyanomolybdate. *J. Am. Chem. Soc.* **2006,** *128* (1), 270-277.
5. Hozumi, T.; Hashimoto, K.; Ohkoshi, S. I., Electrochemical synthesis, crystal structure, and photomagnetic properties of a three-dimensional cyano-bridged copper-molybdenum complex. *J. Am. Chem. Soc.* **2005,** *127* (11), 3864-3869.
6. Ohkoshi, S.-i.; Machida, N.; Zhong, Z. J.; Hashimoto, K., Photo-induced magnetization in copper(II) octacyanomolybdate(IV). *Synth.Met.* **2001,** *122* (3), 523-527.
7. Ohkoshi, S. I.; Machida, N.; Abe, Y.; Zhong, Z. J.; Hashimoto, K., Visible Light-Induced Reversible Photomagnetism in Copper(II) Octacyanomolybdate(IV). *Chem. Lett.* **2001,** (4), 312-313.
8. Korzeniak, T.; Jankowski, R.; Kozieł, M.; Pinkowicz, D.; Sieklucka, B., Reversible Single-Crystal-to-Single-Crystal Transformation in Photomagnetic Cyanido-Bridged Cd_4M_2 Octahedral Molecules. *Inorg. Chem.* **2017,** *56* (21), 12914-12919.
9. Sieklucka, B.; Podgajny, R.; Przychodzeń, P.; Korzeniak, T., Engineering of octacyanometalate-based coordination networks towards functionality. *Coord. Chem. Rev.* **2005,** *249* (21-22), 2203-2221.
10. Willemin, S.; Larionova, J.; Clérac, R.; Donnadieu, B.; Henner, B.; Le Goff, X. F.; Guérin, C., Crystal structures and intercalation reactions of three-dimensional coordination polymers $[M(H_2O)_2]_2[Mo(CN)_8]\cdot 4H_2O$ (M = Co, Mn). *Eur. J. Inorg. Chem.* **2003,** (10), 1866-1872.
11. Rombaut, G.; Verelst, M.; Golhen, S.; Ouahab, L.; Mathonière, C.; Kahn, O., Structural and Photomagnetic Studies of Two Compounds in the System $Cu^{2+}/Mo(CN)_8^{4-}$: From Trinuclear Molecule to Infinite Network. *Inorg. Chem.* **2001,** *40* (6), 1151-1159.
12. Umeta, Y.; Chorazy, S.; Nakabayashi, K.; Ohkoshi, S. I., Synthesis of the Single-Crystalline Form and First-Principles Calculations of Photomagnetic Copper(II) Octacyanidomolybdate(IV). *Eur. J. Inorg. Chem.* **2016,** *2016* (13-14), 1980-1988.
13. Sra, A. K.; Rombaut, G.; Lahitête, F.; Golhen, S.; Ouahab, L.; Mathonière, C.; Yakhmi, J. V.; Kahn, O., Hepta/octa cyanomolybdates with Fe^{2+}: influence of the valence state of Mo on the magnetic behavior. *New J. Chem.* **2000,** *24* (11), 871-876.
14. Rombaut, G.; Mathonière, C.; Guionneau, P.; Golhen, S.; Ouahab, L.; Verelst, M.; Lecante, P., Structural and photo-induced magnetic properties of M_2^{II} $[W^{IV}(CN)_8]\cdot xH_2O$ (M = Fe and x=8, Cu and x=5). Comparison with $Cu_2^{II}[Mo^{IV}(CN)_8]\cdot 7.5H_2O$. *Inorg. Chim. Acta* **2001,** *326* (1), 27-36.
15. Ma, X. D.; Yokoyama, T.; Hozumi, T.; Hashimoto, K.; Ohkoshi, S. I., Electronic states and local structures of the photomagnetic Cu-Mo cyanides $Cu_2Mo(CN)_8\cdot 8H_2O$ and $Cs_{0.5}Cu_{1.75}Mo(CN)_8\cdot 1.5H_2O$ studied by X-ray absorption fine structure spectroscopy. *Phys. Rev. B* **2005,** *72* (9), 094107-1-094107-6.
16. Ohkoshi, S.-i.; Shiraishi, K.; Nakagawa, K.; Ikeda, Y.; Stefanczyk, O.; Tokoro, H.; Namai, A., Reversible photoswitchable ferromagnetic thin film based on a cyanido-bridged RbCuMo complex. *J. Mater. Chem. C* **2021,** *9* (9), 3081-3087.

17. Hennig, H.; Rehorek, A.; Rehorek, D.; Thomas, P., Photocatalytic systems. LXIII. Intervalence transfer (IT) behaviour and IT photochemistry of mixed-valence compounds with cyanometallates. *Inorg. Chim. Acta* **1984,** *86* (1), 41-49.
18. Aguilà, D.; Prado, Y.; Koumousi, E. S.; Mathonière, C.; Clérac, R., Switchable Fe/Co Prussian Blue Networks and Molecular Analogues. *Chem. Soc. Rev.* **2016,** *45* (1), 203-224.
19. Zhang, W.; Sun, H. L.; Sato, O., Synthesis, characterization, and photoresponsive properties of a series of Mo(IV)-Cu(II) complexes. *Dalton Trans.* **2011,** *40* (12), 2735-2743.
20. Bridonneau, N.; Chamoreau, L. M.; Gontard, G.; Cantin, J. L.; von Bardeleben, J.; Marvaud, V., A High-Nuclearity Metal-Cyanide Cluster $[Mo_6Cu_{14}]$ with Photomagnetic Properties. *Dalton Trans.* **2016,** *45* (23), 9412-9418.
21. Magott, M.; Stefanczyk, O.; Sieklucka, B.; Pinkowicz, D., Octacyanidotungstate(IV) Coordination Chains Demonstrate a Light-Induced Excited Spin State Trapping Behavior and Magnetic Exchange Photoswitching. *Angew. Chem. Int. Ed.* **2017,** *56* (43), 13283-13287.
22. Mitroova, Z.; Mihalik, M.; Zentko, A.; Bokor, M. Z.; Kamarás, K., Synthesis, structural and magnetic properties of $TM_2^{2+}[Mo^{IV}(CN)_8]\cdot nH_2O$. *Ceramics-Silikaty* **2005,** *49* (3), 181-187.
23. McGarvey, B. R., The Structure of the Octacyanomolybdate(V) and -tungstate(V) Ions from Electron Spin Resonance. *Inorg. Chem.* **1966,** *5* (3), 476-479.
24. Arimoto, Y.; Ohkoshi, S. I.; Zhong, Z. J.; Seino, H.; Mizobe, Y.; Hashimoto, K., Photoinduced Magnetization in a Two-Dimensional Cobalt Octacyanotungstate. *J. Am. Chem. Soc.* **2003,** *125* (31), 9240-9241.
25. Meske, W.; Babel, D., Kristallstrukturen von Octacyanomolybdaten (IV), I $Ag_4(NH_3)_5Mo(CN)_8\cdot 1,5\,H_2O$. *Z. Naturforsch. B* **1988,** *43* (9), 1167-1173.
26. Kroeker, S.; Wasylishen, R. E.; Hanna, J. V., The Structure of Solid Copper(I) Cyanide: A Multinuclear Magnetic and Quadrupole Resonance Study. *J. Am. Chem. Soc.* **1999,** *121* (7), 1582-1590.
27. Harris, K. J.; Wasylishen, R. E., A ^{13}C and ^{15}N solid-state nmr study of structural disorder and aurophilic bonding in Au^{I} and Au^{III} cyanide complexes. *Inorg. Chem.* **2009,** *48* (5), 2316-2332.
28. Carvajal, M. A.; Caballol, R.; de Graaf, C., Insights on the Photomagnetism in Copper Octacyanomolybdates. *Dalton Trans.* **2011,** *40* (28), 7295-303.
29. Bunau, O.; Arrio, M. A.; Sainctavit, P.; Paulatto, L.; Calandra, M.; Juhin, A.; Marvaud, V.; Cartier dit Moulin, C., Understanding the photomagnetic behavior in copper octacyanomolybdates. *J. Phys. Chem. A.* **2012,** *116* (34), 8678-83.
30. Carvajal, M. A.; Reguero, M.; de Graaf, C., On the Mechanism of the Photoinduced Magnetism in Copper Octacyanomolybdates. *Chem. Commun.* **2010,** *46* (31), 5737-5739.
31. Qi, X.; Pillet, S.; de Graaf, C.; Magott, M.; Bendeif, E. E.; Guionneau, P.; Rouzieres, M.; Marvaud, V.; Stefanczyk, O.; Pinkowicz, D.; Mathoniere, C., Photoinduced Mo-CN Bond Breakage in Octacyanomolybdate Leading to Spin Triplet Trapping. *Angew. Chem. Int. Ed.* **2020,** *59* (8), 3117-3121.
32. Stefańczyk, O.; Majcher, A. M.; Rams, M.; Nitek, W.; Mathonière, C.; Sieklucka, B., Photo-induced magnetic properties of the $[Cu^{II}(bapa)]_2[Mo^{IV}(CN)_8]\cdot 7H_2O$ molecular ribbon. *J. Mater. Chem. C* **2015,** *3* (33), 8712-8719.
33. Herrera, J. M.; Marvaud, V.; Verdaguer, M.; Marrot, J.; Kalisz, M.; Mathonière, C., Reversible Photoinduced Magnetic Properties in the Heptanuclear Complex $[Mo^{IV}(CN)_2(CN\text{-}CuL)_6]^{8+}$: A Photomagnetic High-Spin Molecule. *Angew. Chem. Int. Ed.* **2004,** *43* (41), 5468-5471.
34. Li, D.-f.; Yang, D.-x.; Li, S.-a.; Tang, W.-x., The encapsulation of $[Cu(en)_2]^{2+}$(en= ethylenediamine) by a novel three-dimensional Cu^{II}–Mo^{IV} bimetallic porous coordination polymer containing zigzag-ladder structure. *Inorg. Chem. Commun.* **2002,** *5* (10), 791-795.
35. Zhan, S.-Z.; Wang, J.-G.; Zhao, B.-T.; Huang, Z.-Y.; Cai, M.-L., Poly [bis [bis (ethylenediamine) copper (II)]-tetra-μ-cyano-[tetracyanomolybdate (IV)]]. *Acta Crystallogr. Sect. E: Structure Reports Online* **2006,** *62* (8), m1845-m1846.

General conclusions and perspectives

Photomagnetic materials are of great interest for their addressable magnetic properties by light stimulus. The majority of the photomagnetic studies focus on spin crossover in Fe^{II} complexes or metal-to-metal charge transfer in Fe/Co Prussian Blue networks and molecular analogues. The aim of this thesis is to gain more insights into the photomagnetic mechanisms for complexes based on peculiar 4d/5d octacyanidometallate building blocks, $[M^{IV}(CN)_8]^{4-}$ (M = Mo, W), which are much less investigated. We have carried out our research work on ionic salts with discrete $[M(CN)_8]^{4-}$ anions to understand intrinsic photomagnetic properties of $[M^{IV}(CN)_8]^{4-}$ building blocks and on Cu^{2+}-$[M(CN)_8]^{4-}$ based coordination networks to understand the MMCT process between Cu^{2+} and $[M(CN)_8]^{4-}$.

In chapter I, a general introduction about photomagnetic coordination compounds is presented, followed by a summary of the recent progresses on photomagnetic materials based on octacyanidometallates.

In chapter II, we have focused on the study of the ionic salts in which the $[M^{IV}(CN)_8]^{4-}$ anion is compensated by different alkali cations. Remarkably, the photocrystallography studies at 10 K for $K_4Mo(CN)_8\cdot 2H_2O$ (**1**) and $Rb_4Mo(CN)_8\cdot 2H_2O$ (**3**) unequivocally reveal the photoinduced dissociation of one Mo-C bond in the photoinduced triplet state to generate an isolated CN^- anion. We have shown that the incorporation of $[Mo^{IV}(CN)_8]^{4-}$ with different alkali cations (K^+ (**1**), Rb^+ (**3**), Cs^+ (**4**) and Na^+ (**5**)) leads to different photomagnetic behaviors with markedly different relaxation temperatures. The photomagnetic results reveal that the increase of alkali cations radius facilitates the observation of higher relaxation temperatures. The probable reason is that the bigger size of alkali cations such as Rb^+ and Cs^+ affords more free space in the structure to allow the occurrence of the isomerization of the broken cyanide ligand during relaxation. Surprisingly, no photomagnetic property is demonstrated for $A_4[W(CN)_8]\cdot x H_2O$ (A = K^+ (**7**), Rb^+ (**8**), Cs^+ (**9**)).

In chapter III, a series of new ionic salts based on $[M^{IV}(CN)_8]^{4-}$ charge balanced with coordination cations, $\{Zn(en)_3\}^{2+}$ (**10**) and $[\{M'(tren)\}_3(\mu\text{-tren})]^{6+}$ (M' = Zn^{II} (**11**), Cd^{II} (**12**), Cu^{II} (**13**)), are studied. The photomagnetic properties based on $[Mo^{IV}(CN)_8]^{4-}$ have also been confirmed as a photo-induced singlet-triplet crossover on the $[Mo(CN)_8]^{4-}$. The incorporation of $[Mo^{IV}(CN)_8]^{4-}$ with $\{Zn(en)_3\}^{2+}$ and $[\{M'(tren)\}_3(\mu\text{-tren})]^{6+}$ cations leads to a high thermal stability of the photoexcited state (relaxation temperature above 200 K). Different with octacyanidomolybdate(IV) based complexes, the tungsten analogue $[Zn(en)_3]_2[W(CN)_8]\cdot 5H_2O$ (**14**) is not photomagnetic. However, a significant photomagnetic effect is confirmed for $[\{Zn(tren)\}_3(\mu\text{-tren})]_2[W(CN)_8]_3\cdot$solv. (**15**).

In chapter IV, the photomagnetic effect of the $[Mo^{IV}(CN)_8]^{4-}$ unit is weak in $Cd_2[Mo^{IV}(CN)_8]\cdot x H_2O$ (**16**) when all cyanides are acting as bridges in a three dimensional network. The presence of Cu^I in $KCu^ICu^{II}[Mo(CN)_8]\cdot x H_2O$ (**17**) and $K_2Cu^I_3(\mu\text{-}CN)[Mo(CN)_8]\cdot 4H_2O$ (**18**) indicates a possible MMCT process during synthesis in solution. Both **17** and **18** are photomagnetic, and the preliminary results suggest the possible presence of MMCT mechanism for **17** and S-T mechanism for **18**. Unlike molybdenum, the $[W^{IV}(CN)_8]^{4-}$ building block is not photomagnetic in $K_2Cu^I_3(\mu\text{-CN})[Mo(CN)_8]\cdot 4H_2O$ (**19**). The preliminary photomagnetic studies for $[Cu(en)_2]_2[Mo(CN)_8]$ (**20**) and $[Cu(en)]_2[Cu(en)_2]_2[Mo(CN)_8]_2\cdot 2MeOH\cdot 5H_2O$ (**21**) also suggest S-T mechanism for **20**, and metal-to-metal charge transfer (MMCT) mechanism for **21**, respectively. However, the clear understanding of photomagnetic mechanism for the compounds in this chapter needs further investigations.

Interestingly, our results have provided solid proofs for photoinduced dissociation of one Mo-C bond in the photoinduced triplet state, which could be thermally relaxed around 50 K. However, to fully understand the high thermally stablity of the photoexcited state (relaxation temperature around 300 K) observed in some systems reported in this thesis, we propose that an isomerization of cyanide ligand probably occurs, which needs other experimental proofs. Therefore, other measurements are necessary such as photocrystallography, synchrotron X-ray radiation, IR spectra and UV-Vis spectra. For example, it is interesting to probe IR vibrational

spectroscopy, notably, the Mo–C bond stretch, which occurs at much lower wavenumbers (< 600cm^{-1}).[1] NMR spectroscopy (^{13}C and ^{15}N) would be also a powerful tool in the characterization of binding modes of cyano group.

This phD work has made important progress for this research field, but some results are still unclear. To further explain the crystal structure-photomagnetic property relationship in this class of materials, studies of other well-defined molecular compounds with low nuclearity are still important. This will help the understanding the influence of structural characteristics (such as the geometry of molybdenum site or copper site, the intermolecular interactions, the Mo-C-N bond angles, Cu-N-C bond angles and Cu-N bond distances). The in-depth studies are also needed to reveal the different photomagnetic behaviors between Mo and W compounds.

Our work also opens perspectives for photochemical preparation of new anisotropic building blocks $[Mo^{IV}(CN)_7]^{3-}$ or possible $[Mo^{IV}(CN)_6]^{2-}$ by photoinduced cleavage of cyanide ligands,[2, 3] which provides more opportunities for producing new networks similar to Prussian Blue analogue. It is also interesting to investigate the photomagnetic properties of networks based on $[Mo^{IV}(CN)_7]^{3-}$. In addition, it is worth to study if this photoinduced dissociation of one M-C bond in the photoexcited state is widespread in other cyano metal complexes, i.e., $[Mo^{III}(CN)_7]^{4-}$, $[Nb^{IV}(CN)_8]^{4-}$ and $[Re^{IV}(CN)_7]^{3-}$.[4-6] For example, the networks made of $[Mo^{III}(CN)_7]^{4-}$ form strongly anisotropic magnets. The cleavage of one Mo-C bond can generate $[Mo^{III}(CN)_6]^{3-}$. The resulted network will show less expected anisotropic magnetic behavior, due to a octahedral $[Mo^{III}(CN)_6]^{3-}$ building block with S = 3/2. This route can lead to the light control of magnetic anisotropic behavior. For the strategy of building efficient photomagnetic systems, our results show that the structral reorganization seems to be crucial to stablize high relaxation temperature, but it is not an easy task because this is very dependent on the structure.

References:

1. Hanusa, T. P., Cyanide Complexes of the Transition Metals. Encyclopedia of Inorganic Chemistry , D. J. Burkey2005 **2006,** 1–11.
2. Szklarzewicz, J.; Matoga, D.; Niezgoda, A.; Yoshioka, D.; Mikuriya, M., Missing Link in the Ligand-Field Photolysis of $[Mo(CN)_8]^{4-}$: Synthesis, X-ray Crystal Structure, and Physicochemical Properties of $[Mo(CN)_6]^{2-}$. *Inorg. Chem.* **2007,** *46* (23), 9531-9533.
3. Birk, F. J.; Pinkowicz, D.; Dunbar, K. R., The Heptacyanotungstate (IV) Anion: A New 5d Transition-Metal Member of the Rare Heptacyanometallate Family of Anions. *Angew. Chem. Int. Ed.* **2016,** *55* (38), 11368-11371.
4. Qian, K.; Huang, X. C.; Zhou, C.; You, X. Z.; Wang, X. Y.; Dunbar, K. R., A single-molecule magnet based on heptacyanomolybdate with the highest energy barrier for a cyanide compound. *J. Am. Chem. Soc.* **2013,** *135* (36), 13302-5.
5. Pinkowicz, D.; Rams, M.; Nitek, W.; Czarnecki, B.; Sieklucka, B., Evidence for magnetic anisotropy of $[Nb^{IV}(CN)_8]^{4-}$ in a pillared-layered Mn_2Nb framework showing spin-flop transition. *Chem. Commun.* **2012,** *48* (67), 8323-8325.
6. Freedman, D. E.; Jenkins, D. M.; Iavarone, A. T.; Long, J. R., A Redox-Switchable Single-Molecule Magnet Incorporating $[Re(CN)_7]^{3-}$. *J. Am. Chem. Soc.* **2008,** *130* (10), 2884-2885.

Appendix

Appendix

Appendix 1 - Physical techniques

1. Single crystal X-ray diffraction analysis

a. Data collection and reduction for **4-10, 14-16, 18** and **20** were performed on the Bruker Apex II instrument operating at 50 kV and 30 mA using molybdenum radiation Mo *K*α [λ = 0.71073 Å]. Data collection and reduction for **21** were performed on a Kappa Nonius-Brüker diffractometer (λ = 0.71071 Å). The crystal structures were solved by direct methods using SHELXT and refined using a F2 full-matrix least-squares technique of SHELXL2014 [1] included in the OLEX-2 1.2 software packages.[2] The non-H atoms were refined anisotropically adopting weighted full-matrix least squares on F2.

b. In collaboration with Dr. Sébastien Pillet in the University of Lorraine, data collection and reduction for **1** and **3** were performed on a SuperNova Microfocus diffractometer equipped with a two-dimensional ATLAS detector, using Mo *K*α radiation (λ = 0.71073 Å) and a Helijet He open-flow cryosystem.

   Diffraction data were first collected at 10 K in the ground state (GS) using ω scans. The unit-cell determination and data reduction were performed using the *CrysAlisPRO* program suit on the full data set. A numerical absorption correction was performed. The corresponding structure was refined in the space group *Pnma* on F^2 by weighted full matrix least-squares methods using the *SHELXL2014* program.[1]

   The sample was then irradiated at 10 K with a LED of 405 nm (P = 7 mW/cm^2) for 15 min, until the photo-stationary state was reached indicated by the color change of the crystal. Complete diffraction data were collected in the photo-stationary state at 10 K; no space-group change occurred with respect to the ground state (space group *Pnma*).

   Preliminary structural refinement indicated the simultaneous presence of ground state and photo-excited state structural configurations, so the photoconversion was not complete. As a consequence, the structural model consisted of the two structural configurations with respective populations $P_{\mathbf{1GS}}$ and $P_{\mathbf{1*PES}}$, with the constraint $P_{\mathbf{1GS}}$ + $P_{\mathbf{1*PES}}$ = 1. The GS configuration was introduced in the refinement as a rigid group, while the photo-excited configuration was freely refined with the constraint that the atomic displacement parameters of the ground state and photo-excited state being identical. The refinement converged to a refined population of the photo-irradiated state of $P_{\mathbf{1*PES}}$ = 0.53, indicating that about half of the crystal has been converted.

   The temperature was further raised to 70 K, above the thermal relaxation temperature, and then decreased to 10 K. Complete diffraction data were collected in the relaxed state at 10 K, which proved to be very similar to the 10 K ground state structure.

c. In collaboration with Dr. Dawid Pinkowicz in Jagiellonian University, data collection and reduction for **2** were performed using a Bruker D8 Quest Eco Photon50 CMOS diffractometer (Mo *K*α radiation, graphite monochromator). Absorption corrections, data reduction and unit cell refinements were performed using the SADABS and SAINT programs included in the Apex3 suite. The structure was solved using direct methods and refined anisotropically using weighted full-matrix least-squares on F^2.[1, 3] Hydrogen atoms of ligands were placed in calculated positions and refined as riding on the parent atoms.

d. In collaboration with Dr. Brice Kauffmann in IECB, University of Bordeaux, data collection and reduction for **11**, **13** and **17** were performed on a Microfocus rotating anode (Rigaku FRX) operating at 45 kV and 66 mA at the Cu *K*α edge (λ = 1.54184) with a partial chi goniometer. The X-ray source is equipped with high flux Osmic Varimax mirrors and a Dectris Pilatus 300 K detector.

The structural data presented as figures were prepared with the use of the OLEX-2 or diamond software. X-ray crystallographic files (CIF): CCDC 1914245, 1914246 and 1914247 contain the supplementary crystallographic data for the **1**, **1*** and $\mathbf{1_{relax}}$, respectively. CCDC 1915471 contains the supplementary crystallographic data for $[K(crypt\text{-}222)]_3[Mo^{IV}(CN)_7]\cdot 3CH_3CN$. CCDC 2083835, 2083836 and 2083837 contain the supplementary crystallographic data for **11**, **13** and **15**, respectively. These crystallographic

data can be obtained free of charge from the Cambridge Crystallographic Data Centre via www.ccdc.cam.ac.uk/data_request/cif.

Table A. 1 Experimental conditions of SXRD measurements.

Compounds	Diffractometer	Temperature/K
1, 3	SuperNova Microfocus	10
2	Bruker D8 Quest Eco Photon50 CMOS	100
4, 18	Bruker Apex II	120
5, 6, 8, 15	Bruker Apex II	150
7, 9, 10, 14, 16, 20	Bruker Apex II	RT
11, 13	Microfocus rotating anode (Rigaku FRX)	130
17	Microfocus rotating anode (Rigaku FRX)	RT
21	Kappa Nonius-Brüker diffractometer	RT

2. Powder X-ray diffraction (PXRD) analysis

PXRD analysis was performed on a PANalytical X'PERT MDP-PRO diffractometer (Cu-*K*α radiation) equipped with a graphite monochromator using the *θ*-*θ* Bragg-Brentano geometry. The sample was deposited on a silicon holder for BraggBrentano geometry.

3. Thermogravimetric analysis (TGA)

TGA was performed on NETZCH 402 ED with the protection of Ar.

4. Surface reflectivity measurements

Reflectivity measurements at room temperature were performed on a home-built system at different temperatures ranging from 10 to 300 K. The polycrystalline samples were grounded prior to any measurements. Heating and cooling rates were maintained at 4 K min^{-1} during the measurements. This setup collects the light reflected by the sample (sum of direct and diffuse reflected light) that is analyzed by a high-sensitivity Hamamatsu 10083CA spectrometer between 500 and 1000 nm. The spectra are compared to a white reference obtained with a NIST traceable standard for reflectance (SphereOptics, ref SG3054). The background, collected with the light source switched off, is subtracted from all measurements. The reflectivity can be plotted as a function of temperature, time, or wavelength. Different light emitting diodes (LEDs) operating between 385 and 940 nm bought from Thorlabs were used for excitation measurements. As the samples are potentially very photosensitive, the light exposure time was minimized during all the experiments keeping the samples in the dark except during the spectra measurements when white light is shined on the sample surface (P = 0.4 mW/cm^2). The temperature dependence of the reflectivity spectra was followed during a cycle of cooling−heating. For all the excitation/de-excitation experiments performed at 10 K, the sample was initially placed at this temperature keeping the sample in the dark to avoid any excitation.

5. FT-IR spectra

The FT-IR spectra were recorded in the range of 650 cm^{-1} - 4000 cm^{-1} on a Thermo-Fisher Nicolet™ 6700 ATR (attenuated total reflection) spectrometer equipped with a Smart iTR diamond window.

The IR spectra for **1** at 10 K were collected on a Nicolet 5700 FTIR spectrometer in the range 6000-1000 cm^{-1} with a resolution of 1 cm^{-1}. The sample was recrystallized on CaF_2 optical window, glued with silver paste to a copper sample holder on the cold finger of an Oxford Optistat V01, allowing temperature regulation in the range 9-300 K. Sample irradiation was carried out using a LED light source of 405 nm ($P \approx 20$ mW/cm^2).

6. UV−Vis absorption spectra

Solid-state UV−Vis absorption spectra at room temperature were recorded with a PerkinElmer Lambda 35 UV/Vis spectrophotometer equipped with a PerkinElmer Labsphere.

The UV-Vis spectra for **1** at 10 K were recorded with a Agilent CARY 5000 UV/Vis spectrophotometer. The sample was recrystallized on CaF_2 optical window, glued with silver paste to a copper sample holder on the cold finger of an Oxford Optistat V01, allowing temperature regulation in the range 9-300 K. Sample irradiation was carried out using a LED light source of 405 nm ($P \approx 20$ mW/cm^2).

7. Magnetic and photomagnetic measurements.

All magnetic properties were measured by a Quantum Design MPMS XL system in the range of temperatures 1.8−300 K. Photomagnetic studies were conducted on a smaller sample (ca. 0.5 mg) sealed in a small PVE bag fixed with a Scotch tape, blocked tightly between two transparent polypropylene films and mounted in the probe equipped with an optical fiber entry enabling the transmission of laser light of 405 nm line (P ≈ 3 mW/cm^2) into the sample space. Diamagnetism of the sample holders and of the constituent atoms (Pascal's tables) was accounted for in all the obtained magnetic and photomagnetic data. The magnetic properties (i.e., magnetization versus field at low temperatures and/or χT versus temperature, χ being the magnetic susceptibility and T the temperature) have been first studied in the dark. At 10 K, the samples were irradiated and the time dependence of the magnetic properties was followed during light irradiation. After the light excitations, magnetizations versus field at low temperature were measured. Then the samples were heated again to evaluate the persistence of the photo-induced changes from 2 K to 300 K. Finally, the compounds were measured again in the dark from 300 K to 10 K to check the reversibility of the photo-induced magnetic changes. All the magnetic curves shown below are normalized per Zn_2Mo, Cd_2Mo, Cu_2Mo, $KCu^{I}Cu^{II}Mo$ KCu^{I}_3Mo if needed. This normalization will allow an easier comparison for the discussion of the results.

8. Calculations

a. The analysis of the Geometry of metal center

The geometry of metal centers were obtained with the Continuous Shape Measures (CshM) analysis by the software of SHAPE v2.0.[4]

b. Hydrogen bonding calculation

The hydrogen bonding has been analyzed by the use of the software PLATON.[5]

c. Theoretical calculations

Geometry optimizations for the ground state **1** and photoexcited state (**1*$_{PEScal}$**) were done with the CRYSTAL09 program package[6] applying the B3LYP functional and one-electron basis sets taken from the internal library.[7-10] The exponents and contraction coefficients of the outer shells were optimized for the present structures. Full geometry optimizations were performed relaxing the lattice positions and unit cell parameters under the symmetry restrictions of the *Pnma* space group for both the ground state **1** and photoexcited state (**1*$_{PEScal}$**).

Complete active space self-consistent field (CASSCF) and complete active space second-order perturbation theory (CASPT2) calculations of the lower excitation energies and the magnetic anisotropy parameters were done with the MOLCAS 8.2 code[11] using a $Mo(CN)_8$ fragment embedded in 18 counter cations to model the ground state and a $Mo(CN)_7$ + CN--$(H_2O)_2$ cluster embedded in 13 counter cations to model the photoexcited triplet state.

The molecular orbitals were expanded in the ANO-RCC all electron basis sets[12-13]: Mo (6s, 5p, 4d, 2f), C and N (4s, 3p, 1d), O (3s, 2p), H (2s). Larger basis sets were tested and were found to give essentially the same results. The active space consists of 9 orbitals (2 CN π, 5 Mo-4d and 2 CN π* orbitals) and 6 electrons. The ions used to embed the central cluster are represented with the large core Hay and Wadt effective core potentials[14] with a net charge of +1. Test calculations in which an explicit all electron basis set was used for K does not significantly change the results but hugely increases the

computational cost. State-average CASSCF with 12 singlet and 12 triplets were performed. CASPT2 correlates all the electrons except the deep core ones (C, N, O-1s, Mo-1s...3p). The standard IPEA = 0.25 zeroth-order Hamiltonian was used and an imaginary shift of 0.15 Eh was added to the denominators to avoid the appearance of intruder states. The Cholesky decomposition is used to speed-up the handling of the two-electron integrals with a threshold of 10^{-3} Eh.

The same clusters were used for the time-dependent DFT calculations, which served to explore a wider range of excitation energies and reach shorter wavelengths than in the CASPT2 calculations. The calculations were done with the ORCA 4.1.1 program[15] using the B3LYP density functional. The def2-qzvpp basis set was used for all atoms[16] and the evaluation of the exact exchange term was accelerated through the RIJCOSX algorithm[17] with the universal def2 auxiliary basis set.[18] 150 singlet roots were determined and a fine grid for the numerical integration was specified (grid6).

Additional calculations were performed for **2** using the experimental structure. The large size of the K(crypt-222) countercations makes it unfeasible to include them in the calculations. This reduces the material model to an isolated $Mo^{IV}(CN)_7$ cluster, which might seem somewhat small. However, based on the observation that both for **1** and **1*$_{PES}$** the differences in the excitation energies obtained with this minimal cluster and those with the larger one are never larger than 0.15 eV. It was concluded that this minimal material model also provides useful information about the low energy spectrum of **2**. All other computational parameters were the same as for the calculations on **1** and **1*$_{PES}$**. The ground state of **1*$_{PES}$** and **2** corresponds to a triplet state and two singlet states of similar energy appear below 1 eV and a third one lies around 1.5 eV. All other singlet and triplet states are all at significantly higher energy. By extending the active space with π and π* orbitals of the CN groups, we could also identify ligand-to-metal and ligand-ligand excited states. The lowest relative energies of these states were calculated to be ~4.5 eV.

We have also compared the zero-field splitting or single-ion anisotropy parameters of **1*$_{PES}$** and **2**, as well as in the first excited triplet state in **1**. *D* and *E* were calculated following the effective Hamiltonian procedure. Cluster models of increasing size have been used for **1*$_{PES}$** and the triplet state of **1**, ranging from a simple $Mo(CN)_7$ or $Mo(CN)_8$ cluster in vacuum to more sophisticated representation with explicit waters and K ions, but as far as the ZFS is concerned, all these models give virtually the same values for *D* and *E*. Given that the lowest excited states are of MC character, the choice of the active space and the number of singlets and triplets in the spin-orbit CI is not critical.

References:

1. Sheldrick, G. M., A short history of SHELX. *Acta Crystallogr. Sect. A: Foundations of Crystallography* **2008,** *64* (1), 112-122.
2. Dolomanov, O. V.; Blake, A. J.; Champness, N. R.; Schroder, M., OLEX: new software for visualization and analysis of extended crystal structures. *J. Appl. Crystallogr.* **2003,** *36* (5), 1283-1284.
3. Sheldrick, G. M., Crystal structure refinement with SHELXL. *Acta Crystallogr. Sect. C: Struct. Chem.* **2015,** *71* (1), 3-8.
4. Llunell, M.; Casanova, D.; Cirera, J.; Alemany, M.; Alvarez, S., SHAPE, v. 2.0; University of Barcelona: Barcelona, Spain **2010**.
5. Spek, A., Single-crystal structure validation with the program PLATON. *J. Appl. Crystallogr.* **2003,** *36* (1), 7-13.
6. Dovesi, R.; Orlando, R.; Civalleri, B.; Roetti, C.; Saunders, V. R.; Zicovich-Wilson, C. M., CRYSTAL: a computational tool for the ab initio study of the electronic properties of crystals. *Z. Kristallogr.* **2005,** *220* (5/6), 571-573.
7. Corà, F.; Patel, A.; Harrison, N. M.; Roetti, C.; Catlow, C. R. A., Anab initio Hartree–Fock study of α-MoO3. *J. Mater. Chem.* **1997,** *7* (6), 959-967.

8. Schoenes, J.; Racu, A.-M.; Doll, K.; Bukowski, Z.; Karpinski, J., Phonons and crystal structures of the β-pyrochlore superconductors KOs2O6 and RbOs2O6 from micro-Raman spectroscopy. *Phys. Rev. B* **2008,** *77* (13), 134515.
9. Gatti, C.; Saunders, V.; Roetti, C., Crystal field effects on the topological properties of the electron density in molecular crystals: the case of urea. *J. Chem. Phys.* **1994,** *101* (12), 10686-10696.
10. Dovesi, R.; Roetti, C.; Freyria-Fava, C.; Prencipe, M.; Saunders, V., On the elastic properties of lithium, sodium and potassium oxide. An ab initio study. *Chem. Phys.* **1991,** *156* (1), 11-19.
11. F. Aquilante, J. A., R. K. Carlson, L. Chibotaru, M. G. Delcey, L. De Vico, I. Fernández- Galván, N. Ferré, L. M. Frutos, L. Gagliardi, M. Garavelli, A. Giussani, C. E. Hoyer, G. Li Manni, H. Lischka, D. Ma, P.-Å. Malmqvist, T. Müller, A. Nenov, M. Olivucci, T. B. Pedersen, D. Peng, F. Plasser, B. Pritchard, M. Reiher, I. Rivalta, A. Shapiro, J. Segarra-Martí, M. Stenrup, D. G. Truhlar, L. Ungur, A. Valentini, S. Vancoillie, V. Veryazov, V. P. Vysotskiy, O. Weingart, F. Zapata, R. Lindh, Molcas 8: New capabilities for multiconfigurational quantum chemical calculations across the periodic table. *J. Comput. Chem.* **2016,** *37* (5), 506-541.
12. Roos, B. O.; Lindh, R.; Malmqvist, P.-Å.; Veryazov, V.; Widmark, P.-O., Main group atoms and dimers studied with a new relativistic ANO basis set. *J. Phys. Chem. A* **2004,** *108* (15), 2851-2858.
13. Roos, B. O.; Lindh, R.; Malmqvist, P.-Å.; Veryazov, V.; Widmark, P.-O., New relativistic ANO basis sets for transition metal atoms. *J. Phys. Chem. A* **2005,** *109* (29), 6575-6579.
14. Hay, P. J.; Wadt, W. R., Ab initio effective core potentials for molecular calculations. Potentials for K to Au including the outermost core orbitals. *J. Chem. Phys.* **1985,** *82* (1), 299-310.
15. Neese, F., The ORCA program system. *WIREs Comput. Mol. Sci.* **2012,** *2* (1), 73-78.
16. Weigend, F.; Ahlrichs, R., Balanced basis sets of split valence, triple zeta valence and quadruple zeta valence quality for H to Rn: Design and assessment of accuracy. *Phys. Chem. Chem. Phys.* **2005,** *7* (18), 3297-3305.
17. Izsák, R.; Neese, F., An overlap fitted chain of spheres exchange method. *J. Chem. Phys.* **2011,** *135* (14), 144105.
18. Weigend, F., Accurate Coulomb-fitting basis sets for H to Rn. *Phys. Chem. Chem. Phys.* **2006,** *8* (9), 1057-1065.

Appendix 2 - List of publications

1. Qi, X.; Pillet, S.; de Graaf, C.; Magott, M.; Bendeif, E. E.; Guionneau, P.; Rouzieres, M.; Marvaud, V.; Stefanczyk, O.; Pinkowicz, D.; Mathoniere, C., Photoinduced Mo-CN Bond Breakage in Octacyanomolybdate Leading to Spin Triplet Trapping. *Angew. Chem. Int. Ed.;* 2**020**, *59* (8), 3117.

2. Qi, X.; Guionneau, P.; Lafon, E.; Perot, S.; Kauffmann, B.; Mathonière, C. New Photomagnetic Ionic Salts Based on $[Mo^{IV}(CN)_8]^{4-}$ and $[W^{IV}(CN)_8]^{4-}$ Anions. *Magnetochemistry;* **2021**, *7*, 97.

Résumé

Thèse de Xinghui QI

Ecole Doctorale des Sciences Chimiques de l'Université de Bordeaux EDSC N°40
Spécialité du doctorat : Physico-chimie de la Matière Condensée
Date de soutenance : 8 décembre 2021
Lieu : Visioconférence

Titre de la thèse :
Composés photomagnétiques à base de précurseurs $[M^{IV}(CN)_8]^{4-}$ (M = Mo et W)

Membres du jury :
Mme Corine Mathonière, Université de Bordeaux, directrice de thèse
Mme Li-Lin Zheng, Nanjing University, rapportrice
M. Talal Mallah, Université Paris Saclay, rapporteur
Mme Xin Bao, Nanjing University of Science and Technology, examinatrice
M. Guillaume Chastanet, Université de Bordeaux, examinateur
M. Mario Maglione, Université de Bordeaux, examinateur

Résumé

Au cours des deux dernières décennies, les mécanismes photomagnétiques pour des complexes $[M^{IV}(CN)_8]^{4-}$ (M = Mo, W) ont fait l'objet d'un débat continu. Par conséquent, des recherches sur ces systèmes sont nécessaires pour clarifier les comportements observés. Nous avons mené nos travaux de recherche dans deux directions: i) l'étude d'anions $[M(CN)_8]^{4-}$ discrets pour évaluer leurs propriétés photomagnétiques intrinsèques par l'assemblage structural judicieux de divers cations simples avec/sans ligands bloquants et de l'anion $[M(CN)_8]^{4-}$; ii) l'étude de complexes pontés par le cyanure pour examiner l'influence des groupes pontants sur le comportement photomagnétique de systèmes à base de $[M(CN)_8]^{4-}$ et le rôle du transfert de charge métal-métal impliquant les unités Cu^{II}-$[[M(CN)_8]^{4-}$. Dans le chapitre I, nous donnons une introduction générale sur les composés de coordination photomagnétiques avec un focus sur des matériaux photomagnétiques à base d'octacyanidométallates. Dans le chapitre II, nous avons systématiquement étudié les sels ioniques dans lesquels la charge négative du complexe $[M(CN)_8]^{4-}$ est compensée par différents cations alcalins : $A_4[M(CN)_8]\cdot xH_2O$ (A = cations alcalins). Nous avons mis en évidence pour la première fois dans ces systèmes une rupture photo-induite à 10 K d'une liaison Mo-CN. Cet effet est réversible par une augmentation de température. Dans le chapitre III, nous étendons nos travaux de recherche à d'autres composés ioniques en incorporant différents cations métalliques avec des ligands bloquants simples (i.e., $[Zn(en)_3]^{2+}$ (en = éthylènediamine) et $[\{M'(tren)\}_3(\mu\text{-tren})]^{6+}$ (M' = Cu^{2+}, Zn^{2+} et Cd^{2+} ; tren = tris(2-amino)éthylamine)). Dans le chapitre IV, pour mieux comprendre le processus de transfert d'électrons impliquant les unités Cu^{II}–NC–Mo^{IV}, nous nous sommes concentrées sur l'étude de systèmes Cu^{II}-$[M^{IV}(CN)_8]^{4-}$.

Mots clés: Photomagnétisme, Transition de spin, Commutation moléculaire, Chimie de coordination, Transfert d'electron.

Les matériaux photomagnétiques présentent un grand intérêt pour leurs propriétés magnétiques manipulables par irradiation lumineuse. Les systèmes photomagnétiques les plus étudiés sont les complexes à base d'ions Fe^{II} à conversion de spin et les complexes présentant un transfert de charge métal-métal (abrégé par la suite MMCT), comme notamment dans les analogues du bleu de Prusse $Co^{n+}/[Fe(CN)_6]^{m-}$. Après avoir rappelé dans le chapitre 1 les principaux résultats de la littérature sur ces deux types de systèmes, nous avons présenté les composés photomagnétiques contenant des complexes octacyanidometallates, $[M(CN)_8]^{4-}$ (M = Mo, W) qui ont été beaucoup moins étudiés que les analogues du bleu de Prusse. Nous avons montré que les mécanismes photomagnétiques de cette famille de composés étaient encore mal comprises. Le but de cette thèse est donc de mieux comprendre les mécanismes photomagnétiques de complexes construits à partir de blocs de construction à base d'ions 4d/5d, les octacyanidometallates, $[M(CN)_8]^{4-}$ (M = Mo, W). Nous avons donc effectué nos travaux de recherche d'abord sur des sels ioniques (chapitres 2 et 3) à base d'anions $[M(CN)_8]^{4-}$ isolés pour comprendre les propriétés photomagnétiques intrinsèques des blocs de construction $[M(CN)_8]^{4-}$. Ensuite, dans le chapitre 4, nous avons étudié des réseaux de coordination à base de $Cu^{2+}/[M(CN)_8]^{4-}$ pour comprendre le processus MMCT entre les entités Cu^{2+} et $[M(CN)_8]^{4-}$.

Dans le chapitre I, une introduction générale sur les composés de coordination photomagnétiques est présentée, suivie d'un résumé des progrès récents sur les matériaux photomagnétiques à base d'octacyanidométallates. Il est important de noter que dans toutes les études reportées dans la littérature sur les systèmes à base d' octacyanidométallates, il y a toujours des discussions sur les mécanismes photomagnétiques impliquant soit le processus MMCT entre les entités Cu^{2+} et $[M(CN)_8]^{4-}$, soit une transition singulet (S=0) – triplet (S=1) (notée par la suite S-T) sur l'entité $[Mo(CN)_8]^{4-}$, soit les deux mécanismes en même temps (Figure R.1).

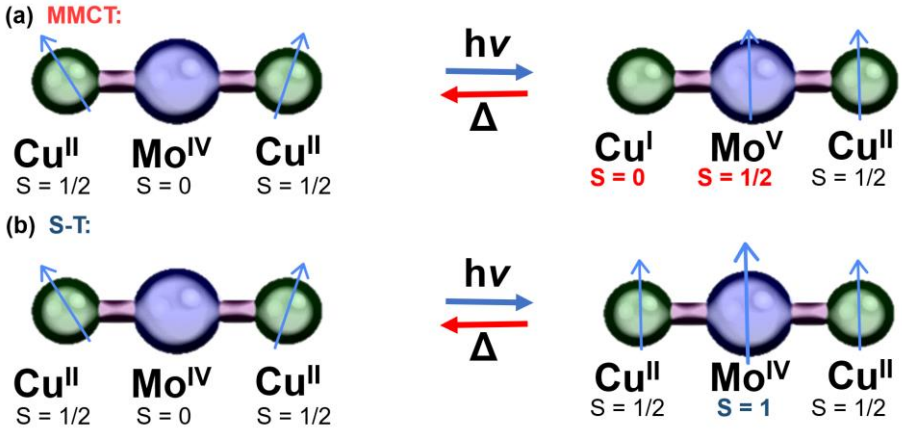

Figure R.1 Illustration schématique de (a) un transfert de charge métal-métal induit par la lumière (MMCT) et (b) une transition singulet-triplet (S-T) dans le système $Cu^{2+}/[Mo(CN)_8]^{4-}$.

Dans le chapitre II, nous avons réalisé des études systématiques sur des sels ioniques dans lesquels la charge négative de $[M^{IV}(CN)_8]^{4-}$ est compensée par différents cations alcalins. Avant irradiation, toutes les unités $[M^{IV}(CN)_8]^{4-}$ sont diamagnétiques, les 2 électrons des ions Mo^{4+} ou W^{4+} étant appariés sur la même orbitale, conséquence de la géométrie octa-coordinée autour de l'ion métallique. De façon remarquables, les études spectroscopiques, cristallographiques et magnétiques sur le complexe $K_4Mo(CN)_8{\cdot}2H_2O$ (**1**) révèlent la dissociation photo-induite d'une liaison Mo-C avec la formation d'un état triplet (S=1) à la fois à l'état solide et en solution (Figure R.2). Ces études expérimentales ont été complétées par des études théoriques qui valident nos interprétations.

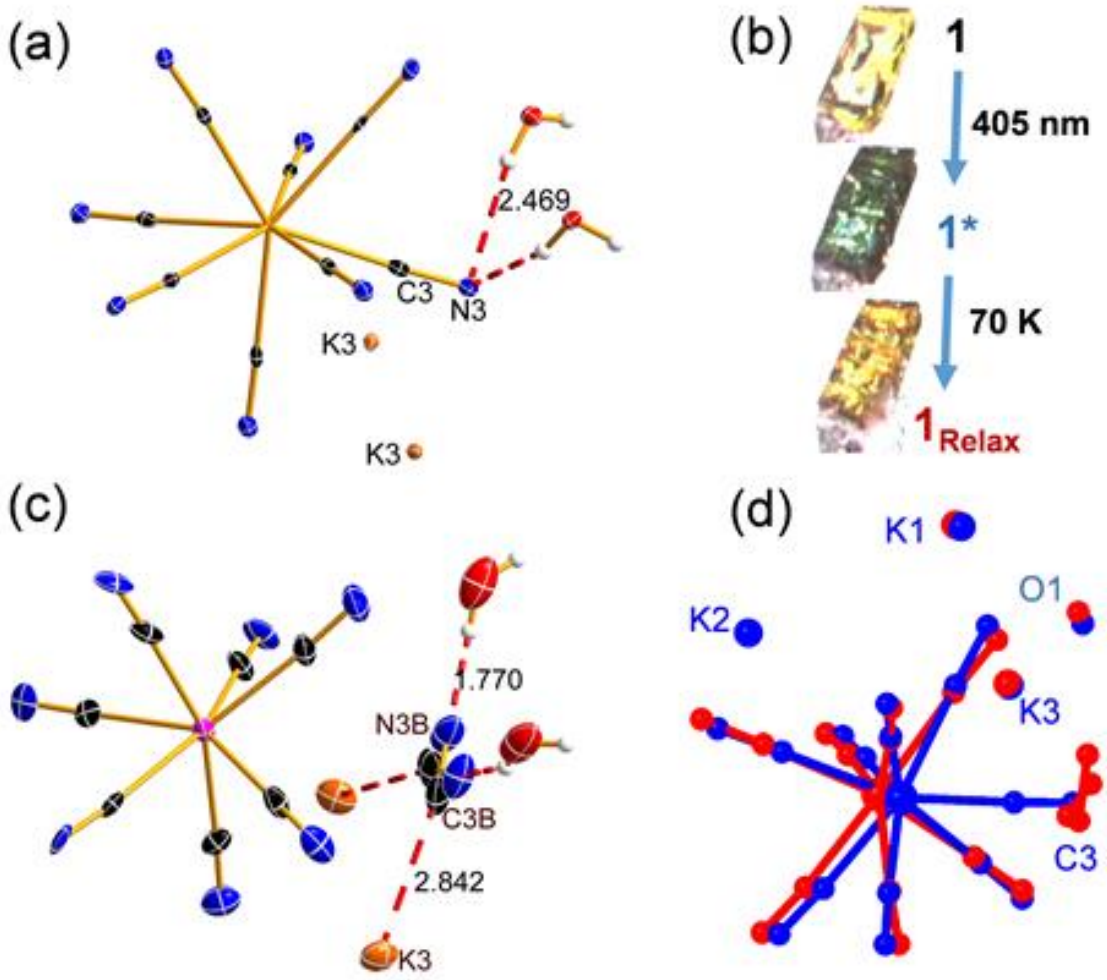

Figure R.2 Structures cristallines du composé $K_4Mo(CN)_8 \cdot 2H_2O$ (**1**) représentées avec des ellipsoïdes thermiques de probabilité de 70 % pour **1** (a), $\mathbf{1^*_{PES}}$ (état obtenu après photo-excitation) (c) avec liaisons H (lignes en pointillés rouges). (b) Structrues cristallines pour **1**, **1*** et $\mathbf{1_{relax}}$ (état obtenu après photo-excitation suivie de la relaxation thermique) à 10 K. (d) Superposition des fragments pertinents pour **1** (bleu) et **1*** (rouge).

Dans le chapitre II, nous avons également montré que l'incorporation de différents cations alcalins (K^+ (**1**), Rb^+ (**3**), Cs^+ (**4**), Na^+ (**5**)) avec l'unité de $[Mo^{IV}(CN)_8]^{4-}$ conduit à des comportements photomagnétiques différents présentant une relaxation se déroulant à différente températures (Tableau R.1). Il convient de noter que les mêmes études de $Rb_4Mo(CN)_8 \cdot 2H_2O$ (**3**) démontrent également sans équivoque la dissociation photo-induite d'une liaison Mo-C dans l'état triplet photo-induit à 10 K, avec un taux de photo-conversion supérieur à celui mesuré pour le composé **1** (≈ 50 %). Malgré leurs similitudes structurales $K_4Mo(CN)_8 \cdot 2H_2O$ (**1**) présente une relaxation en une seule étape achevée à 65 K, le composé $Rb_4Mo(CN)_8 \cdot 2H_2O$ (**3**) présente une relaxation thermique plus complexe, avec deux étapes distinctes : une étape vers 65 K (comme pour le composé **1**), et une seconde étape qui se termine à 250 K. L'isomérisation possible de la liaison Mo-C≡N (c'est-à-dire Mo-N≡C) pour le ligand cyanure qui est éjecté de la sphère de coordination de l'ion métallique pourrait expliquer le comportement de relaxation en plusieurs étapes. Mais cette hypothèse exige d'autres preuves expérimentales pour être confirmée.

Tableau R.1 Résumé des paramètres structurales et des propriétés photomagnétiques des sels ioniques étudiés dans la thèse.

Composés	**1**	**3**	**4**	**5**
$d_{Mo...Mo}$/Å	7.53	7.81	8.56/7.73/7.83/7.83/7.50	6.58
Propriétés photomagnétiques	$\Delta\chi T$ = 0.37 cm^3 mol^{-1} K; T_{Relax} = 65 K	$\Delta\chi T$ = 0.6 cm^3 mol^{-1} K; T_{Relax} = 75 K and 250 K	$\Delta\chi T$ = 0.6 cm^3 mol^{-1} K; T_{Relax} = 250 K	Pas de réponse photomagnétique
Composés	**10**	**11**	**13**	**15**
$d_{Mo...Mo}$/Å	9.48	9.65-9.80	9.46-9.48	9.40-9.45
Propriétés photomagnétiques	$\Delta\chi T$ = 1.2 cm^3 mol^{-1} K; T_{Relax} = 300 K	$\Delta\chi T$ = 0.89 cm^3 mol^{-1} K; T_{Relax} = 300 K, relaxation complète (χT = 0 cm^3 mol^{-1} K)	$\Delta\chi T$ = 0.89 cm^3 mol^{-1} K; T_{Relax} = 300 K, relaxation partielle (χT = 0.2 cm^3 mol^{-1} K)	$\Delta\chi T$ = 0.66 cm^3 mol^{-1} K; T_{Relax} = 250 K Relaxation complète (χT = 0.8 cm^3 mol^{-1} K)

Dans le chapitre III, nous avons préparé de nouveaux composés de coordination en mélangeant les anions $[M^{IV}(CN)_8]^{4-}$ avec des cations de plus grande taille que les cations alcalins. Nous avons étudié l'incorporation de $[Mo^{IV}(CN)_8]^{4-}$ avec différents cations de coordination $\{Zn(en)_3\}^{2+}$ (**10**) et $[\{M'(tren)\}_3(\mu\text{-tren})]^{6+}$ (M' = Zn^{II} (**11**), Cd^{II} (**12**), Cu^{II} (**13**)). La structure du composé **11** est présentée Figure R.3.

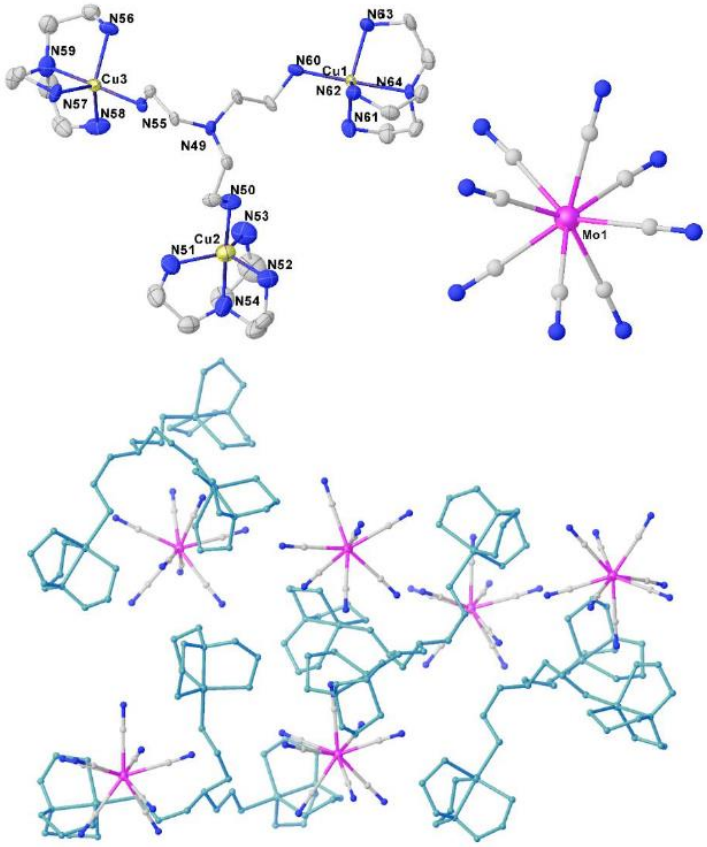

Figure R.3 (en haut) Fragments sélectionnés de $[\{Cu(tren)\}_3(\mu\text{-tren})]^{6+}$ (gauche), $[Mo(CN)_8]^{4-}$ (droit) avec label des atomes. (en bas) Unité asymétrique de **13** (sans les molécules de solvant) avec $[\{Cu(tren)\}_3(\mu\text{-tren})]^{6+}$ unités en turquoise. Codes couleurs : N, bleu ; C, gris ; Cu, jaune ; Mo, rose.

Les propriétés photomagnétiques de ces composés ont été étudiées et montrent l'observation de températures de relaxation plus élevées (Tableau R.1). Les résultats

photomagnétiques pour ces sels ioniques suggèrent que l'augmentation de la taille des cations conduit à un empilement cristallin moins dense comme le montrent les valeurs de $d_{Mo...Mo}$ dans les différents composés synthétisés. Plus cette distance est grande, plus les températures de relaxation paraissent élevées. De manière étonnante, aucune propriété photomagnétique n'a été obtenue pour tous les analogues analogies à base de tungstène, $[W^{IV}(CN)_8]^{4-}$, à l'exception d'un effet photomagnétique notable pour $[\{Zn(tren)\}_3(\mu\text{-tren})]_2[W(CN)_8]_3\cdot$solv. (**15**).

Dans le chapitre IV, l'effet photomagnétique de l'unité $[Mo^{IV}(CN)_8]^{4-}$ est faible dans le réseau 3D- $Cd_2[Mo^{IV}(CN)_8]\cdot xH_2O$ (**16**), réseau dans lequel tous les cyanures agissent comme des ponts dans le réseau tridimensionnel. La présence de Cu^+ dans le composés $KCu^ICu^{II}[Mo(CN)_8]\cdot xH_2O$ (**17**) et 3D- $K_2Cu^I_3(\mu\text{-CN})[Mo(CN)_8]\cdot 4H_2O$ (**18**) indique un possible processus MMCT lors de la synthèse en solution de ces composés. Les composés **17** et **18** sont photomagnétiques, et ces résultats préliminaires suggèrent la présence possible d'un mécanisme MMCT pour **17** et d'un mécanisme S-T pour **18**, respectivement. Contrairement à l'ion molybdène, l'unité $[W^{IV}(CN)_8]^{4-}$ n'est pas photomagnétique dans le réseau 3D, $K_2Cu^I_3(\mu\text{-CN})[Mo(CN)_8]\cdot 4H_2O$ (**19**). De plus, les études photomagnétiques préliminaires pour $[Cu(en)_2]_2[Mo(CN)_8]$ (**20**) et $[Cu(en)]_2[Cu(en)_2]_2[Mo(CN)_8]_2\cdot 2MeOH\cdot 5H_2O$ (en pour ethylène diamine) (**21**) suggèrent également un mécanisme S-T pour le composé **20**, et un mécanisme de transfert de charge métal-métal (MMCT) pour le composés **21**, respectivement. Cependant, la compréhension claire du mécanisme photomagnétique pour les composés de ce chapitre IV nécessite des investigations supplémentaires (Figure R. 3).

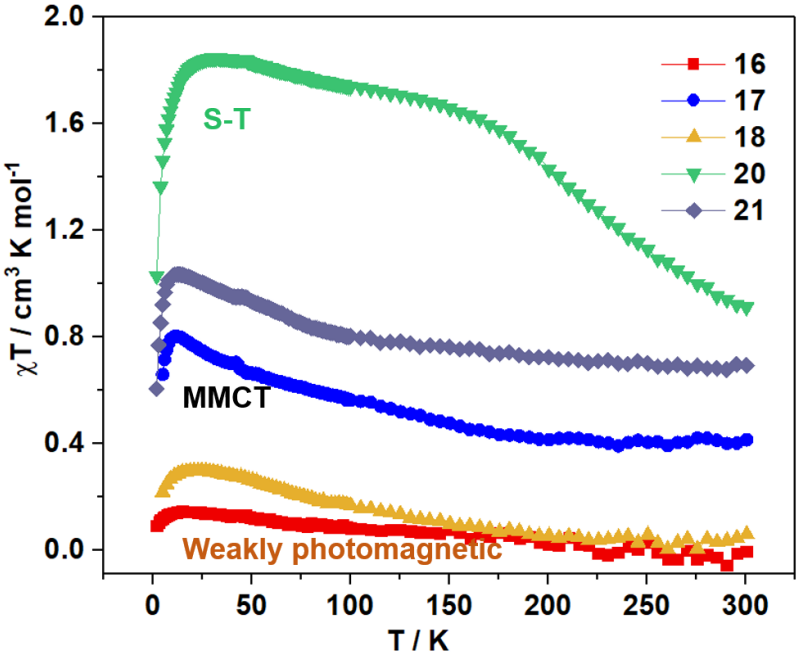

Figure R.3 Comparaison des courbes χT = f(T) pour les composés **16**, **17**, **18**, **20** and **21** mesurés après une irradiation à 405 nm à 10 K.

Pour conclure, nous nous sommes consacrés à la compréhension des mécanismes photomagnétiques pour ces composés de coordination à base d'octacyanidométallates. Pour atteindre cet objectif, nous avons délibérément synthétisé 21 composés, qui ont été préparés par des méthodes de cristallisation en solution. Des résultats fructueux ont été obtenus. Nos résultats montrent pour la première fois un mécanisme photomagnétique lié à une rupture de liaison Mo-CN photo-induite dans $K_4[Mo^{IV}(CN)_8]\cdot 2H_2O$ (**1**) et $Rb_4[Mo^{IV}(CN)_8]\cdot 2H_2O$ (**3**). De plus, nous avons effectué des études systématiques sur d'autres composés photomagnétiques à base d'octacyanométallates qui démontrent la complexité des mécanismes photomagnétiques dans ce type de systèmes. Cependant, pour encore mieux comprendre la relation entre les différentes structures et les propriétés photomagnétiques pour cette famille de composés, des mesures systématiques de tous les composés après irradiation à basse température sont nécessaires telles que la photocristallographie, la spectroscopie d'absorption X, les spectres IR, Raman et UV-Vis.

A ce jour, les travaux de cette thèse ont été publiés à 2 reprises :

1. Qi, X.; Pillet, S.; de Graaf, C.; Magott, M.; Bendeif, E. E.; Guionneau, P.; Rouzieres, M.; Marvaud, V.; Stefanczyk, O.; Pinkowicz, D.; Mathoniere, C., Photoinduced Mo-CN Bond Breakage in Octacyanomolybdate Leading to Spin Triplet Trapping. *Angew Chem Int Ed Engl;* **2020**, *59* (8), 3117.

2. Qi, X.; Guionneau, P.; Lafon, E.; Perot, S.; Kauffmann, B.; Mathonière, C. New Photomagnetic Ionic Salts Based on $[Mo^{IV}(CN)_8]^{4-}$ and $[W^{IV}(CN)_8]^{4-}$ Anions. *Magnetochemistry;* **2021**, *7*, 97.

Le 10 Janvier 2022.

Composés photomagnétiques à base de précurseurs $[M^{IV}(CN)_8]^{4-}$ (M = Mo et W)

Au cours des deux dernières décennies, les mécanismes photomagnétiques pour des complexes $[M^{IV}(CN)_8]^{4-}$ (M = Mo, W) ont fait l'objet d'un débat continu. Par conséquent, des recherches sur ces systèmes sont nécessaires pour clarifier les comportements observés. Nous avons mené nos travaux de recherche dans deux directions: i) l'étude d'anions $[M(CN)_8]^{4-}$ discrets pour évaluer leurs propriétés photomagnétiques intrinsèques par l'assemblage structural judicieux de divers cations simples avec/sans ligands bloquants et de l'anion $[M(CN)_8]^{4-}$; ii) l'étude de complexes pontés par le cyanure pour examiner l'influence des groupes pontants sur le comportement photomagnétique de systèmes à base de $[M(CN)_8]^{4-}$ et le rôle du transfert de charge métal-métal impliquant les unités Cu^{II}-$[[M(CN)_8]^{4-}$. Dans le chapitre I, nous donnons une introduction générale sur les composés de coordination photomagnétiques avec un focus sur des matériaux photomagnétiques à base d'octacyanidométallates. Dans le chapitre II, nous avons systématiquement étudié les sels ioniques dans lesquels la charge négative du complexe $[M(CN)_8]^{4-}$ est compensée par différents cations alcalins : $A_4[M(CN)_8]\cdot xH_2O$ (A = cations alcalins). Nous avons mis en évidence pour la première fois dans ces systèmes une rupture photo-induite à 10 K d'une liaison Mo-CN. Cet effet est réversible par une augmentation de température. Dans le chapitre III, nous étendons nos travaux de recherche à d'autres composés ioniques en incorporant différents cations métalliques avec des ligands bloquants simples (i.e., $[Zn(en)_3]^{2+}$ (en = éthylènediamine) et $[\{M'(tren)\}_3(\mu\text{-tren})]^{6+}$ (M' = Cu^{2+}, Zn^{2+} et Cd^{2+} ; tren = tris(2-amino)éthylamine)). Dans le chapitre IV, pour mieux comprendre le processus de transfert d'électrons impliquant les unités Cu^{II}−NC−Mo^{IV}, nous nous sommes concentré sur l'étude de systèmes Cu^{II}-$[M^{IV}(CN)_8]^{4-}$.
Mots clés: Photomagnétisme, Transition de spin, Commutation moléculaire, Chimie de coordination, Transfert d'electron.

Photomagnetic compounds based on $[M^{IV}(CN)_8]^{4-}$ (M = Mo and W)

During the last two decades, the photomagnetic mechanism involving the $[M^{IV}(CN)_8]^{4-}$ (M = Mo, W) building blocks have been subjected to a continuous debate. Therefore, investigations for these peculiar octacyanometallate systems are needed to clarify the observed behaviors. We carry out our research work in two directions: *i)* studies of discrete $[M(CN)_8]^{4-}$ anions to evaluate their intrinsic photoinduced magnetic properties by the judicious structural assembling of various simple types of cations with/without blocking ligands and $[M(CN)_8]^{4-}$ anions; *ii)* studies of the cyanide-bridged complexes to examine the influence of cyanide bridged groups on the photomagnetic behaviors in $[M(CN)_8]^{4-}$ systems and the role of the MMCT process in the Cu^{II}-$[M^{IV}(CN)_8]^{4-}$ units. In chapter I, we give a general introduction on the photomagnetic coordination compounds with a focus on photomagnetic materials based on octacyanidometallates. In chapter II, to better understand the photomagnetic mechanism based solely on the $[M(CN)_8]^{4-}$ units, we have systematically studied the ionic salts in which the negative charge of the $[M^{IV}(CN)_8]^{4-}$ complex is compensated by different alkali cations: $A_4[M(CN)_8]\cdot xH_2O$ (A = Alkali cations). For the first time, we have demonstrated a photo-induced rupture at 10 K of a Mo-CN bond. This effect is reversible by an increase in temperature. In chapter III, we extend our research work to other ionic compounds by incorporating different metal cations with simple blocking ligands (i.e., $[Zn(en)_3]^{2+}$ (en = ethylenediamine) and $[\{M'(tren)\}_3(\mu\text{-tren})]^{6+}$ (M' = Cu^{2+}, Zn^{2+} and Cd^{2+}; tren = tris(2-amino)ethylamine)). In chapter IV, we focus on the study of Cu^{II}-$[M^{IV}(CN)_8]^{4-}$ to gain insights into the electron transfer process.
Keywords: Photomagnetism, Spin Crossover, Molecular Switching, Coordination Chemistry, Electron Transfer.

Unité de recherche
ICMCB, UMR 5026, 87 avenue du Dr Albert Schweitzer 3600 Pessac